

SPECTROSCOPY OF LARGE MOLECULES IN THE GAS PHASE

by

Philip John Morgan

B.A., Thiel College, 2004

Submitted to the Graduate Faculty of
Arts and Sciences in partial fulfillment
of the requirements for the degree of
Doctor of Philosophy

University of Pittsburgh

2010

UNIVERSITY OF PITTSBURGH

ARTS AND SCIENCES

This dissertation was presented by

Philip John Morgan

It was defended on

August 17, 2010

and approved by

Committee Members:

Dr. Lillian T. Chong, Assistant Professor
Department of Chemistry, University of Pittsburgh

Dr. Sanford H. Leuba, Associate Professor
Department of Cell Biology and Physiology, University of Pittsburgh

Dr. David H. Waldeck, Professor and Departmental Chair
Department of Chemistry, University of Pittsburgh

Dissertation Director:

Dr. David W. Pratt, Professor
Department of Chemistry, University of Pittsburgh

Copyright © by Philip John Morgan

2010

David W. Pratt, PhD

SPECTROSCOPY OF LARGE MOLECULES IN THE GAS PHASE

Philip John Morgan, Ph.D.

University of Pittsburgh, 2010

Abstract

Structural and dynamical properties of molecular systems in both the ground and excited electronic states can be studied using rotationally resolved electronic spectroscopy in the gas phase. Analyses based on the collected experimental measurements and their spectral details supplemented by *ab initio* calculations provide the structural and dynamical information. In this work, relatively large molecules are studied, leading to conformational assignments of several molecules, the potential barriers for hindered methyl group torsional motion, the identity of different possible van der Waals complexes, evidence of excited state intramolecular proton transfer, and the determination of the ground and excited state dipole moments of several molecules.

FOREWORD

All that I have accomplished at the University of Pittsburgh could not be possible without the help and guidance of my advisor Professor David W. Pratt. His passion for science and patience in the lab has allowed me to broaden my views about science as well as accomplish my own research goals. I am very thankful to have had the opportunity to work under him.

I also owe a great deal of thanks to the many members of the Pratt group through the years. Without some of their help in my beginning years in the lab, learning the “high resolution” technique would not have been possible. In particular, Diane M. Miller proved to be an extremely valuable colleague and I cannot be thankful enough for her constant camaraderie in the laboratory. Dr. David Plusquellic provided constant support on programming issues regarding JB95 as well as his help on data analysis. Since 2004, Dr. Joseph “Rob” Roscioli, Alexei Nikolaev, Dr. Tri Nguyen, Dr. John Yi, Dr. Cheolhwa Kang, Dr. Leonardo Alvarez, Justin Young, Adam J. Fleisher, and Ryan Bird have all helped my experimental and theoretical work and the writing of my thesis, I thank them for all of their help.

Without the skill of the machine, glass, and electronic shop staff at the University of Pittsburgh, none of the experiments would have been possible. I am grateful for all of their help, especially Tom Gasmire and Jeff Sicher in the machine shop, Bob Greer in the glass shop, and Bob Muha, Chuck Fleishaker, and Jim McNerney in the electronic shop.

I would also like to thank my whole family for their support: My parents, brothers, relatives, and family-in-law. Most of all I would like to thank my wife, Brynn Ellen, who was always patient and provided encouragement, support, and love when I

needed it. I cannot thank her enough and cannot wait to begin the new chapter in our lives together.

Philip John Morgan

TABLE OF CONTENTS

1.0.	INTRODUCTION.....	1
1.1	REFERENCES.....	5
2.0	HIGH RESOLUTION ELECTRONIC SPECTROSCOPY OF <i>P</i>- VINYLPHENOL IN THE GAS PHASE.....	6
2.1	ABSTRACT.....	7
2.2	INTRODUCTION.....	7
2.3	EXPERIMENTAL.....	9
2.4	RESULTS AND INTERPRETATION.....	11
2.5	DISCUSSION.....	16
2.6	ACKNOWLEDGEMENTS.....	20
2.7	REFERENCES.....	21
3.0	MEASURING THE CONFORMATIONAL PROPERTIES OF 1, 2, 3, 6, 7, 8-HEXAHYDROPYRENE AND ITS VAN DER WAALS COMPLEXES.....	23
3.1	ABSTRACT.....	24
3.2	INTRODUCTION.....	24
3.3	EXPERIMENTAL.....	26
3.4	RESULTS.....	28
3.5	DISCUSSION.....	38
3.5.1	CONFORMATIONAL ASSIGNMENTS OF THE BARE MOLECULE.....	38
3.5.2	EXCITED STATE STRUCTURES OF HHP.....	39

3.5.3	AXIS TILTING.....	40
3.5.4	ASSIGNMENT OF COMPLEX I.....	43
3.5.5	ASSIGNMENT OF COMPLEX II.....	46
3.6	CONCLUSIONS.....	49
3.7	ACKNOWLEDGEMENTS.....	49
3.8	REFERENCES.....	50
4.0	HIGH RESOLUTION ELECTRONIC SPECTROSCOPY OF <i>o</i> - AND <i>m</i> - TOLUIDINE IN THE GAS PHASE. BARRIER HEIGHT DETERMINATIONS FOR THE METHYL GROUP TORSIONAL MOTIONS.....	52
4.1	ABSTRACT.....	53
4.2	INTRODUCTION.....	53
4.3	EXPERIMENTAL.....	54
4.4	RESULTS.....	56
4.5	DISCUSSION.....	66
4.5.1	GROUND AND EXCITED STATE CONFORMERS.....	66
4.5.2	METHYL TORSIONAL BARRIERS.....	70
4.5.3	ORIGINS OF THE TORSIONAL BARRIERS.....	73
4.6	CONCLUSIONS.....	75
4.7	ACKNOWLEDGEMENTS.....	75
4.8	REFERENCES.....	76
5.0	HIGH RESOLUTION ELECTRONIC SPECTROSCOPY OF 4- METHYLANISOLE IN THE GAS PHASE. BARRIER HEIGHT DETERMINATIONS FOR THE METHYL GROUP TORSIONAL MOTION....	78

5.1	ABSTRACT.....	79
5.2	INTRODUCTION.....	79
5.3	EXPERIMENTAL.....	80
5.4	RESULTS.....	82
5.5	DISCUSSION.....	89
	5.5.1 GROUND AND EXCITED STATE CONFORMERS.....	89
	5.5.2 METHYL TORSIONAL BARRIERS.....	92
	5.5.3 TORSIONAL DYNAMICS.....	95
5.6	CONCLUSIONS.....	98
5.7	ACKNOWLEDGEMENTS.....	98
5.8	REFERENCES.....	99
6.0	EXCITED STATE INTRAMOLECULAR PROTON TRANSFER IN 2-(2'-PYRIDYL)PYRROLE IN THE GAS PHASE VIA HIGH RESOLUTION ELECTRONIC SPECTROSCOPY.....	101
	6.1 ABSTRACT.....	102
	6.2 INTRODUCTION.....	102
	6.3 EXPERIMENTAL.....	105
	6.4 RESULTS.....	107
	6.5 DISCUSSION.....	111
	6.5.1 GROUND AND EXCITED STATE STRUCTURES.....	111
	6.5.2 ESIPT.....	116
6.6	CONCLUSIONS.....	119
6.7	ACKNOWLEDGEMENTS.....	119

6.8	REFERENCES.....	120
7.0	CONCLUSION.....	122
	APPENDIX A.....	124
	A.1 REFERENCES.....	125
	APPENDIX B PUSH-PULL MOLECULES IN THE GAS PHASE. STARK- EFFECT MEASUREMENTS OF THE PERMANENT DIPOLE MOMENTS OF <i>P</i> - AMINOBenzoic acid in its ground and electronically excited STATES.....	126
	B.1 ABSTRACT.....	127
	B.2 INTRODUCTION.....	127
	B.3 EXPERIMENTAL.....	129
	B.4 RESULTS.....	131
	B.5 DISCUSSION.....	139
	B.6 CONCLUSIONS.....	144
	B.7 ACKNOWLEDGEMENTS.....	145
	B.8 REFERENCES.....	146
	APPENDIX C ON THE ELECTRIC DIPOLE MOMENTS OF ASYMMETRIC TOPS. MEASUREMENT BY HIGH RESOLUTION ELECTRONIC SPECTROSCOPY IN THE GAS PHASE.....	148
	C.1 ABSTRACT.....	149
	C.2 INTRODUCTION.....	149
	C.3 EXPERIMENTAL.....	151
	C.4 RESULTS.....	153

C.5	DISCUSSION.....	162
C.6	ACKNOWLEDGEMENTS.....	170
C.7	REFERENCES.....	171
APPENDIX D	CHARGE TRANSFER BY ELECTRONIC EXCITATION: DIRECT MEASUREMENT BY HIGH RESOLUTION SPECTROSCOPY IN THE GAS PHASE.....	173
D.1	ABSTRACT.....	174
D.2	INTRODUCTION.....	174
D.3	EXPERIMENTAL.....	176
D.4	RESULTS.....	178
D.5	DISCUSSION.....	189
D.5.1	ELECTRIC DIPOLE MOMENTS OF THE BARE NAPHTHOL CONFORMERS.....	189
D.5.2	ELECTRIC DIPOLE MOMENTS OF THE NAPHTHOL AMMONIA COMPLEX.....	194
D.6	CONCLUSIONS.....	201
D.7	ACKNOWLEDGEMENTS.....	201
D.8	REFERENCES.....	202

LIST OF TABLES

Table 2.1. Inertial parameters derived from fits of the rotationally resolved S_1 - S_0 fluorescence excitation spectra of Bands I and II.....	15
Table 2.2. Comparison of experimental and <i>ab initio</i> rotational constants of trans-pCA and cis-pVP and trans-pVP.....	15
Table 2.3. Dominant one-electron excitations for the listed molecules.....	19
Table 3.1. Inertial parameters obtained from fits of the two origin bands, Bands I and II.....	33
Table 3.2. Inertial parameters obtained from fits of the two complex bands.....	37
Table 3.3. Comparison of the ground state rotational constants of Complex I with theoretical predictions for HHP-Ar.....	44
Table 3.4. Kraitchman analysis of Complex I and Complex II.....	45
Table 3.5. Comparison of the ground state rotational constants of Complex II with theoretical predictions for HHP-H ₂ O.....	47
Table 4.1. Rotational constants of <i>o</i> -toluidine in its ground and excited electronic states.....	62
Table 4.2. Rotational constants of <i>m</i> -toluidine in its ground and excited electronic states.....	65
Table 4.3. First-order torsion-rotation perturbation coefficients in the Hamiltonian and deduced barrier heights for e-symmetry torsional bands in <i>o</i> - and <i>m</i> -toluidine.....	71
Table 5.1. Rotational constants of 4MA in its ground and excited electronic states.....	88
Table 5.2. First-order torsion-rotation perturbation coefficients in the Hamiltonian and deduced barrier heights for e-symmetry torsional band in 4MA.....	88
Table 5.3. Experimental rotational constants of the origin bands ($0a_1 \leftarrow 0a_1$) of 4MA, 3MA, and 2MA in their ground and excited electronic states.....	90
Table 6.1. Inertial parameters of 2PP in its ground and excited electronic states.....	111

Table B.1. Experimental inertial parameters of PABA. (Parameters calculated at the MP2/6-31G** and CIS/6-31G** levels of theory have also been included for comparison.).....	134
Table B.2. Experimental dipole moment values for PABA. (Parameters calculated at the MP2/6-31G** and CIS/6-31G** levels of theory have also been included for comparison.).....	140
Table B.3. Comparison of experimental dipole moment values of PABA and AN.....	143
Table C.1. Experimental inertial parameters of 2ABN and 3ABN. Theoretical values calculated using the MP2/6-31G** and CIS/6-31G** methods also have been included for comparison.....	157
Table C.2. Experimental dipole moment values of 2ABN and 3ABN. Theoretical values calculated using the MP2/6-31G** and CIS/6-31G** methods also have been included for comparison.....	162
Table C.3. Predicted and measured dipole moments of 2ABN and 3ABN, compared to the previously measured values for AN, BN, and 4ABN, based on the vector addition model.....	167
Table D.1. Inertial parameters obtained from fits of trans- and cis-2HN origin bands...	180
Table D.2. Inertial parameters obtained from fits of 0_{a1} and 1_e bands of cis-2HNA....	181
Table D.3. Experimentally determined location of ammonia, treated as a point mass of 17 amu, within the inertial frame of cis-2HN and cis-2HNA, respectively. The error in the ammonia position is limited by the accuracy in rotational constants (0.1 MHz).....	182
Table D.4. Experimentally determined permanent dipole moments of trans- and cis-2HN.....	185
Table D.5. Experimentally determined permanent dipole moments of cis-2HNA along with theoretical values.....	189
Table D.6. Dominant one-electron excitations for the listed molecules.....	191
Table D.7. Electronic properties of cis-2HN and NH ₃ needed to use Equation 6. All quantities are expressed in the inertial frame of the complex.....	196
Table D.8. Comparison of both the induced and total dipole moments from the VAM of Equation 5 and from experiment.....	196

Table D.9. Calculated dipole-dipole, polarizability-electric field, and charge-charge interaction energies of cis-2HNA. Below, cis-2HN is designated as 1, and NH₃ is designated as 2. The angles θ_1 and θ_2 are the angles μ_1 and μ_2 make with the line R_{CM}.....200

LIST OF FIGURES

- Figure 2.1. Vibrationally resolved $S_1 \leftarrow S_0$ excitation spectrum of *p*CA (*p*VP). Bands I and II are split by $\sim 4 \text{ cm}^{-1}$ 11
- Figure 2.2. Rotationally resolved electronic excitation spectrum of Band I, with origin at $33,207.3 \text{ cm}^{-1}$. The lower part of the figure shows a close-up in the Q-branch region. In the close-up, the upper trace is the experimental spectrum, and the lower trace is the simulated spectrum. The individual lines represent the transitions responsible for the spectrum. The band was fit using a Voigt lineshape profile.....13
- Figure 2.3. Rotationally resolved electronic excitation spectrum of Band II, with origin at $33,211.8 \text{ cm}^{-1}$. See the Fig. 2.2 caption for more details.14
- Figure 2.4. Structures of styrene and phenol on top, left to right. Red arrows indicate the $S_1 \leftarrow S_0$ transition moment orientations. Structure of *trans* and *cis* conformers of *p*VP on bottom, left to right. Red and blue arrows indicate the two possible orientations of the $S_1 \leftarrow S_0$ transition moment for each conformer.....17
- Figure 2.5. Molecular orbitals for *trans*-*p*VP, *cis*-*p*VP, styrene and phenol. Dominant one-electron excitations for all four molecules are HOMO \rightarrow LUMO and HOMO-1 \rightarrow LUMO+1. All calculations were performed at the CIS/6-31G** level of theory.....19
- Figure 3.1. Chair-HHP (left) and boat-HHP (right).....26
- Figure 3.2. Vibrationally resolved $S_1 \leftarrow S_0$ excitation spectrum of HHP. The two origin bands, Band I and II, are split by $\sim 11 \text{ cm}^{-1}$ 29
- Figure 3.3. Rotationally resolved electronic excitation spectrum of Band I in HHP, with origin at 30648.0 cm^{-1} . The lower part of the figure shows a close-up of a portion of the Q-branch region. The upper trace is the experimental spectrum, and the lower trace is the simulated spectrum; the individual lines represent the transitions responsible for the spectrum.....31
- Figure 3.4. Rotationally resolved electronic excitation spectrum of Band II in HHP, with origin at 30658.8 cm^{-1} . The lower part of the figure shows a close up of a portion of the Q-branch region. The upper trace is the experimental spectrum, and the lower trace is the simulated spectrum; the individual lines represent the transitions responsible for the spectrum.....32
- Figure 3.5. A single rovibronic line in the Band II origin. No tunneling splitting was observed down to $\sim 5 \text{ MHz}$34

Figure 3.6. Rotationally resolved electronic excitation spectrum of Complex I, with origin at 30633.0 cm^{-1} . The lower part of the figure shows a close up of a portion of the P-branch region. The upper trace is the experimental spectrum, and the lower trace is the simulated spectrum; the individual lines represent the transitions responsible for the spectrum.....35

Figure 3.7. Rotationally resolved electronic excitation spectrum of Complex II, with origin at 30622.0 cm^{-1} . The lower part of the figure shows a close up of a portion of the R-branch region. The upper trace is the experimental spectrum, and the lower trace is the simulated spectrum; the individual lines represent the transitions responsible for the spectrum.....36

Figure 3.8. Naphthalene, left, and chair-HHP, right, depicting reorientation of *a* and *b* inertial axes. The *c* inertial axes are out of plane.....39

Figure 3.9. Axis-tilting in the spectrum of Complex I. The upper trace is the experimental spectrum, and the lower traces are the simulated spectra. The two arrows indicate two transition intensities that are affected by rotation of the *ac* plane about the *b* axis. The upper trace with 0° of *ac* axis tilt does not account for the obscured intensities, but the lower trace with 3° of *ac* axis tilt does.....42

Figure 3.10. Three possible Ar complex conformers for HHP.....43

Figure 4.1. Vibrationally resolved fluorescence excitation spectra of *o*-toluidine (top) and *m*-toluidine (bottom). (Ref. 2).....57

Figure 4.2. Rotationally resolved fluorescence excitation spectrum of the $0a_1$ band of *o*-toluidine, with origin at 34316.9 cm^{-1} . The lower part of the figure shows an expanded view of the Q-branch region. In this view, the upper trace is the experimental spectrum, and the lower trace is the simulated spectrum. Individual lines represent the transitions responsible for the spectrum. The band was fit using a Voigt lineshape profile.....58

Figure 4.3. Rotationally resolved fluorescence excitation spectrum of the $1e$ band of *o*-toluidine, with origin at 34320.2 cm^{-1} . The lower part of the figure shows an expanded view of the P-branch region. In this view, the upper trace is the experimental spectrum, and the lower trace is the simulated spectrum. Individual lines represent the transitions responsible for the spectrum. The band was fit using a Voigt lineshape profile.....59

Figure 4.4. Rotationally resolved fluorescence excitation spectrum of the $0a_1$ band of *m*-toluidine, with origin at 33820.2 cm^{-1} . The lower part of the figure shows an expanded view of the Q-branch region. In this view, the upper trace is the experimental spectrum, and the lower trace is the simulated spectrum. Individual lines represent the transitions responsible for the spectrum. The band was fit using a Voigt lineshape profile.....63

Figure 4.5. Rotationally resolved fluorescence excitation spectrum of the 1e band of <i>m</i> -toluidine, with origin at 33814.9 cm ⁻¹ . The lower part of the figure shows an expanded view of the Q-branch region. In this view, the upper trace is the experimental spectrum, and the lower trace is the simulated spectrum. Individual lines represent the transitions responsible for the spectrum. The band was fit using a Voigt lineshape profile.....	64
Figure 4.6. Ground state structures and S ₁ ← S ₀ TM orientation vectors in the <i>o</i> - and <i>m</i> -toluidines.....	67
Figure 4.7. Frontier molecular orbitals calculated at the CIS/6-31G(d,p) level of toluene, <i>o</i> -toluidine, <i>m</i> -toluidine, and aniline. All transitions are primarily HOMO→LUMO.....	68
Figure 4.8. Torsional energy curves of <i>o</i> -toluidine (left) and <i>m</i> -toluidine (right).....	72
Figure 5.1. Vibrationally resolved fluorescence excitation spectra of 4MA.....	83
Figure 5.2. Rotationally resolved fluorescence excitation spectrum of the 0a ₁ band of 4MA, with origin at 35400.5 cm ⁻¹ . The 1e band starts to grow in at the end of the R-branch. The lower part of the figure shows an expanded view of the P-branch region. In this view, the upper trace is the experimental spectrum, and the lower trace is the simulated spectrum. Individual lines represent the transitions responsible for the spectrum. The band was fit using a Voigt lineshape profile.....	86
Figure 5.3. Rotationally resolved fluorescence excitation spectrum of the 1e band of 4MA, with origin at 35402.6 cm ⁻¹ . The end of the 0a ₁ band is present within the P-branch of the 1e band. The lower part of the figure shows an expanded view of the R-branch region. In this view, the upper trace is the experimental spectrum, and the lower trace is the simulated spectrum. Individual lines represent the transitions responsible for the spectrum. The band was fit using a Voigt lineshape profile.....	87
Figure 5.4. Inertial axes and S ₁ ← S ₀ TM orientation vectors in the experimentally observed conformers of 4MA, 3MA and 2MA.....	91
Figure 5.5. Torsional energy curves of 4MA in its ground (S ₀) and first excited (S ₁) electronic states.....	94
Figure 5.6. Changes in electronic structure and methyl group orientation that occur upon electronic excitation.....	97
Figure 6.1. Image depicts the <i>syn</i> and <i>anti</i> conformers of 2PP.....	103
Figure 6.2. Fluorescence spectra of 2PP in n-hexane at 298 K depicting the two observed fluorescence bands; F ₁ is attributed to the normal fluorescence of <i>syn</i> 2PP and F ₂ is attributed to the fluorescence of the 2PP tautomer.....	104
Figure 6.3. LIF spectra obtained while monitoring either the F ₁ region (a) or F ₂ region (b). The UV/UV fluorescence dip spectrum (c) is obtained by probing at 32377 cm ⁻¹ ..	107

Figure 6.4. Rotationally resolved electronic excitation spectrum of the origin band transition of 2PP, with origin at 31404.1 cm ⁻¹ . The lower part of the figure shows a close up of a portion of the P-branch region. The upper trace is the experimental spectrum, and the lower trace is the simulated spectrum; the individual lines represent the transitions responsible for the spectrum.....	109
Figure 6.5. Rotationally resolved electronic excitation spectrum of the +144 vibrational band transition of 2PP. The lower part of the figure shows a close up of a portion of the P-branch region, as can be seen, no individual transitions can be detected due to their inherent linewidth from the extremely short excited state fluorescence lifetime.....	110
Figure 6.6. Ground state structures and S ₁ ← S ₀ TM orientation vectors in 2PP, pyridine and pyrrole. Red and blue arrows indicate the two possible orientations of the TM for 2PP. (TMs for pyridine and pyrrole were calculated from theory).....	113
Figure 6.7. Frontier molecular orbitals calculated at the CIS/6-31G(d,p) level of 2PP, pyridine, and pyrrole. The 2PP transition is solely HOMO→LUMO, whereas pyridine is a combination of HOMO→LUMO and HOMO-1→LUMO+1 and pyrrole a combination of HOMO-1→LUMO and HOMO→LUMO+1.....	115
Figure 6.8. Contour fit of the rotationally resolved electronic excitation spectrum of the +144 vibrational band transition of 2PP.....	117
Figure A.1. Trans- <i>p</i> -coumaric acid, PYP chromophore, on left and HBDI, GFP chromophore, on right.....	124
Figure B.1. Structure of PABA.....	128
Figure B.2. Low-resolution fluorescence excitation spectrum of PABA.....	132
Figure B.3. The field-free origin spectrum of PABA, occurring at 34172.8 cm ⁻¹ . Also shown in the bottom panel is a comparison of a small portion of the experimental spectrum (black trace) with two simulated spectra (blue trace), with and without a convoluted lineshape function.....	133
Figure B.4. Origin spectrum of PABA, at a calibrated electric field strength of 1184 V/cm. The black trace is the experimental spectrum, and the red trace is the simulated spectrum. The top portion shows the whole spectrum, while the bottom trace shows a close up of the highlighted section, again with and without a convoluted lineshape function.....	136

Figure B.5. Several simulations, both with and without a convoluted lineshape function, are compared to a portion of the Q-branch of the experimental spectrum to illustrate the dependence of the Stark spectra on the various dipole moment components. Simulation (a) is the zero-field spectrum, and traces (b) - (e) are at a calibrated field strength of 1184 V/cm. All simulations use the experimental rotational constants in Table 1. Simulation (b) assumes $\mu_a'' = 3.12$ and $\mu_a' = 4.21$ D, with the other components set to zero. The experimental spectrum (c) is shown for comparison. Below, simulation (d) is shown with $\mu_a'' = 3.12$, $\mu_a' = 4.21$, $\mu_b'' = 1.2$, $\mu_b' = 1.3$, $\mu_c'' = 0.0$ and $\mu_c' = 0.0$ D (the parameters obtained from our fits). Finally, simulation (e) was created with non-zero values of all dipole moment components, with $\mu_a'' = 3.12$, $\mu_a' = 4.21$, $\mu_b'' = 1.2$, $\mu_b' = 1.3$, $\mu_c'' = -1.26$ and $\mu_c' = -0.86$ D. The assumed values of μ_c are the calculated ones (Table A.2).....138

Figure B.6. HOMO-1 (ϕ_2), HOMO (ϕ_3), LUMO (ϕ_4), and LUMO+1 (ϕ_5) orbitals of PABA and AN, as predicted by CIS/6-31G** calculations. The bottom portion shows the result of multiplication of the signs of the ϕ_3 and ϕ_4 orbitals, giving predicted transition moment orientations.....141

Figure B.7. Arrows depicting the dipole moment magnitudes and directions of PABA and AN in both the ground and excited states.....142

Figure B.8. Electron density difference plots for AN and PABA. Light areas represent regions of electron gain, and dark areas represent regions of electron loss.....144

Figure C.1. Vibrationally resolved fluorescence excitation spectra of 2ABN (a) and 3ABN (b).....154

Figure C.2. (a) Field-free origin band spectrum of 2ABN, occurring at 31263.5 cm^{-1} . The bottom panel shows a comparison of a small portion of the experimental spectrum (black trace) with two simulated spectra (blue trace), with and without a convoluted lineshape function. (b) Field-free origin band spectrum of 3ABN, occurring at 31708.6 cm^{-1} . The bottom panel shows a comparison of a small portion of the experimental spectrum (black trace) with two simulated spectra (blue trace), with and without a convoluted lineshape function.....156

Figure C.3. Origin band spectrum of 2ABN, in presence of an electric field of 950 V/cm. The top panel shows the entire spectrum, and the bottom panel shows a comparison of a portion of the experimental spectrum (black trace) with two simulated spectra (blue trace), with and without a convoluted lineshape function.....159

Figure C.4. Origin band spectrum of 3ABN, in presence of an electric field of 950 V/cm. The top panel shows the entire spectrum, and the bottom panel shows a comparison of a portion the experimental spectrum (black trace) with two simulated spectra (blue trace), with and without a convoluted lineshape function.....161

Figure C.5. Structures of 2ABN and 3ABN with the a and b inertial axes shown for reference. The red arrows represent the predicted transition moment orientations.....	163
Figure C.6. HOMO-1 (ϕ_2), HOMO (ϕ_3), LUMO (ϕ_4), and LUMO+1 (ϕ_5) molecular orbitals of AN, 2ABN, 3ABN, and BN as predicted by CIS/6-31G** calculations.....	164
Figure C.7. Measured dipole moments are shown on the structures of 2ABN (a) and 3ABN (b) in both the ground and excited electronic states.....	166
Figure C.8. Stark-splitting energy level diagram for the ground state $J = 1$ and 2 rotational levels of 2ABN as a function of electric field. The simulation was run with the experimentally determined rotational constants and dipole moments. The labels on the right designate the J , τ , and M values of the represented levels.....	169
Figure D.1. Field-free rotationally resolved electronic spectrum of trans-2HN.....	179
Figure D.2. Field-free rotationally resolved electronic spectrum of cis-2HN.....	179
Figure D.3. Field-free rotationally resolved electronic spectrum of cis-2HNA.....	181
Figure D.4. Rotationally resolved electronic spectrum of trans-2HN in the P-branch at a) zero field, b) 211, c) 634, and d) 2115 V/cm, respectively. The most intense line in a) is assigned to the $ 8,5,4\rangle \leftarrow 9,6,3\rangle$ transition.....	183
Figure D.5. Rotationally resolved electronic spectrum of cis-2HN in the P-branch at a) zero field, b) 211, c) 634, and d) 1776 V/cm, respectively. The most intense line in a) is assigned to the $ 8,5,4\rangle \leftarrow 9,6,3\rangle$ transition.....	184
Figure D.6. The top portion is the entire cis-2HNA spectrum at an applied voltage of 1269 V/cm. The bottom portion shows the A band transitions in red and E band transitions in blue, respectively, at rotational resolution.....	187
Figure D.7. Shown in (a) is the zero-field origin of the $S_1 \leftarrow S_0$ electronic spectrum of cis-2HNA, containing the overlapping A and E sub-bands. At full rotational resolution, (b) contains the zero-field experimental spectrum (black trace) compared to the simulated spectrum (blue trace, A sub-band transitions in blue, E sub-band transitions in red) using a convoluted line shape at a rotational temperature of 5 K and the addition of both simulated sub-bands. Spectra obtained at (c) 423 V/cm and (d) 1269 V/cm are shown along with simulated spectra.....	188
Figure D.8. Calculated frontier molecular orbitals of trans- and cis-2HN at the CIS/6-31G** level. The calculated molecular orbitals of naphthalene (N) are included for comparison.....	190

Figure D.9. Experimental ground and excited state dipole moments of trans- and cis-2HN (scale: 1.0 D = 4.0 Å). The center images are the weighted electron density differences upon $S_1 \leftarrow S_0$ excitation calculated at the CIS/6-31G** level. Purple indicates electron density gain upon excitation, whereas yellow indicates electron density loss.....192

Figure D.10. The S_0 and S_1 dipole moments of *cis*-2HNA (black). This figure illustrates the components of Equation 7, where $\vec{\mu}_{c2HN}$ (red), $\vec{\mu}_{NH_3}$ (blue), $\vec{\mu}_{ind}$ (orange), and $\vec{\mu}_{CT}$ (green) add to reproduce $\vec{\mu}_{c2HNA}$ (black).....199

LIST OF SCHEMES

Scheme 2.1.....	7
Scheme 2.2.....	8
Scheme 4.1.....	74

LIST OF EQUATIONS

Equation 4.1.....	60
Equation 4.2.....	60
Equation 4.3.....	60
Equation 5.1.....	84
Equation 5.2.....	84
Equation 5.3.....	84
Equation 5.4.....	85
Equation B.1.....	135
Equation B.2.....	135
Equation B.3.....	135
Equation C.1.....	157
Equation C.2.....	157
Equation C.3.....	157
Equation D.1.....	182
Equation D.2.....	182
Equation D.3.....	182
Equation D.4.....	195
Equation D.5.....	195
Equation D.6.....	195
Equation D.7.....	197
Equation D.8.....	197

Equation D.9.....	198
Equation D.10.....	198
Equation D.11.....	198
Equation D.12.....	198

1.0 INTRODUCTION

Advances in science have led to the discovery of many interesting dynamical processes in molecules. These include large amplitude vibrational motions, chemical reactions in ground and excited electronic states, and energy transfer processes between electronic states. Rotationally resolved electronic spectroscopy is one experimental technique that can be used to probe all of these processes, by monitoring motions along the $3N-6$ dimensional potential energy surfaces that govern them. Usually these dynamical processes manifest themselves in rotationally resolved spectra as tunneling splittings, linewidth broadenings, and anomalous line intensities. Analyses of these spectral details in the rotationally resolved spectra leads to information about the structures that are being transformed, and on what time scales. The possible role of solvent molecules in influencing the dynamics may also be explored.

The general goal of research is to elucidate properties and processes that are not well understood. *Ab initio* calculations are nowadays able to accurately predict the electronic ground state structures and properties of many molecules, containing as many as 10-12 atoms. The structural and dynamical properties of even larger molecules remain hard to describe using *ab initio* methods, in particular, weakly bound van der Waals complexes, hindered methyl group internal rotation, and intramolecular proton transfer. The excited state structural and dynamical properties of molecules, such as transition dipole moment directions and methyl group internal rotations, are even harder for *ab initio* calculations to predict. Many dynamical processes of molecules are highly

sensitive to its electronic and geometric structure, making experimental measurements crucial to understanding these processes.

Our studies are of molecules in the gas phase. Thus, the research described in this thesis focuses on the study of molecules or molecular complexes that are not under the influence of any external forces. In all of these experiments, the objective is to understand the molecule's structure and electronic distribution and how these structural properties can influence certain dynamical processes. This is done by determining the structure of these molecules by means of rotationally resolved electronic spectroscopy. In addition, the dynamical process of some of these molecules can be detected in the recorded spectrum. Since these measurements are completed on the isolated molecule in the gas phase in the absence of external forces, these measurements can be used to aid in the advancement of excited state *ab initio* calculations.

In Chapter 2, a controversy regarding the proper assignment of two closely spaced bands in the $S_1 \leftarrow S_0$ electronic transition of *trans-p*-coumaric acid (*pCA*) has been addressed by recording their spectra at full rotational resolution.¹ The results show unambiguously that the carrier of these two bands is *p*-vinylphenol (*pVP*), a thermal decomposition product of *pCA*. The two bands belong to two conformers of *pVP*; *trans-pVP* at 33207.3 cm^{-1} and *cis-pVP* at 33211.8 cm^{-1} .

In Chapter 3, the molecule 1, 2, 3, 6, 7, 8-hexahydropyrene was studied. The resulting spectra lead to the assignment of two conformers, chair and boat, to their respective origin bands. Two additional red shifted bands were also analyzed, and were found to be due to a single Ar van der Waals complex and single H_2O van der Waals complex, both for the chair-HHP conformer. Assignments were made for both the bare

and complexed molecules by comparing experimental rotational constants with those from theory using Gaussian03.²

In Chapter 4, we direct our attention to the dynamics of the methyl group torsional motion, studying the molecules *o*- and *m*-toluidine. Their high resolution electronic spectra were recorded for the $S_1 \leftarrow S_0$ origin band transitions of the isolated molecules. Each spectrum is split into two sub-bands owing to tunneling motions along the methyl group torsional coordinate. Analyses of these data provide information about the preferred configurations of the methyl groups and the barriers opposing their motions in both the ground and excited electronic states. Despite their apparent similarities, the experiments reveal that these properties are quite different in the two molecules.

In Chapter 5, we present the study of the rotationally resolved fluorescence excitation spectra of the $0a_1$ and $1e$ torsional bands in the $S_1 \leftarrow S_0$ electronic spectrum of 4-methylanisole. Previous experiments in our laboratory were performed on 2- and 3-methylanisole.³ The analyses of the collected data again provides insight about the torsional methyl group motion in the ground and excited states of the different structural isomers.

In Chapter 6, the dynamical process of excited state intramolecular proton transfer (ESIPT) was studied. Rotationally resolved fluorescence excitation spectra of the $S_1 \leftarrow S_0$ origin band and $+144 \text{ cm}^{-1}$ vibrational band transitions of 2-(2'-pyridyl)pyrrole (2PP) have been recorded in the collision free environment of a molecular beam. Analyses of these data provide new information about the changes in geometry that occur when 2PP absorbs light. Additionally, significant line broadening is observed in both spectra,

which we attribute to the excited state intramolecular proton transfer (ESIPT) reaction, for which time scales have been determined.

In the Appendix, results from various Stark-effect studies are included. Appendix A discusses the application of Stark-effect measurements on a push-pull molecule, *p*-aminobenzoic acid, in the gas phase. In Appendix B, the electric dipole moments of asymmetric tops, 2-aminobenzonitrile and 3-aminobenzonitrile, are discussed. It is shown that each structural isomer has a unique dipole moment, in both its ground and electronically excited states, thereby providing a means of distinguishing them. Appendix C discusses the determination of the ground and excited state dipole moments of an acid-base complex, 2-naphthol (2HN) and its single ammonia complex. A quantitative measurement of the amount of charge that is transferred when the single ammonia complex (2HNA) is excited by light has been determined. The measurement was made by comparing the permanent electric dipole moments of *cis*-2HNA in its ground (S_0) and excited (S_1) states. While the increase in electron transfer from the donor (NH_3) to the acceptor (2HN) upon excitation is small ($\sim 0.05 e$), it is sufficient to red-shift the electronic spectrum of the complex by $\sim 600 \text{ cm}^{-1}$ ($\sim 0.1 \text{ eV}$).

1.1 REFERENCES

1. Ryan, W. L.; Gordon, D. J.; Levy, D. H., *Journal of the American Chemical Society* **2002**, 124, 6194.
2. Frisch, M. J.; Trucks, G. W.; Schlegel, H. B.; Scuseria, G. E.; Robb, M. A.; Cheeseman, J. R.; Montgomery, J. A. J.; Vreven, T.; Kudin, K. N.; Burant, J. C.; Millam, J. M.; Iyengar, S. S.; Tomasi, J.; Barone, V.; Mennucci, B.; Cossi, M.; Scalmani, G.; Rega, N.; Petersson, G. A.; Nakatsuji, H.; Hada, M.; Ehara, M.; Toyota, K.; Fukuda, R.; Hasegawa, J.; Ishida, M.; Nakajima, T.; Honda, Y.; Kitao, O.; Nakai, H.; Klene, M.; Li, X.; Knox, J. E.; Hratchian, H. P.; Cross, J. B.; Bakken, V.; Adamo, C.; Jaramillo, J.; Gomperts, R.; Stratmann, R. E.; Yazyev, O.; Austin, A. J.; Cammi, R.; Pomelli, C.; Ochterski, J. W.; Ayala, P. Y.; Morokuma, K.; Voth, G. A.; Salvador, P.; Dannenberg, J. J.; Zakrzewski, V. G.; Dapprich, S.; Daniels, A. D.; Strain, M. C.; Farkas, O.; Malick, D. K.; Rabuck, A. D.; Raghavachari, K.; Foresman, J. B.; Ortiz, J. V.; Cui, Q.; Baboul, A. G.; Clifford, S.; Cioslowski, J.; Stefanov, B. B.; Liu, G.; Liashenko, A.; Piskorz, P.; Komaromi, I.; Martin, R. L.; Fox, D. J.; Keith, T.; Al-Laham, M. A.; Peng, C. Y.; Nanayakkara, A.; Challacombe, M.; Gill, P. M. W.; Johnson, B.; Chen, W.; Wong, M. W.; Gonzalez, C.; Pople, J. A. *Gaussian 03, Revision 6.0*, Gaussian, Inc., Wallingford CT: 2004.
3. Alvarez-Valtierra, L.; Yi, J. T.; Pratt, D. W., *J. Phys. Chem. B* **2006**, 110, 19914.

2.0 HIGH RESOLUTION ELECTRONIC SPECTROSCOPY OF *P*- VINYLPHENOL IN THE GAS PHASE.

Philip J. Morgan, Diane M. Mitchell, and David W. Pratt

Department of Chemistry, University of Pittsburgh
Pittsburgh, PA 15260 USA

This work is published in *Chem. Phys.* **347**, (2008), 340.

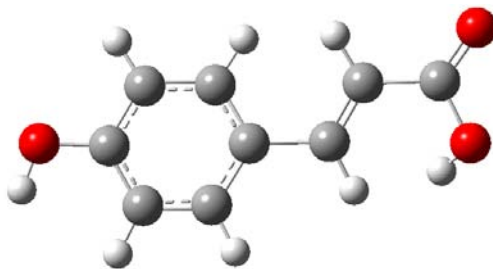
P. J. Morgan and D. M. Mitchell performed the experimental measurements; P. J. Morgan analyzed the spectra and wrote the paper.

2.1 ABSTRACT

A recent controversy regarding the proper assignment of two closely spaced bands in the $S_1 \leftarrow S_0$ electronic transition of *trans-p*-coumaric acid (*pCA*) has been addressed by recording their spectra at full rotational resolution. The results show unambiguously that the carrier of these two bands is *p*-vinylphenol (*pVP*), a thermal decomposition product of *pCA*. The two bands belong to two conformers of *pVP*; *trans-pVP* at 33207.3 cm^{-1} and *cis-pVP* at 33211.8 cm^{-1} .

2.2 INTRODUCTION

Photosensory proteins transform light energy into a cellular response *via* a photocycle. An example is photoactive yellow protein (PYP). Here, the photocycle is believed to be triggered by a photoinduced *trans*-to-*cis* isomerization about the double bond in the PYP chromophore, *trans-p*-coumaric acid (*pCA*) (Chart 2.1).¹ Extensive studies have been

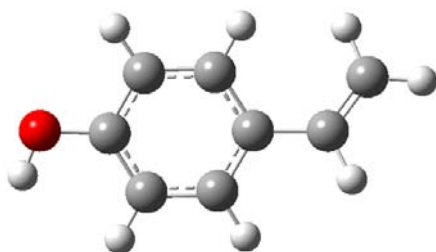


Scheme 2.1. *Trans-pCA*.

performed on *pCA* and its derivatives, to examine this process in more detail. Issues of concern include the degree of isomerization in solution, the possible role of water, and

whether or not the protein environment might inhibit motion along the reaction coordinate.²⁻⁵

Recently, a new controversy about *pCA* has developed. Ryan *et al.*⁶ reported the first vibrationally resolved fluorescence excitation spectrum of *trans-pCA* in 2002. They found the spectrum to consist of three regions, a structured region (Region I) at lowest excitation energy, and two less structured regions (II and III) at higher energy. Two origin bands, separated by approximately 4 cm⁻¹, were observed in Region I, and assigned to the two possible orientations of the –OH group with respect to the phenyl ring. Later, de Groot and Buma⁷ studied the same spectrum using the REMPI method, and found that the two bands were associated with an ion having a mass of 120 amu, rather than the expected mass of 164 amu. They then assigned the spectrum to the thermal decarboxylation product of *trans-pCA*, *p*-vinylphenol (*pVP*), (Chart 2.2). Here, we use the method of high resolution electronic spectroscopy in the gas phase to resolve this issue.



Scheme 2.2. *Trans-pVP*.

2.3 EXPERIMENTAL

*p*CA was purchased from Sigma Aldrich and used without further purification. Vibrationally resolved $S_1 \leftarrow S_0$ excitation spectra were recorded in the following manner. The second harmonic of a Quanta Ray Nd³⁺:Yag (Model DCR-1A) laser was used to pump a dye laser (Model PDL-1) containing Kiton Red dye in order to achieve the desired frequency. The visible light output was externally frequency doubled using a potassium dihydrogen phosphate (KDP) crystal. The visible light was then filtered out and the ultraviolet (UV) light with a spectral resolution of $\sim 1 \text{ cm}^{-1}$ was then passed into the vacuum chamber containing the sample source. *p*CA was heated to $\sim 185^\circ \text{ C}$ and seeded into ~ 2000 Torr of dry helium gas ($>90\%$ purity). The sample mixture was then expanded through a 1 mm diameter orifice pulsed valve, a General Valve Series 9 operating at 10 Hz, into the vacuum chamber (10^{-5} Torr). The sample was crossed 2 cm downstream with the UV light. The fluorescence was collected using a photomultiplier tube (PMT) which is positioned at right angles to both the molecular and laser beams. The data were processed using a boxcar integrator (Stanford Research Systems), interfaced with Quick Data Acquisition software (Version 1.0.5) to record the data.

Rotationally resolved $S_1 \leftarrow S_0$ excitation spectra were recorded using a molecular beam laser spectrometer, described elsewhere.⁸ Briefly, the sample was heated to $\sim 200^\circ \text{ C}$ in a quartz source, seeded in dry helium gas ($>90\%$ purity), and then expanded through a 240 μm tip nozzle. The expansion was skimmed ~ 2 cm downstream with a 1 mm diameter skimmer to form a molecular beam and then crossed 15 cm downstream with the UV laser output of a modified continuous ring dye laser. A mix of Rhodamine

590 and Kiton Red dyes was used to achieve the correct visible frequency, along with a 600 nm LiIO₃ crystal for intracavity frequency doubling in order to achieve the ultraviolet frequency. Intracavity frequency doubling produced ~120 μW of UV light. Fluorescence was collected with spatially selective optics and detected by a photon counting system and a PMT. All spectra were recorded using the jba95 data acquisition software.⁹ Typical scan lengths were 4 cm⁻¹ over 1000 s. Frequency calibration was performed by simultaneously collecting an iodine spectrum and relative frequency markers. The I₂ absorption spectrum was collected to determine the absolute transition frequencies of the excitation spectrum to an accuracy of ± 30 MHz. A stabilized etalon was used to produce the relative frequency markers having a mode-matched free spectral range of 599.5040 ± 0.0005 MHz in the UV, corresponding to a free spectral range of 299.7520 ± 0.0005 MHz in the visible. The resulting spectra were fit using the jb95 least squares fitting program.¹⁰

Theoretical calculations were performed using the Gaussian 03 suite of programs to supplement the experiments.¹¹ Geometry optimizations using *ab initio* calculations of the ground state of *trans-p*CA were performed at the Møller Plesset 2nd order (MP2) perturbation theory level with a 3-21G basis set. Geometry optimizations of both conformers of *p*VP were performed at the MP2 level of theory with a 6-31G** basis set. Configuration interaction singles (CIS) calculations with a 6-31G** basis set were performed for excited state calculations of both *p*VP conformers, styrene, and phenol.

2.4 RESULTS AND INTERPRETATION

The vibrationally resolved $S_1 \leftarrow S_0$ excitation spectrum of *p*CA is shown in Figure 2.1.

The first of the two origin bands is located at $\sim 33,208 \text{ cm}^{-1}$; they are separated by

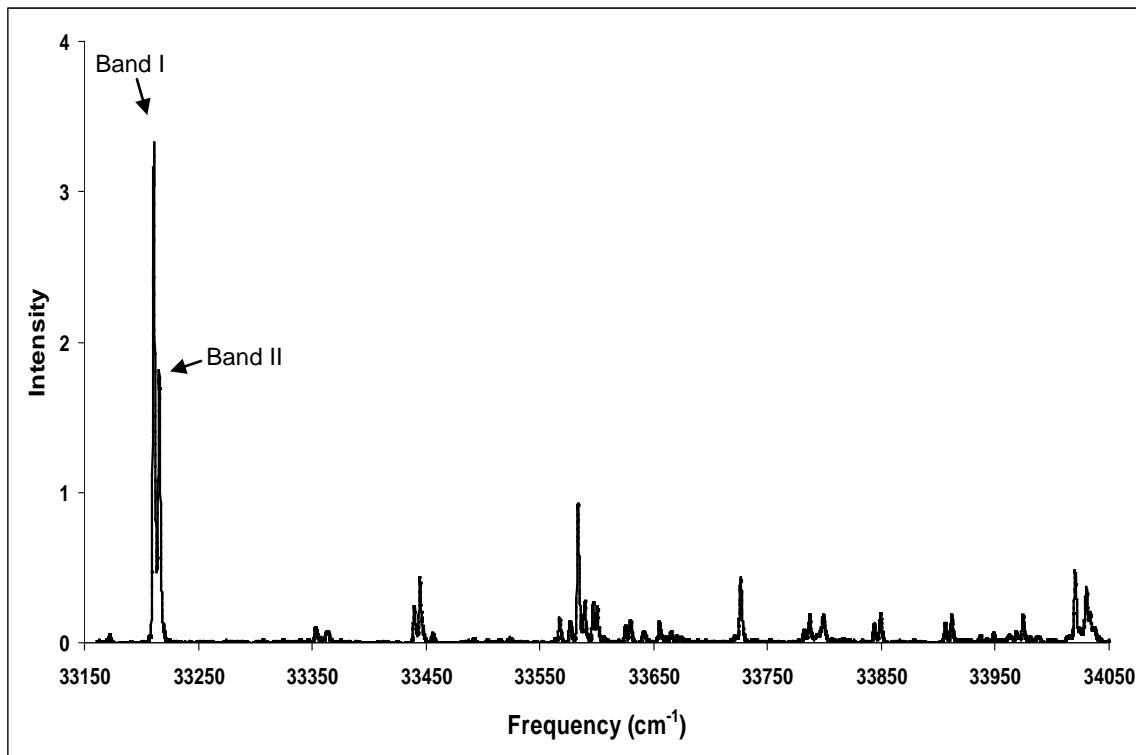


Figure 2.1. Vibrationally resolved $S_1 \leftarrow S_0$ excitation spectrum of *p*CA (*p*VP). Bands I and II are split by $\sim 4 \text{ cm}^{-1}$.

4 cm^{-1} . The splitting of the origin into two bands is believed to be due to the two possible orientations of the hydroxyl group with respect to the phenyl ring. The two origin bands are labeled Band I and Band II. Approximately 1000 cm^{-1} to the red of the two origin bands was scanned to ensure that there were no other peaks present in this portion of the spectrum. To determine which of these bands correspond to the *cis* and *trans* isomers of

the chromophore, the rotationally resolved electronic spectrum of each band was obtained and analyzed.

Figures 2.2 and 2.3 display the experimental spectra of Band I and Band II. The middle traces show a portion of each spectrum at full rotational resolution and the bottom traces show the corresponding calculated spectrum. The spectra were fit using rigid rotor Hamiltonians¹² for both electronic states. At first, an *a*-type spectrum was simulated for each of the spectra due to the presence of a central Q-branch. Upon fitting the spectra, it became apparent that transitions were missing from the simulated spectrum. The addition of *b*-type character provided the missing transitions, therefore resulting in a hybrid-band character for both spectra.

Table 2.1 lists the inertial parameters extracted from fits of both spectra. The two sets of rotational constants are clearly different from one another, denoting two molecular configurations. It is evident upon examination of the experimental rotational constants and the calculated constants of *trans*-*pCA* that they are remarkably different, shown in Table 2.2. It is therefore obvious that the carrier of these two bands is not *trans*-*pCA*, as suggested by Ryan *et al.*⁶, but rather is due to the thermal decarboxylation product, *pVP*, as suggested by de Groot and Buma⁷. The predicted rotational constants of *pVP* are very similar to those determined from fits of the spectra. Additionally, de Groot and Buma⁷ have also shown that a *bona fide* sample of *pVP* shows a spectrum that is identical to Figure 2.1.

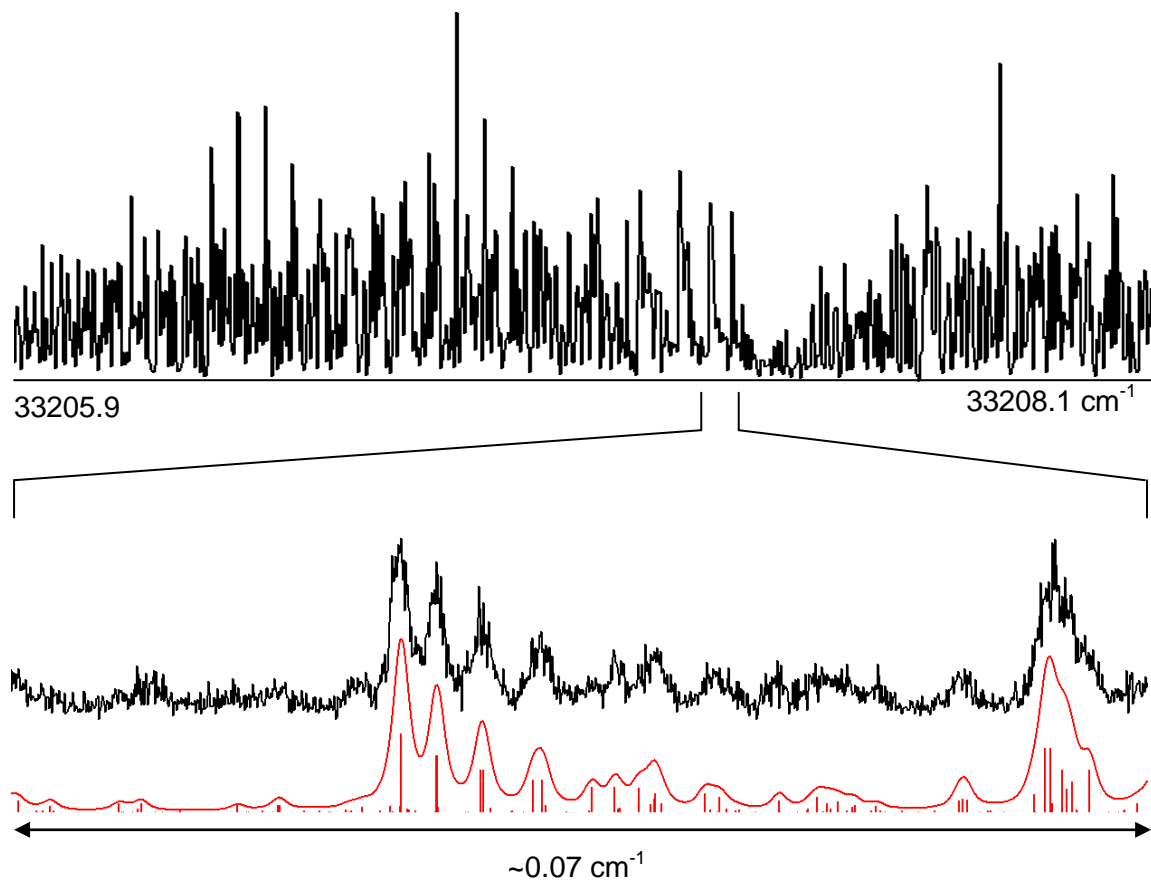


Figure 2.2. Rotationally resolved electronic excitation spectrum of Band I, with origin at 33,207.3 cm⁻¹. The lower part of the figure shows a close-up in the Q-branch region. In the close-up, the upper trace is the experimental spectrum, and the lower trace is the simulated spectrum. The individual lines represent the transitions responsible for the spectrum. The band was fit using a Voigt lineshape profile.

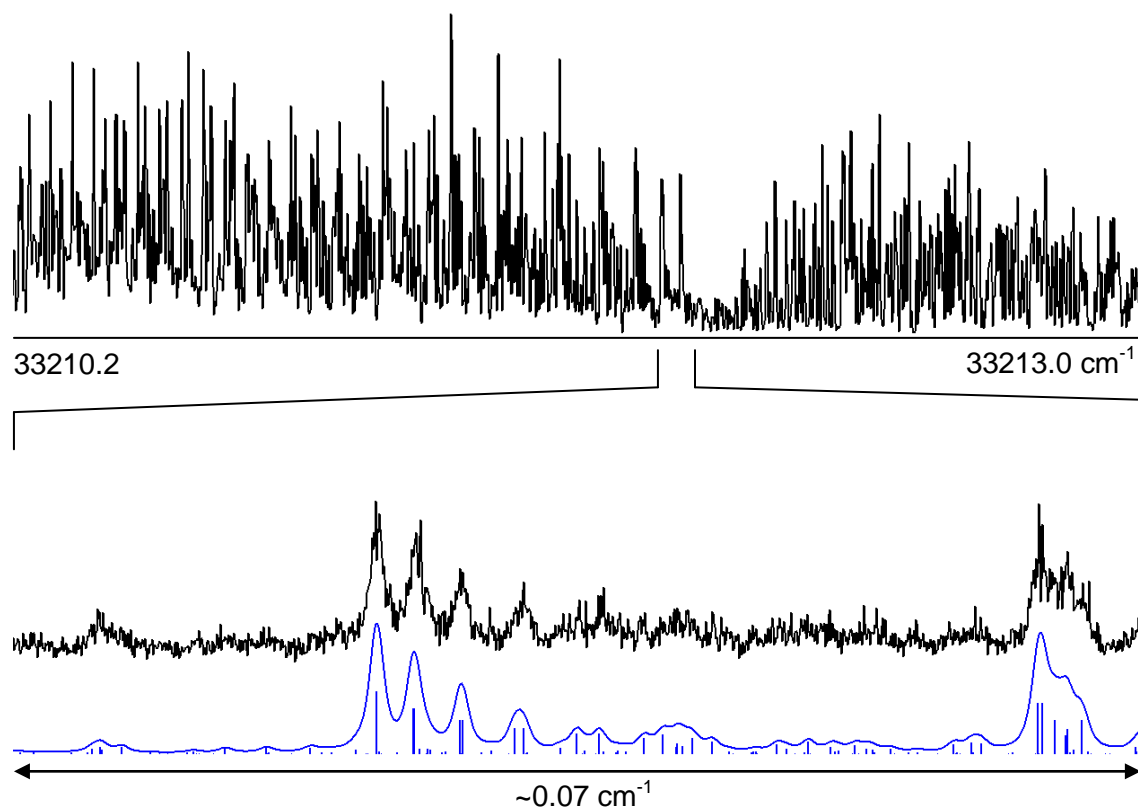


Figure 2.3. Rotationally resolved electronic excitation spectrum of Band II, with origin at $33,211.8 \text{ cm}^{-1}$. See the Fig. 2.2 caption for more details.

Table 2.1. Inertial parameters derived from fits of the rotationally resolved S₁-S₀ fluorescence excitation spectra of Bands I and II.

Parameter	Band I	Band II
A'' (MHz)	5024.4(5)	5031.8(5)
B'' (MHz)	989.6(1)	988.9(1)
C'' (MHz)	828.0(1)	827.7(1)
ΔI'' (amu Å ²)	-0.902	-0.874
A' (MHz)	4767.2(5)	4762.9(54)
B' (MHz)	1004.4(1)	1004.6(1)
C' (MHz)	830.4(1)	830.3(1)
ΔI' (amu Å ²)	-0.560	-0.457
Origin (cm ⁻¹)	33207.3	33211.8
# Lines Assigned	123	113
OMC (MHz)	2.0	2.7
Band Type (<i>a/b/c</i>)	64/36/0	64/36/0

Table 2.2. Comparison of experimental and *ab initio* rotational constants of *trans*-pCA and *cis*-pVP and *trans*-pVP.

Rotational Constants	Band I	Band II	<i>trans</i> -pVP ¹	<i>cis</i> -pVP ¹	<i>trans</i> -pCA ²
A'' (MHz)	5024.4(5)	5031.8(5)	4973.8	4979.9	3449.1
B'' (MHz)	989.6(1)	988.9(1)	992.2	991.6	344.8
C'' (MHz)	828.0(1)	827.7(1)	833.6	834.1	321.0
ΔA (MHz)	-257.2(5)	-268.9(5)	-152.7	-162.0	129.1
ΔB (MHz)	14.8(1)	15.7(1)	28.0	30.0	7.9
ΔC (MHz)	2.4(1)	2.6(1)	8.4	8.8	1.3

¹ Values calculated at MP2/6-31G** and CIS/6-31G** levels of theory.

² Values calculated at MP2/3-21G and CIS/3-21G levels of theory.

Both Band I and the *ab initio trans* conformer of *pVP* have larger ground state A constants and smaller B constants, when compared to the corresponding rotational constants of Band II and the *ab initio cis* conformer of *pVP*. Similarly, the ΔA , ΔB , and ΔC values of Band I ($\Delta A = A(S_1) - A(S_0)$, *etc.*) and the *ab initio trans* conformer of *pVP*, and of Band II and the *ab initio cis* conformer of *pVP* are also very similar. It can therefore be concluded that Band I is the origin of *trans-pVP* and that Band II is the origin of *cis-pVP*.

2.5 DISCUSSION

The two substituents in *pVP* are *para* to each other, as indicated by its name, and are incapable of communicating electronically without significant distortion of the benzene ring. It is therefore intriguing to ask whether one substituent “dominates” in the excitation of *pVP*. Figure 2.4 shows the structures of styrene, phenol and the two conformers of *pVP*, together with the approximate locations of their *a* and *b* inertial axes. The $S_1 \leftarrow S_0$ spectrum of styrene is principally an *a*-type spectrum, whereas the corresponding spectrum of phenol is principally *b*-type. But both conformers of *pVP* exhibit $S_1 \leftarrow S_0$ spectra that are *a/b* hybrid bands; the transition moment (TM) is oriented neither along *a* nor along *b*, but somewhere in between. The angle with respect to *a* is $\pm 37 \pm 3^\circ$. Since this is closer to *a* than to *b*, the vinyl group on *pVP* seems to be the dominating substituent.

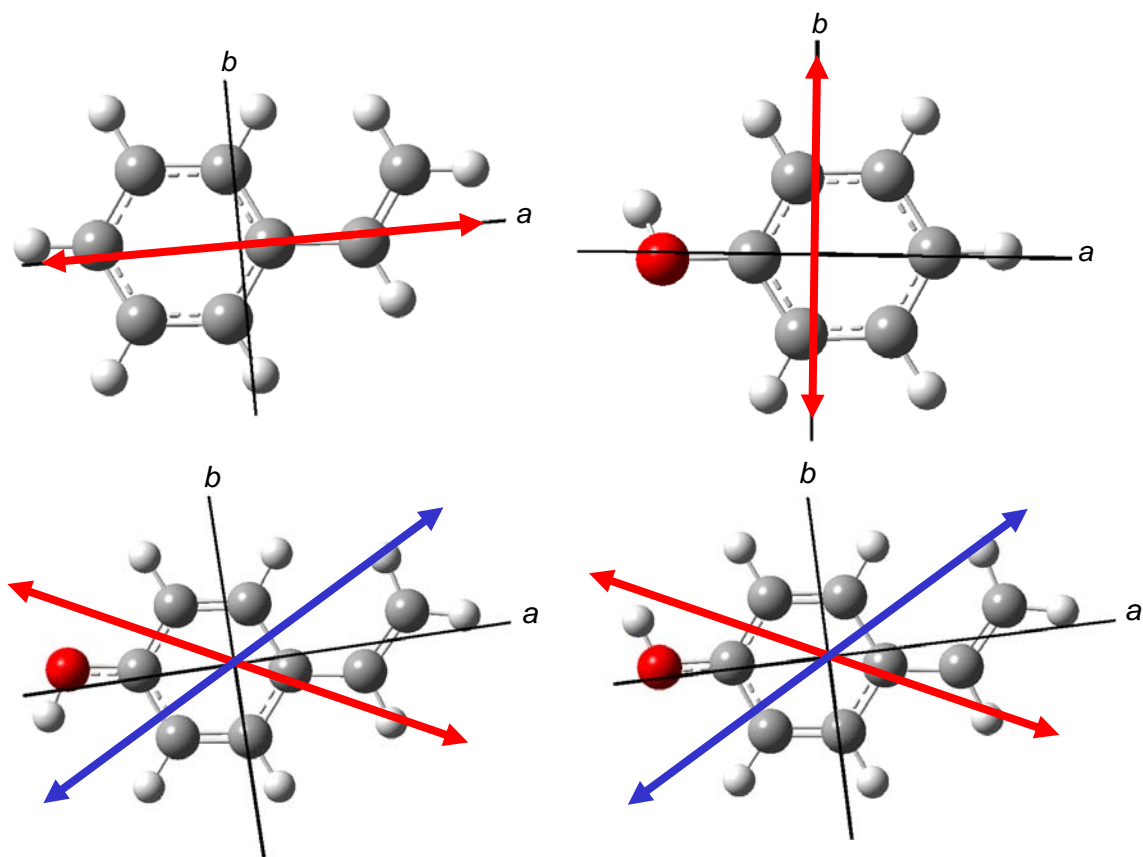


Figure 2.4. Structures of styrene and phenol on top, left to right. Red arrows indicate the $S_1 \leftarrow S_0$ transition moment orientations. Structure of *trans* and *cis* conformers of *p*VP on bottom, left to right. Red and blue arrows indicate the two possible orientations of the $S_1 \leftarrow S_0$ transition moment for each conformer.

There are four possible excited states for benzene, $B_a(\psi_2\psi_5-\psi_3\psi_4)$, $B_b(\psi_2\psi_4+\psi_3\psi_5)$, $L_a(\psi_2\psi_5+\psi_3\psi_4)$, and $L_b(\psi_2\psi_4-\psi_3\psi_5)$, derived from the Platt perimeter model.¹³ The 1L_a and 1L_b states of benzene are forbidden. Substitution of the benzene ring lifts the degeneracy of all four transitions and lowers the symmetry, making the transitions to L_a and L_b orbitally allowed. Substitution of one of the carbons on the benzene ring causes the TM of the ${}^1L_b \leftarrow S_0$ transition to be perpendicular to the C_2 axis (a axis) of the molecule and lie along the b axis, resulting in b -type spectra. The TM of the ${}^1L_a \leftarrow S_0$ transition lies along the a axis, resulting in a -type spectra. Whether or not the monosubstituted benzenes exhibit a or b -type character in their $S_1 \leftarrow S_0$ spectra depends upon whether the 1L_b or 1L_a state lies lower in energy.

Table 2.3 lists the dominant one-electron excitations that participate in the $S_1 \leftarrow S_0$ transition in the four molecules. 1L_a clearly lies lower in styrene, since its $S_1 \leftarrow S_0$ spectrum is principally a -type.¹⁴⁻¹⁶ As seen in Figure 2.5, the vinyl group stabilizes ψ_5 with respect to ψ_4 , making it an “off-axis” conjugating substituent.¹⁷ In contrast, ψ_4 lies lower than ψ_5 for phenol, resulting in a $S_1 \leftarrow S_0$ spectrum that is principally b -type.¹⁸ The nodal patterns exhibited by both conformers of pVP are more similar to those of styrene, predicting the excited states to be 1L_a in nature. However, since both conformers have significant b -type character, it is evident that the excited states are not pure 1L_a states, but rather a linear combination of 1L_a and 1L_b , as has been discussed previously.¹⁹

Table 2.3. Dominant one-electron excitations for the listed molecules.

One-Electron Excitation	<i>trans</i> -pVP ¹	<i>cis</i> -pVP ¹	Styrene ¹	Phenol ¹
HOMO→LUMO	0.67	0.67	0.67	0.61
HOMO-1→LUMO+1	0.15	0.15	0.16	0.35

¹Values calculated at CIS/6-31G** level of theory.

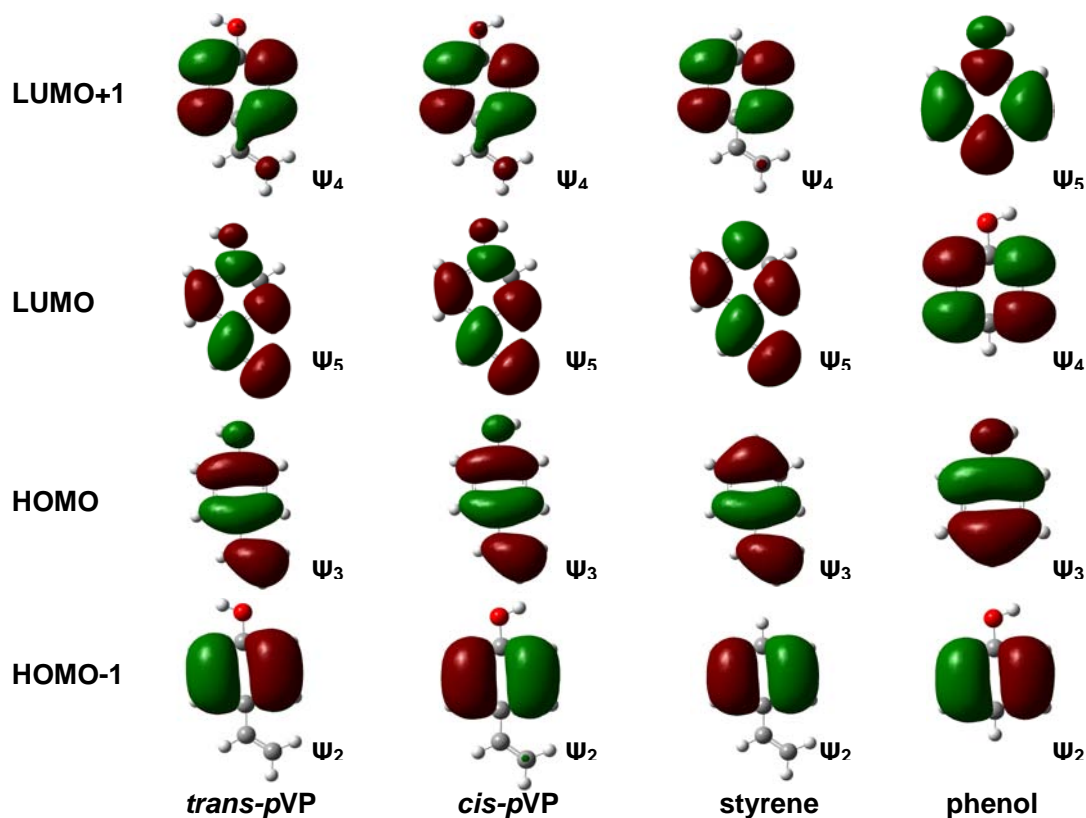


Figure 2.5. Molecular orbitals for *trans*-pVP, *cis*-pVP, styrene and phenol. Dominant one-electron excitations for all four molecules are HOMO→LUMO and HOMO-1→LUMO+1. All calculations were performed at the CIS/6-31G** level of theory.

Ryan *et al.*⁶ also gave interpretations of the two less structured regions of their spectrum, Regions II and III. They suggested that the less broadened features in Region II were due to coupling to another excited state electronic state, *cis-pCA*, and that the more broadened features in Region III were due to excitation to the second electronic state of *trans-pCA*. Our results, and those of de Groot and Buma⁷, suggest that *pVP* is the carrier of both these features, that Region II is a region in which the 1L_b state dominates, and that Region III is a region in which the couplings between these states (and perhaps others) leads to irreversible photodynamics.

2.6 ACKNOWLEDGEMENTS

Some theoretical calculations were performed using the Center for Molecular and Materials Simulations (CMMS). This research has been supported by the National Science Foundation (CHE-0615755). We thank W. J. Buma for bringing this problem to our attention.

2.7 REFERENCES

1. Sprenger, W. W.; Hoff, W. D.; Armitage, J. P.; Hellingwerf, K. J. *Journal of bacteriology* **1993**, *175*, 3096.
2. Larsen, D. S.; van Stokkum, I. H. M.; Vengris, M.; van der Horst, M. A.; de Weerd, F. L.; Hellingwerf, K. J.; van Grondelle, R. *Biophysical Journal* **2004**, *87*, 1858.
3. Larsen, D. S.; Vengris, M.; van Stokkum, I. H. M.; van der Horst, M. A.; de Weerd, F. L.; Hellingwerf, K. J.; van Grondelle, R. *Biophysical journal* **2004**, *86*, 2538.
4. Vengris, M.; Larsen, D. S.; van der Horst, M. A.; Larsen, O. F. A.; Hellingwerf, K. J.; van Grondelle, R. *Journal of Physical Chemistry B* **2005**, *109*, 4197.
5. Toniolo, A.; Olsen, S.; Manohar, L.; Martinez, T. J. *Faraday Discussions* **2004**, *127*, 149.
6. Ryan, W. L.; Gordon, D. J.; Levy, D. H. *Journal of the American Chemical Society* **2002**, *124*, 6194.
7. de Groot, M.; Buma, W. J. *Journal of Physical Chemistry A* **2005**, *109*, 6135.
8. Majewski, W. A.; Pfanstiel, J. F.; Plusquellic, D. F.; Pratt, D. W. *Laser Techniques of Chemistry*, A. B. Myers and T. R. Rizzo, J Wiley & Sons, New York, **1995**, p. 101.
9. Plusquellic, D. F., Ph.D. Thesis, University of Pittsburgh, 1992.
10. Plusquellic, D. F.; Suenram, R. D.; Mate, B.; Jensen, J. O.; Samuels, A. C. *Journal of Chemical Physics* **2001**, *115*, 3057.
11. Frisch, M. J.; Trucks, G. W.; Schlegel, H. B.; Scuseria, G. E.; Robb, M. A.; Cheeseman, J. R.; Montgomery, J. A. J.; Vreven, T.; Kudin, K. N.; Burant, J. C.; Millam, J. M.; Iyengar, S. S.; Tomasi, J.; Barone, V.; Mennucci, B.; Cossi, M.; Scalmani, G.; Rega, N.; Petersson, G. A.; Nakatsuji, H.; Hada, M.; Ehara, M.; Toyota, K.; Fukuda, R.; Hasegawa, J.; Ishida, M.; Nakajima, T.; Honda, Y.; Kitao, O.; Nakai, H.; Klene, M.; Li, X.; Knox, J. E.; Hratchian, H. P.; Cross, J. B.; Bakken, V.; Adamo, C.; Jaramillo, J.; Gomperts, R.; Stratmann, R. E.; Yazyev, O.; Austin, A. J.; Cammi, R.; Pomelli, C.; Ochterski, J. W.; Ayala, P. Y.; Morokuma, K.; Voth, G. A.; Salvador, P.; Dannenberg, J. J.; Zakrzewski, V. G.; Dapprich, S.; Daniels, A. D.; Strain, M. C.; Farkas, O.; Malick, D. K.; Rabuck, A. D.; Raghavachari, K.; Foresman, J. B.; Ortiz, J. V.; Cui, Q.; Baboul, A. G.; Clifford, S.; Cioslowski, J.; Stefanov, B. B.; Liu, G.; Liashenko, A.; Piskorz, P.; Komaromi, I.; Martin, R. L.; Fox, D. J.; Keith, T.; Al-Laham, M. A.; Peng, C. Y.; Nanayakkara, A.; Challacombe, M.; Gill, P. M. W.; Johnson, B.; Chen, W.; Wong, M.

W.; Gonzalez, C.; Pople, J. A. Gaussian 03, Revision 6.0; Gaussian, Inc., Wallingford CT, 2004.

12. Gordy, W.; Cook, R. L. *Microwave Molecular Spectra*, 3rd ed.; Wiley-Interscience: New York, 1984.
13. Salem, L. *The Molecular Orbital Theory of Conjugated Systems*; W. A. Benjamin, Inc.: New York, 1966.
14. Ribblett, J. W.; Borst, D. R.; Pratt, D. W. *Journal of Chemical Physics* **1999**, *111*, 8454.
15. Hemley, R. J.; Dinur, U.; Vaida, V.; Karplus, M. *Journal of the American Chemical Society* **1985**, *107*, 836.
16. Zilberg, S.; Haas, Y. *Journal of Chemical Physics* **1995**, *103*, 20.
17. Kroemer, R. T.; Liedl, K. R.; Dickinson, J. A.; Robertson, E. G.; Simons, J. P.; Borst, D. R.; Pratt, D. W. *Journal of the American Chemical Society* **1998**, *120*, 12573.
18. Berden, G.; Meerts, W. L.; Schmitt, M.; Kleinermanns, K. *Journal of Chemical Physics* **1996**, *104*, 972.
19. Nguyen, T. V.; Ribblett, J. W.; Pratt, D. W. *Chemical Physics* **2002**, *283*, 279.

**3.0 MEASURING THE CONFORMATIONAL PROPERTIES OF
1, 2, 3, 6, 7, 8 – HEXAHYDROPYRENE AND ITS VAN DER WAALS
COMPLEXES.**

Philip J. Morgan, Joseph R. Roscioli,^a Adam J. Fleisher and David W. Pratt

^aPresent address : Joint Institute for Laboratory Astrophysics, University of Colorado,
Boulder, Colorado 80309.

Department of Chemistry, University of Pittsburgh
Pittsburgh, PA 15260 USA

This work is published in *J. Chem. Phys.*, **133**, (2010), 024302.

P.J. Morgan, J. R. Roscioli, and A. J. Fleisher performed the experimental measurements;
P.J. Morgan analyzed the spectra and wrote the paper.

3.1 ABSTRACT

Rotationally resolved fluorescence excitation spectra of the $S_1 \leftarrow S_0$ origin band transitions of two conformers of 1, 2, 3, 6, 7, 8 - hexahydropyrene (HHP) have been recorded in the gas phase. The band at $30,648.0 \text{ cm}^{-1}$ has been assigned as the origin band of the chair conformer and the band at $30,658.8 \text{ cm}^{-1}$ has been assigned as the origin band of the boat conformer on the basis of differences in their rotational constants. In addition, rotationally resolved fluorescence excitation spectra of single Ar and H_2O van der Waals complexes of chair-HHP have been observed. Analyses of these results indicate that the weakly attached argon atom (water molecule) is located on top of the plane of the bare molecule at $\sim 3.4 \text{ \AA}$ ($\sim 4.1 \text{ \AA}$) from its center of mass in the S_0 electronic state. No complexes of boat-HHP were detected.

3.2 INTRODUCTION

Naphthalene and its derivatives have been studied extensively in the gas phase by high resolution laser techniques over the past 30 years.¹⁻⁶ The unsubstituted molecule is a favorable candidate for such studies because of its high symmetry and long fluorescence lifetime. Also, by attaching different functional groups (*e.g.*; -OH, -NH₂, and -CH₃) to the naphthalene frame, other molecular motions have been explored, including isomerization, inversion, and torsion, in both ground and excited electronic states. Often, such motions produce splittings and/or shifts in the resolved spectra, from which

information about the potential energy surfaces that control the dynamics can be obtained.

The molecule 1, 2, 3, 6, 7, 8-hexahdropyrene (HHP) also is a substituted naphthalene species. It contains two $-(\text{CH}_2)_3-$ chains symmetrically attached to the naphthalene moiety; see Figure 3.1. HHP can exist in one of four possible configurations, two equivalent chair and two equivalent boat conformations, with each set of equivalent pairs having identical energy. The vibrationally resolved fluorescence excitation spectrum of HHP has been reported by Chakraborty *et al.*,⁷ and appears to show two electronic origin bands. According to *ab initio* calculations and the dispersed fluorescence spectra of both bands, Chakraborty *et al.*⁷ assigned the band at $\sim 30,648 \text{ cm}^{-1}$ as the origin band of the chair conformer and the band at $\sim 30,659 \text{ cm}^{-1}$ as the origin band of the boat conformer.

It is the intent of this present study to validate these conclusions and to investigate the possible dynamical properties of HHP, such as tunneling between conformers, using the technique of rotationally resolved electronic spectroscopy. We find that the two bands in question are both origin bands and assign them to specific conformers on the basis of differences in their rotational constants. We also report the observation of two van der Waals (vdW) complexes of chair-HHP with a single Ar atom and a single H_2O molecule and describe their properties in both electronic states. Surprisingly, analogous complexes of boat-HHP were not detected.

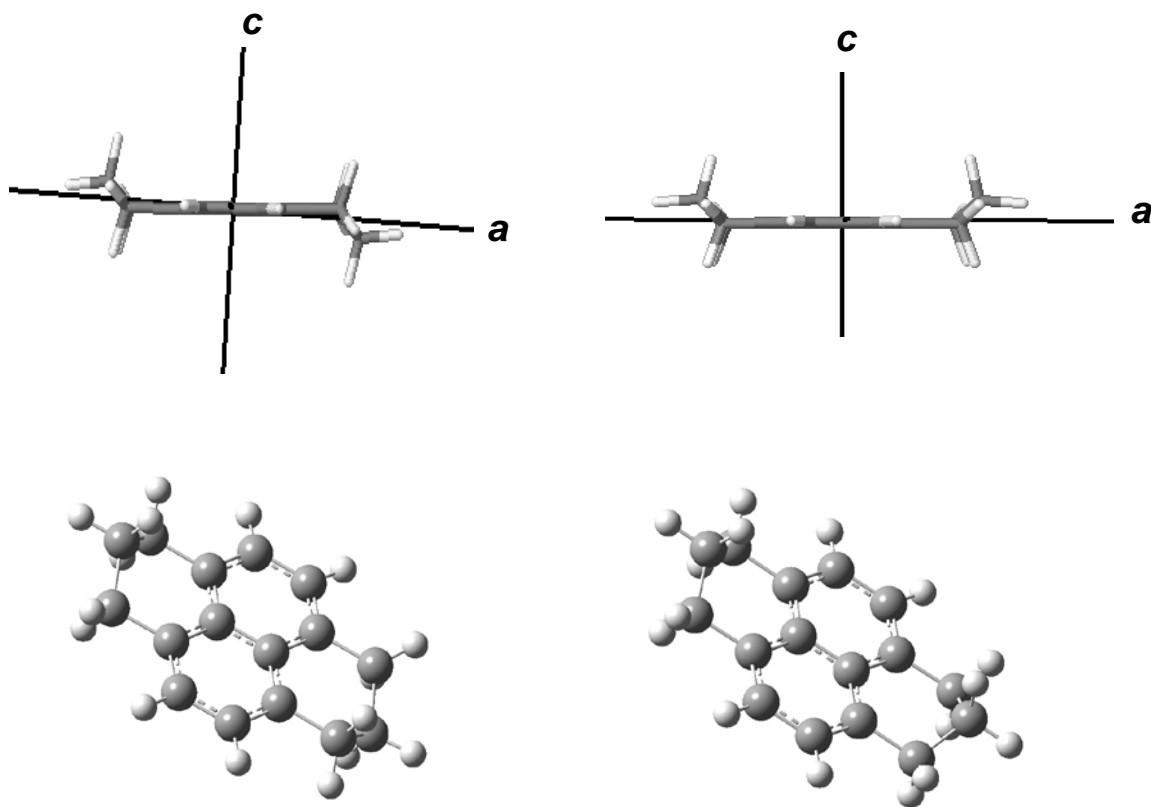


Figure 3.1. Chair-HHP (left) and boat-HHP (right).

3.3 EXPERIMENTAL

HHP was purchased from Sigma Aldrich and used without further purification. Vibrationally resolved $S_1 \leftarrow S_0$ excitation experiments were conducted in the following manner. The second harmonic of a Quanta Ray Nd^{3+} :YAG (Model DCR-1A) laser was used to pump a dye laser (Model PDL-1) containing 4-(dicyanomethylene)-2-methyl-6-(4-dimethylaminostyryl)-4*H*-pyran (DCM) dye in order to achieve the desired frequency.

The visible light output was externally frequency doubled using a potassium dihydrogen phosphate (KDP) crystal. The filtered ultraviolet (UV) light with a spectral resolution of $\sim 1 \text{ cm}^{-1}$ was passed into the vacuum chamber containing the sample source. HHP was heated to $\sim 130^\circ \text{ C}$ and seeded into ~ 2500 Torr of dry helium gas ($> 90\%$ purity). The sample mixture was expanded through a 1 mm diameter orifice pulsed valve, a General Valve Series 9 operating at 10 Hz, into a vacuum chamber (10^{-5} Torr). The sample was crossed 2 cm downstream with the UV light. The fluorescence was collected using a photomultiplier tube (PMT) which is positioned at right angles to both the molecular and laser beams. The data were processed using a boxcar integrator (Stanford Research Systems) interfaced with Quick Data Acquisition software (Version 1.0.5) to record the data.

Rotationally resolved $S_1 \leftarrow S_0$ excitation experiments were performed in the collision-free environment of a molecular beam, described elsewhere.⁸ Briefly, for the bare molecule spectra, the sample was heated to $\sim 130^\circ \text{ C}$ in a quartz source, seeded in dry argon gas ($> 90\%$ purity), and expanded through a 240 μm nozzle. The expansion was skimmed ~ 2 cm downstream with a 1 mm diameter skimmer to form a molecular beam, and then crossed 15 cm downstream of the nozzle with a laser beam operating in the UV. The laser radiation was generated by a modified continuous ring dye laser (Spectra-Physics 380D) operating in the visible (DCM dye) along with a 660 nm LiIO_3 crystal for intracavity frequency doubling, producing $\sim 300 \mu\text{W}$ of UV radiation with a linewidth of ~ 1 MHz. In studies of the spectra of vdW complexes, the visible output of the dye laser was externally frequency doubled by a Spectra-Physics Wavetrain using a 655 nm LBO crystal, producing $\sim 750 \mu\text{W}$ of UV. In all cases, fluorescence was

collected with spatially selective optics and detected by a photon counting system and a PMT. All spectra were recorded using the jba95 data acquisition software.⁹ Typical scan lengths were 3 cm^{-1} over 2000-8000 sec. The I_2 absorption spectrum¹⁰ was used to determine the absolute transition frequencies in the excitation spectra to an accuracy of $\pm 30 \text{ MHz}$. A stabilized etalon was used to produce relative frequency markers having a mode-matched free spectral range of $299.7520 \pm 0.0005 \text{ MHz}$ in the visible, corresponding to a free spectral range of $549.5040 \pm 0.0005 \text{ MHz}$ in the UV. The resulting spectra were fit using the jb95 least squares fitting program.¹¹

Supplementing the experimental work, *ab initio* calculations at ground state MP2/6-31G** and excited-state CIS/6-31G** levels were performed by using the Gaussian 03¹² suite of electronic structure programs on personal computers.

3.4 RESULTS

Figure 3.2 shows the vibrationally resolved $S_1 \leftarrow S_0$ excitation spectrum of HHP. The two strongest bands appear at $\sim 30,648 \text{ cm}^{-1}$ (Band I) and $\sim 30,659 \text{ cm}^{-1}$ (Band II). Previously, Chakraborty *et al.*⁷ assigned Band I to chair-HHP and Band II to boat-HHP. No other strong bands appear in the region $\sim 1000 \text{ cm}^{-1}$ below these two bands, confirming their identity as origin bands.

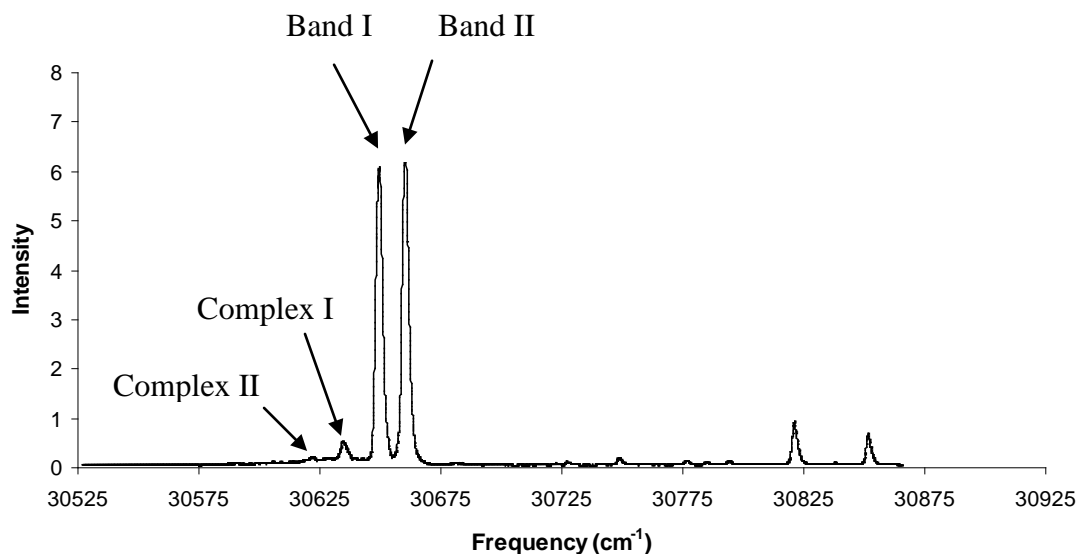


Figure 3.2. Vibrationally resolved $S_1 \leftarrow S_0$ excitation spectrum of HHP. The two origin bands, Band I and II, are split by $\sim 11 \text{ cm}^{-1}$.

Rotationally resolved $S_1 \leftarrow S_0$ fluorescence excitation spectra of Bands I and II are shown in Figures 3.3 and 3.4. Both spectra span approximately 2.2 cm^{-1} and exhibit nearly fully resolved rotational structure, despite the size of HHP (32 atoms). (Baba and co-workers¹³ have reported a similar study of a 32-atom molecule, perylene). The two origin bands were fit using rigid-rotor Hamiltonians for both the ground and excited states.¹⁴ A simulated spectrum was first generated using estimated rotational constants from the *ab initio* calculations. Single transitions from the simulated spectrum were then assigned to corresponding transitions in the experimental spectrum using the fitting program jb95.¹¹ A linear least-squares fitting procedure was finally used to optimize the rotational constants from a comparison of the observed and calculated transitions. Examples of these fits are shown in Figures 3.3 and 3.4. The standard deviation (OMC observed minus calculated) of both fits are $\sim 1.5 \text{ MHz}$ and were fit with rotational

temperatures of ~ 4 K. The inertial parameters obtained from the fits of both spectra are listed in Table 3.1. The two sets of rotational constants are very similar, as expected from the similarities in structure of the two conformers.

Despite the size of the molecule, individual transitions were observed in some regions of the spectrum. Figure 3.5 shows an example. This line, and others like it, has a FWHM of 9 MHz. These were fit to Voigt lineshape profiles, resulting in equal Gaussian and Lorentzian widths of ~ 8 MHz. The Gaussian width of 8 MHz is substantially smaller than observed in most previous high resolution studies, apparently owing to a reduced Doppler width produced by an adventitious vertical adjustment of the laser and molecular beam. The Lorentzian width of 8 MHz yields a fluorescence lifetime of ~ 20 ns, in reasonable agreement with the measured value of ~ 18 ns reported by Chakraborty *et al.*⁷ The high resolution spectra of both bands are 100% *b*-type. No tunneling splittings were observed in either of the bands.

Unfortunately, subsequent experiments on HHP failed to reproduce the reduced Doppler width observed in the original experiments. However, in the course of this investigation, two weak bands were discovered to the red of Band I; see Fig. 3.2. High resolution spectra of these two bands, called “Complex I” and “Complex II”, are shown in Figures 3.6 and 3.7. Both spectra span approximately 1.6 cm^{-1} . These were fit in a manner similar to the two origin bands; the addition of Watson’s centrifugal distortion terms¹⁴ for both bands and both electronic states were used to improve the fits. Individual lines in both spectra also were fit with Voigt lineshape profiles with Gaussian widths of 20 MHz and Lorentzian widths of 8 MHz. Examples of these fits are shown in

Figures 3.6 and 3.7. The inertial parameters derived from these fits are listed in Table 3.2.

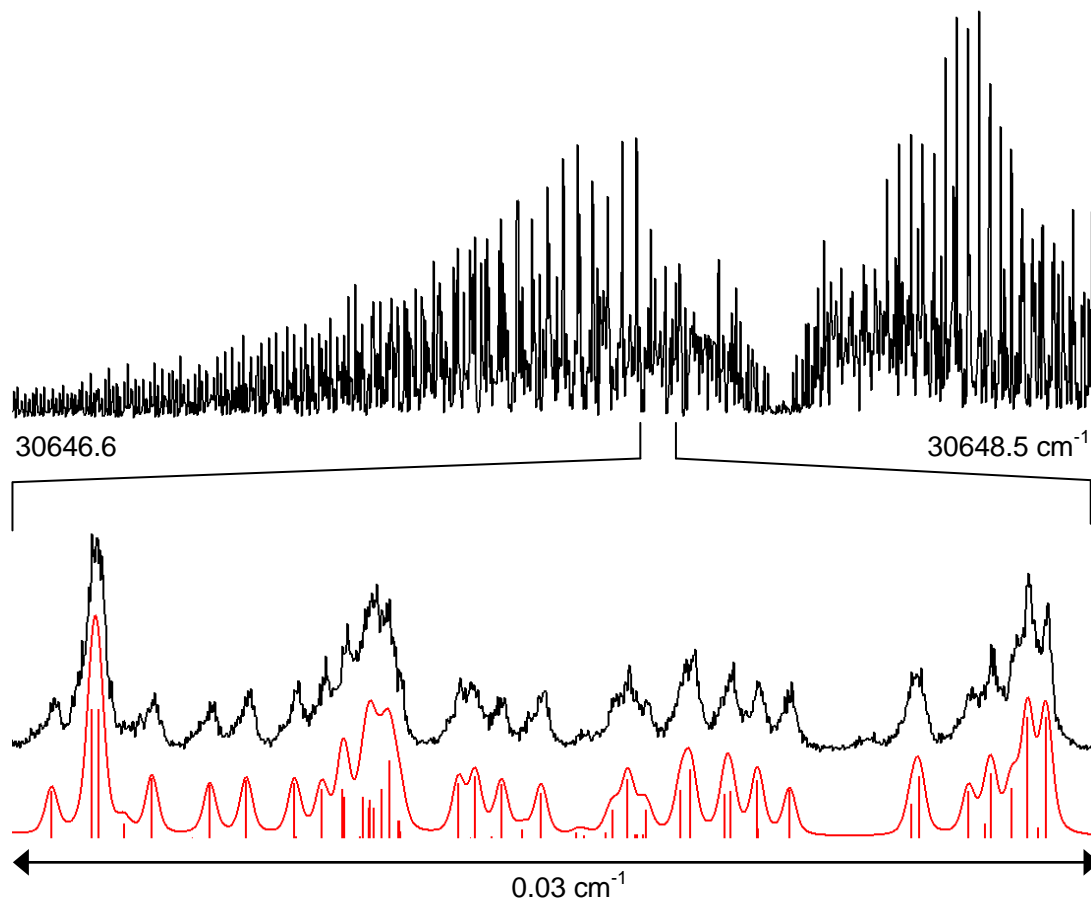


Figure 3.3. Rotationally resolved electronic excitation spectrum of Band I in HHP, with origin at 30648.0 cm^{-1} . The lower part of the figure shows a close-up of a portion of the Q-branch region. The upper trace is the experimental spectrum, and the lower trace is the simulated spectrum; the individual lines represent the transitions responsible for the spectrum.

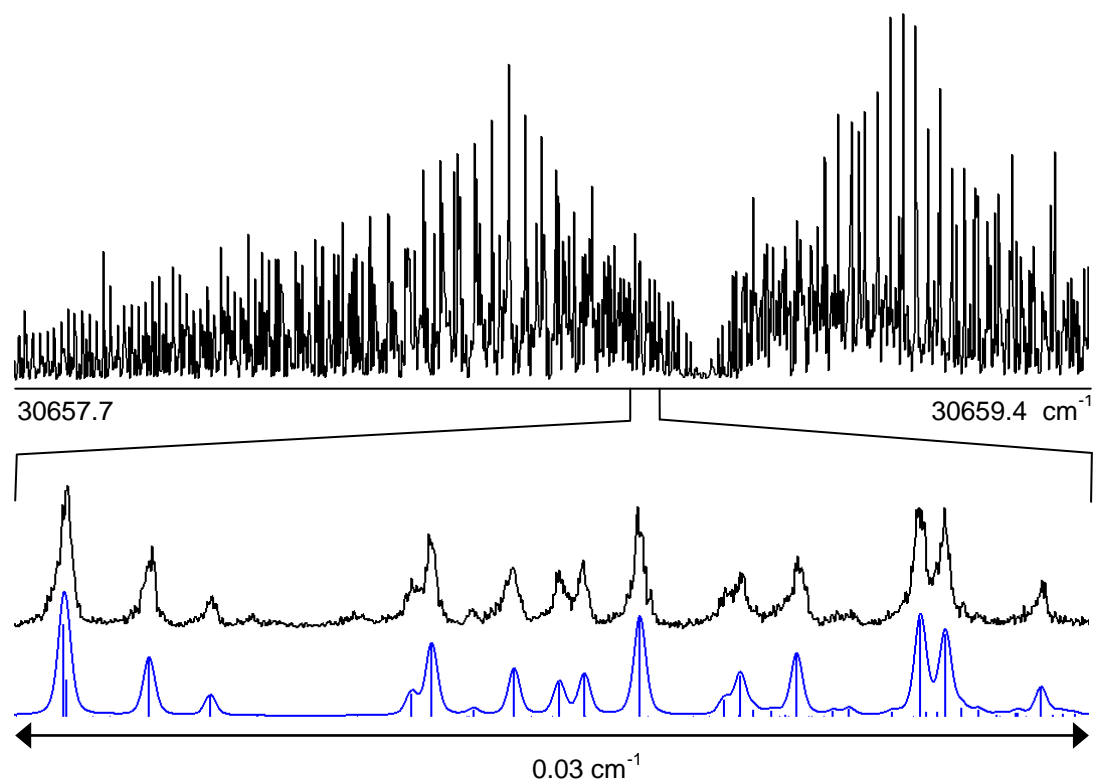


Figure 3.4. Rotationally resolved electronic excitation spectrum of Band II in HHP, with origin at 30658.8 cm⁻¹. The lower part of the figure shows a close up of a portion of the Q-branch region. The upper trace is the experimental spectrum, and the lower trace is the simulated spectrum; the individual lines represent the transitions responsible for the spectrum.

Table 3.1. Inertial parameters obtained from fits of the two origin bands, Bands I and II.

Parameters	Experimental			Theoretical		
	Band I	Band II	Δ Bands(I-II)	chair-HHP ^a	boat-HHP ^a	Δ (chair-boat)
A" (MHz)	971.8 (1)	967.5 (1)	4.3	973.2	968.6	4.6
B" (MHz)	495.6 (1)	496.3 (1)	-0.7	496.7	497.6	-0.9
C" (MHz)	336.5 (1)	337.4 (1)	-0.9	337.1	338.0	-0.9
$\Delta I''$ (amu Å ²)	-38.0	-42.7	4.7	-37.6	-42.2	4.6
A' (MHz)	959.4 (1)	955.6 (1)	3.8	962.7	958.5	4.2
B' (MHz)	492.0 (1)	492.4 (1)	-0.4	499.2	499.8	-0.6
C' (MHz)	333.2 (1)	333.9 (1)	-0.7	336.4	337.2	-0.8
$\Delta I'$ (amu Å ²)	-37.2	-41.5	4.3	-35.0	-39.7	4.7
Origin(cm ⁻¹)	30648.0	30658.8				
<i>a/b/c</i> type	0/100/0	0/100/0				
OMC (MHz)	1.2	1.5				
assigned lines	401	348				

^aCalculations performed at the MP2/6-31G** and CIS/6-31G** levels of theory.

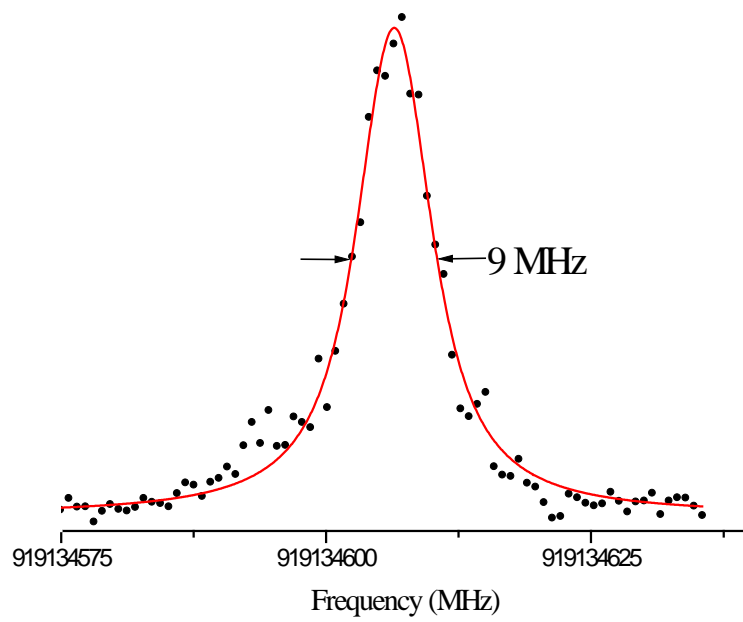


Figure 3.5. A single rovibronic line in the Band II origin. No tunneling splitting was observed down to ~5 MHz.

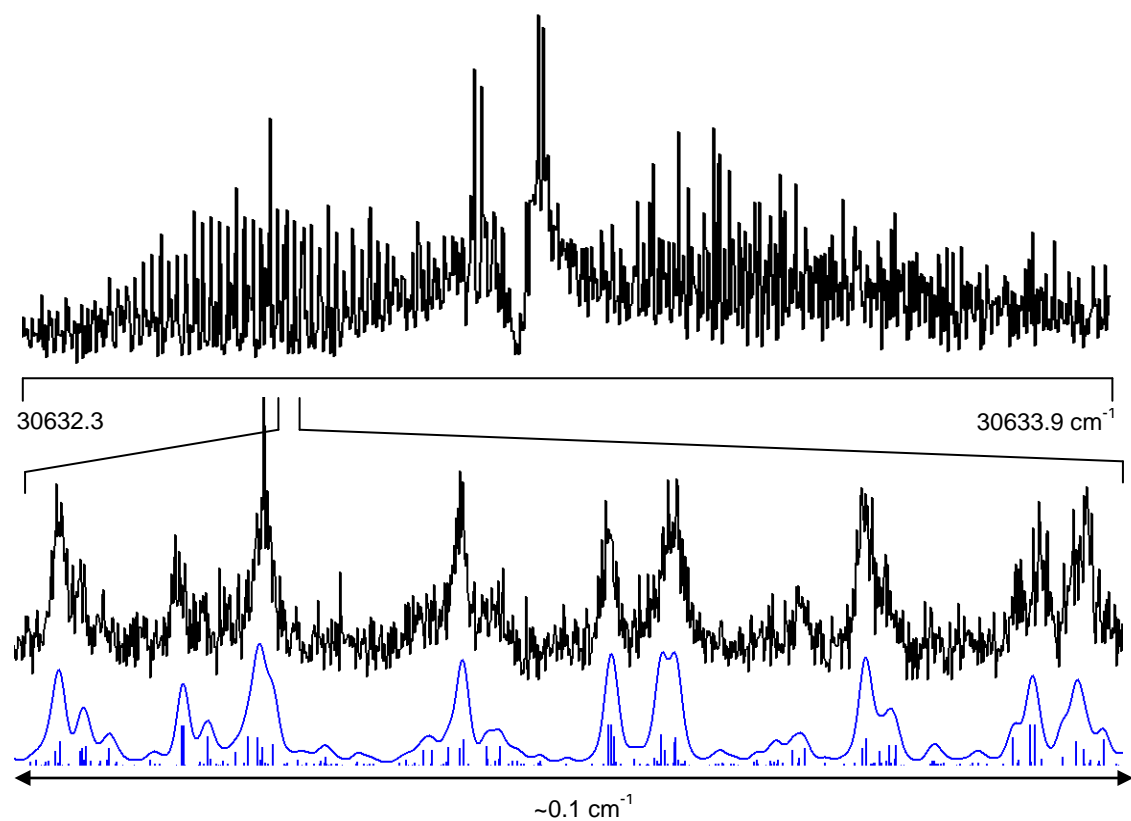


Figure 3.6. Rotationally resolved electronic excitation spectrum of Complex I, with origin at 30633.0 cm^{-1} . The lower part of the figure shows a close up of a portion of the P-branch region. The upper trace is the experimental spectrum, and the lower trace is the simulated spectrum; the individual lines represent the transitions responsible for the spectrum.

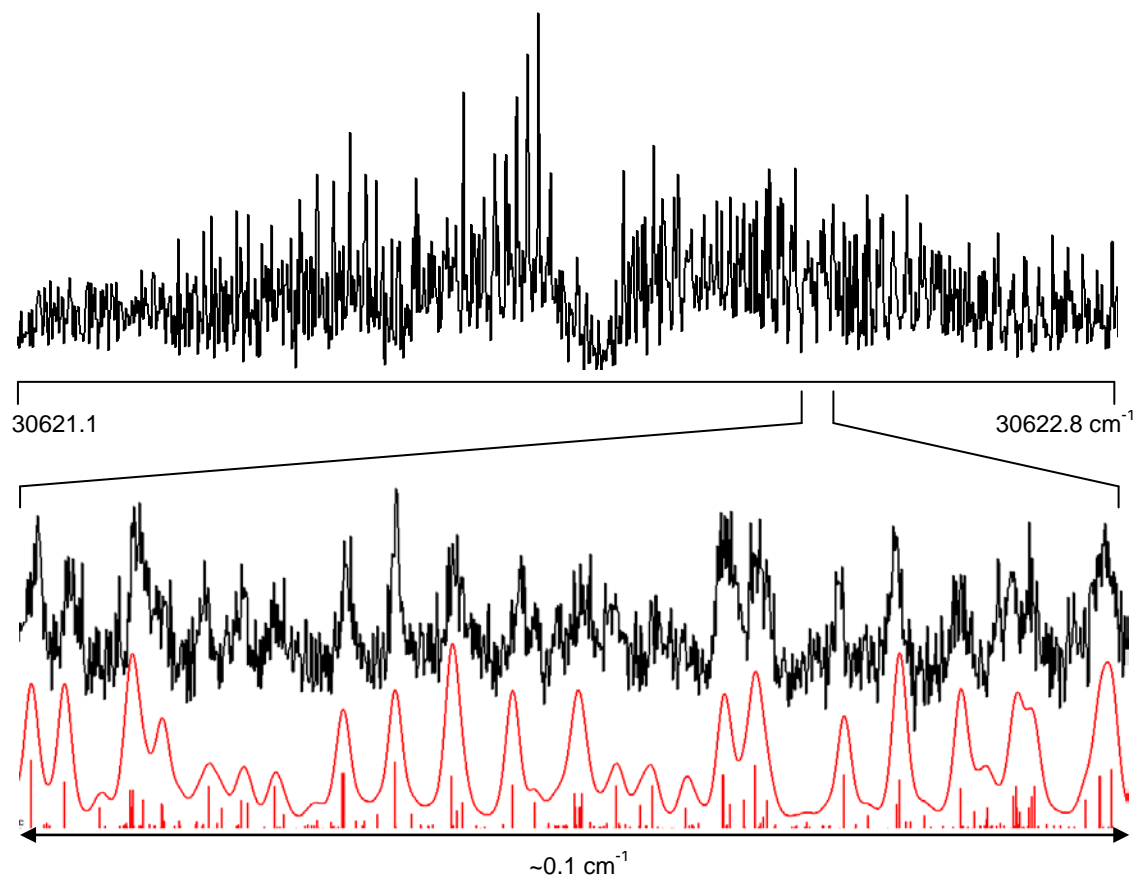


Figure 3.7. Rotationally resolved electronic excitation spectrum of Complex II, with origin at 30622.0 cm^{-1} . The lower part of the figure shows a close up of a portion of the R-branch region. The upper trace is the experimental spectrum, and the lower trace is the simulated spectrum; the individual lines represent the transitions responsible for the spectrum.

Table 3.2. Inertial parameters obtained from fits of the two complex bands.

Parameters	Experimental	
	Complex I ^a	Complex II ^b
A'' (MHz)	548.4 (1)	628.5 (1)
B'' (MHz)	355.2 (1)	386.2 (1)
C'' (MHz)	337.2 (1)	335.3 (1)
$\Delta I''$ (amu Å ²)	-845.5	-605.5
A' (MHz)	1.1 (1)	3.3 (1)
B' (MHz)	0.1 (1)	0.7 (1)
C' (MHz)	-3.6 (1)	-3.5 (1)
$\Delta I'$ (amu Å ²)	-826.9	-583.1
Origin(cm ⁻¹)	30633.0	30622.0
<i>a/b/c</i> type	0/85/15	0/94/6
<i>ac</i> plane axis tilt	3.0±0.5°	2.8±0.5°
OMC	5.0	5.3
assigned lines	104	103

^aThe following Watson distortion terms were required in the fit:

$\Delta J''=-0.00092$, $\Delta JK''=0.00591$, $\Delta K''=-0.00398$, $\delta J''=-0.00042$, $\delta K''=-0.01870$;
 $\Delta J'=-0.00082$, $\Delta JK'=-0.00455$, $\Delta K'=-0.00304$, $\delta J'=-0.00036$, $\delta K'=-0.00995$ MHz

^bThe following Watson distortion terms were required in the fit:

$\Delta J''=0.00022$, $\Delta JK''=0.00702$, $\Delta K''=-0.00609$, $\delta J''=0.00024$, $\delta K''=-0.03347$;
 $\Delta J'=-0.00091$, $\Delta JK'=-0.00185$, $\Delta K'=-0.00159$, $\delta J'=-0.00045$, $\delta K'=-0.00189$ MHz

3.5 DISCUSSION

3.5.1 Conformational Assignments of the Bare Molecule

Compared in Table 3.1 are the inertial parameters obtained from the fits of the two origin bands, Bands I and II. They are very similar; the two ground state A'' values differ by only 4.3 MHz, and the two ground state B'' and C'' values differ by less than 1.0 MHz. Still, the two conformers can be distinguished from each other with the aid of theory. MP2/6-31G** values of the rotational constants are also listed in Table 3.1. The difference between the predicted values of A'' for the two conformers is 4.6 MHz, in excellent agreement with experiment. Theory also correctly reproduces the small differences in B'' and C'' . Thus, we assign Band I to the chair conformer and Band II to the boat conformer of HHP. The chair conformer also is predicted to be slightly more stable than the boat conformer ($\sim 10 \text{ cm}^{-1}$), a fact that nicely accounts for the small intensity difference in the low resolution spectrum. Thus, we conclude that the previous assignments of the two bands to specific conformers of HHP by Chakraborty *et al.*⁷ are correct.

Both conformers of HHP have larger inertial defects than naphthalene itself, owing to the two $-(\text{CH}_2)_3-$ groups lying above and below the naphthalene plane. Interestingly, the inertial defect of the boat form of HHP is both predicted and observed to be larger in magnitude than the chair form. The reason for this difference is apparent from Fig. 3.1; the long in-plane a axis in chair-HHP is significantly tilted out of the plane. Once again, we are reminded of the sensitivity of the moments of inertia to molecular structure.

3.5.2 Excited State Structures of HHP

All rotational constants of excited state chair- and boat-HHP are smaller than their ground state counterparts, evidencing small ring expansions in all directions. The observed ΔA , ΔB , and ΔC values are larger in magnitude than those in naphthalene itself,¹ owing to the dominant contribution of the $-(CH_2)_3-$ groups lying further from the center of mass. These groups are symmetrically attached to the naphthalene moiety, as illustrated in Fig. 3.8. The added mass of the $-(CH_2)_3-$ groups causes a switching of the in-plane a and b inertial axes. Thus, the $S_1 \leftarrow S_0$ transition of HHP is b -axis polarized, instead of a -axis polarized, as it is in naphthalene. There is no evidence that the $-(CH_2)_3-$ groups play any active role in the excitation process, although the 0_0^0 band of HHP is red shifted by $\sim 1400 \text{ cm}^{-1}$ with respect to the corresponding band in the parent molecule.¹

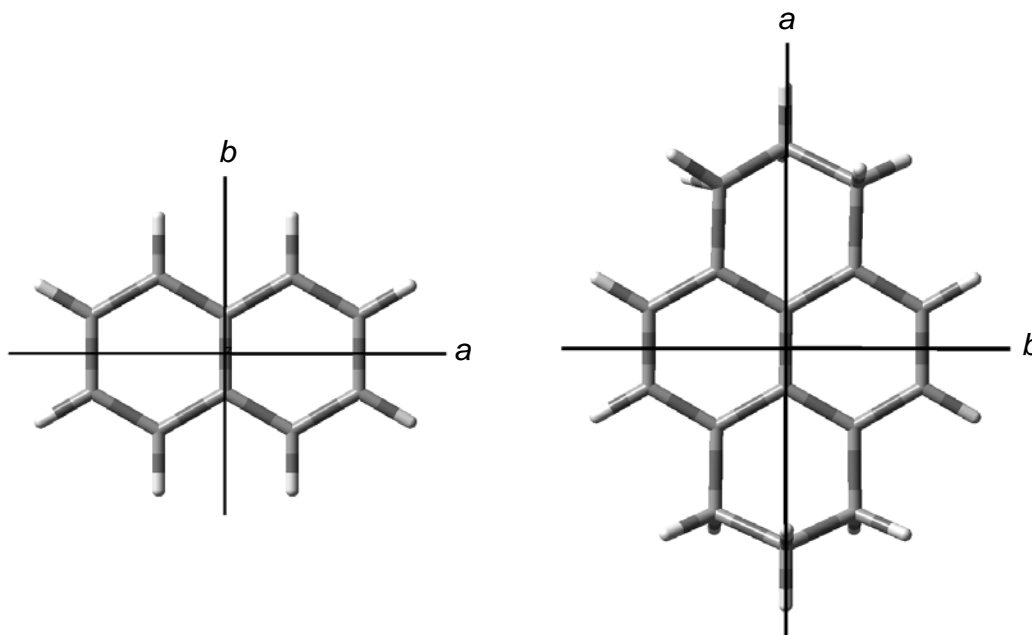


Figure 3.8. Naphthalene, left, and chair-HHP, right, depicting reorientation of a and b inertial axes. The c inertial axes are out of plane.

Tunneling between equivalent conformers has been observed in several similar systems, such as 9,10-dihydroanthracene (DHA) and 9,10-dihydrophenanthrene (DHPH).¹⁵⁻¹⁷ The excited state barrier heights for DHA and DHPH were determined to be $\sim 94 \text{ cm}^{-1}$ and $\sim 2650 \text{ cm}^{-1}$, respectively. The potential barrier for DHPH decreases upon excitation of several quanta of the ring twisting mode.¹⁷ The barrier between the chair and boat forms of HHP was calculated by Chakraborty *et al.*⁷ to be $\sim 1200 \text{ cm}^{-1}$ in the S_1 state. However, no tunneling splitting was detected in either of the HHP origin bands down to $\sim 5 \text{ MHz}$, as shown in Figure 3.5. It can therefore be concluded that the barrier heights in the excited states of both conformers of HHP are too high for a tunneling motion to be observed along any vibrational coordinate, at our experimental resolution. The relatively large reduced mass of the $-(\text{CH}_2)_3-$ groups may also significantly reduce the magnitude of this splitting.

3.5.3 Axis Tilting

Next, attention was focused on the two weak bands lying ~ 15 and $\sim 26 \text{ cm}^{-1}$ to the red of the chair-HHP (Band I) origin, “Complex I” and “Complex II”. Initially, since the two bare molecule origins are separated by $\sim 11 \text{ cm}^{-1}$, it was assumed that single Ar atom complexes of the two conformers were responsible for these two weak bands, each red shifted by $\sim 26 \text{ cm}^{-1}$ with respect to their respective origins. But a careful analysis of the rotational structure of these two bands revealed a different interpretation.

The first challenge that was encountered in this analysis is axis tilting. Assuming that the Ar atom would be attached $\sim 3.5 \text{ \AA}$ above the naphthalene ring, as is usual for

such systems,¹⁸⁻²² we first simulated spectra for each of the three possible conformers of an Ar-HHP complex and compared them to the high resolution spectrum of the “Complex I” band. One such comparison is shown in Fig. 3.9. The band was found to consist mainly of *b*-type transitions as is evident from the lack of a strong central Q-branch in the spectrum. Once the *b*-type transitions were fit, the possible hybrid band character of the spectrum was examined by including *a*- and *c*-type transitions in the spectrum. It was determined that a significant amount of *c*-type character was needed to account for all of the line intensities in the P- and R-branches of the spectrum. However, the intensity fit in the Q-branch was still quite poor. It was therefore apparent that this particular spectrum exhibits axis tilting upon excitation.

Axis tilting occurs when the orientations of the principal inertial axes in the two electronic states are not the same. The phenomenon is revealed by anomalous intensities in the spectrum because the projections of the transition moment vector on the inertial axes are different in the two electronic states. A detailed discussion is given elsewhere of the “quantum interference” effects that result from axis tilting and the procedures that are used to account for them.²³⁻²⁶ Briefly, rigid-rotor Hamiltonians are used for the ground and excited states as before. Then, three Euler angles (ϕ_T, θ_T, χ_T) are used to specify the orientation of the principal moment of inertia tensor of the excited state in the coordinate system of the ground state. Transforming the Hamiltonian matrix of the excited state into the coordinate system of the ground state then produces new off-diagonal terms that can affect the intensities. The excited state Hamiltonian is no longer “rigid” and now contains bilinear terms as well as quadratic ones.

Figure 3.9 shows the results of these calculations. When no axis tilting parameters were included in the simulation of the spectrum of Complex I, certain transitions (marked by arrows) exhibited anomalous intensities. Including axis tilting rectifies this problem; a “best-fit” of these intensities requires a rotation of the *ac* plane about the *b* axis of 3.0° ($\phi_T, \theta_T, \chi_T = 90^\circ, 3.0^\circ, -90^\circ$).

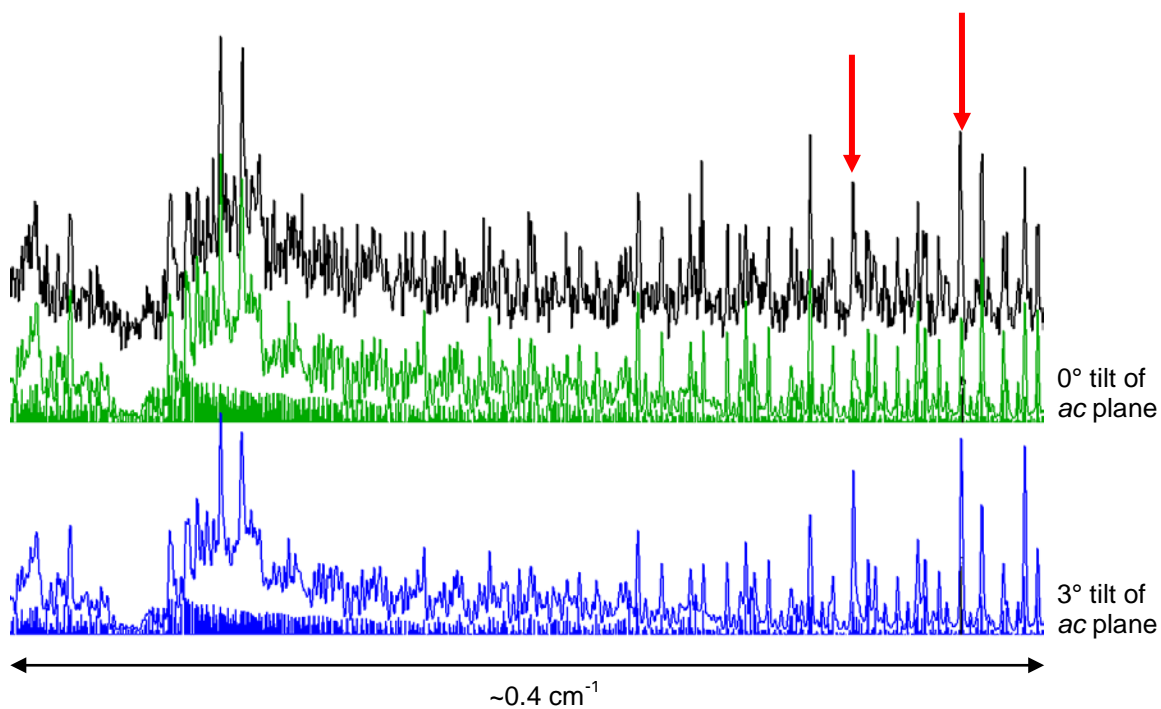


Figure 3.9. Axis-tilting in the spectrum of Complex I. The upper trace is the experimental spectrum, and the lower traces are the simulated spectra. The two arrows indicate two transition intensities that are affected by rotation of the *ac* plane about the *b* axis. The upper trace with 0° of *ac* axis tilt does not account for the obscured intensities, but the lower trace with 3° of *ac* axis tilt does.

3.5.4 Assignment of Complex I

Three possible single atom Ar complexes of HHP are possible, as shown in Fig. 3.10. In order to determine which of these is the carrier of the spectrum of Complex I, we first minimized the energy of each of the structures and calculated their rotational constants. These are listed in Table 3.3. Comparing the observed experimental rotational constants obtained from the fit of the spectrum with those predicted for the three possible structures, we note that the calculated values for the chair-HHP-Ar structure are significantly closer to the observed ones, with the maximum error being +1.00 % in A. The predicted inertial defect of -820.6 amu \AA^2 also is much closer to the experimental value of -845.5 amu \AA^2 . It therefore can be concluded that the closest red shifted band with respect to the origin bands of HHP can be assigned to the chair-HHP Ar complex. We also note that the observed 15 cm^{-1} red shift of this complex is similar to those observed in the Ar complexes of several other naphthalene-like molecules.^{18,20-22}

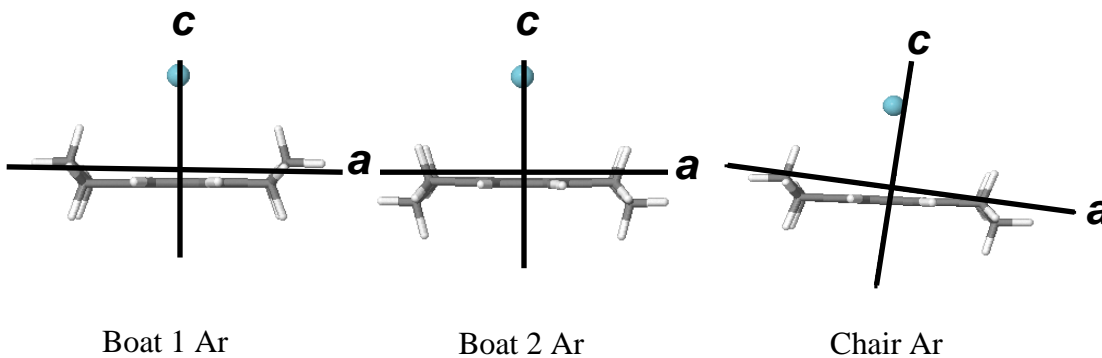


Figure 3.10. Three possible Ar complex conformers for HHP.

Table 3.3. Comparison of the ground state rotational constants of Complex I with theoretical predictions for HHP-Ar.

Parameters	Experimental		Theoretical	
	Complex I	Boat 1 Ar ^a	Boat 2 Ar ^a	Chair Ar ^a
A" (MHz)	548.4 (1)	559.8	535.2	553.9
B" (MHz)	355.2 (1)	362.3	351.3	357.5
C" (MHz)	337.2 (1)	337.9	337.9	335.7
$\Delta I''$ (amu Å ²)	-845.5	-802.0	-887.2	-820.6

*Calculated values obtained at MP2/6-31G** and CIS/6-31G** levels of theory

We can use the differences in the rotational constants of the bare molecule and the complex to determine the center-of-mass (COM) coordinates of the Ar atom in the principal axis frame of the bare molecule and complex frame, using Kraitchman's equations.¹⁴ The assumption in this analysis is that complex formation does not change the structure of the isolated molecule.¹⁹ These data (see Table 3.4) show that the Ar atom is displaced above the naphthalene ring unit by $|c| = 3.46$ Å, and also is displaced from the COM of HHP in the plane by $|a| = 0.11$ and $|b| = 0.11$ Å in the S_0 state. There is a sign ambiguity in each of these coordinates owing to the quadratic dependence of the displacements of the atoms from the three inertial axes on the moments of inertia. This creates four possible binding sites, and in this particular case results in two sets of equivalent pairs owing to the symmetry of the bare molecule.

The derived positions of the attached Ar atom are likely to be affected significantly by vibrational averaging. There have been many studies of such effects, both experimental and theoretical. A relevant example is the study of naphthalene-Ar using a 3D DVR method by Mandziuk and Bacic.²⁷ These authors parameterized the intermolecular PES as a sum of atom-atom Lennard-Jones 6-12 potentials, and found two

equivalent minima, at $(x, y, z) = (\pm 0.412, 0.0, \text{and } 3.467 \text{ \AA})$. The isomerization barrier separating the two minima is very low, only 0.294 cm^{-1} ; the depths of the minima were found to be -383 cm^{-1} . Now, x and y are reversed in HHP (see Fig. 3.8); thus, we expect a non-zero value of $|b|$. Vibrational averaging along x (*nee* y) also would lead to a non-zero value of $|a|$. The fact that $|a|$ and $|b|$ have about the same value in the ground state suggests that if a barrier exists along either coordinate, it must be very small.

Table 3.4. Kraitchman analysis of Complex I and Complex II

State	Parameter	Complex I (\AA) ^a	Complex II (\AA) ^b
S ₀	$ a $	0.11	0.47
	$ b $	0.11	0.08
	$ c $	3.46	4.15
S ₁	$ a $	0.09	0.52
	$ b $	0.11	0.05
	$ c $	3.43	4.07

^achair-HHP-Ar in HHP Chair frame.

^bchair-HHP-H₂O in HHP Chair frame.

Only small changes are observed in each of the three coordinates upon excitation of chair-HHP to its S₁ state (Table 3.4). $|a|$ decreases from 0.11 to 0.09, $|b|$ remains essentially the same, and $|c|$ decreases from 3.46 to 3.43 \AA. The 0.03 \AA decrease in $|c|$ is a likely consequence of a stronger van der Waals bond in the S₁ state and is consistent with the observation that the transition of Complex I is redshifted relative to the corresponding origin band of the bare molecule. The decrease in $|a|$ suggests that there

are increased repulsive interactions between the Ar atom with the hydrogen atoms on the symmetrically attached chains when it moves closer to the naphthalene ring. The decreases in $|a|$ and $|c|$ values are responsible for the 3° rotation of the ac plane around the b axis when the photon is absorbed.

The spectrum of Complex I was fit with 0/85/15 ($a/b/c$) hybrid band character, indicating that the transition moment vector makes a small projection on the c -inertial axis as well as on the b -inertial axis. The only possible explanation for this is that the *equilibrium* value of $|b|$ is not zero. Displacement of the Ar atom away from b will produce a slight rotation of the bc plane around the a axis, resulting in a non-zero projection of the transition moment on c .

3.5.5 Assignment of Complex II

Finally, the identity of Complex II needs to be established. Comparison of its rotational constants with those predicted for all single atom Ar complexes (see Tables 3.2 and 3.3) shows that they are quite different, compared to the calculated values. Particularly noticeable is the large experimental value of A'' (628.6 MHz, compared to 548.4 MHz for chair-HHP-Ar). If Complex II was a single Ar atom complex of HHP, the Ar atom would need to be less than 3.0 \AA away from the naphthalene ring. This does not seem plausible. Nor does a two-atom Ar complex, since its rotational constants would be smaller than those for a single atom complex.

Given its larger rotational constants, we then postulated that Complex II is a weakly bound water complex of HHP, formed adventitiously during the expansion. (He atom complexes also would be a possibility, but their red shifts are typically much smaller than 26 cm^{-1} .) Table 3.5 lists the rotational constants of three optimized water-HHP complexes; boats 1 and 2, and chair, compared to the observed values for Complex II. As will be seen, there is a reasonable match between the calculated rotational constants of all three structures and the measured values. The best agreement is obtained for the chair-HHP- H_2O complex, whose rotational constants differ from the experimental values by 0.07 % (A), 4.4 % (B), and -2.1 % (C).

Table 3.5. Comparison of the ground state rotational constants of Complex II with theoretical predictions for HHP- H_2O .

Parameters	Experimental		Theoretical	
	Complex II	Boat 1 H_2O^a	Boat 2 H_2O^a	Chair H_2O^a
A" (MHz)	628.5 (1)	650.8	620.9	633.3
B" (MHz)	386.2 (1)	398.8	399.0	403.3
C" (MHz)	335.3 (1)	332.0	328.6	328.3
$\Delta I''$ ($\text{amu } \text{Å}^2$)	-605.5	-521.6	-542.6	-511.7

*Calculated values obtained at MP2/6-31G** level of theory.

Several other factors support this assignment. A Kraitchman analysis of the data (see Table 3.4) shows that the COM of the H_2O molecule is displaced above the naphthalene ring unit of the HHP chair conformer by $|c| = 4.15 \text{ Å}$, and is further displaced by $|a| = 0.47$ and $|b| = 0.08 \text{ Å}$ in the S_0 state. The distance between the COM's of H_2O and HHP is similar to the distance found by Gotch and Zwier for the benzene- H_2O complex in its electronic ground state (3.32 Å).^{28,29} In benzene- H_2O , it is believed that the H_2O binds “protons-down”, on or near the six-fold axis, and undergoes internal

rotation about that axis, though later microwave studies³⁰ dispute this point. The derived values of the two in-plane coordinates in the presumed chair-HHP-H₂O complex are quite different, suggesting that the water molecule might be bound significantly off the perpendicular axis. From the coordinates calculated from the Kraitchman analysis, the most likely orientation of the H₂O is with both hydrogens atoms along the *a* inertial axis, due to the small $|b|$ displacement. *Ab initio* calculations predict that the H₂O is approximately 3.3 Å above the HHP naphthalene ring with the protons pointing down, as in the case of benzene-H₂O, and with the oxygen atom located almost directly above the C2 atom of HHP, where the -(CH₂)₃- chain points toward the opposite side. Also, no tunneling splittings were observed in the high resolution spectrum of Complex II, suggesting that the putative water molecule might be rather tightly held in place.

Upon excitation, there are again slight changes in the rotational constants of Complex II, resulting in differences between the H₂O substitution coordinates in the two electronic states. $|a|$ increases from 0.47 to 0.52, $|b|$ decreases from 0.08 to 0.05, and $|c|$ decreases from 4.15 to 4.07 Å (Table 3.6). (As in the case of Complex I, this leads to axis tilting in the spectrum of Complex II; a rotation of the *ac* plane about the *b* axis of $2.8 \pm 0.5^\circ$ reproduces the intensity patterns in all three branches in the spectrum of Complex II.) The 0.08 Å decrease in $|c|$ is again a consequence of the stronger van der Waals interaction in the S₁ state and is also consistent with the observation that the complex transition is redshifted by 26 cm⁻¹ from the corresponding origin band of the bare molecule.

3.6 CONCLUSIONS

Rotationally resolved $S_1 \leftarrow S_0$ fluorescence excitation spectra of two electronic origin bands of 1, 2, 3, 6, 7, 8- hexahdropyrene (HHP) have been observed and fit using rigid-rotor Hamiltonians for both electronic states. Based on differences in their rotational constants, Band I at 30648.0 cm^{-1} has been assigned to chair-HHP and Band II at 30658.8 cm^{-1} has been assigned to boat-HHP. In addition, two red-shifted bands also were observed at high resolution and assigned. Comparison of their rotational constants with those predicted by theory suggests that the band at 30633.0 cm^{-1} is due to the chair-HHP Ar complex, and that the band at 30622.0 cm^{-1} is most likely due to a single H_2O complex of chair-HHP, not an Ar complex. No bands that could be attributed to the boat conformer of HHP were detected. It is possible that such bands are obscured by the much stronger Band I origin, but we consider this unlikely.

3.7 ACKNOWLEDGMENTS

Some theoretical calculations were performed using at the University of Pittsburgh's Center for Molecular and Materials Simulations. This research has been supported by the National Science Foundation (CHE-0911117). We thank both organizations for their support.

3.8 REFERENCES

- 1 W. L. Meerts and W. A. Majewski, *J. Mol. Spectrosc.* **104**, 271 (1984).
- 2 W. A. Majewski, D. F. Plusquellic, and D. W. Pratt, *J. Chem. Phys.* **90**, 1362 (1989).
- 3 P. U. De Haag, R. Spooren, M. Ebben, W. L. Meerts, and J. T. Hougen, *Mol. Phys.* **69**, 265 (1990).
- 4 J. R. Johnson, K. D. Jordan, D. F. Plusquellic, and D. W. Pratt, *J. Chem. Phys.* **93**, 2258 (1990).
- 5 X. Q. Tan, D. J. Clouthier, R. H. Judge, D. F. Plusquellic, J. L. Tomer, and D. W. Pratt, *J. Chem. Phys.* **95**, 7862 (1991).
- 6 X. Q. Tan, W. A. Majewski, D. F. Plusquellic, and D. W. Pratt, *J. Chem. Phys.* **94**, 7721 (1991).
- 7 A. Chakraborty, D. Nath, M. Halder, N. Guchhait, and M. Chowdhury, *J. Chem. Phys.* **114**, 865 (2000).
- 8 W. A. Majewski, J. F. Pfanstiel, D. F. Plusquellic, and D. W. Pratt, in *Laser Techniques in Chemistry*, edited by T.R. Rizzo and A. B. Myers, (Wiley, New York, 1995), p.101.
- 9 D. F. Plusquellic, Ph. D. Thesis, University of Pittsburgh (1992).
- 10 S. Gerstenkorn and P. Luc, *Atlas du spectroscopie d'absorption de la molecule d'iode*, CRNS, Paris (1978 and 1982).
- 11 D. F. Plusquellic, R. D. Suenram, B. Mate, J. O. Jensen, and A. C. Samuels, *J. Chem. Phys.* **115**, 3057 (2001).
- 12 M. J. Frisch, G. W. Trucks, H. B. Schlegel, G. E. Scuseria, M. A. Robb, J. R. Cheeseman, J. A. J. Montgomery, T. Vreven, K. N. Kudin, J. C. Burant, J. M. Millam, S. S. Iyengar, J. Tomasi, V. Barone, B. Mennucci, M. Cossi, G. Scalmani, N. Rega, G. A. Petersson, H. Nakatsuji, M. Hada, M. Ehara, K. Toyota, R. Fukuda, J. Hasegawa, M. Ishida, T. Nakajima, Y. Honda, O. Kitao, H. Nakai, M. Klene, X. Li, J. E. Knox, H. P. Hratchian, J. B. Cross, V. Bakken, C. Adamo, J. Jaramillo, R. Gomperts, R. E. Stratmann, O. Yazyev, A. J. Austin, R. Cammi, C. Pomelli, J. W. Ochterski, P. Y. Ayala, K. Morokuma, G. A. Voth, P. Salvador, J. J. Dannenberg, V. G. Zakrzewski, S. Dapprich, A. D. Daniels, M. C. Strain, O. Farkas, D. K. Malick, A. D. Rabuck, K. Raghavachari, J. B. Foresman, J. V.

- Ortiz, Q. Cui, A. G. Baboul, S. Clifford, J. Cioslowski, B. B. Stefanov, G. Liu, A. Liashenko, P. Piskorz, I. Komaromi, R. L. Martin, D. J. Fox, T. Keith, M. A. Al-Laham, C. Y. Peng, A. Nanayakkara, M. Challacombe, P. M. W. Gill, B. Johnson, W. Chen, M. W. Wong, C. Gonzalez, and J. A. Pople, Gaussian 03, Revision 6.0 (Gaussian, Inc., Wallingford CT, 2004).
13. Y. Kowaka, Y. Suganuma, N. Ashizawa, N. Nakayama, H. Goto, T. Ishimoto, U. Nagashima, and M. Baba, *J. Mol. Spectrosc.* **260**, 72 (2010).
 14. W. Gordy and R. L. Cook, *Microwave Molecular Spectra*, 3rd ed. (Wiley, New York, 1984).
 15. T. Chakraborty and M. Chowdhury, *Chem. Phys. Lett.* **171**, 25 (1990).
 16. T. Chakraborty and M. Chowdhury, *Chem. Phys. Lett.* **177**, 223 (1991).
 17. L. Alvarez-Valtierra and D. W. Pratt, *J. Chem. Phys.* **126**, 224308 (2007).
 18. T. Troxler and S. Leutwyler, *J. Chem. Phys.* **95**, 4010 (1991).
 19. T. Brupbacher, J. Makarewicz, and A. Bauder, *J. Chem. Phys.* **101**, 9736 (1994).
 20. B. B. Champagne, J. F. Pfanstiel, D. W. Pratt, and R. C. Ulsh, *J. Chem. Phys.* **102**, 6432 (1995).
 21. T. Vondrak, S. Sato, and K. Kimura, *Chem. Phys. Lett.* **261**, 481 (1996).
 22. L. Alvarez-Valtierra, Ph. D. Thesis, University of Pittsburgh (2007).
 23. J. T. Hougen and J. K. G. Watson, *Can. J. Phys.* **43**, 298 (1965).
 24. A. Held, B. B. Champagne, and D. W. Pratt, *J. Chem. Phys.* **95**, 8732 (1991).
 25. D. F. Plusquellic and D. W. Pratt, *J. Chem. Phys.* **97**, 8970 (1992).
 26. T. M. Korter, J. Kupper, and D. W. Pratt, *J. Chem. Phys.* **111**, 3946 (1999).
 27. M. Mandziuk and Z. Bacic, *J. Chem. Phys.* **98**, 7165 (1993).
 28. J. D. Augspurger, C. E. Dykstra, and T. S. Zwier, *J. Phys. Chem.* **96**, 7252 (1992).
 29. A. J. Gotch and T. S. Zwier, *J. Chem. Phys.* **96**, 3388 (1992).
 30. H. S. Gutowsky, T. Emilsson, and E. Arunan, *J. Chem. Phys.* **99**, 4883 (1993).

**4.0 HIGH RESOLUTION ELECTRONIC SPECTROSCOPY OF *O*- AND *M*-
TOLUIDINE IN THE GAS PHASE. BARRIER HEIGHT DETERMINATIONS
FOR THE METHYL GROUP TORSIONAL MOTIONS.**

Philip J. Morgan, Leonardo Alvarez-Valtierra,^a and David W. Pratt^b

^aPresent address: División de Ciencias e Ingenierías, Universidad de Guanajuato, Campus León. León, Gto. 37150, México.

^bDepartment of Chemistry, University of Pittsburgh
Pittsburgh, PA 15260 USA

This work is published in *J. Phys. Chem. A.*, **113**, (2009), 13221.

P. J. Morgan and L. Alvarez-Valtierra performed the experimental measurements; P. J. Morgan analyzed the spectra and wrote the paper.

4.1 ABSTRACT

High resolution electronic spectra of *o*- and *m*-toluidine have each been recorded for the $S_1 \leftarrow S_0$ origin band transitions of the isolated molecules. Each spectrum is split into two sub-bands owing to tunneling motions along the methyl group torsional coordinate. Analyses of these data provide information about the preferred configurations of the methyl groups and the barriers opposing their motions in both the ground and excited electronic states. Despite their apparent similarities, the experiments reveal that these properties are quite different in the two molecules. Possible reasons for this behavior are discussed.

4.2 INTRODUCTION

The subject of internal rotation has been studied extensively for many years, especially concerning molecules containing an attached methyl group.¹⁻⁸ Of particular interest is the effect that different neighboring groups have on the potential barrier heights of a methyl group attached to a benzene ring. In toluene itself, internal rotation of the methyl group is relatively free in both the ground electronic state (S_0) and the lowest excited electronic state (S_1). The measured barriers are ~ 5 and ~ 25 cm^{-1} , respectively.⁶ However, substitution of a second ring hydrogen atom with a methoxy group changes this situation dramatically. A recent study of 2- and 3-methylanisole⁷ showed that the methyl group internal motions are significantly more rigid in one of the electronic states and less rigid

in the other, with the corresponding barriers depending on the positions of the two groups relative to one another.

In this contribution, we report on a similar study of 2- and 3-methylaniline (*o*- and *m*-toluidine), in which an amino group replaces the methoxy group in the methylanisoles. This problem has been addressed before by Ito and co-workers² using low resolution fluorescence excitation spectroscopy (FES). These studies showed that the potential barrier of the methyl rotor in *o*-toluidine is very large in the ground state, but very small in the first excited electronic state. The opposite behavior was observed for *m*-toluidine, with nearly free internal rotation in the ground state and much more rigid internal rotation in the excited state. Okuyama *et al.*² found no change in conformation of the methyl group upon excitation in either *o*- or *m*-toluidine. It is the goal of the present work to determine if these conclusions are correct and to explore in greater detail the factors that might be responsible for these remarkable effects. Our tool is high resolution FES, as in the case of the methylanisoles.⁷

4.3 EXPERIMENTAL

Both *o*-toluidine and *m*-toluidine were purchased from Sigma Aldrich and used as received. Rotationally resolved $S_1 \leftarrow S_0$ excitation spectra were recorded using a molecular beam laser spectrometer, described elsewhere.⁹ Briefly, samples were heated to $\sim 45^\circ$ C in a quartz source, seeded in dry argon gas ($> 90\%$ purity), and then expanded through a 240 μm tip nozzle. The expansion was skimmed ~ 2 cm downstream with a 1

mm diameter skimmer to form a molecular beam and then crossed 15 cm downstream of the nozzle with a laser beam operating in the UV. The laser radiation was generated by a ring dye laser operating in the visible (Rhodamine 590 dye) whose output was externally doubled using a Wavetrain frequency doubler (572 and 600 BBO nm crystals) to produce ~ 2 mW of UV radiation with a linewidth of ~ 1 MHz. Fluorescence was collected with spatially selective optics and detected by a photon counting system and a PMT. All spectra were recorded using the jba95 data acquisition software.¹⁰ Typical scan lengths were 4 cm^{-1} over 1000 sec. The I_2 absorption spectrum was used to determine the absolute transition frequencies of the excitation spectrum to an accuracy of ± 30 MHz. A stabilized etalon was used to produce relative frequency markers having a mode-matched free spectral range of 599.5040 ± 0.0005 MHz in the UV, corresponding to a free spectral range of 299.7520 ± 0.0005 MHz in the visible. The resulting spectra were fit using the jb95 least squares fitting program.¹¹

Theoretical calculations were performed using the Gaussian 03 suite of programs¹² to supplement the experiments. Geometry optimizations of both *o*-toluidine and *m*-toluidine in the ground state were performed at the MP2 level of theory with a 6-31G** basis set. Configuration interaction singles (CIS) calculations with a 6-31G** basis set were performed on the excited state.

4.4 RESULTS

Figure 4.1 shows the vibrationally resolved fluorescence excitation spectra of *o*-toluidine and *m*-toluidine obtained by Ito and coworkers.⁵ In this figure, a labeling scheme of the vibrational bands $0a_1$, $1e$, $2e$, *etc.* is used, where a number indexes the upper state torsional levels and a letter designates their symmetries. In the infinite barrier limit, the levels $0a_1$ and $1e$, $2e$ and $3a_1$, *etc.* are degenerate. Reduction of this barrier leads to a methyl group tunneling motion that lifts the degeneracy of the $0a_1$, $1e$; $2e$, $3a_1$; *etc.* levels, in both electronic states. The origin band of *o*-toluidine appears at 34316.9 cm^{-1} , red shifted with respect to toluene by more than 3000 cm^{-1} . The origin band of *m*-toluidine is red shifted by an even larger amount, appearing at 33820.2 cm^{-1} . As assigned by Okuyama *et al.*⁴, the $1e$ band is blue shifted with respect to the $0a_1$ band for *o*-toluidine, but is red shifted with respect to the $0a_1$ band for *m*-toluidine. These assignments suggest that the potential barriers for the methyl group torsional motion in both electronic states are significantly influenced by the relative positions of the methyl and amino groups on the benzene ring.

High resolution experiments have been performed to validate these conclusions. Figure 2.2 shows the rotationally resolved $S_1 \leftarrow S_0$ fluorescence excitation spectrum of band $0a_1$ in *o*-toluidine. The spectrum spans approximately 2.9 cm^{-1} and exhibits both *a*- and *b*-type transitions. The spectrum was fit using rigid-rotor Hamiltonians¹³ for both electronic states, confirming its identity as the $0a_1$ vibronic band. First, a simulated spectrum was generated using estimated rotational constants from the *ab initio* calculations. Single transitions from the simulated spectrum were then assigned to

corresponding transitions in the experimental spectrum, using the fitting program jb95.¹¹ A linear least-squares fitting procedure was finally used to optimize the rotational constants from a comparison of the observed and calculated transitions. The bottom of Figure 4.2 shows a portion of the fit spectrum, where a standard deviation of 1.40 MHz was obtained by fitting 135 lines. The band was found to be a hybrid band, having 59% *a*-type and 41% *b*-type transition character. The spectrum was fit using a Voigt lineshape profile for individual transitions, with Gaussian widths of 20 MHz and Lorentzian widths

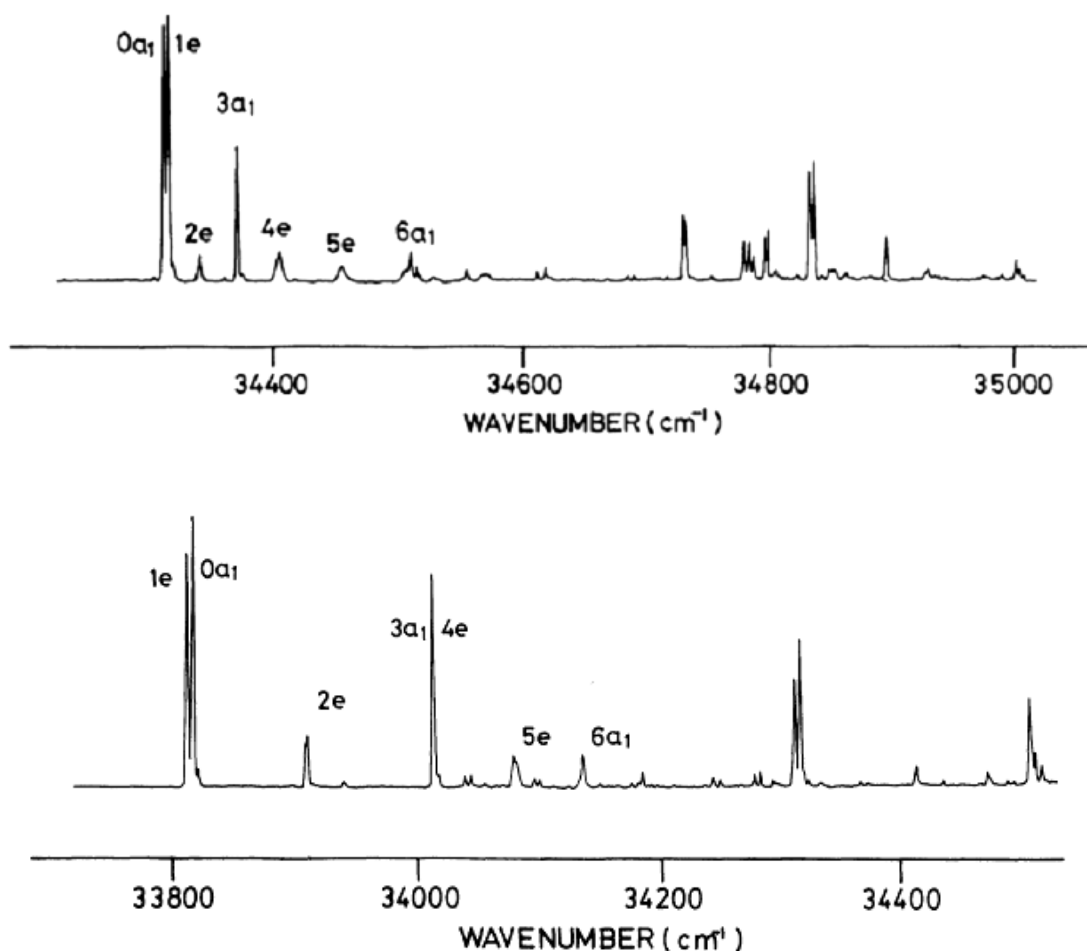


Figure 4.1. Vibrationally resolved fluorescence excitation spectra of *o*-toluidine (top) and *m*-toluidine (bottom). (Ref. 2)

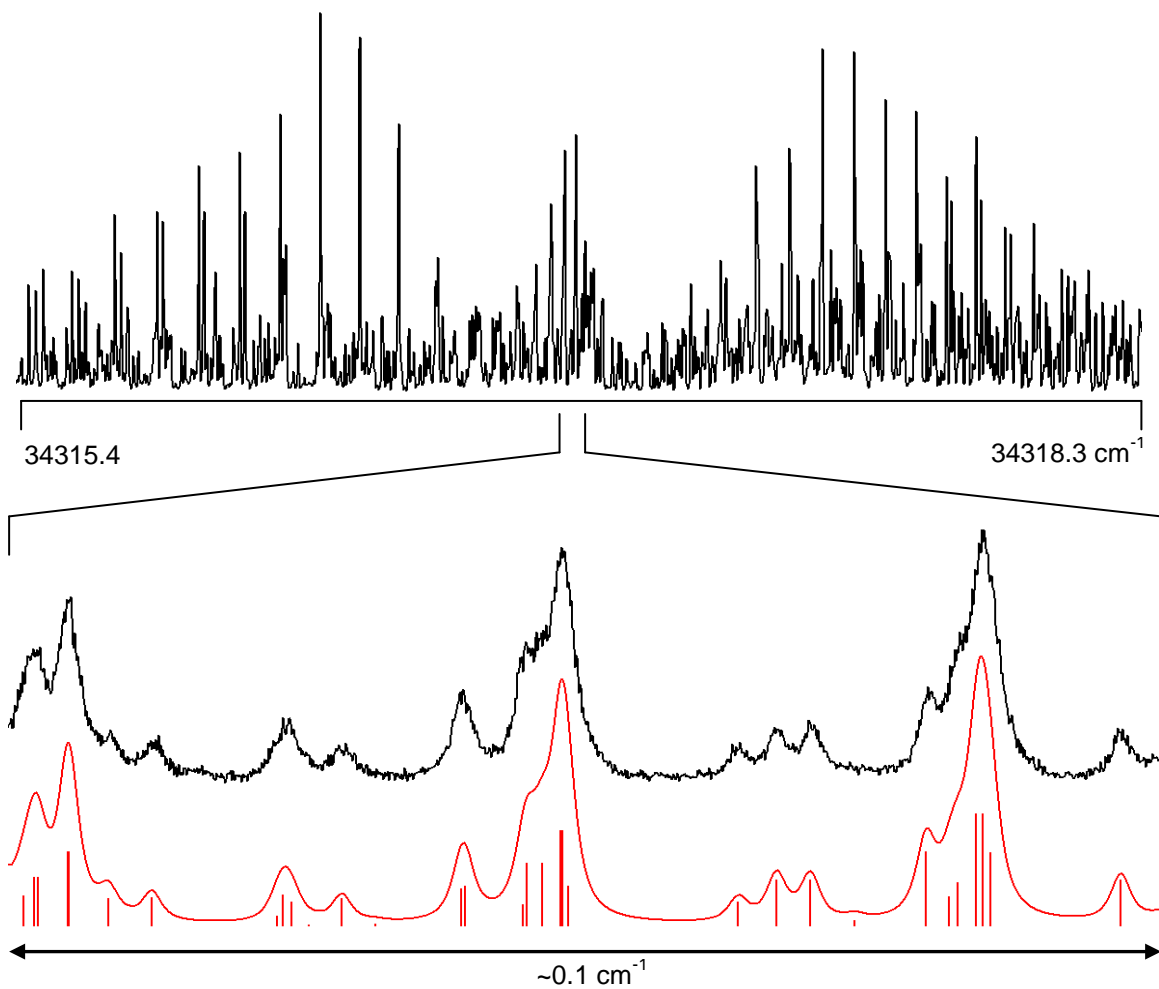


Figure 4.2. Rotationally resolved fluorescence excitation spectrum of the $0a_1$ band of *o*-toluidine, with origin at 34316.9 cm^{-1} . The lower part of the figure shows an expanded view of the Q-branch region. In this view, the upper trace is the experimental spectrum, and the lower trace is the simulated spectrum. Individual lines represent the transitions responsible for the spectrum. The band was fit using a Voigt lineshape profile.

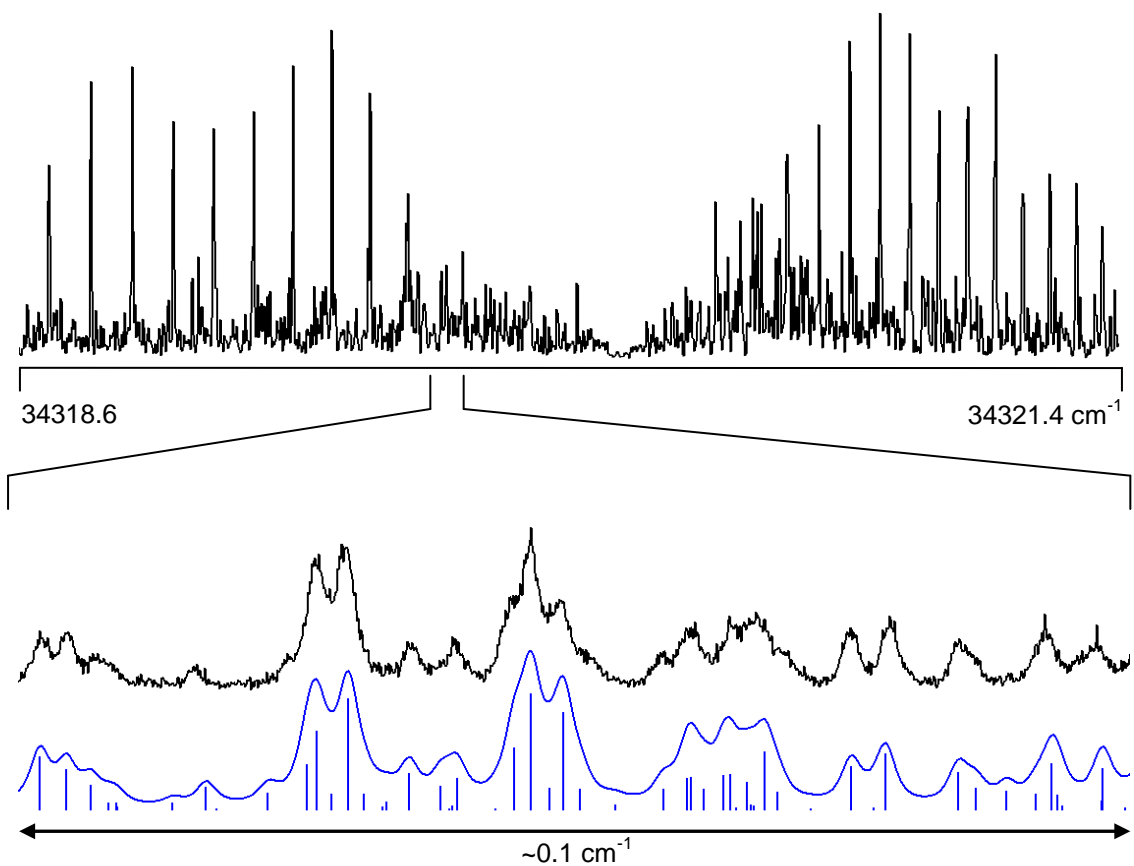


Figure 4.3. Rotationally resolved fluorescence excitation spectrum of the 1e band of *o*-toluidine, with origin at 34320.2 cm⁻¹. The lower part of the figure shows an expanded view of the P-branch region. In this view, the upper trace is the experimental spectrum, and the lower trace is the simulated spectrum. Individual lines represent the transitions responsible for the spectrum. The band was fit using a Voigt lineshape profile.

of 38 MHz, corresponding to a fluorescence lifetime of $\tau = 4.2$ ns. Table 4.1 lists all of the inertial parameters obtained from the fit of the spectrum.

Band 1e of *o*-toluidine located at 34320.2 cm^{-1} is shown in Figure 4.3 and spans approximately 2.8 cm^{-1} . Unlike the $0a_1$ band in this molecule, the high resolution spectrum of the 1e band in *o*-toluidine exhibits further splittings of the individual rovibronic transitions into two components. This confirms its identity as the 1e band. The normally degenerate rovibronic transitions in this band are coupled by the torsion-rotation interaction, leading to a K-dependent splitting in the high resolution spectrum.¹⁴ These splittings are described by the following “non-rigid” rotor Hamiltonian for both electronic states,^{3,13}

$$H_{eff}^E = A_E P_a^2 + B_E P_b^2 + C P_c^2 + F W_E^{(1)} (\rho_a P_a + \rho_b P_b). \quad (4.1)$$

Here, A_E and B_E are the effective rotational constants given by

$$A_E = A + F W_E^{(2)} \rho_a^2, \quad B_E = B + F W_E^{(2)} \rho_b^2. \quad (4.2)$$

F is the internal rotor constant, $W_E^{(1)}$ and $W_E^{(2)}$ are the first- and second-order perturbation terms, first written down by Herschbach,¹⁵ and ρ_a and ρ_b are weighted direction cosines of the angle between the axis of internal rotation and the *a*- and *b*-inertial axes of the molecule, where $\rho_a = \lambda_a (I_\alpha / I_a)$. I_α is the moment of inertia of the methyl group, and r is a reduction factor

$$r = 1 - \sum (\lambda_g^2 I_\alpha / I_g), \quad g = a, b, c. \quad (4.3)$$

A portion of the fit spectrum of the 1e band of *o*-toluidine is shown at the bottom of Figure 3; a standard deviation of 7.82 MHz was obtained from a fit of 100 lines. The inertial parameters obtained from the fit of the spectrum are also listed in Table 4.1. The

inertial parameters obtained for the 1e band of *o*-toluidine are consistent with those obtained by Kalkman and Meerts.¹⁶

The rotationally resolved spectrum of the 0a₁ band of *m*-toluidine spans approximately 3.0 cm⁻¹ and is shown in Figure 4.4. No additional splittings appear in this spectrum. Hence, it was fit using rigid-rotor Hamiltonians for both electronic states, confirming its identity as an a₁ vibronic band. The bottom of Figure 4 shows a portion of the fit at full experimental resolution; 153 lines were assigned and a standard deviation of 1.73 MHz was obtained. The spectrum was again fit with a Voigt lineshape profile, with Gaussian widths of 18 MHz and Lorentzian widths of 38 MHz, corresponding to a lifetime of $\tau = 4.2$ ns. The origin band of *m*-toluidine was also found to be a hybrid band, with 48% *a*-type and 52% *b*-type transition character. The inertial parameters obtained from the fit of the spectrum are listed in Table 4.2.

Figure 4.5 shows the rotationally resolved spectrum of the 1e band of *m*-toluidine located at 33814.9 cm⁻¹. As in the case of the 1e band for *o*-toluidine, this band could not be fit using a rigid-rotor Hamiltonian, and required the addition of perturbation terms. This is again a result of the torsion-rotation interaction lifting the degeneracies of certain rovibronic transitions, confirming the identity of this vibronic band as the 1e band. The Hamiltonian in Eq. 1 was again used to obtain a fit with a standard deviation of 3.24 MHz for the 115 assigned lines. A comparison of the simulated spectrum to the experimental shows excellent agreement and can be seen in the bottom of Figure 5. The inertial parameters obtained from the fit are also listed in Table 4.2. Neither 1e band required the use of Watson distortion terms in the fit.¹⁷

Table 4.1. Rotational constants of *o*-toluidine in its ground and excited electronic states.^a

Parameter	<i>o</i>-Toluidine 0a₁	<i>o</i>-Toluidine 1e^b	Theoretical^c
A" (MHz)	3230.9 (1)	3228.5 (1)	3243.6
B" (MHz)	2189.0 (1)	2189.1 (1)	2185.9
C" (MHz)	1316.8 (1)	1316.9 (1)	1318.7
ΔA (MHz)	-74.3 (1)	-113.4 (1)	-91.5
ΔB (MHz)	-1.8 (1)	-8.3 (1)	21.1
ΔC (MHz)	-20.8 (1)	-20.5 (1)	-9.8
ΔI" (amu Å ²)	-3.51	-3.65	-3.77
ΔI' (amu Å ²)	-1.21	-4.15	-3.21
TM angle to <i>a</i> -inertial axis	±40(2) ^o	±40(2) ^o	+42 ^o

^aNumbers in parentheses are the standard deviations of the last significant figure.

^bSee Table 3 for additional information about the first-order torsion-rotation perturbation coefficients that were used in the fit of this spectrum.

^cGeometry optimization calculation done at the MP2/6-31G** and CIS/6-31G** levels of theory.

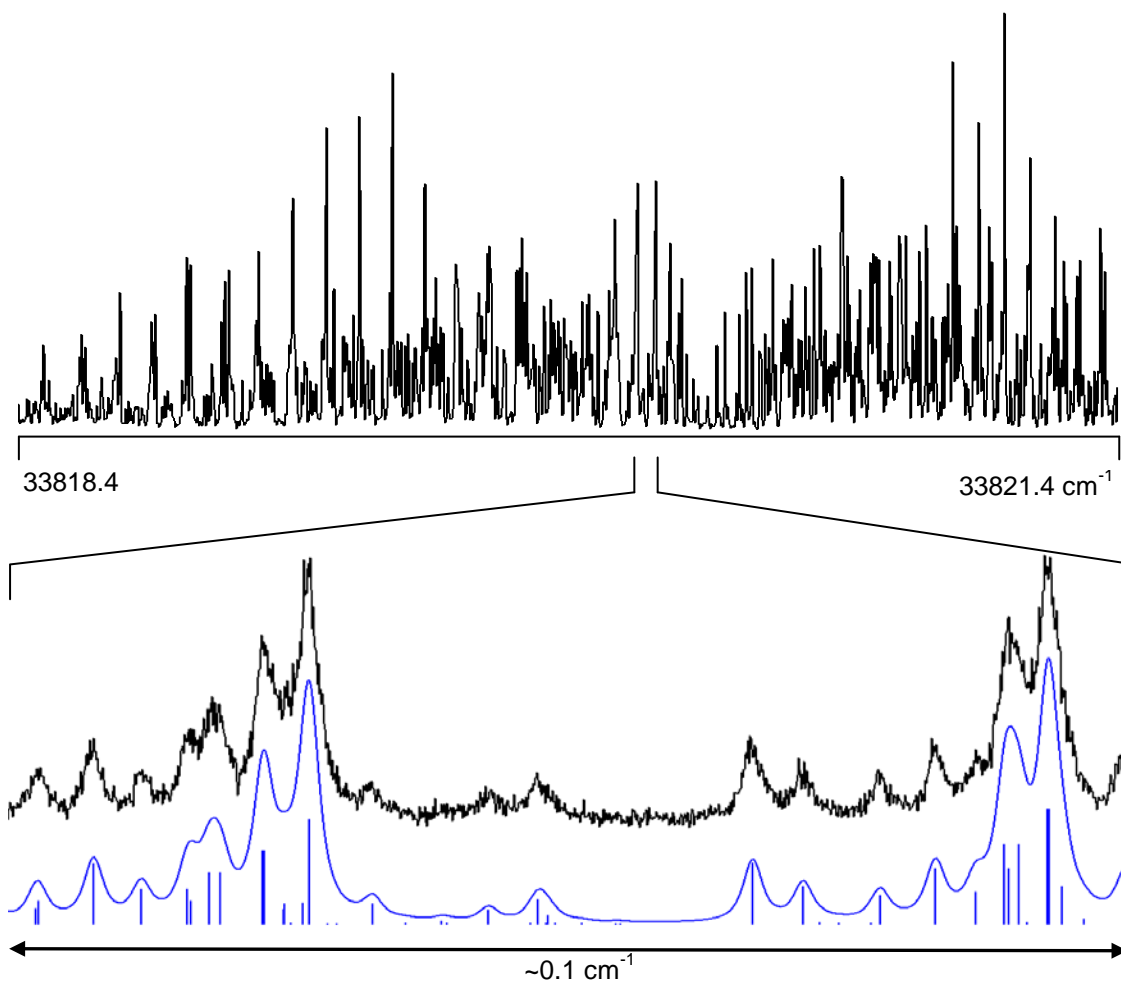


Figure 4.4. Rotationally resolved fluorescence excitation spectrum of the $0a_1$ band of *m*-toluidine, with origin at 33820.2 cm^{-1} . The lower part of the figure shows an expanded view of the Q-branch region. In this view, the upper trace is the experimental spectrum, and the lower trace is the simulated spectrum. Individual lines represent the transitions responsible for the spectrum. The band was fit using a Voigt lineshape profile.

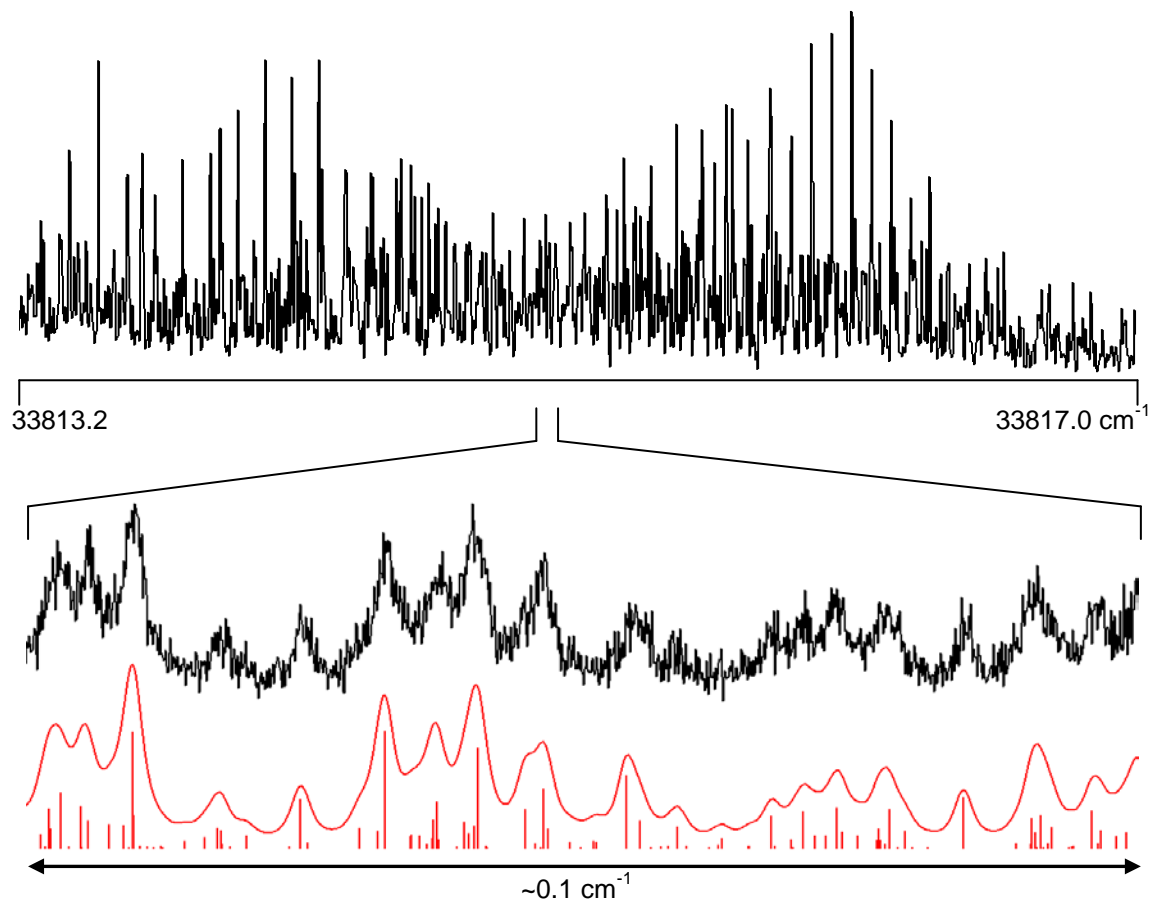


Figure 4.5. Rotationally resolved fluorescence excitation spectrum of the 1e band of *m*-toluidine, with origin at 33814.9 cm⁻¹. The lower part of the figure shows an expanded view of the Q-branch region. In this view, the upper trace is the experimental spectrum, and the lower trace is the simulated spectrum. Individual lines represent the transitions responsible for the spectrum. The band was fit using a Voigt lineshape profile.

Table 4.2. Rotational constants of *m*-toluidine in its ground and excited electronic states.^a

Parameter	<i>m</i>-Toluidine 0a₁	<i>m</i>-Toluidine 1e^b	Theoretical^c
A" (MHz)	3701.3 (1)	3700.2 (1)	3637.7
B" (MHz)	1795.9 (1)	1795.4 (1)	1796.3
C" (MHz)	1210.4 (1)	1210.3 (1)	1211.5
ΔA (MHz)	-164.7 (1)	-164.9 (1)	-46.5
ΔB (MHz)	-7.1 (1)	-7.0 (1)	9.0
ΔC (MHz)	-12.9 (1)	-12.9 (1)	-1.3
ΔI" (amu Å ²)	-0.414	-0.508	-3.12
ΔI' (amu Å ²)	-3.40	-3.50	-3.06
TM angle to <i>a</i> -inertial axis	±46(2) ^o	±46(2) ^o	+45 ^o

^aNumbers in parentheses are the standard deviations of the last significant figure.

^bSee Table 3 for additional information about the first-order torsion-rotation perturbation coefficients that were used in the fit of this spectrum.

^cGeometry optimization calculation done at the MP2/6-31G** and CIS/6-31G** levels of theory.

4.5 DISCUSSION

4.5.1 Ground and Excited State Conformers

Tables 4.1 and 4.2 list the ground and excited state rotational constants for both origin bands of *o*-toluidine and *m*-toluidine, respectively, along with the corresponding theoretical values. Comparisons between the theoretical and experimental rotational constants of both molecules confirm their respective identities. It can be seen that the set of rotational constants obtained for both *o*- and *m*-toluidine are very different from one another.

These differences in the values of the ground and excited rotational constants can be easily understood from Figure 4.6, which depicts the ground state molecular structures of *o*- and *m*-toluidine in their *ab* inertial planes. The *a* and *b* axes are rotated with respect to their “canonical” positions owing to the simultaneous presence of the $-\text{NH}_2$ and $-\text{CH}_3$ groups. In *o*-toluidine, the *a* axis lies between the two substituents, passing through the connecting ring C-C bond, whereas in *m*-toluidine, the *b* axis lies between them, passing through the adjacent C-H bond. As a result, the $-\text{NH}_2$ group in *m*-toluidine lies closer to the *a* inertial axis, giving it the larger A value. Correspondingly, the $-\text{NH}_2$ group in *o*-toluidine lies closer to the *b* axis, giving it the larger B value. The C value of *o*-toluidine is larger than that of *m*-toluidine owing to the displacement of its COM relative to the center of the ring.

The ground state inertial defect values of the $0a_1$ and $1e$ methyl torsional bands in *o*-toluidine are close to the value expected for an attached methyl group ($-3.30 \text{ amu } \text{\AA}^2$),

-3.51 and -3.65 amu Å², respectively. (The slightly more negative values of ΔI can be attributed to some non-planar character of the attached -NH₂ group.) However, the inertial defect values of the 0a₁ and 1e methyl torsional bands in *m*-toluidine are significantly less in magnitude, -0.414 and -0.508 amu Å², respectively. Moreover, the ΔI value of the 0a₁ level in *o*-toluidine decreases in magnitude to -1.21 amu Å², the ΔI value of the 1e level in *o*-toluidine increases in magnitude to -4.15 amu Å², and the ΔI values of the 0a₁ and 1e level in *m*-toluidine increase in magnitude to -3.40 and -3.50 amu Å², respectively, when the molecules are excited to their S₁ states.

Figure 4.6 also shows the S₁ ← S₀ transition moment (TM) orientations in the inertial frames of both molecules. Two orientations are possible, making angles of approximately $\theta = \pm 45^\circ$ with respect to *a* in both *o*- and *m*-toluidine. Taking θ to be negative orients the TM vector approximately parallel to the C-N bond in both molecules, whereas taking θ to be positive orients the TM vector approximately perpendicular to the C-N bond in both molecules. If the S₁ states of *o*- and *m*-toluidine are both L_b states, then the perpendicular orientation is expected, if the -NH₂ group is the ‘dominant’ substituent.

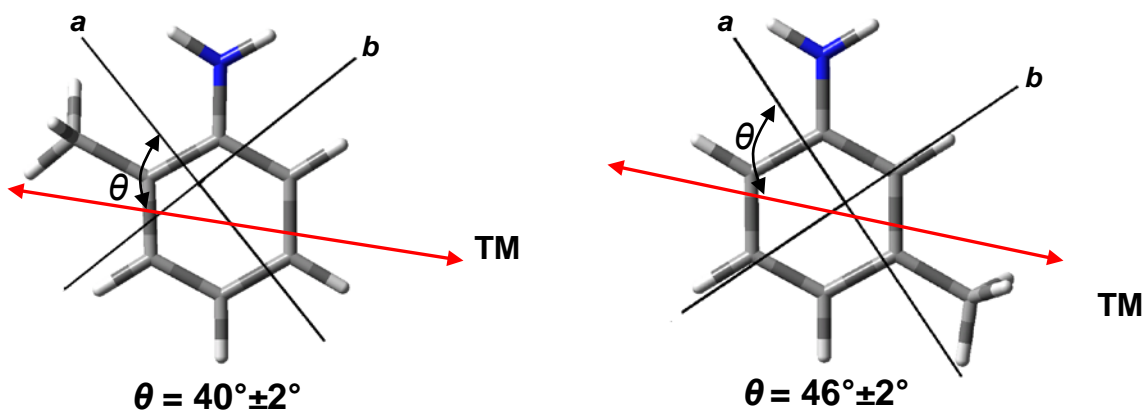


Figure 4.6. Ground state structures and S₁ ← S₀ TM orientation vectors in the *o*- and *m*-toluidines.

The molecular orbitals (MO's) that participate in the $S_1 \leftarrow S_0$ transitions of the two molecules are shown in Figure 4.7, together with the corresponding MO's of toluene and aniline. Each transition is predicted by theory to be primarily HOMO-LUMO in nature. But the relevant MO's in *o*- and *m*-toluidine are clearly much more similar to those of aniline than to those of toluene. The TM orientations are also similar, as is clear from Figure 4.7. Thus, we conclude that the amino group is the dominant substituent in the two molecules, and that the $S_1 \leftarrow S_0$ TM vector is oriented approximately perpendicular to the C-N bond in both species.

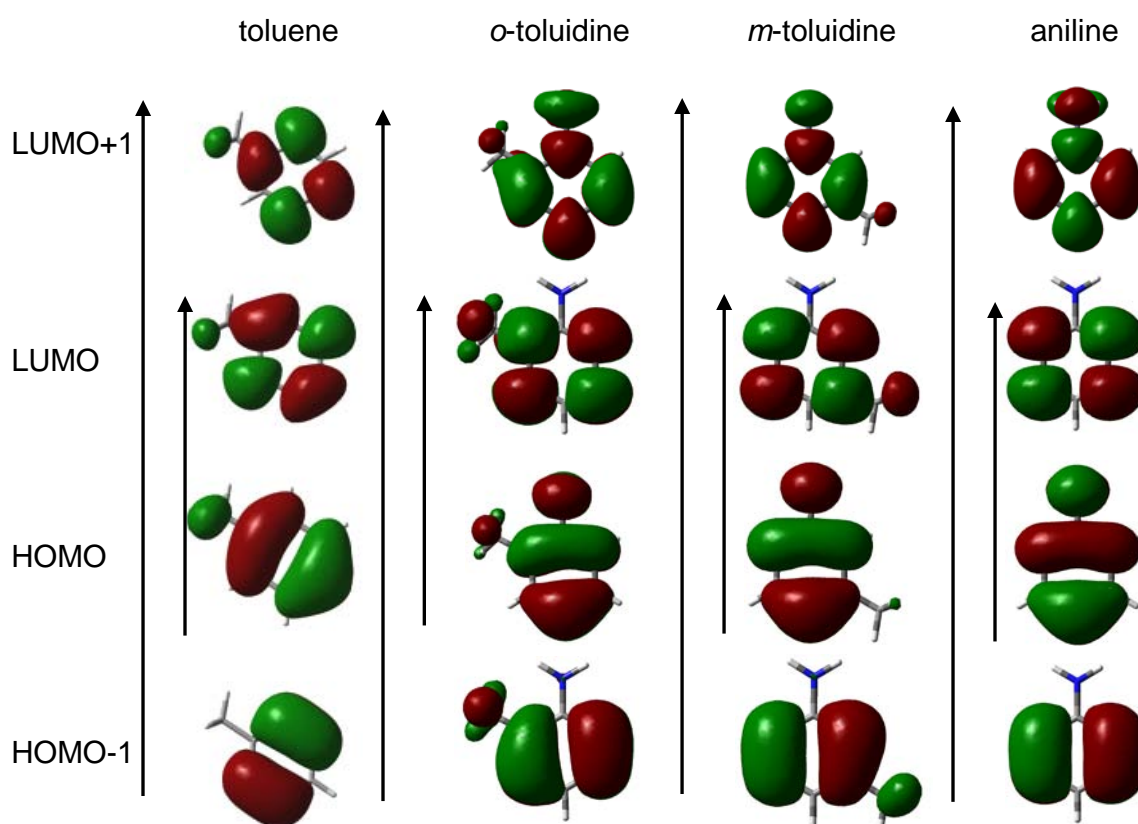


Figure 4.7. Frontier molecular orbitals calculated at the CIS/6-31G(d,p) level of toluene, *o*-toluidine, *m*-toluidine, and aniline. All transitions are primarily HOMO \rightarrow LUMO.

Experimental confirmation of this conclusion can be done using an analysis first carried out by Plusquellic and Pratt.¹⁸ If we take the inertial axes frames to be those shown in Figure 4.6, we know that the torsion-rotation parameters D_a and D_b , and ρ_a and ρ_b must have the same signs in this configuration (*cf.* Table 4.3). Therefore, either $\rho_a > 0$ and $\rho_b > 0$, or $\rho_a < 0$ and $\rho_b < 0$, depending on the sense of rotation of the methyl rotor relative to its own C_3 axis. It has been found in the previous study that the line positions in the computed $E \rightarrow E$ torsional bands are insensitive to the choice of signs, but that the calculated line intensities are sensitive to choice of signs. Therefore, the correct relative intensities of the a - and b -type lines would be given by either $\rho_a > 0$ and $\rho_b > 0$ or $\rho_a < 0$ and $\rho_b < 0$ if $\theta_{TM} > 0$, and $\rho_a < 0$ and $\rho_b > 0$ or $\rho_a > 0$ and $\rho_b < 0$ if $\theta_{TM} < 0$. Since we know that ρ_a and ρ_b must have the same signs, we can deduce that the θ_{TM} must be positive, which is also the sign choice that gives the correct relative intensities. Theory agrees with these determinations (Tables 4.1 and 4.2).

Upon excitation, both molecules exhibit a large decrease in the A rotational constant and much smaller decreases in B (and C) $\Delta A \sim -100$ and $\Delta B \sim -10$ MHz in *o*-toluidine and $\Delta A \sim -150$ and $\Delta B \sim -10$ MHz in *m*-toluidine. Aniline, by contrast, has $\Delta A \sim -300$ and $\Delta B \sim +40$ MHz.¹⁹ The changes in aniline have their origin in a quinoidal distortion of the S_1 state; the “perpendicular” C-C ring bonds are longer than the “parallel” ones. The smaller (in-magnitude) values ΔA and ΔB in the toluidines, in which similar distortions are occurring, may be attributed to the tilts of their inertial axes with respect to those of aniline. Curiously, the values of ΔA and ΔB are significantly different in the $0a_1$ and $1e$ torsional levels of the S_1 state of *o*-toluidine.

4.5.2 Methyl Torsional Barriers

The torsional parameters $D_g (= FW_E^{(1)} \rho_g, g = a, b, c)$ obtained from the fits of the 1e bands of *o*- and *m*-toluidine are listed in Table 4.3. Using Herschbach's tables, both the reduced barrier heights (s) and the corresponding three-fold barriers $V_3 (= \frac{9}{4} F \cdot s)$ could be calculated. Due to the very large barrier in the ground electronic state, values of the torsion-rotation terms for *o*-toluidine in the S_0 state were not experimentally measured. Instead, they were calculated from the barrier height of $V_3'' = 703 \text{ cm}^{-1}$ obtained by Okuyama *et al.*² Barrier heights much larger than 500 cm^{-1} do not produce measurable perturbations at our experimental resolution. A reduced barrier height of 59.202 was calculated and the first-order perturbation coefficient ($W_E^{(1)} = 7.64 \times 10^{-5}$) was obtained through interpolation, yielding torsion-rotation terms of $D_a'' = 0.23$ and $D_b'' = 0.069$ MHz. In the S_1 state, the torsion-rotation terms were found to be much larger and could be determined by experiment ($D_a' = 2628.4$ and $D_b' = 1004.7$ MHz). The reduced barrier height was obtained through interpolation of the first-order perturbation coefficient ($W_E^{(1)} = 0.873$) and a value of 3.702 ($V_3' = 44.89 \text{ cm}^{-1}$) was calculated.

Table 4.3. First-order torsion-rotation perturbation coefficients in the Hamiltonian and deduced barrier heights for *e*-symmetry torsional bands in *o*- and *m*-toluidine.^a

Parameter	<i>o</i> -Toluidine 1e band	<i>m</i> -Toluidine 1e band
D _a ^{''} (MHz)	0.23 ^b	6406.1 (1)
D _b ^{''} (MHz)	0.069 ^b	1719.7 (1)
W ^{(1)''}	7.64 × 10 ⁻⁵	1.911
s ^{''}	59.202	0.769
V ₃ ^{''} (cm ⁻¹)	703 ^b	9.45
D _a ['] (MHz)	2628.4 (1)	21.5 (1)
D _b ['] (MHz)	1004.7 (1)	26.4 (30)
W ^{(1)'}	0.873	0.006
s [']	3.702	27.269
V ₃ ['] (cm ⁻¹)	44.9	322

^aNumbers in parentheses are the standard deviations of the last significant figure.

^bTorsion-rotation terms derived from an assumed barrier height of 703 cm⁻¹ (Ref. 2).

Interestingly, the opposite behavior was observed in *m*-toluidine, where the torsion-rotation terms in the S₀ state are quite large ($D_a'' = 6406.1$ and $D_b'' = 1719.7$ MHz) but much smaller in the S₁ state ($D_a' = 21.5$ and $D_b' = 26.4$ MHz). This resulted in calculated reduced barrier heights of 0.769 ($V_3'' = 9.45$ cm⁻¹) in the ground state and 27.269 ($V_3' = 322.23$ cm⁻¹) in the excited state. These results are consistent with the finding that the 1e band is blue-shifted with respect to the 0a₁ origin band in *o*-toluidine and red-shifted in *m*-toluidine. The corresponding potential energy curves for both *o*- and *m*-toluidine are shown in Figure 4.8.

As mentioned earlier, the observed inertial defect values of *o*-toluidine in the excited state (~ -1.2 amu Å²) and *m*-toluidine in the ground state (~ -0.5 amu Å²) are much smaller than the expected value for a methyl group attached to an aromatic plane (-3.3

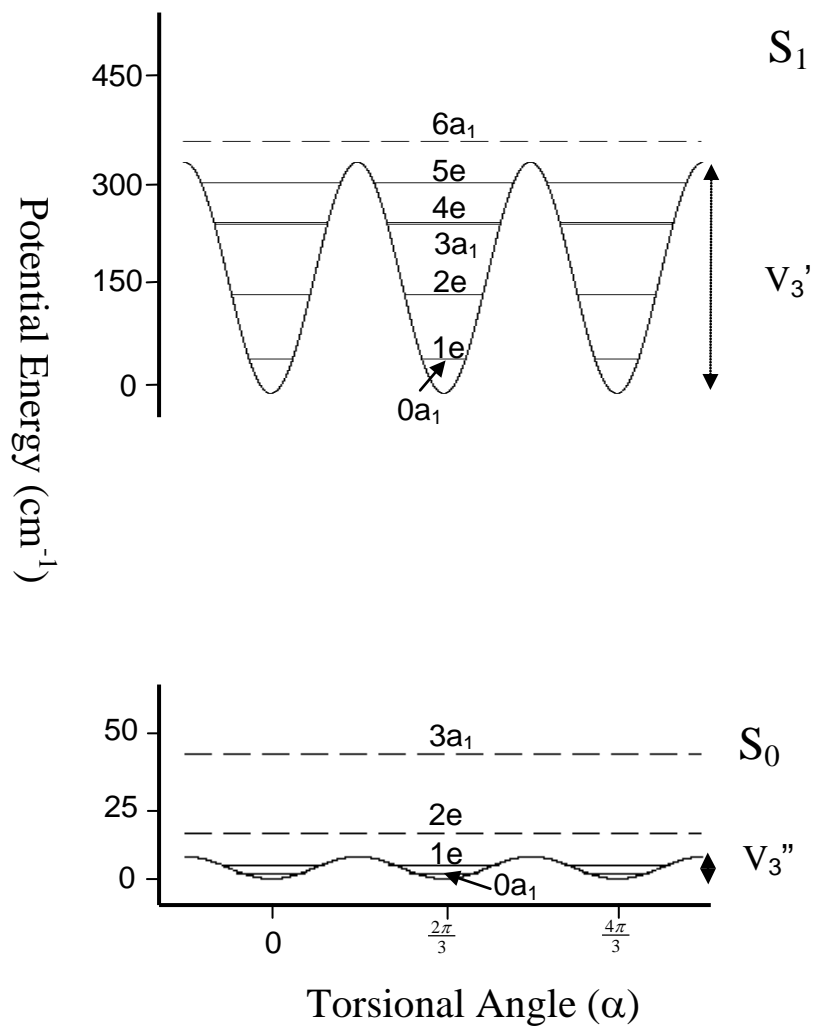
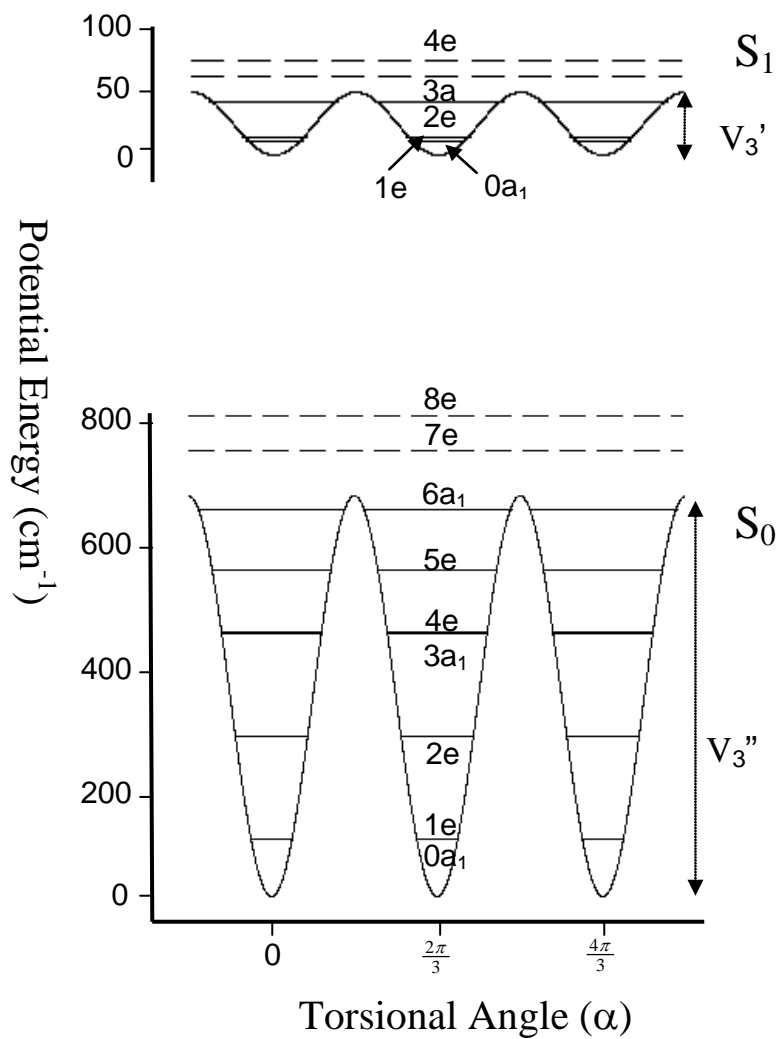


Figure 4.8. Torsional energy curves of *o*-toluidine (left) and *m*-toluidine (right).

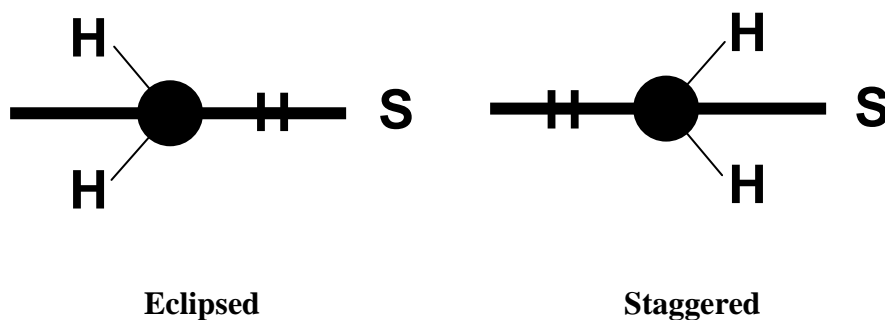
amu \AA^2). It can be seen that the small inertial defect values occur whenever the three-fold potential barrier heights are small, while the expected and larger values occur when the barrier heights are much larger. This general trend has been observed before, most notably in 2- and 3-methylanisole.³ Due to the planarity of the ring to which the methyl group is attached, the inertial defect is zero in the free rotor limit for an internal rotor that is collinear with an inertial axis of the molecule. This also holds to a good approximation for an arbitrary orientation of the symmetry axis of the methyl group in the symmetry plane of the molecule.²⁰ The smaller the barrier height, the more the inertial defect value approaches zero, as observed in both molecules.

The barrier heights obtained for the ground and excited states for both molecules are consistent with those obtained by Okuyama *et al.*²

4.5.3 Origins of the Torsional Barriers

As has been previously shown in the methylpyrimidines² and the methylanisoles,³ the preferred configuration (staggered or eclipsed) and the potential energy curve along the torsional coordinate have their origins in two factors; the position of the methyl group relative to other ring substituents and differences in the π -bond orders of the adjacent C-C bonds. (The staggered and eclipsed configurations are shown below in Scheme I, where S denotes the attached substituent in the plane of the benzene ring.) According to theory, the methyl group in *o*-toluidine is staggered, whereas the methyl group in *m*-toluidine is eclipsed, in the electronic ground states of the two molecules. The staggered configuration of the methyl group in *o*-toluidine can be attributed to both factors. There is

a repulsive steric interaction of the in-plane hydrogen atom with the amino group, and the C₂-C₃ bond has a higher π -bond order than the C₁-C₂ bond. (The C₁-C₂ bond is 1.18 pm longer than the C₂-C₃ bond.) The repulsive steric interaction is absent in *m*-toluidine, so the small preference for the eclipsed conformation of the methyl group in this molecule can be traced to the slightly higher π -bond order of the C₂-C₃ bond. (The C₃-C₄ bond is 0.02 pm longer than the C₂-C₃ bond.)



Scheme 4.1.

Excitation of the two molecules to their S₁ states has a significant impact on the methyl rotor potentials, owing to the quinoidal distortion of the aromatic ring. Thus, in *m*-toluidine, this results in a larger difference of the S₁ π -bond orders of the adjacent C-C bonds. The difference between the C₂-C₃ and C₃-C₄ bond lengths is now about 0.14 pm, an increase of 0.12 pm. This further stabilizes the eclipsed form and produces a significant increase in the magnitude of the barrier height, $V_3(S_0) = 9.45 \rightarrow V_3(S_1) = 322 \text{ cm}^{-1}$. In *o*-toluidine, the difference between the C₁-C₂ and C₂-C₃ bond lengths is now 0.86 pm on excitation of the S₁ state, a decrease of about 0.3 pm. Therefore, the staggered form is still favored in the S₁ state but there is a significant decrease in the magnitude of the barrier height, $V_3(S_0) = 703 \rightarrow V_3(S_1) = 44.9 \text{ cm}^{-1}$. Some reduction in the magnitude of the repulsive term also would be expected, since all C-C bonds in the S₁ state are

longer than in the S_0 state. Thus, light-induced changes in the π -electron distributions of the aromatic rings have a major impact on the preferred geometries and dynamic behaviors of the attached methyl groups.

4.6 CONCLUSIONS

Rotationally resolved $S_1 \leftarrow S_0$ fluorescence excitation studies of *o*- and *m*-toluidine have been performed. Analysis of the results reveals that the amino group is the dominant substituent in the electronic transition; the S_1 - S_0 transition moment is essentially perpendicular to the position of attachment of this group in both molecules. The resulting S_1 states have significantly different π -electron distributions in the aromatic ring, compared to the ground states. As a consequence, the preferred configurations and potential barriers that govern the motion of the attached methyl groups in the two molecules are quite different.

4.7 ACKNOWLEDGMENTS

We thank David F. Plusquellic (NIST) for the JB95 fitting program used for the data analysis and Jens-Uwe Grabow (U. Hannover) for helpful discussions. This work has been supported by NSF (CHE-0615755).

4.8 REFERENCES

1. Review: Spangler, L. H.; Pratt, D. W., In *Jet Spectroscopy and Molecular Dynamics* (ed. by Hollas, J. M., Phillips, D.) Chapman & Hall, London, **1995**; p 366-398 and references therein.
2. Okuyama, K.; Yoshihara, K.; Ito, M. *Laser Chem.* **1987**, *7*, 197-212.
3. Tan, X. Q.; Majewski, W. A.; Plusquellic, D. F.; Pratt, D. W. *J. Chem. Phys.* **1991**, *94*, 7721-33.
4. Tan, X. Q.; Clouthier, D. J.; Judge, R. H.; Plusquellic, D. F.; Tomer, J. L.; Pratt, D. W. *J. Chem. Phys.* **1991**, *95*, 7862-71.
5. Tan, X. Q.; Pratt, D. W. *J. Chem. Phys.* **1994**, *100*, 7061-7.
6. Borst, D. R.; Pratt, D. W. *J. Chem. Phys.* **2000**, *113*, 3658-3669.
7. Alvarez-Valtierra, L.; Yi, J. T.; Pratt, D. W. *J. Phys. Chem.* **2006**, *110B*, 19914-19922.
8. Alvarez-Valtierra, L.; Tan, X.-Q.; Pratt, D. W. *J. Phys. Chem.* **2007**, *111A*, 12802-12809.
9. Majewski, W. A.; Pfanstiel, J. F.; Plusquellic, D. F.; Pratt, D. W. In *Techniques of Chemistry*. (ed. by Rizzo, T. R., Myers, A. B.) Wiley & Sons, New York, **1995**, *23*, 101-48.
10. Plusquellic, D. F., Ph.D. Thesis, University of Pittsburgh, 1992.
11. Plusquellic, D. F.; Suenram, R. D.; Mate, B.; Jensen, J. O.; Samuels, A. C. *J. Chem. Phys.* **2001**, *115*, 3057-3067.
12. Frisch, M. J.; Trucks, G. W.; Schlegel, H. B.; Scuseria, G. E.; Robb, M. A.; Cheeseman, J. R.; Montgomery, J. A. J.; Vreven, T.; Kudin, K. N.; Burant, J. C.; Millam, J. M.; Iyengar, S. S.; Tomasi, J.; Barone, V.; Mennucci, B.; Cossi, M.; Scalmani, G.; Rega, N.; Petersson, G. A.; Nakatsuji, H.; Hada, M.; Ehara, M.; Toyota, K.; Fukuda, R.; Hasegawa, J.; Ishida, M.; Nakajima, T.; Honda, Y.; Kitao, O.; Nakai, H.; Klene, M.; Li, X.; Knox, J. E.; Hratchian, H. P.; Cross, J. B.; Bakken, V.; Adamo, C.; Jaramillo, J.; Gomperts, R.; Stratmann, R. E.; Yazyev, O.; Austin, A. J.; Cammi, R.; Pomelli, C.; Ochterski, J. W.; Ayala, P. Y.; Morokuma, K.; Voth, G. A.; Salvador, P.; Dannenberg, J. J.; Zakrzewski, V. G.; Dapprich, S.; Daniels, A. D.; Strain, M. C.; Farkas, O.; Malick, D. K.; Rabuck, A. D.; Raghavachari, K.; Foresman, J. B.; Ortiz, J. V.; Cui, Q.; Baboul, A. G.; Clifford, S.; Cioslowski, J.; Stefanov, B. B.; Liu, G.; Liashenko, A.; Piskorz, P.; Komaromi, I.; Martin, R. L.; Fox, D. J.; Keith, T.; Al-Laham, M. A.; Peng, C. Y.;

Nanayakkara, A.; Challacombe, M.; Gill, P. M. W.; Johnson, B.; Chen, W.; Wong, M. W.; Gonzalez, C.; Pople, J. A. *Gaussian 03, Revision 6.0*, Gaussian, Inc., Wallingford CT: 2004.

13. Gordy, W.; Cook, R. L., *Microwave Molecular Spectra*. 3rd ed.; John Wiley & Sons: New York, 1984.

14. Tan, X. Q.; Majewski, W. A.; Plusquellic, D. F.; Pratt, D. W.; Meerts, W. L. *J. Chem. Phys.* **1989**, *90*, 2521-2.

15. Herschbach, D. R. *J. Chem. Phys.* **1959**, *31*, 91-108.

16. Kalkman, I. V., Ph.D. Thesis, Radboud University Nijmegen, 2008.

17. Watson, J. K. G. In *Vibrational Spectra and Structure*; Durig, J. R., Ed.; Elsevier: Amsterdam, The Netherlands, 1977, Vol. 6, 1-89.

18. Plusquellic, D. F.; Pratt, D. W. *J. Chem. Phys.* **1992**, *97*, 8970-8976.

19. Sinclair, W. E.; Pratt, D. W. *J. Chem. Phys.* **1996**, *105*, 7942-7956.

20. Trinkaus, A. Diplom Thesis, University of Freiburg, 1967.

5.0 High Resolution Electronic Spectroscopy of 4-Methylanisole in the Gas Phase. Barrier Height Determinations for the Methyl Group Torsional Motion.

Philip J. Morgan, Leonardo Alvarez-Valtierra^a, and David W. Pratt^b

^aPresent address: División de Ciencias e Ingenierías, Universidad de Guanajuato, Campus León. León, Gto. 37150, México.

^bDepartment of Chemistry, University of Pittsburgh
Pittsburgh, PA 15260 USA

This work is published in *Phys. Chem. Chem. Phys.*, **2010**, 10.1039/c000757a

P. J. Morgan and L. Alvarez-Valtierra performed the experimental measurements; P. J. Morgan analyzed the spectra and wrote the paper.

5.1 ABSTRACT

Rotationally resolved fluorescence excitation spectra of the $S_1 \leftarrow S_0$ origin band transition of 4-methylanisole (4MA) have been recorded in the gas phase. The origin band spectrum is split into two subbands owing to tunneling motions along the methyl group torsional coordinate. An analysis of this data provides information about the preferred configuration of the methyl group and the barrier opposing its motion in both the ground and excited electronic states. The results show that electronic excitation has a significant impact on the torsional dynamics of the isolated molecule.

5.2 INTRODUCTION

Rotationally resolved electronic spectroscopy is an extremely sensitive probe of the motions of atoms (or small groups of atoms) in large molecules. In past reports, we have described applications of this technique to proton transfer dynamics in base-pair dimers linked by hydrogen bonds,¹ to the internal rotation dynamics of water molecules in weakly bound complexes of aromatic molecules,² and to large amplitude vibrations in “floppy” molecules,³ in both their ground and excited electronic states. It has even proved possible to identify using high resolution methods the specific vibrational pathways that lead to conical intersections involving two electronically excited states in a relatively rigid molecule.⁴

In this report, we focus on the hindered internal rotation of a methyl group attached to an aromatic frame. Previous investigations of the molecules 2-methylanisole

(2MA) and 3-methylanisole (3MA) revealed that the barriers opposing the methyl group torsional motion depend on the relative positions of the substituent groups, in both electronic states.^{5,6} These studies have shown that 2-methylanisole (2MA) possesses a relatively large ground state barrier and a significantly reduced excited barrier, while 3-methylanisole (3MA) possesses a small ground state barrier and a much larger excited state barrier. A recent study of the methylanilines *o*- and *m*-toluidine has also been performed to further investigate this phenomenon.⁷

On the other hand, if the two substituent groups are in the *para* position with respect to each other, it also has been shown that the methyl group torsional motion is relatively free in both the ground and excited states, as in the case of *p*-toluidine.⁸ The present study focuses on another molecule of this type, 4-methylanisole (4MA). Our objective is to determine the methyl group torsional barriers in 4MA and compare them to those for 2MA and 3MA.

5.3 EXPERIMENTAL

4MA was purchased from Sigma Aldrich and used as received. Vibrationally resolved $S_1 \leftarrow S_0$ excitation spectra were recorded in the following manner. The second harmonic of a Quanta Ray Nd³⁺:YAG (Model DCR-1A) laser was used to pump a dye laser (Model PDL-1) containing Rhodamine 575 dye in order to achieve the desired frequency. The visible light output was externally frequency doubled using a potassium dihydrogen phosphate (KDP) crystal. The visible light was then filtered out and the ultraviolet (UV)

light with a spectral resolution of $\sim 1 \text{ cm}^{-1}$ was then passed into the vacuum chamber containing the sample source. 4MA was heated to $\sim 45^\circ \text{ C}$ and seeded into $\sim 780 \text{ Torr}$ of dry argon gas ($>90\%$ purity). The sample mixture was then expanded through a 1 mm diameter orifice pulsed valve, a General Valve Series 9 operating at 10 Hz, into the vacuum chamber (10^{-5} Torr). The sample was crossed 2 cm downstream with the UV light. The fluorescence was collected using a photomultiplier tube (PMT) which is positioned at right angles to both the molecular and laser beams. The data were processed using a boxcar integrator (Stanford Research Systems), interfaced with Quick Data Acquisition software (Version 1.0.5) to record the data.

Rotationally resolved $S_1 \leftarrow S_0$ excitation spectra were recorded using a molecular beam laser spectrometer, described elsewhere.⁹ Briefly, samples were heated to $\sim 45^\circ \text{ C}$ in a quartz source, seeded in dry argon gas ($> 90\%$ purity), and expanded through a 240 μm tip nozzle. The expansion was skimmed $\sim 2 \text{ cm}$ downstream with a 1 mm diameter skimmer to form a molecular beam and then crossed 15 cm downstream of the nozzle with a laser beam operating in the UV. The laser radiation was generated by a modified continuous ring dye laser operating in the visible (Rhodamine 590 dye) along with a 560 nm BBO crystal for intracavity frequency doubling, producing $\sim 100 \mu\text{W}$ of UV radiation with a linewidth of $\sim 1 \text{ MHz}$. Fluorescence was collected with spatially selective optics and detected by a photon counting system and a PMT. All spectra were recorded using the jba95 data acquisition software.¹⁰ Typical scan lengths were 5 cm^{-1} over 1000 sec. The I_2 absorption spectrum was used to determine the absolute transition frequencies of the excitation spectrum to an accuracy of $\pm 30 \text{ MHz}$. A stabilized etalon was used to produce relative frequency markers having a mode-matched free spectral range of

599.5040 \pm 0.0005 MHz in the UV, corresponding to a free spectral range of 299.7520 \pm 0.0005 MHz in the visible. The resulting spectra were fit using the jb95 least squares fitting program.¹¹

Theoretical calculations were performed using the Gaussian 03 suite of programs¹² to supplement the experiments. Geometry optimization of 4MA in the ground state was performed at the MP2 level of theory with a 6-31G** basis set. Configuration interaction singles (CIS) calculations with a 6-31G** basis set were performed on the excited state.

5.4 RESULTS

Figure 5.1 shows the vibrationally resolved fluorescence excitation spectrum of 4MA. The labeling scheme of the vibrational bands 0a₁, 1e, 2e, *etc.* is used, where a number indexes the upper state torsional levels and a letter designates their symmetries. In the infinite barrier limit, the levels 0a₁ and 1e, 2e and 3a₁, *etc.* are degenerate. Reduction of this barrier leads to a methyl group tunneling motion that lifts the degeneracy of the 0a₁, 1e; 2e, 3a₁; *etc.* levels, in both electronic states. The origin band of 4MA is located at 35400.5 cm⁻¹, red shifted with respect to toluene by more than 2000 cm⁻¹. Ichimura and Suzuki² have suggested that the 1e band is slightly blue shifted with respect to the 0a₁ band.

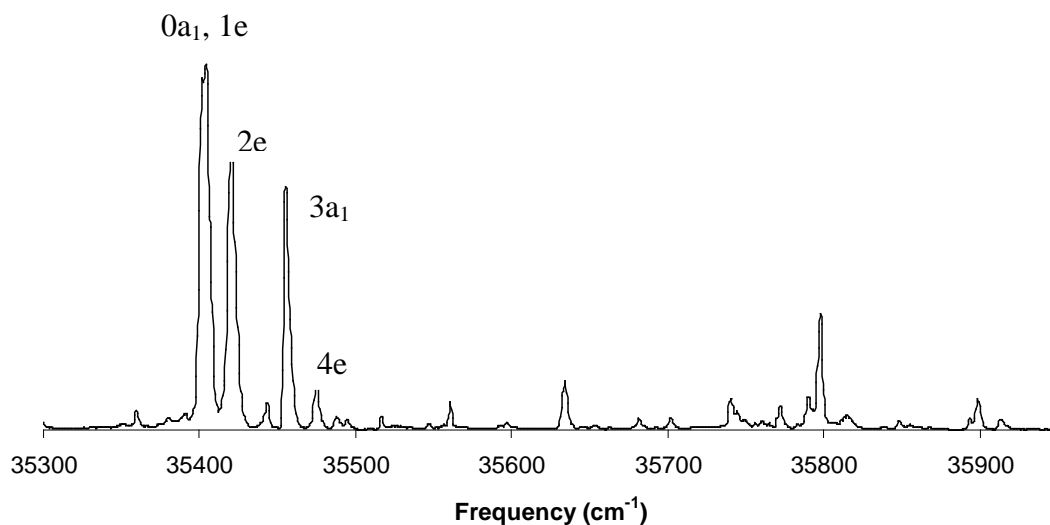


Figure 5.1. Vibrationally resolved fluorescence excitation spectra of 4MA.

High resolution experiments have been performed to validate this conclusion as well as to provide further information about the methyl rotor dynamics. Figures 5.2 and 5.3 show the rotationally resolved $S_1 \leftarrow S_0$ fluorescence excitation spectrum of the $0a_1$ and $1e$ bands of 4MA. The two spectra span approximately 5.5 cm^{-1} and exhibit almost purely b -type transition character; this is consistent with assignment of the S_1 state of anisole as a 1L_b state.¹³ The vibronic band further to the red was fit using rigid-rotor Hamiltonians¹⁴ for both electronic states, confirming its identity as the $0a_1$ torsional band. A simulated spectrum was first generated using estimated rotational constants from the *ab initio* calculations. Single transitions from the simulated spectrum were then assigned to corresponding transitions in the experimental spectrum, using the fitting program *jb95*. A linear least-squares fitting procedure was finally used to optimize the rotational

constants from a comparison of the observed and calculated transitions. Figure 5.2 shows a portion of the fit spectrum of the 0a₁ band, where a standard deviation of 1.28 MHz was obtained by fitting 111 lines with a rotational temperature of 4 K. The spectrum was fit using a Voigt lineshape profile for individual transitions, with Gaussian widths of 18 MHz and Lorentzian widths of 23 MHz, corresponding to a fluorescence lifetime of $\tau = 6.9$ ns. Table 5.1 lists all of the inertial parameters obtained from the fit of the spectrum.

Band 1e of 4MA located at 35402.6 cm⁻¹ is shown in Figure 5.3. Unlike the 0a₁ band in this molecule, the high resolution spectrum of the 1e band in 4MA exhibits further splittings of the individual rovibronic transitions into two components (*i.e.*, the band contains two subbands). This confirms its identity as the 1e band. The normally degenerate rovibronic transitions in this band are coupled by the torsion-rotation interaction, leading to a K-dependent splitting in the high resolution spectrum.¹⁵ These splittings are described by the following “non-rigid” rotor Hamiltonian for both electronic states,^{14, 16}

$$H_{eff}^E = A_E P_a^2 + B_E P_b^2 + C P_c^2 + F W_E^{(1)} (\rho_a P_a + \rho_b P_b). \quad (5.1)$$

Here, A_E and B_E are the effective rotational constants given by

$$A_E = A + F W_E^{(2)} \rho_a^2, \quad B_E = B + F W_E^{(2)} \rho_b^2. \quad (5.2)$$

F is the internal rotor constant given by

$$F = \hbar^2 / 2rI_\alpha. \quad (5.3)$$

$W_E^{(1)}$ and $W_E^{(2)}$ are the first- and second-order perturbation terms, first written down by Herschbach,¹⁷ and ρ_a and ρ_b are weighted direction cosines of the angle between the

axis of internal rotation and the a - and b -inertial axes of the molecule, where $\rho_a = \lambda_a(I_\alpha / I_a)$. I_α is the moment of inertia of the methyl group, and r is a reduction factor

$$r = 1 - \sum (\lambda_g^2 I_\alpha / I_g), \quad g = a, b, c. \quad (5.4)$$

A portion of the fit spectrum of the 1e band is shown in Figure 5.3; a standard deviation of 9.96 MHz was obtained from a fit of 103 lines. The spectrum was also fit using a Voigt lineshape profile for individual transitions, with Gaussian widths of 18 MHz and Lorentzian widths of 23 MHz. The inertial parameters obtained from the fit of the spectrum are also listed in Table 5.1; the torsion-rotation terms used in the fit are listed in Table 5.2.

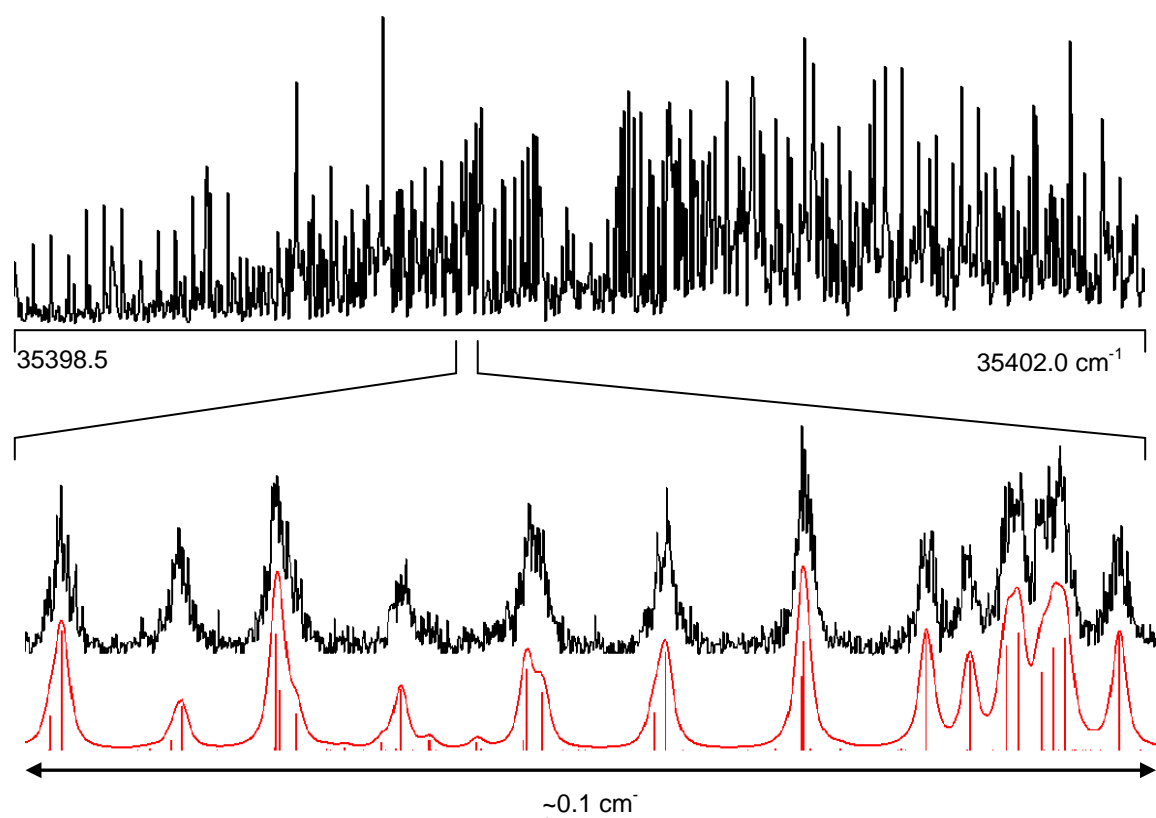


Figure 5.2. Rotationally resolved fluorescence excitation spectrum of the $0a_1$ band of 4MA, with origin at 35400.5 cm^{-1} . The $1e$ band starts to grow in at the end of the R-branch. The lower part of the figure shows an expanded view of the P-branch region. In this view, the upper trace is the experimental spectrum, and the lower trace is the simulated spectrum. Individual lines represent the transitions responsible for the spectrum. The band was fit using a Voigt lineshape profile.

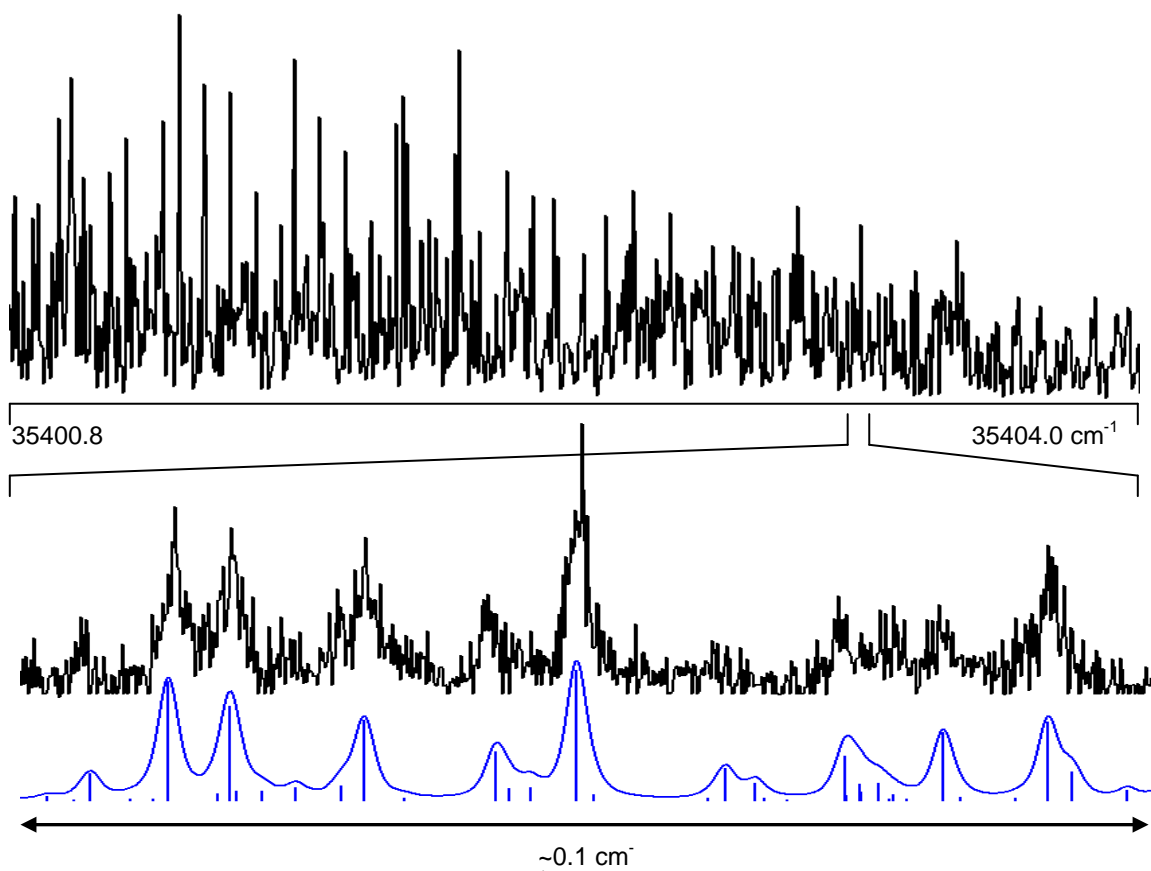


Figure 5.3. Rotationally resolved fluorescence excitation spectrum of the 1e band of 4MA, with origin at 35402.6 cm^{-1} . The end of the $0a_1$ band is present within the P-branch of the 1e band. The lower part of the figure shows an expanded view of the R-branch region. In this view, the upper trace is the experimental spectrum, and the lower trace is the simulated spectrum. Individual lines represent the transitions responsible for the spectrum. The band was fit using a Voigt lineshape profile.

Table 5.1. Rotational constants of 4MA in its ground and excited electronic states.^a

Parameter	4MA 0a ₁	4MA 1e ^{b,c}	Theoretical ^d
A'' (MHz)	4878.5 (1)	4762.8 (1)	4586.8
B'' (MHz)	983.7 (1)	983.2 (1)	982.9
C'' (MHz)	824.8 (1)	824.8 (1)	860.9
ΔA (MHz)	-196.5 (1)	-96.3 (1)	-91.5
ΔB (MHz)	0.8 (1)	-0.1 (1)	21.1
ΔC (MHz)	-6.3 (1)	-5.8 (1)	-9.8
ΔI'' (amu Å ²)	-4.60	-7.43	-3.77
ΔI' (amu Å ²)	-3.82	-5.29	-3.21
a/b/c type	1/99/0	1/99/0	

^aNumbers in parentheses are the standard deviations of the last significant figure.

^bSee Table 2 for additional information about the first-order torsion-rotation perturbation coefficients that were used in the fit of this spectrum.

^cThe following A-reduced Watson centrifugal distortion terms were applied to the S₁ state:

ΔJ'=-0.00299, ΔJK'=0.00930, ΔK'=0.145, δJ'=0.000037, δK'=-0.217 MHz

^dGeometry optimization calculation done at the MP2/6-31G** and CIS/6-31G** levels of theory.

Table 5.2. First-order torsion-rotation perturbation coefficients in the Hamiltonian and deduced barrier heights for e-symmetry torsional band in 4MA.^a

Parameter	4MA 1e band
D _a '' (MHz)	3867.7 (1)
D _b '' (MHz)	98.2 (1)
W ^{(1)''}	0.771
s''	4.096
V ₃ '' (cm ⁻¹)	48.9 (2)
V ₆ '' (cm ⁻¹)	-18 (1)
F'' (cm ⁻¹)	5.44 (4)
D _a ' (MHz)	8384.9 (1)
D _b ' (MHz)	215.5 (1)
W ^{(1)'}	1.671
s'	0.944
V ₃ ' (cm ⁻¹)	-11.3 ^b (2)
V ₆ ' (cm ⁻¹)	-6 (1)
F' (cm ⁻¹)	5.31 (4)

^aNumbers in parentheses are the standard deviations of the last significant figure.

^bNegative value refers to 60° conformational change that occurs upon S₁←S₀ excitation.

5.5 DISCUSSION

5.5.1 Ground and Excited State Conformers

Table 5.1 lists the ground and excited state rotational constants for the measured vibronic bands of 4MA along with the theoretical values. Comparisons between the theoretical and experimental rotational constants confirm that the carrier of the two transitions is 4MA. Table 5.3 lists the inertial parameters for the $0a_1$ band of 4MA along with the *cis*- and *trans*-conformers of 3MA and 2MA.⁶ The differences between the ground and excited state rotational constants can be easily understood from Figure 5.4, which shows the ground state geometry optimized structures of all the conformers in their *ab* inertial planes. As can be seen in Table 5.3, the conformers of 4MA, 3MA and 2MA are listed in order of decreasing A'' rotational constant value. The A'' rotational constant is the largest in 4MA because the methyl and methoxy groups lie essentially along the *a*-inertial axis. In *trans*-2MA, the methyl group is displaced from the *a*-axis by the largest amount, resulting in the smallest A'' rotational constant. *Trans*-3MA and *cis*-3MA lie between these extremes, with *trans*-3MA having the larger of the two A'' rotational constants. Owing to the position of the *a*-inertial axis in each of the conformers, the B'' and C'' rotational constant values follow the reverse trend; 4MA possesses the smallest B'' and C'' values and *trans*-2MA possesses the largest B'' and C'' values.

Table 5.3. Experimental rotational constants of the origin bands ($0a_1 \leftarrow 0a_1$) of 4MA, 3MA, and 2MA in their ground and excited electronic states.

Parameter	4MA	<i>trans</i> -3MA ^a	<i>cis</i> -3MA ^a	<i>trans</i> -2MA ^a
A" (MHz)	4878.5 (1)	3573.1 (1)	2766.7 (1)	2490.0 (1)
B" (MHz)	983.7 (1)	1124.2 (1)	1297.5 (1)	1558.9 (1)
C" (MHz)	824.8 (1)	861.1 (1)	890.7 (1)	970.7 (1)
ΔA (MHz)	-196.5 (1)	-166.6 (1)	-89.3 (1)	-82.1 (1)
ΔB (MHz)	0.8 (1)	-12.9 (1)	-17.9 (1)	-8.9 (1)
ΔC (MHz)	-6.3 (1)	-13.9	-14.9 (1)	-19.5 (1)
$\Delta I''$ (amu \AA^2)	-4.60	-4.06	-4.76	-6.51
$\Delta I'$ (amu \AA^2)	-3.82	-6.62	-6.64	-4.64
TM angle to <i>b</i> -inertial axis	6 (2) ^o	34 (2) ^o	25 (2) ^o	14 (2) ^o

^aValues taken from Ref. 1.

The inertial defect values of each conformer were expected to be approximately $-6.6 \text{ amu } \text{\AA}^2$, the value expected for four out-of-plane hydrogen atoms, two from the methyl group and two from the methoxy group. However, some of the experimental values are different; *trans*-2MA is the only conformer to possess the expected $-6.6 \text{ amu } \text{\AA}^2$ value in the ground state. The other conformers all exhibit ΔI values in the -4 to $-5 \text{ amu } \text{\AA}^2$ range. Upon excitation, the inertial defect values of both *trans*-3MA and *cis*-3MA change to the expected value of approximately $-6.6 \text{ amu } \text{\AA}^2$, whereas the ΔI value of 4MA decreases even further and the ΔI value of *trans*-2MA decreases to about $-4.6 \text{ amu } \text{\AA}^2$. As will be seen, these results are a direct consequence of the barrier heights in the ground and excited states.

Figure 5.4 also displays the experimentally determined $S_1 \leftarrow S_0$ transition moment (TM) orientations in the inertial frames of all the conformers. The TM orientations of all four conformers are approximately perpendicular to the C-O bond of the methoxy group.

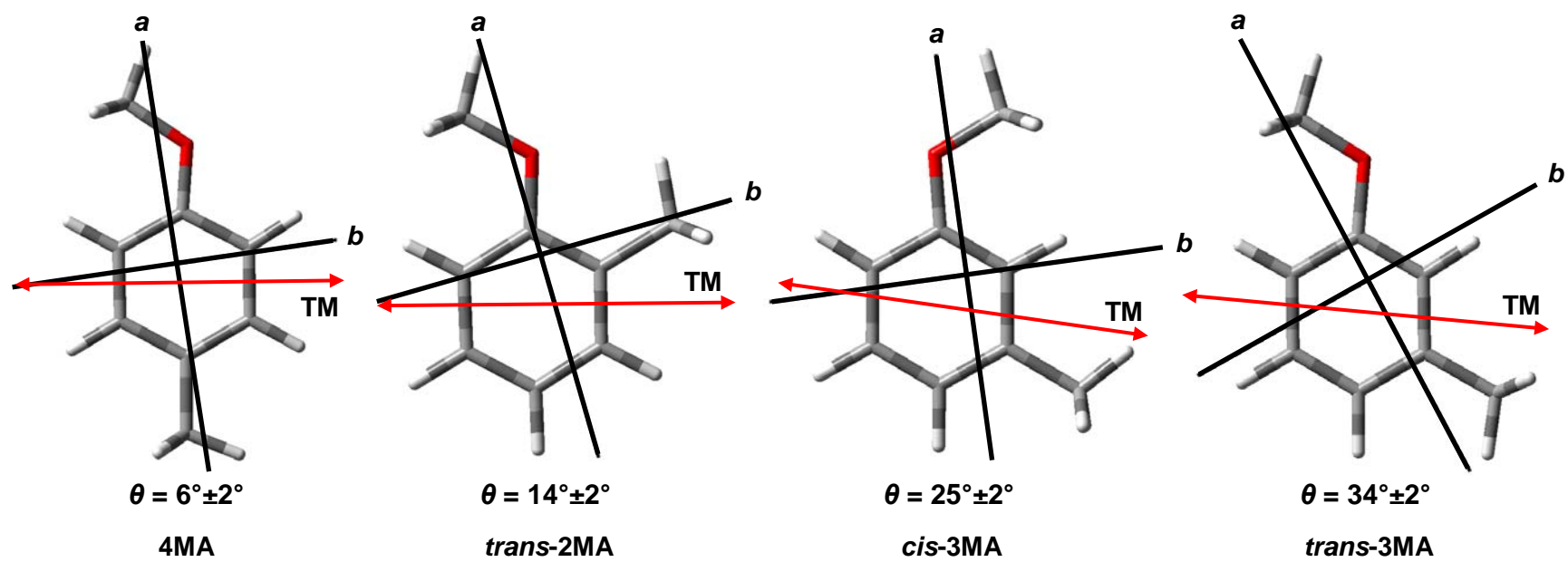


Figure 5.4. Inertial axes and $S_1 \leftarrow S_0$ TM orientation vectors in the experimentally observed conformers of 4MA, 3MA and 2MA.

This is again consistent with the $S_1 \leftarrow S_0$ transitions being “anisole-like” in nature, corresponding to the S_1 state as a 1L_b state.

Upon excitation, 4MA exhibits a large decrease in the A rotational constant, a much smaller decrease in the C rotational constant and a very slight increase in the B rotational constant. This is a consequence of the “quinoidal” nature of the S_1 state, expanded relative to the ground state with shorter “parallel” C-C bonds than perpendicular ones, as was found to be the case in the S_1 state of anisole.^{18,19} This explains the observed decrease of the A rotational constant upon excitation in 4MA, as well as in the 3MA and 2MA conformers. The slight decrease in the C rotational constant is also attributed to the expanded ring in the S_1 state. The slight increase in the B rotational constant, $\Delta B \sim 1$ MHz, can be attributed the shorter “parallel” C-C bonds the molecule possesses in its S_1 state.

5.5.2 Methyl Torsional Barriers

Torsional parameters $D_g (= F W_E^{(1)} \rho_g, g = a, b, c)$ obtained from fits of the 1e band of 4MA are listed in Table 5.2. Using Herschbach’s tables,¹⁷ both the reduced barrier heights (s) and the corresponding three-fold barriers $V_3 (= \frac{9}{4} F \cdot s)$ could be calculated.

In both the S_0 and S_1 states, large torsion-rotation terms for D_a ($D_a'' = 3867.7$ and $D_a' = 8384.9$ MHz) were found, whereas small torsion-rotation term were found for D_b ($D_b'' = 98.2$ and $D_b' = 215.5$ MHz). This is due to the position of the attached

methyl group with respect to the a inertial axis, as well as relatively small barriers in both the ground and excited states. The projection of the internal rotation of the methyl group on the molecular frame is mainly along the a axis, resulting in the larger D_a torsion-rotation terms and smaller D_b torsion-rotation terms. The reduced barrier heights for the S_0 and S_1 states were obtained through interpolation of the first-order perturbation coefficients ($W_E^{(1)''} = 0.771, W_E^{(1)'} = 1.671$) and values of $s'' = 4.096$ and $s' = 0.944$ ($V_3'' = 48.9 \text{ cm}^{-1}, V_3' = 11.3 \text{ cm}^{-1}$) were calculated. These results are consistent with the finding that the $1e$ band is blue-shifted with respect to the $0a_1$ origin band in 4MA. The corresponding potential energy curves for 4MA are shown in Figure 5.5. The results for 4MA are in close agreement with the ones obtained by Ichimura and Suzuki.⁵

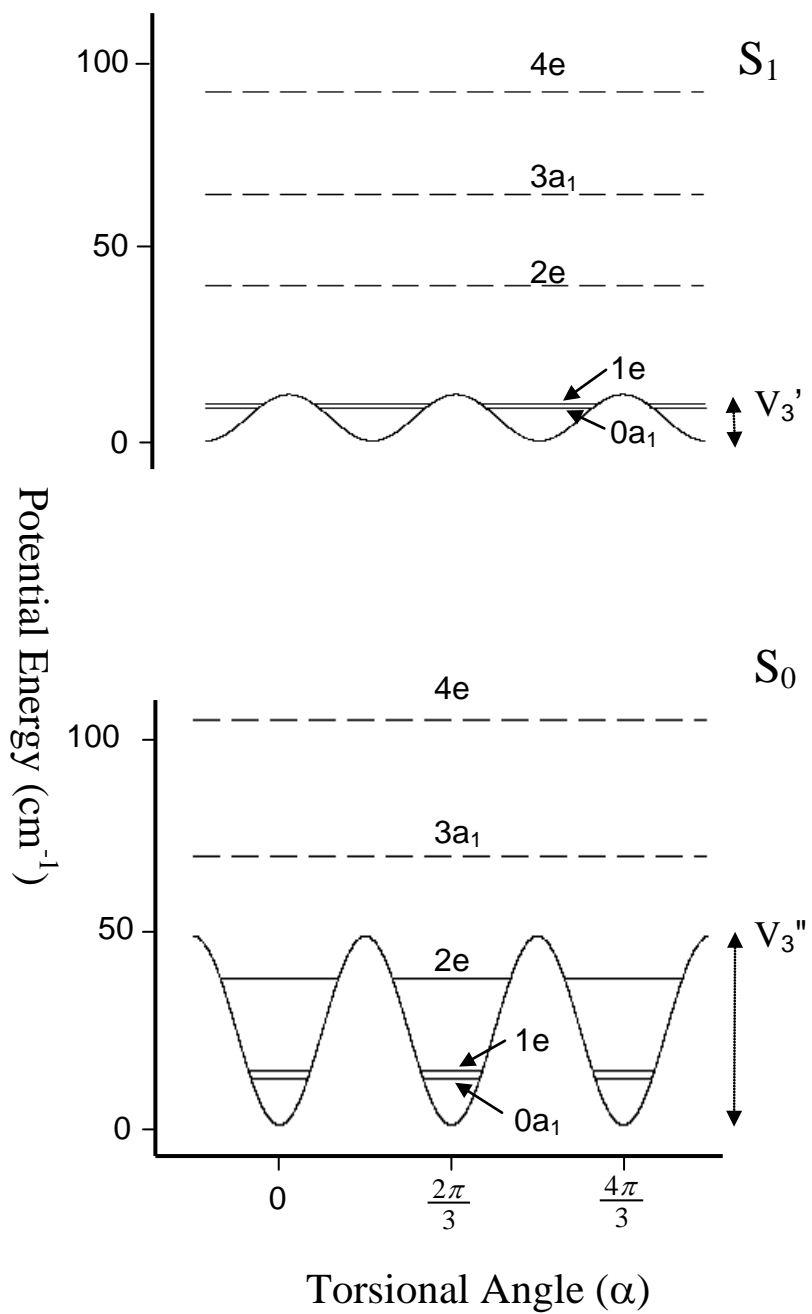


Figure 5.5. Torsional energy curves of 4MA in its ground (S₀) and first excited (S₁) electronic states.

5.5.3 Torsional Dynamics

As mentioned earlier, the expected inertial defect value of $-6.6 \text{ amu } \text{\AA}^2$ was not observed for 4MA in both the ground and excited electronic states. Values of $-4.6 \text{ amu } \text{\AA}^2$ in the S_0 state and $-3.82 \text{ amu } \text{\AA}^2$ in the S_1 state were determined. This effect has been observed before in similar systems.^{6, 7, 8, 20, 21} When comparing inertial defect values with their relative barrier heights in the corresponding electronic state, it can be seen that they decrease in value as the barrier approaches zero. Owing to the planarity of the ring to which the methyl group is attached, the inertial defect is zero in the free rotor limit for an internal rotor that is collinear with an inertial axis of the molecule. This also holds to a good approximation for an arbitrary orientation of the symmetry axis of the methyl group in the symmetry plane of the molecule.²² In this particular case, the methyl group is almost completely collinear with the a inertial axis of the molecule. Therefore, the inertial defect values should approach $-3.3 \text{ amu } \text{\AA}^2$ as the barrier height approaches zero, which is the value for the two out-of-plane hydrogen atoms of the methoxy group.

The S_0 and S_1 barrier heights are both relatively small, as is the case for most *para* substituted molecules.^{8,20} However, instead of possessing a 6-fold barrier in both states, 4MA has a 3-fold potential barrier due to the asymmetry of the attached methoxy group. In the case of *trans*-2MA, *cis*-3MA and *trans*-3MA, it can be seen that one of their barrier heights is large, while the other is relatively small.⁶ This is due to the methyl group's position on the benzene ring relative to the methoxy group as well as the electronic structure of the molecules. Upon excitation, electrons from the oxygen atom are transferred to the ring, resulting in a quinoidal shape. This changes the π -bond order

of the C-C bonds in the ring, thereby changing the barrier height in the excited state. Figure 5.6 depicts the change in electronic structure for 4MA. In the ground state, the adjacent C-C bonds have slightly different π -bond orders resulting in a V_3 barrier height of $\sim 49 \text{ cm}^{-1}$. However, in the excited state, the methyl rotor is able to rotate almost freely, $V_3' = \sim 11 \text{ cm}^{-1}$. This is due to the quinoidal shape of the ring, resulting in the adjacent C-C bonds having almost identical π -bond orders. Thus, the dynamics of methyl group torsional motion is significantly influenced by electronic excitation.

Although the barrier to internal rotation is principally a 3-fold barrier, there also are relatively substantial V_6 terms in both the ground and excited electronic states. These were fit by performing absolute frequency calculations to match the torsional energy level spacings that were observed experimentally by Ichimura and Suzuki.⁵ In this study, the V_3 barrier height values were fixed at the values obtained from the fits of the rotationally resolved spectra, and the F and V_6 terms were varied until the calculated torsional energy level spacings matched the experimental values in both the ground and excited states. These values also are listed in Table 5.2.

As in the case of *trans*-2MA and *trans*-3MA, there is evidence of Franck-Condon activity in the low frequency region of the vibrationally resolved spectrum of 4MA (*cf.* Fig. 5.1). In *trans*-2MA and *trans*-3MA, this is a direct consequence of the preferred orientation of the methyl group changing upon excitation and results in an A/E intensity ratio of about 2. There was no evidence of any Franck-Condon activity in the vibrationally resolved spectrum of *cis*-3MA which possesses an A/E intensity of about 1. 4MA possesses an A/E intensity ratio of about 2. Therefore, due to the presence of

Frank-Condon activity in 4MA and its A/E intensity ratio of 2, it can be concluded that the preferred orientation of the methyl group changes upon electronic excitation. A methyl group hydrogen atom eclipses the C-C bond possessing higher π -bond order in the ground state, and then eclipses the opposite C-C bond upon excitation, as shown in Figure 5.6. This causes a phase shift in the excited state potential energy surface by 60° (*cf.* Fig. 5.5).

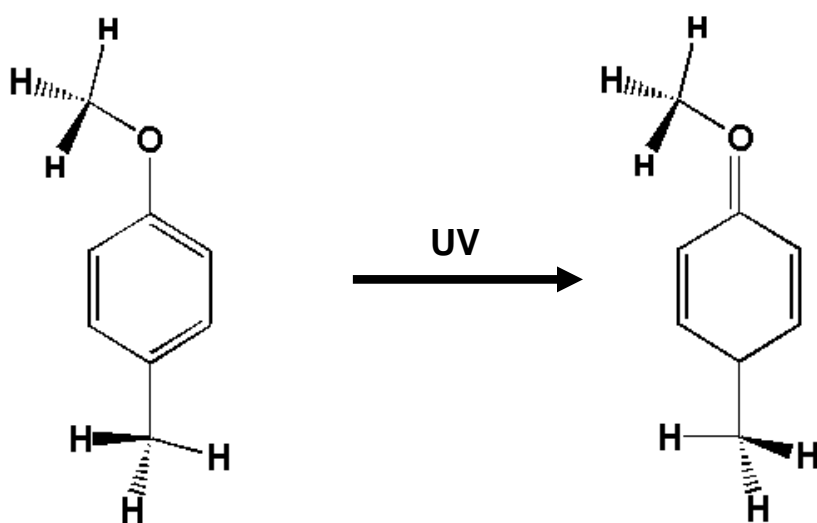


Figure 5.6. Changes in electronic structure and methyl group orientation that occur upon electronic excitation.

5.6 CONCLUSIONS

Rotationally resolved $S_1 \leftarrow S_0$ fluorescence excitation spectra of the $0a_1$ and $1e$ vibronic bands of 4MA provide a detailed view of the torsional potential energy surfaces of the ground and excited states of the isolated molecule. Analysis of the results reveals that the methoxy group is the dominant substituent in the electronic transition; the S_1 - S_0 transition moment is essentially perpendicular to the position of attachment of this group. The resulting S_1 state has significantly different π -electron distributions in the aromatic ring due to the transfer of electrons from the oxygen on the methoxy group to the ring, creating a quinoidal shape upon excitation. As a consequence, the excited state potential barrier decreases in value, causing the methyl group to rotate more freely, and centrifugal distortion terms are necessary to fit the spectra. A change in the preferred orientation of the methyl group also occurs upon excitation of the isolated molecule with UV light.

5.7 ACKNOWLEDGMENTS

We thank David F. Plusquellic (NIST) for the JB95 fitting program used for the data analysis. This work has been supported by NSF (CHE-0615755 and CHE-0911117).

5.8 REFERENCES

1. Roscioli, J. R.; Pratt, D. W.; Smedarchina, Z.; Siebrand, W.; Fernandez-Ramos, A. *J. Chem. Phys.* **2004**, *120*, 11351.
2. Yi, J. T.; Ribblett, J. W.; Pratt, D. W., *J. Phys. Chem. A* **2005**, *109*, 9456.
3. Alvarez-Valtierra, L.; Pratt, D. W.; *J. Chem. Phys.* **2007**, *126*, 224308.
4. Kuepper, J.; Pratt, D. W.; Meerts, W. L.; Brand, Ch.; Tatchen, J.; Schmitt, M. *Phys. Chem. Chem. Phys.*, in press.
5. Ichimura, T.; Suzuki, T. *J. Photochem. Photobiol.* **2000**, *1*, 79.
6. Alvarez-Valtierra, L.; Yi, J. T.; Pratt, D. W. *J. Phys. Chem. B* **2006**, *110*, 19914.
7. Morgan, P. J.; Alvarez-Valtierra, L.; Pratt, D. W. *J. Phys. Chem. A* **2009**, *113*, 13221.
8. Tan, X. Q.; Pratt, D. W. *J. Chem. Phys.* **1994**, *100*, 7061.
9. Majewski, W. A.; Pfanstiel, J. F.; Plusquellic, D. F.; Pratt, D. W. *Laser Techniques in Chemistry*, ed. by A. B. Myers and T. R. Rizzo (Wiley, New York) **1995**, *23*, 101.
10. Plusquellic, D. F. Thesis, University of Pittsburgh, **1992**.
11. Plusquellic, D. F.; Suenram, R. D.; Mate, B.; Jensen, J. O.; Samuels, A. C. *J Chem Phys.* **2001**, *115*, 3057.
12. Frisch, M. J.; Trucks, G. W.; Schlegel, H. B.; Scuseria, G. E.; Robb, M. A.; Cheeseman, J. R.; Montgomery, J. A. J.; Vreven, T.; Kudin, K. N.; Burant, J. C.; Millam, J. M.; Iyengar, S. S.; Tomasi, J.; Barone, V.; Mennucci, B.; Cossi, M.; Scalmani, G.; Rega, N.; Petersson, G. A.; Nakatsuji, H.; Hada, M.; Ehara, M.; Toyota, K.; Fukuda, R.; Hasegawa, J.; Ishida, M.; Nakajima, T.; Honda, Y.; Kitao, O.; Nakai, H.; Klene, M.; Li, X.; Knox, J. E.; Hratchian, H. P.; Cross, J. B.; Bakken, V.; Adamo, C.; Jaramillo, J.; Gomperts, R.; Stratmann, R. E.; Yazyev, O.; Austin, A. J.; Cammi, R.; Pomelli, C.; Ochterski, J. W.; Ayala, P. Y.; Morokuma, K.; Voth, G. A.; Salvador, P.; Dannenberg, J. J.; Zakrzewski, V. G.; Dapprich, S.; Daniels, A. D.; Strain, M. C.; Farkas, O.; Malick, D. K.; Rabuck, A. D.; Raghavachari, K.; Foresman, J. B.; Ortiz, J. V.; Cui, Q.; Baboul, A. G.; Clifford, S.; Cioslowski, J.; Stefanov, B. B.; Liu, G.; Liashenko, A.; Piskorz, P.;

- Komaromi, I.; Martin, R. L.; Fox, D. J.; Keith, T.; Al-Laham, M. A.; Peng, C. Y.; Nanayakkara, A.; Challacombe, M.; Gill, P. M. W.; Johnson, B.; Chen, W.; Wong, M. W.; Gonzalez, C.; Pople, J. A. Gaussian 03, Revision 6.0; Gaussian, Inc., Wallingford CT, **2004**.
13. Ribblett, J. W.; Sinclair, W. E.; Borst, D. R.; Yi, J. T.; Pratt, D. W. *J. Phys. Chem. A* **2006**, *110*, 1478.
 14. Gordy, W.; Cook, R. L. *Microwave Molecular Spectra*, 3rd ed.; (Wiley-Interscience: New York), **1984**.
 15. Tan, X. Q.; Majewski, W. A.; Plusquellic, D. F.; Pratt, D. W.; Meerts, W. L. *J. Chem. Phys.* **1989**, *90*, 2521.
 16. Tan, X. Q.; Majewski, W. A.; Plusquellic, D. F.; Pratt, D. W. *J. Chem. Phys.* **1991**, *94*, 7721.
 17. Herschbach, D. R. *J. Chem. Phys.* **1959**, *31*, 91.
 18. Eisenhardt, C. G.; Pietraperzia, G.; Becucci, M. *Phys. Chem. Chem. Phys.* **2001**, *3*, 1407.
 19. Pasquini, M.; Schiccheri, N.; Becucci, M.; Pietraperzia, G. *J. Mol. Struct.* **2009**, *924-926*, 457.
 20. Borst, D. R.; Pratt, D. W. *J. Chem. Phys.* **2000**, *113*, 3658.
 21. Alvarez-Valtierra, L.; Tan, X.-Q.; Pratt, D. W. *J. Phys. Chem. A* **2007**, *111*, 12802.
 22. Trinkaus, A. Diplom Thesis, University of Freiburg, **1967**.

**6.0 EXCITED STATE INTRAMOLECULAR PROTON TRANSFER IN
2-(2'-PYRIDYL)PYRROLE IN THE GAS PHASE
VIA HIGH RESOLUTION ELECTRONIC SPECTROSCOPY.**

Philip J. Morgan, Adam J. Fleisher and David W. Pratt
Department of Chemistry, University of Pittsburgh
Pittsburgh, PA 15260 USA

Michal Kijak and Jacek Waluk
Institute of Physical Chemistry, Polish Academy of Sciences, Kasprzaka 44/52, 01-224
Warsaw, Poland

P. J. Morgan, A. J. Fleisher, M. Kijak, and J. Waluk performed the experimental measurements; P. J. Morgan analyzed the rotationally resolved spectra and wrote the paper.

6.1 ABSTRACT

Rotationally resolved fluorescence excitation spectra of the $S_1 \leftarrow S_0$ origin band and +144 cm^{-1} vibrational band transitions of 2-(2'-pyridyl)pyrrole (2PP) have been recorded in the collision free environment of a molecular beam. Analyses of these data provide new information about the changes in geometry that occur when 2PP absorbs light. Additionally, significant line broadening is observed in both spectra, which we attribute to an excited state intramolecular proton transfer (ESIPT) reaction. The dynamics and vibrational mode dependence of ESIPT in 2PP will be discussed.

6.2 INTRODUCTION

Recently, Waluk *et al.* have studied various systems that possess excited state intramolecular proton transfer (ESIPT).¹⁻⁸ In particular, ESIPT has been observed in a molecular beam for 2-(2'-pyridyl)pyrrole (2PP).⁸ Structurally similar pyridyl pyrazoles also possess ESIPT, as shown by Yu *et al.*⁹ Both of these systems possess fairly weak intramolecular hydrogen bonds, resulting in a larger barrier and relatively smaller proton transfer rates for photoinduced tautomerization. It is therefore surprising to detect ESIPT in both of these systems, due to these weak intramolecular hydrogen bonds. Other systems, such as methyl salicylate¹⁰⁻¹³ and salicylic acid^{14, 15}, possess strong intramolecular hydrogen bonds, resulting in an extremely rapid photoinduced tautomerization.

2-(2'-pyridyl)pyrrole, shown in Figure 6.1, can exist as two possible conformers, *syn* and *anti* forms. The *syn* form is more energetically favorable due to the weak intramolecular hydrogen bond between the H on the pyrrole nitrogen and the pyridine nitrogen atom. Evidence of the tautomeric form was first discovered when the fluorescence spectrum was taken. The appearance of two emission bands was observed, a strong band in the UV and the weaker band in the visible, shown in Figure 6.2.^{7, 8} The strong emission band, F₁, was attributed to the normal fluorescence of the *syn* conformer and the weaker band, F₂, to the tautomeric form. The phenomenon of dual fluorescence was first witnessed when the fluorescence spectrum of methyl salicylate was observed in 1924¹⁶ and was not explained until later when Weller *et al.* proposed that the two observed bands were from two different excited state species of one of the methyl salicylate conformers.¹⁷⁻¹⁹

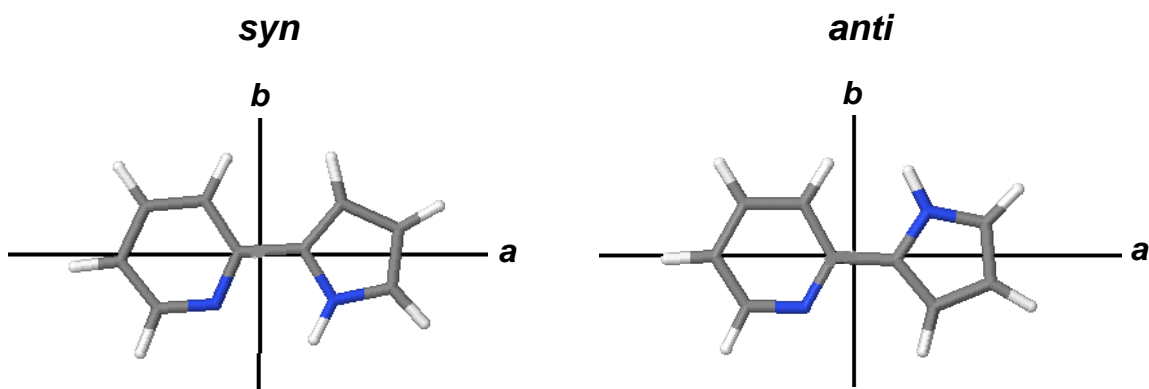


Figure 6.1. Image depicts the *syn* and *anti* conformers of 2PP.

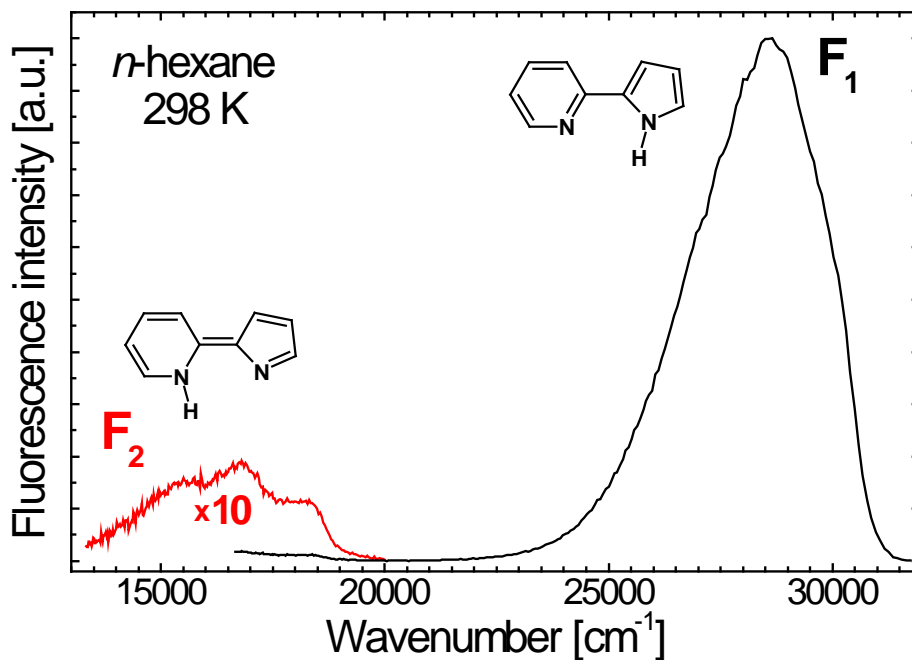


Figure 6.2. Fluorescence spectra of 2PP in *n*-hexane at 298 K depicting the two observed fluorescence bands; F_1 is attributed to the normal fluorescence of *syn* 2PP and F_2 is attributed to the fluorescence of the 2PP tautomer. (Taken from Ref. 8)

Upon further investigation by Kijak *et al.*⁷, it was determined that the ESIPT process was mode-selective. In particular, a prominent low-frequency mode of 144 cm^{-1} was found to enhance the ESIPT rate. However, certain other vibrations did not result in the appearance of the phototautomer at all, and have been assigned to out-of-plane vibrational modes. The vibrational modes that were found to increase the rate of ESIPT were assigned to in-plane vibrations, which actively alters the distance between the pyrrole and pyridine nitrogen atoms, and therefore directly affecting the intramolecular hydrogen bond strength.

In this particular study, rotationally resolved fluorescence excitation spectroscopy was used to probe the origin and $+144\text{ cm}^{-1}$ vibrational band transitions. Analyses of

these data has led to the confirmation of the observed species and its ground and excited state structures. The excited state lifetimes gives insight into the ESIPT rate.

6.3 EXPERIMENTAL

The synthesis and purification of 2PP have been described previously.² Vibrationally resolved laser induced fluorescence excitation experiments were carried out in Warsaw, Poland, using a previously described setup.²⁰ Briefly, the second harmonic of a Nd³⁺:Yag laser was used to pump a home-built narrow-band tunable dye laser containing DCM laser dye in order to achieve the desired frequency. The visible light output was externally frequency doubled using a BBO crystal with a spectral resolution of 0.7 cm⁻¹ and was passed into the vacuum chamber containing the sample source. A 2PP/helium gas mixture at a stagnation pressure of 2600 Torr was expanded through a 0.5 mm orifice of a pulsed valve nozzle heated to about 340 K. The sample was crossed with the UV light at a distance of 4-8 mm from the nozzle and fluorescence was collected using a photomultiplier tube (PMT) positioned at right angles to both the molecular and laser beams. Laser scattering was eliminated by using a 2mm WG360 glass Schott filter. The proton-transferred species' excitation spectrum was taken with a 2mm OG515 glass Schott filter to absorb the normal fluorescence of the non-proton-transferred species. The data were processed by a 300 MHz oscilloscope (LeCroy 9310), interfaced to a personal computer. The LIF excitation spectra were corrected for laser intensity.

Rotationally resolved $S_1 \leftarrow S_0$ excitation experiments were performed in the collision-free environment of a molecular beam, described elsewhere.²¹ Briefly the 2PP sample was heated to ~ 343 K in a quartz source, seeded in dry helium gas ($>90\%$ purity), and expanded through a $240 \mu\text{m}$ nozzle. The expansion was skimmed ~ 2 cm downstream with a 1 mm diameter skimmer to form a molecular beam and then crossed 15 cm downstream of the nozzle with a laser beam operating in the UV. The laser radiation was generated by a modified continuous wave ring dye laser operating in the visible (DCM dye) whose output was externally doubled using a Wavetrain frequency doubler (630 BBO nm crystal) producing $\sim 300 \mu\text{W}$ of UV radiation. Fluorescence was collected with spatially selective optics and detected by a photon counting system and a PMT. All spectra were recorded using the jba95 data acquisition software.²² Typical scan lengths were 4 cm^{-1} over 2000 sec. The I_2 absorption spectrum was used to determine the absolute transition frequencies of the excitation spectrum to an accuracy of ± 30 MHz. A stabilized etalon was used to produce relative frequency markers having a mode-matched free spectral range of 599.5040 ± 0.0005 MHz in the UV, corresponding to a free spectral range of 299.7520 ± 0.0005 MHz in the visible. The resulting spectra were fit using the jb95 least squares fitting program.²³

Supplementing the experimental work, *ab initio* calculations were performed using the Gaussian 03²⁴ suite of electronic structure programs. Ground state geometry optimizations of 2PP were performed at the M052X level of theory with a 6-31+G* basis set. Configuration interaction singles (CIS) calculations with a 6-31+G* basis set were performed on the excited state. Configuration interaction singles (CIS) calculations with a 6-31G** basis set were performed on the excited states of pyridine and pyrrole.

6.4 RESULTS

The vibrationally resolved $S_1 \leftarrow S_0$ excitation spectra of both the F_1 and F_2 fluorescence bands of 2PP are shown in Figure 6.3. Previous studies have already assigned the low-frequency modes with the aid of IR measurements, LIF spectra, dispersed fluorescence spectra (SVLF), UV-UV hole-burning spectrum, and frequency calculations performed in Gaussian03 at several levels of theory and basis sets.⁷ The UV-UV hole-burning spectra confirms that all of the spectral features observed in the LIF spectrum in Figure 3 originate from only one ground state species.

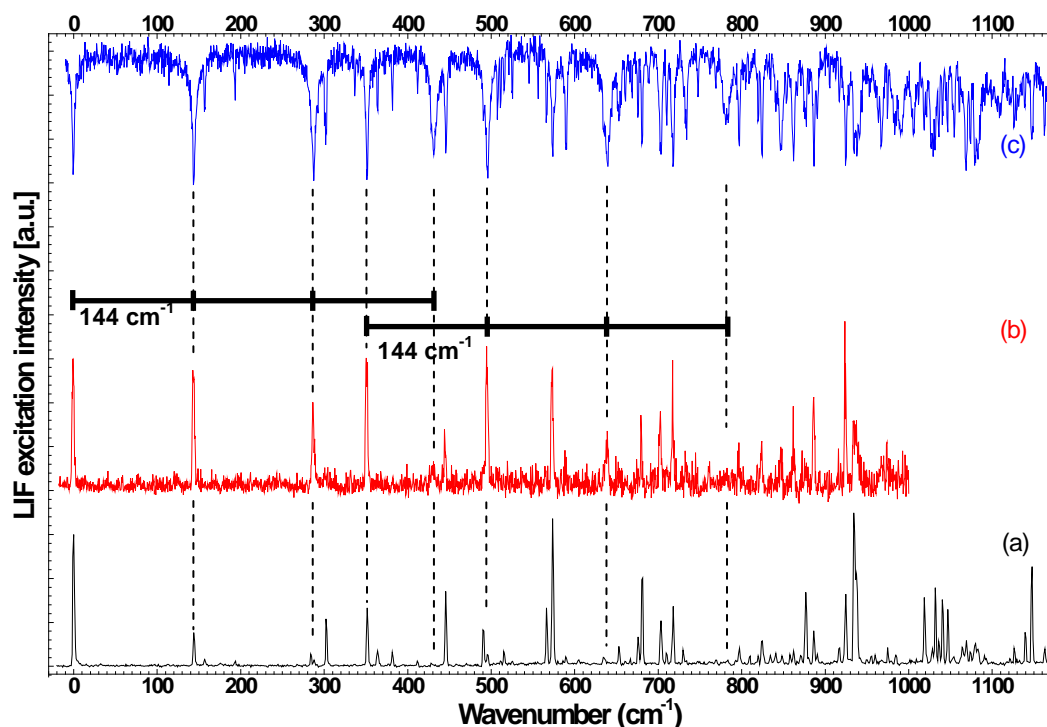


Figure 6.3. LIF spectra obtained while monitoring either the F_1 region (a) or F_2 region (b). The UV/UV fluorescence dip spectrum (c) is obtained by probing at 32377 cm^{-1} . (Taken from Ref. 8)

Rotationally resolved $S_1 \leftarrow S_0$ excitation spectra of the origin and $+144 \text{ cm}^{-1}$ vibrational band transitions are shown in Figure 6.4 and 6.5, respectively. Both spectra span approximately 2 cm^{-1} . Upon viewing the spectra at full experimental resolution, it is immediately apparent that significant line broadening is present in the origin band transition. More intriguing, when viewing the $+144 \text{ cm}^{-1}$ transition at full experimental resolution, it reveals even more extreme line broadening effects associated with this particular vibrational band. The spectrum is essentially completely “washed out”, making its analysis an impossibility.

The origin band was fit using rigid-rotor Hamiltonians for both the ground and excited states.²⁵ A simulated spectrum using estimated rotational constants from the *ab initio* calculations was first generated. Single transitions from the simulated spectrum were then assigned to corresponding transitions in the experimental spectrum, using the fitting program *jb95*.²³ A linear least-squares fitting procedure was finally used to optimize the rotational constants from a comparison of the observed and calculated transitions. An example of the fit is shown in Figures 6.4. A standard deviation (OMC observed minus calculated) of 5.7 MHz was obtained and was fit with a rotational temperature of $\sim 5 \text{ K}$. The spectrum was fit using a Voigt lineshape profile, resulting in a Gaussian width of 20 MHz and a Lorentzian component of 210 MHz. The spectrum was fit with 90% *a*-type and 10% *b*-type transition character. The inertial parameters obtained from the fit of the 2PP origin band are listed in Table 6.1.

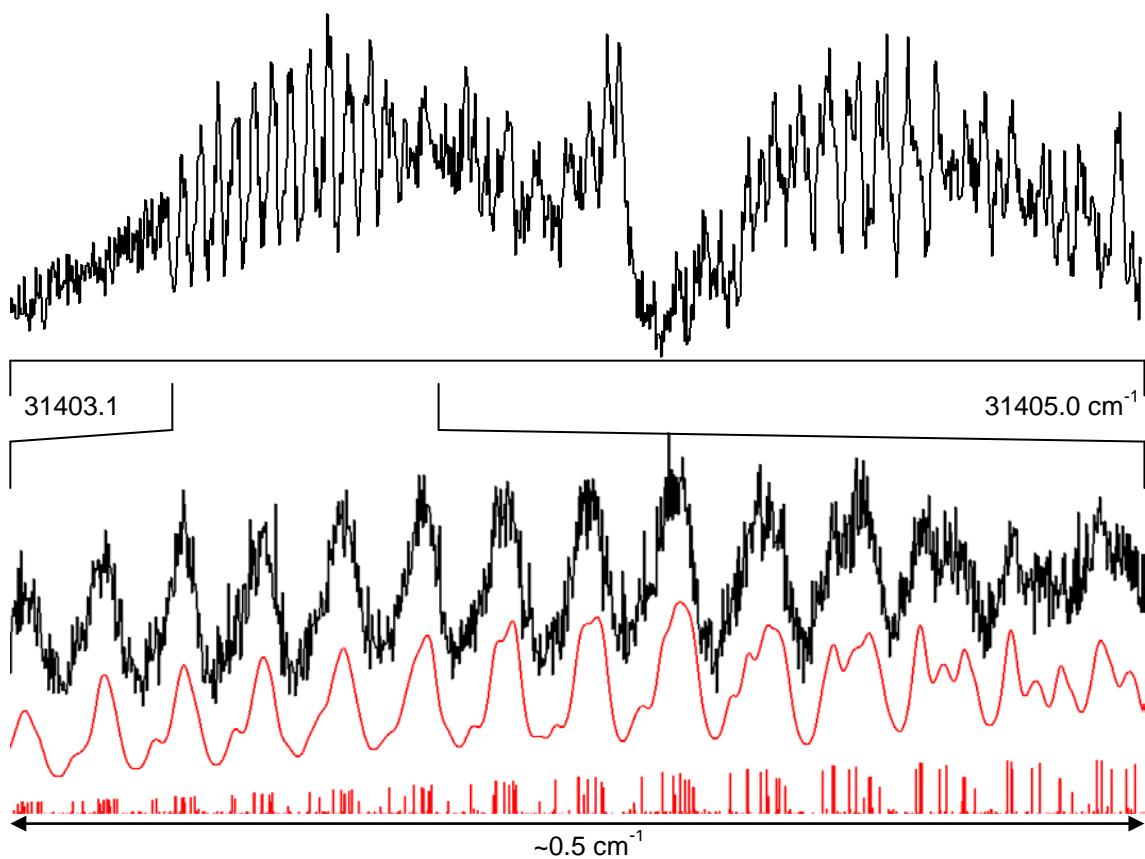


Figure 6.4. Rotatorially resolved electronic excitation spectrum of the origin band transition of 2PP, with origin at 31404.1 cm^{-1} . The lower part of the figure shows a close up of a portion of the P-branch region. The upper trace is the experimental spectrum, and the lower trace is the simulated spectrum; the individual lines represent the transitions responsible for the spectrum.

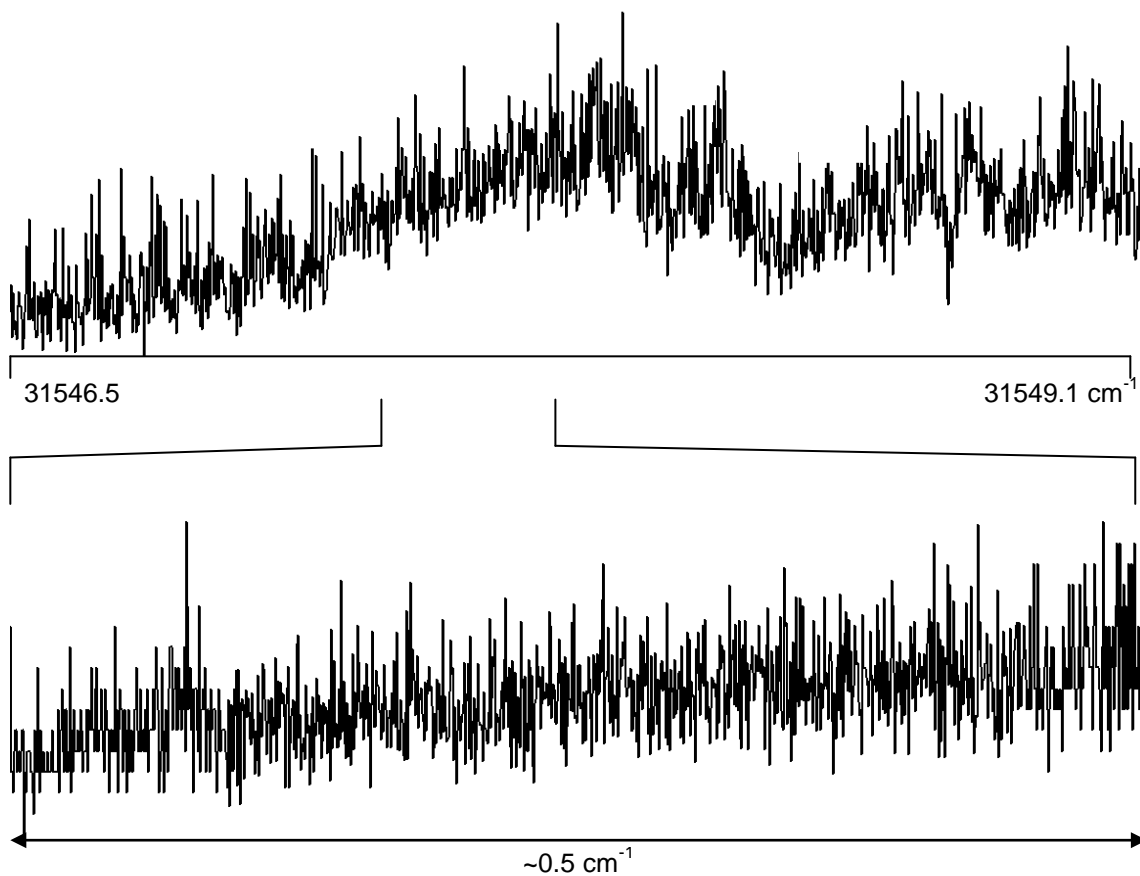


Figure 6.5. Rotationally resolved electronic excitation spectrum of the +144 vibrational band transition of 2PP. The lower part of the figure shows a close up of a portion of the P-branch region, as can be seen, no individual transitions can be detected due to their inherent linewidth from the extremely short excited state fluorescence lifetime.

Table 6.1. Inertial parameters of 2PP in its ground and excited electronic states.^a

Parameter	2PP origin band	Theoretical ^b
A" (MHz)	3755 ± 20	3582.8
B" (MHz)	710.7 ± 1	711.9
C" (MHz)	591.9 ± 1	593.9
ΔA (MHz) ^c	-134 ± 1	-95.6
ΔB (MHz) ^c	15.3 ± 1	13.2
ΔC (MHz) ^c	6.6 ± 1	6.4
ΔI" (amu Å ²)	8.2 ± 1	-0.01
ΔI' (amu Å ²)	8.9 ± 1	-0.02
Origin (cm ⁻¹)	31404.1	
<i>a/b/c</i> type	90/10/0	
OMC (MHz)	5.7	
assigned lines	70	

^aNumbers in parentheses are the standard deviations of the last significant figure.

^bGeometry optimization calculations done at the M05-2X/6-31+G* and CIS/6-31+G* levels of theory.

^cΔA(B,C) = A' - A".

^dΔI = I_c - I_a - I_b.

6.5 DISCUSSION

6.5.1 Ground and Excited State Structures

Table 6.1 lists the ground and excited state rotational constants for the origin band of 2PP, along with the rotational constants obtained from theoretical calculations. A comparison between the theoretical and experimental rotational constants confirms that the identity of the molecule responsible for the obtained spectra is indeed 2PP.

Theoretical calculations have predicted 2PP to be planar in both the ground and excited electronic states, but the experimental inertial defect values possess a fairly large positive value. The experimentally obtained B and C ground state rotational constant values are very similar to those from theory. The difference in the calculated and experimental molecular geometries then lies within the A ground state rotational constant

values. The experimentally obtained A ground state value is almost 200 MHz larger than that from theory, indicating a molecular structure with more mass oriented closer to the *a* inertial axis than predicted by theory.

Upon excitation, 2PP exhibits a large decrease in the A rotational constant and much smaller increases in the B and C; $\Delta A \sim -134$, $\Delta B \sim 15$ and $\Delta C \sim 6$ MHz. The large decrease in A reflects expansion of the pyridine and pyrrole rings upon excitation. The slight increase in the B rotational constant value indicates that the pyridine and pyrrole rings are moving closer together in the excited state, as predicted by theory, with the C-C bond between rings being 146 pm in the S_0 and 139 pm in the S_1 . This displacement is also responsible for the slight increase in C rotational constant value.

The inertial defect values $\Delta(I)$ in both the ground and excited state are quite peculiar. If a molecular is planar, the inertial defect value is usually very close to zero or slightly positive in smaller molecules.²⁶ If a molecule is non-planar, the inertial defect value starts to proceed toward more negative values with increasing non-planarity. 2PP possesses rather large positive inertial defect values. This peculiarity will be discussed later.

Figure 6.6 depicts the two possible $S_1 \leftarrow S_0$ transition moment (TM) orientations in the inertial frame of 2PP. Using the percent *a* and *b* type transition character obtained in the fit of the origin band, the TM was calculated to be at an angle of $\theta = \pm 18 \pm 5^\circ$ with respect to the *a* inertial axis. Figure 6.6 depicts the theoretically obtained TM orientations of pyridine and pyrrole, both are predicted to be pure *a*-type transitions. However, the inertial axes are essentially switched from pyridine to pyrrole, resulting in perpendicularly oriented TMs. The first excited singlet state of pyridine predicts a TM

that is purely *c*-type, corresponding to an $n\pi^*$ transition, but will be disregarded for comparison since there was no appearance of any *c*-type transition character in the 2PP origin band spectrum. The second excited singlet state predicts a transition that is purely *a*-type, corresponding to a $\pi\pi^*$ transition, where the corresponding TM is depicted in Figure 6.6. The first two excited states of pyrrole have previously been calculated as Rydberg states ($\pi\sigma^*$).²⁷ When two methyl groups were attached, the $\pi\pi^*$ becomes bound and was observed in its corresponding (1+1) REMPI spectrum²⁷, the corresponding TM is shown in Figure 6.6. The question then arises, which conjugated ring system is responsible for the excited state transitions observed in the LIF spectrum? Upon comparison of the TMs of all three molecules, it is very difficult to tell whether the TM of pyridine or pyrrole matches the experimentally obtained TM orientation for 2PP.

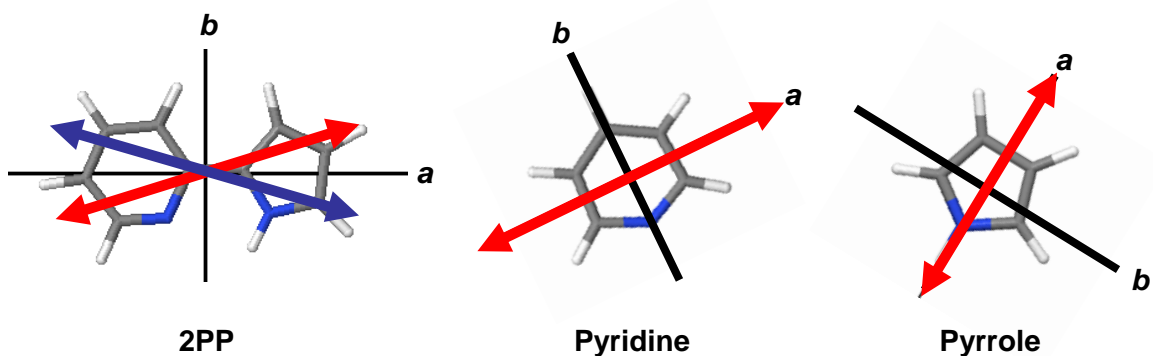


Figure 6.6. Ground state structures and $S_1 \leftarrow S_0$ TM orientation vectors in 2PP, pyridine and pyrrole. Red and blue arrows indicate the two possible orientations of the TM for 2PP. (TMs for pyridine and pyrrole were calculated from theory)

The molecular orbitals (MO's) that participate in the $S_1 \leftarrow S_0$ transition of 2PP are shown in Figure 6.7, along with the corresponding MO's responsible for the TMs depicted in Figure 6.6 of pyridine and pyrrole. The dominant one-electron excitations responsible for the TM of pyridine are calculated to be mostly HOMO \rightarrow LUMO with a considerable amount of HOMO-1 \rightarrow LUMO+1. The nodal patterns of the MO's exhibited by pyridine match very closely to those for pyrrole. The calculated dominant one-electron excitations for pyrrole are different, resulting in a combination of HOMO-1 \rightarrow LUMO and HOMO \rightarrow LUMO+1. This accounts for the differences in the calculated TM orientations between pyridine and pyrrole. The dominant one-electron excitation for 2PP is calculated to be solely HOMO \rightarrow LUMO. The nodal patterns of the MO's responsible for the observed transition in 2PP appears to be a combination of both pyridine and pyrrole.

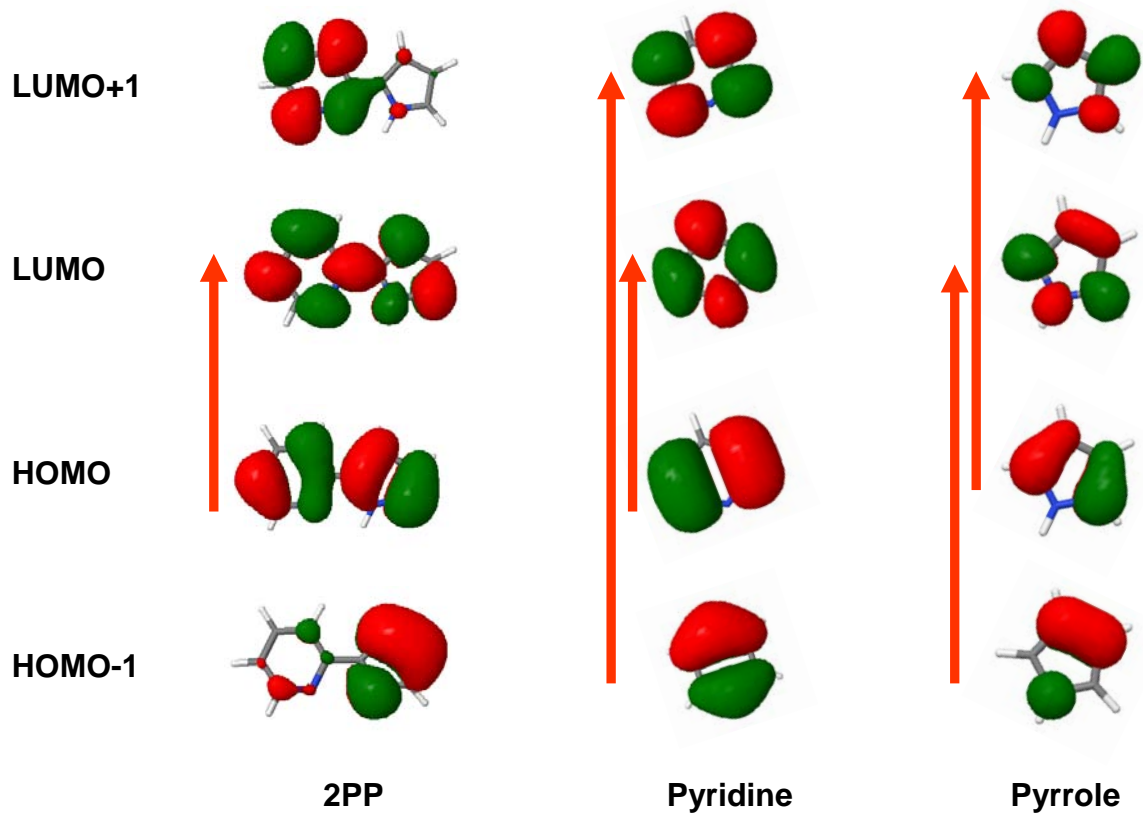


Figure 6.7. Frontier molecular orbitals calculated at the CIS/6-31G(d,p) level of 2PP, pyridine, and pyrrole. The 2PP transition is solely HOMO→LUMO, whereas pyridine is a combination of HOMO→LUMO and HOMO-1→LUMO+1 and pyrrole a combination of HOMO-1→LUMO and HOMO→LUMO+1.

6.5.2 Excited State Intramolecular Proton Transfer

Previous studies by Kijak *et al.*^{7,8} have already attributed the existence of an extreme red shifted fluorescence band to ESIPT in 2PP. The fluorescence excitation spectra of both the F₁ and F₂ bands provide evidence that ESIPT not only occurs in the +144 vibrational band progressions, but also in the origin band itself. The rotationally resolved fluorescence excitation spectra of the origin and +144 bands also provide direct evidence of ESIPT.

The origin band transition shows significant line broadening effects in its rotationally resolved spectrum. The spectrum was fit with a Voigt lineshape profile, resulting in a Gaussian width of 20 MHz and a Lorentzian component of 210 MHz. The Lorentzian component corresponds to an excited state lifetime of ~0.8 ns. This lifetime is relatively small, pointing to the possibility that some dynamical process is indeed occurring upon excitation. If ESIPT is occurring, it would be expected that the excited state lifetime of the original species would be relatively short, thus indicating that the tautomeric species is formed ~0.8 ns after excitation. The observation of ESIPT in the 2PP origin band confirms that ESIPT can occur in the gas phase without vibrational activation.

It was concluded that an in-plane vibrational mode is responsible for the two vibrational progressions observed in the LIF spectra of both the F₁ and F₂ fluorescence bands (see Figure 6.3).^{7,8} If this vibration is responsible for increasing the rate of ESIPT by decreasing the N-N bond distance in 2PP and therefore increasing the intramolecular hydrogen bonding coordinate, then an even shorter excited state lifetime should exist for

the +144 vibrational band. This is confirmed upon the analysis of the recorded rotationally resolved fluorescence excitation spectrum of the +144 vibrational band. As mentioned previously, the effects of the extreme line broadening in the spectrum made its analysis impossible. It is therefore concluded that the vibrational mode responsible for this particular band does indeed increase the rate of ESIPT. Using the origin band experimentally obtained rotational constants, an approximate lifetime can be obtained by increasing the Lorentzian component of the linewidth in the +144 band spectrum until individual transitions are no longer observable, as shown in Figure 6.8. The excited state lifetime for the +144 band was then deduced to be <80 ps, indicating that the ESIPT process is occurring faster by at least a factor of 10 in the $+144\text{ cm}^{-1}$ band.

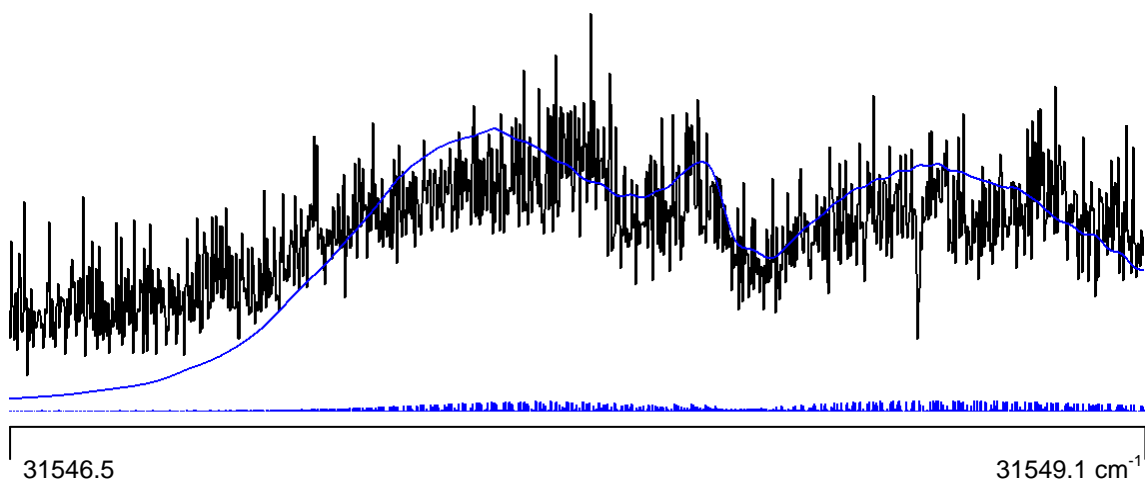


Figure 6.8. Contour fit of the rotationally resolved electronic excitation spectrum of the +144 vibrational band transition of 2PP.

The experimental evidence of ESIPT in the observed rotationally resolved fluorescence excitation spectra might also be directly responsible for the experimentally obtained inertial defect values of the 2PP origin band, 8.2 and 8.9 amu Å², respectively, in the ground and excited electronic states. It has been established that the inertial defect values of small planar molecules are slightly positive in the ground vibrational state when no out-of-plane vibrations of low frequency are present, thus the slight positive value results mostly from in-plane vibrations of the molecule.²⁶ However, the contributions from Coriolis interactions associated with the in-plane vibrations will not be large enough to be responsible for the observed positive inertial defect values.

A similar result by Weida *et al.* studying the weakly bound HeCO₂ complex was also obtained, where large positive inertial defect values were observed in the ground state zero point and ν_4 levels.²⁸ This was attributed to a large amplitude bending motion, resulting in an A rotational constant 8% larger than predicted, lowering the average moment of inertia about the I_{aa} axis. The ESIPT process in 2PP results from a completely in-plane coordinate along the a inertial axis. The large amplitude motion associated with the proton transfer coordinate must therefore be directly responsible for the observed positive inertial defect values.

How can the positive inertial defect value in the ground state be explained? If the observed inertial defect values originate from this large amplitude motion along the proton transfer reaction coordinate, then it must be true that large amplitude motion is occurring to some degree in the ground electronic state as well. The increased positive inertial defect value upon excitation indicates that proton transfer occurs more readily in the excited state, indicating a smaller barrier in the excited state, as calculated by Kijak *et*

*al.*² It is also apparent from the recorded +144 vibrational band spectrum that the in-plane vibration associated with this band enhances the proton transfer upon excitation.

6.6 CONCLUSIONS

Rotationally resolved $S_1 \leftarrow S_0$ fluorescence excitation spectra of the origin and +144 vibrational bands have been recorded in the gas phase. Both spectra exhibit line broadening effects associated with ESIPT. The excited state lifetime of the origin band transition is ~0.8 ns, indicating a relatively fast reaction rate process to the tautomeric species. The in-plane vibrational mode responsible for the +144 vibrational band transition increases the reaction rate of the ESIPT process, drastically increasing the Lorentzian contributions of the observed linewidth and making its analysis impossible. It has also been determined that proton transfer is not only occurring in the excited electronic state, but in ground electronic state as well.

6.7 ACKNOWLEDGMENTS

Some theoretical calculations were performed using the Center for Molecular and Materials Simulations (CMMS). We extensively thank Randolph P. Thummel from the University of Houston for the synthesis of 2PP. This research has been supported by the National Science Foundation (CHE-0911117) and we thank them for their support.

6.8 REFERENCES

1. Kijak, M.; Zielinska, A.; Thummel, R. P.; Herbich, J.; Waluk, J., *Chemical Physics Letters* **2002**, 366, 329.
2. Kijak, M.; Zielinska, A.; Chamchoumis, C.; Herbich, J.; Thummel, R. P.; Waluk, J., *Chemical Physics Letters* **2004**, 400, 279.
3. Wiosna-Salyga, G.; Dobkowski, J.; Mudadu, M. S.; Sazanovich, I.; Thummel, R. P.; Waluk, J., *Chemical Physics Letters* **2006**, 423, 288.
4. Kyrychenko, A.; Waluk, J., *Journal of Physical Chemistry A* **2006**, 110, 11958.
5. Vdovin, A.; Sepiol, J.; Urbanska, N.; Pietraszkiewicz, M.; Mordzinski, A.; Waluk, J., *Journal of the American Chemical Society* **2006**, 128, 2577.
6. Gil, M.; Waluk, J., *Journal of the American Chemical Society* **2007**, 129, 1335.
7. Kijak, M.; Nosenko, Y.; Singh, A.; Thummel, R. P.; Brutschy, B.; Waluk, J., *Journal of Molecular Structure* **2007**, 844-845, 286-299.
8. Kijak, M.; Nosenko, Y.; Singh, A.; Thummel, R. P.; Waluk, J., *Journal of the American Chemical Society* **2007**, 129, 2738.
9. Yu, W.-S.; Cheng, C.-C.; Cheng, Y.-M.; Wu, P.-C.; Song, Y.-H.; Chi, Y.; Chou, P.-T., *Journal of the American Chemical Society* **2003**, 125, 10800.
10. Heimbrook, L. A.; Kenny, J. E.; Kohler, B. E.; Scott, G. W., *J. Chem. Phys.* **1981**, 75, 5201.
11. Felker, P. M.; Lambert, W. R.; Zewail, A. H., *J. Chem. Phys.* **1982**, 77, 1603.
12. Herek, J. L.; Pedersen, S.; Banares, L.; Zewail, A. H., *J. Chem. Phys.* **1992**, 97, 9046.
13. Douhal, A.; Lahmani, F.; Zewail, A. H., *Chem. Phys.* **1996**, 207, 477.
14. Bisht, P. B.; Petek, H.; Yoshinara, K.; Nagashima, U., *J. Chem. Phys.* **1995**, 103, 5290.
15. Lahmani, F.; Zehnacker-Rentien, A., *J. Phys. Chem.* **1997**, 101, 6141.
16. Marsh, J. K., *J. Chem. Soc., Trans.* **1924**, 125, 418.

17. Weller, A., *Z. Elektrochem. Angew. Phys. Chem.* **1956**, 60, 1144.
18. Weller, A., *Progr. in Reaction Kinetics (G. Porter, editor. Pergamon Press)* **1961**, 1, 187.
19. Beens, H.; Grellmann, K. H.; Gurr, M.; Weller, A. H., *Discuss. Faraday Soc.* **1965**, No. 39, 183.
20. Vdovin, A. V.; Sepiol, J.; Jasny, J.; Kauffman, J. M.; Mordzinski, A., *Chem. Phys. Lett.* **1998**, 296, 557.
21. Majewski, W. A.; Pfanstiel, J. F.; Plusquellic, D. F.; Pratt, D. W., *Techniques of Chemistry (New York)* **1995**, 23, 101.
22. Plusquellic, D. F. Jb95 Spectral fitting program.
23. Plusquellic, D. F.; Suenram, R. D.; Mate, B.; Jensen, J. O.; Samuels, A. C., *Journal of Chemical Physics* **2001**, 115, 3057.
24. Frisch, M. J.; Trucks, G. W.; Schlegel, H. B.; Scuseria, G. E.; Robb, M. A.; Cheeseman, J. R.; Montgomery, J. A. J.; Vreven, T.; Kudin, K. N.; Burant, J. C.; Millam, J. M.; Iyengar, S. S.; Tomasi, J.; Barone, V.; Mennucci, B.; Cossi, M.; Scalmani, G.; Rega, N.; Petersson, G. A.; Nakatsuji, H.; Hada, M.; Ehara, M.; Toyota, K.; Fukuda, R.; Hasegawa, J.; Ishida, M.; Nakajima, T.; Honda, Y.; Kitao, O.; Nakai, H.; Klene, M.; Li, X.; Knox, J. E.; Hratchian, H. P.; Cross, J. B.; Bakken, V.; Adamo, C.; Jaramillo, J.; Gomperts, R.; Stratmann, R. E.; Yazyev, O.; Austin, A. J.; Cammi, R.; Pomelli, C.; Ochterski, J. W.; Ayala, P. Y.; Morokuma, K.; Voth, G. A.; Salvador, P.; Dannenberg, J. J.; Zakrzewski, V. G.; Dapprich, S.; Daniels, A. D.; Strain, M. C.; Farkas, O.; Malick, D. K.; Rabuck, A. D.; Raghavachari, K.; Foresman, J. B.; Ortiz, J. V.; Cui, Q.; Baboul, A. G.; Clifford, S.; Cioslowski, J.; Stefanov, B. B.; Liu, G.; Liashenko, A.; Piskorz, P.; Komaromi, I.; Martin, R. L.; Fox, D. J.; Keith, T.; Al-Laham, M. A.; Peng, C. Y.; Nanayakkara, A.; Challacombe, M.; Gill, P. M. W.; Johnson, B.; Chen, W.; Wong, M. W.; Gonzalez, C.; Pople, J. A. *Gaussian 03, Revision 6.0*, Gaussian, Inc., Wallingford CT: 2004.
25. Gordy, W.; Cook, R. L., *Microwave Molecular Spectra*. 3rd ed.; Wiley-Interscience: New York, 1984.
26. Herschbach, D. R.; Laurie, V. W., *J. Chem. Phys.* **1964**, 40, 3142.
27. Beames, J. M.; Nix, M. G. D.; Hudson, A. J., *J. Chem. Phys.* **2009**, 131, 174305/1.
28. Weida, M. J.; Sperhac, J. M.; Nesbitt, D. J.; Hutson, J. M., *J. Chem. Phys.* **1994**, 101, 8351.

7.0 CONCLUSION

Using rotationally resolved electronic spectroscopy, the structural and dynamical properties of several molecules have been investigated. In particular, the excited state dynamical processes of several of these molecules were determined, unveiling how excited state electronic and geometric structures play a role in these processes. The research described in this thesis is fundamental in nature. Its main goal is to better understand the interactions within a molecule which determine its structure and function. All of the systems investigated can serve as models for intramolecular interactions and preferred geometries of larger systems, such as amino acids, small peptides, and proteins.

In Chapter 2, the conformational assignments of the two conformers of *p*VP were made for their respective origin bands. *Ab initio* calculations were not able to accurately predict the excited state transition moment directions for both conformers, making these experimental measurements crucial in understanding the shortcomings of excited state *ab initio* calculations.

In Chapter 3, the conformational assignments of the two conformers of 1, 2, 3, 6, 7, 8-hexahydropyrene were also made for their respective origin bands. In addition, the role of intermolecular forces via van der Waals interactions was also investigated. Evidence for the chair-HHP-Ar and chair-HHP-H₂O complexes was provided and their structural properties were determined. With the aid of ground state *ab initio* calculations, the assignments of the van der Waals complexes to their respective bands were made possible.

The dynamics of the methyl group torsional motion for *o*-toluidine, *m*-toluidine, and 4-methylanisole were investigated in Chapters 4 and 5. Their rotationally resolved S₁

← S_0 origin band transitions are split into two sub-bands owing to tunneling motions along the methyl group torsional coordinate. Analyses of these data provided valuable information about the ground and excited state barrier heights of the 3-fold torsional motion of the attached methyl groups. In 4-methylansiole, the local electronic environment is found to play a vital role in determining the preferred methyl group configuration in the ground and excited electronic states, as well as influencing their potential energy barrier heights. In *o*- and *m*-toluidine, the electronic structure in the ground and excited electronic states significantly influence the potential barrier heights for the methyl group torsional motion. In particular, the steric hindrance that exists between the amino and methyl group in *o*-toluidine results in a substantially large excited state barrier. Steric hindrance plays a very important role in protein folding. Studying the effects of steric hindrance on dynamical processes in small molecular systems provides information about how these effects relate to the local electronic environments of molecules and how they can be related to large systems, such as proteins.

Chapter 6 discusses excited state intramolecular proton transfer in 2-(2'-pyridyl)pyrrole. The proton transfer rate was shown to increase dramatically upon excitation of a low-frequency in-plane vibration in comparison to its origin band transition. Proton transfer occurs in many biological systems, such as DNA and proteins. Understanding the intramolecular proton transfer process in smaller molecular systems helps to elucidate the process in these larger biological systems.

APPENDIX A

Photoactive proteins play extensive roles in biology.¹ Two examples are photoactive yellow protein (PYP) and green fluorescent protein (GFP). In both cases, absorption of light by the chromophore transduces light energy into biological response, amplifying molecular motion (isomerization) on small length scales to bacterial motion on much larger length scales. However, a molecular level understanding of these processes is currently lacking.

For this reason, several experiments were attempted on both chromophores (see below), using samples provided by Professor W. J. Buma at the University of Amsterdam.

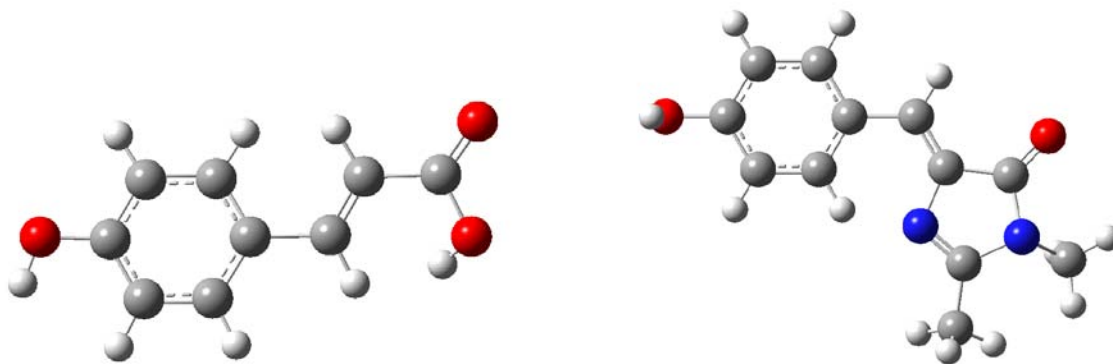


Figure A.1. Trans-*p*-coumaric acid, PYP chromophore, on left and HBDI, GFP chromophore, on right.

Rotationally resolved electronic spectroscopy experiments on a methyl oxyester derivative of *p*-coumaric acid, the chromophore in PYP, were attempted along with its single H₂O complexes. There was no observed signal for both the bare molecule and water complex species. Vibrationally resolved electronic spectroscopy techniques also failed to provide recorded spectra for either species.

Attempted efforts to find evidence for the spectrum of the GFP chromophore, HBDI and its methylester and ethylester derivatives, also failed. Vibrationally resolved electronic spectra scans for all three molecules were performed spanning a vast region of the UV, 320-360 nm. Efforts in the microwave chamber on HBDI have also failed to produce a microwave spectrum. The methylester and ethylester derivatives were not attempted with the microwave system. It is believed that thermal decomposition occurs upon heating the samples, resulting in fragments of the original molecules. It is also possible that rapid non-radiative decays quench the excited state photoemission below detectable levels.

A.1 REFERENCES

1. See, for example, Tsien, R. Y. *Annu. Rev. Biochem.* **1998**, *67*, 509.

APPENDIX B

PUSH-PULL MOLECULES IN THE GAS PHASE. STARK-EFFECT MEASUREMENTS OF THE PERMANENT DIPOLE MOMENTS OF *P*-AMINOBENZOIC ACID IN ITS GROUND AND ELECTRONICALLY EXCITED STATES.*

D. M. Mitchell, P. J. Morgan, and D. W. Pratt[†]

Department of Chemistry, University of Pittsburgh
Pittsburgh, Pennsylvania 15260

*Work supported by NSF (CHE-0615755).

[†]Email. pratt@pitt.edu

This work was published in *J. Phys. Chem. A.* **112** (2008) 12597.

D. M. Mitchell and P. J. Morgan performed the experimental measurements; D. M. Mitchell analyzed the spectra and wrote the paper.

B.1 ABSTRACT

Stark effect measurements of the permanent electric dipole moments of *p*-aminobenzoic acid (PABA) in the gas phase are reported, based on studies of its fully resolved $S_1 \leftarrow S_0$ electronic spectrum in the presence of an electric field. Ground state (S_0) PABA has $\mu = 3.3$ D, whereas excited state (S_1) PABA has $\mu = 4.4$ D. Despite PABA's reputation as a "push-pull" molecule, the photon-induced change in both the magnitude and orientation of μ is relatively small. Possible reasons for this behavior are discussed.

B.2 INTRODUCTION

Knowledge of the permanent electric dipole moment of a molecule can give us a wealth of information. Among other things, it can allow us to determine a molecule's conformation.^{1,2} Electric deflection experiments are currently being used to measure the ground state dipole moments of biomolecules in the gas phase, and these values have been used to make conclusions about peptide motion and shape.^{3,4} Recently, helix formation in alanine-based peptides was investigated; on the basis of dipole measurements, it was suggested that the peptides formed β -sheets in the gas phase, which was surprising, as they usually form α -helices in solution.⁴

Dugourd and coworkers have also studied some smaller molecules, such as *p*-aminobenzoic acid (PABA).⁵ PABA, shown in Figure B.1, can be classified as a "push-pull" molecule, with two substituents, an amino group and a carboxyl group, that may

donate or withdraw electron density to or from the benzene ring. PABA has been the focus of other gas phase studies,⁶ including deflection studies of its dimer.^{7,8}

High resolution fluorescence excitation spectroscopy performed in the presence of an electric field is a powerful tool that allows us to determine the electric dipole moments of isolated molecules by tracking the Stark shifts of individual transitions.⁹ Here, this technique has been applied to PABA. We measure both the ground and excited state permanent electric dipole moments of PABA in the gas phase. Comparison is made to the electric deflection results, and also to aniline (AN).

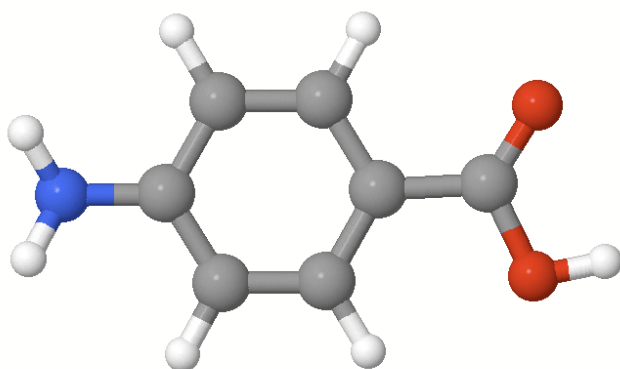


Figure B.1. Structure of PABA.

B.3 EXPERIMENTAL

PABA (99% purity) was purchased from Sigma-Aldrich and used without further purification. To obtain vibrationally resolved LIF spectra, a 50/50 mixture of PABA and diatomaceous earth was heated to ~ 130 °C, seeded into ~ 2 kTorr of dry helium gas ($> 90\%$ purity), and expanded through a 1 mm diameter orifice pulsed valve (General Valve Series 9), operating at 10 Hz, into a vacuum chamber (10^{-5} Torr). Diatomaceous earth was used in order to limit decomposition of PABA. The gaseous sample was then crossed 2 cm downstream with the output of a Quanta Ray Nd³⁺: YAG (Model DCR-1A) pumped dye laser (Model PDL-1), using a mixture of Kiton Red and Rhodamine 590 dyes. Frequency doubling was done externally with a potassium dihydrogen phosphate (KDP) crystal. The visible portion of the laser output was filtered, leaving ultraviolet (UV) light with a spectral resolution of ~ 1 cm⁻¹. A photomultiplier tube (EMI 9813QB), positioned at right angles to both the laser and molecular beams, was used to collect the fluorescence. The data were processed by a boxcar integrator (Stanford Research Systems) and recorded using Quick Data Acquisition software (version 1.0.5).

Rotationally resolved experiments were performed using a molecular beam laser spectrometer, described elsewhere.¹⁰ Briefly, the sample was heated to ~ 190 °C, seeded in dry argon gas ($> 99\%$ purity), and expanded into a vacuum through a 240 μ m quartz nozzle. The molecular beam was skimmed 2 cm downstream with a 1 mm diameter skimmer and then crossed 15 cm downstream with the frequency-doubled output of the dye laser. Rhodamine 590 dye was used, and ~ 1 mW of UV light was produced. Fluorescence was collected using spatially selective optics and detected by a

photomultiplier tube (EMI 9813 QB) and photon counting system. An iodine absorption spectrum and relative frequency markers were simultaneously collected. All information was processed using the jba95 data acquisition system.¹⁰ Absolute transition frequencies in the excitation spectrum were determined by comparison with the I₂ absorption spectrum (accuracy ~ 30 MHz). The frequency markers were generated by a stabilized etalon with a free spectral range of 299.7520 ± 0.0005 MHz at the fundamental frequency of the dye. Fitting of the field-free spectrum was done using the jb95 least squares fitting program.¹¹ The experimental setup of the Stark cell and general analysis of Stark spectra have been described elsewhere.⁹

The high resolution spectra of PABA both in the presence and absence of an applied electric field are relatively weak; we presume that this is due to the decomposition of PABA upon heating (the fluorescence quantum yield is fairly high).¹² For this reason, the intracavity frequency doubler in our modified Spectra-Physics 380D ring laser was replaced by a Wavetrain external frequency doubler, also manufactured by Spectra-Physics. UV power levels of ~ 1 mW were generated using the Kiton Red/Rhodamine 590 dye mixture and a BBO doubling crystal cut for 600 nm, a factor of 5 improvement over intracavity doubling in this frequency region. Details of the setup are provided elsewhere.¹³

B.4 RESULTS

Figure B.2 shows the vibrationally resolved fluorescence excitation spectrum (FES) of PABA. It is similar in many respects to the resonance-enhanced multiphoton ionization spectrum of laser-desorbed PABA taken by Meijer *et al.*⁶ The electronic origin is the strongest band in both spectra, and their frequencies are very nearly the same. There is also extensive vibrational structure in both spectra. However, there are significant differences in both the frequencies and intensities of the observed vibronic bands in the two spectra. Possibly, these differences may be traced to the different sample preparation methods; some decomposition of PABA no doubt occurs at the high temperatures that were used in our experiment. But it is also possible that there are some differences in the quantum yields of fluorescence and ionization when exciting different vibronic bands.

The rotationally resolved FES spectrum of the origin band of PABA is shown in Figure B.3. Lacking a strong Q-branch, it is a *b*-type spectrum, with the transition moment lying primarily along the *b*-axis. A simulation was created using rotational constants obtained from *ab initio* calculations,¹⁴ and these constants were varied until there was good overall agreement between the experimental spectrum and the simulation. Figure B.3 shows a portion of the simulation; each individual line in the simulation represents an individual $|J'K_a'K_c'\rangle \leftarrow |J''K_a''K_c''\rangle$ transition, and width has been added to reproduce the overall shape seen in the experiment. Over 100 transitions were assigned, and the best fit had an OMC (observed minus calculated standard deviation) of 2.4 MHz.

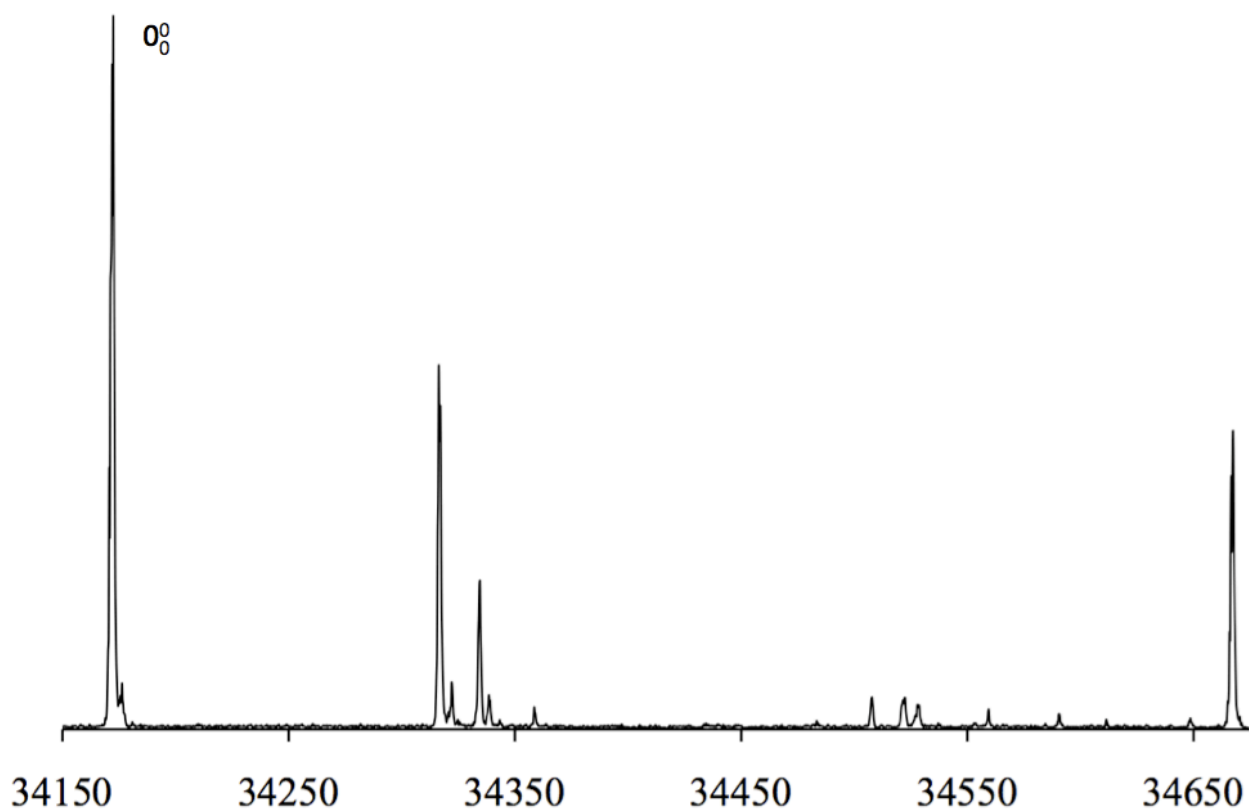


Figure B.2. Low-resolution fluorescence excitation spectrum of PABA.

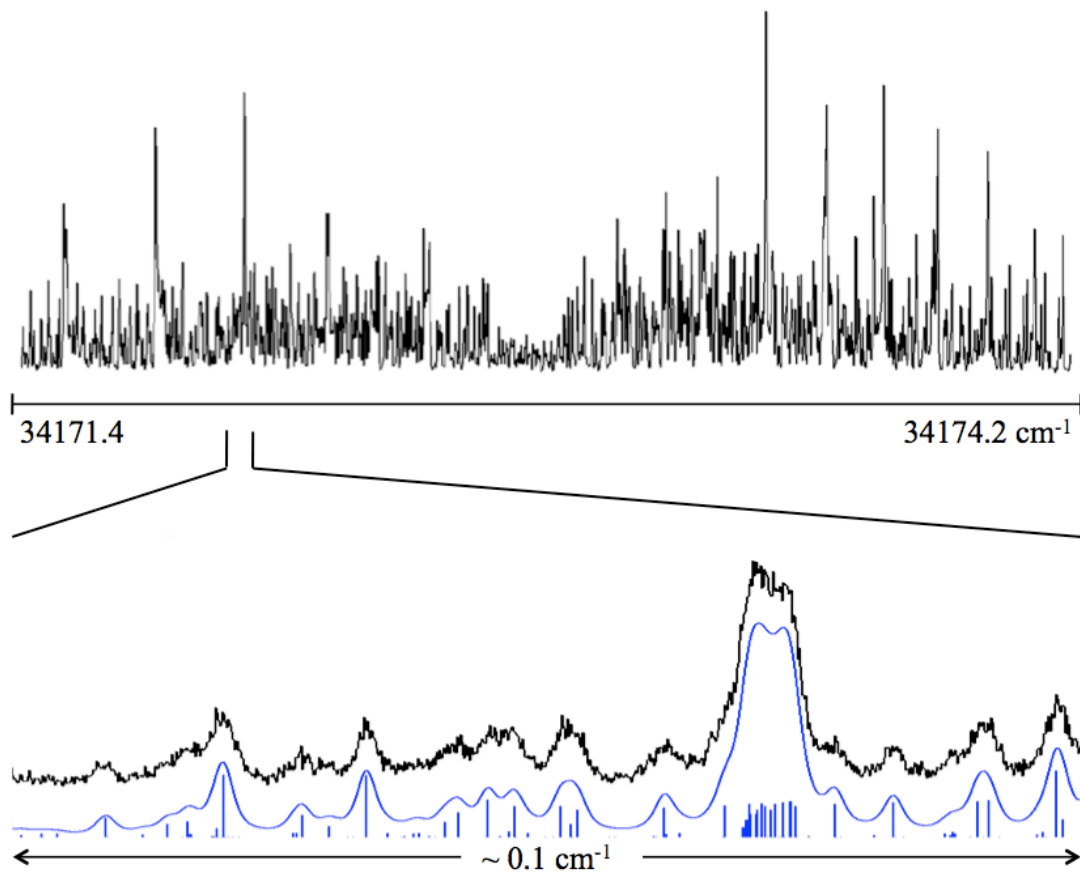


Figure B.3. The field-free origin spectrum of PABA, occurring at 34172.8 cm^{-1} . Also shown in the bottom panel is a comparison of a small portion of the experimental spectrum (black trace) with two simulated spectra (blue trace), with and without a convoluted lineshape function.

Table B.1. Experimental inertial parameters of PABA. (Parameters calculated at the MP2/6-31G and CIS/6-31G** levels of theory have also been included for comparison.)**

	Experimental	Calculated	% Error
S₀			
A (MHz)	3833.6 (1)	3821.3	0.3
B (MHz)	793.2 (1)	791.8	0.2
C (MHz)	657.8 (1)	656.3	0.2
ΔI (amu Å ²)	-0.66	-0.48	
S₁			
A (MHz)	3692.3 (1)	3740.2	1.3
B (MHz)	795.5 (1)	804.7	1.2
C (MHz)	655.1 (1)	662.5	1.1
ΔI (amu Å ²)	-0.67	-0.32	
<i>a/b/c</i>	5/95/0		
Origin (cm ⁻¹)	34172.8		

The parameters obtained from this fit are given in Table B.1. Rotational constants are in good agreement with calculations, with differences of 1% or less, less for the ground state.

The line width of individual transitions in the rotationally resolved origin band was fit using a Voigt profile comprised of a Gaussian line width of 18 MHz and a Lorentzian line width of ~ 30 MHz. The Gaussian component is due to Doppler broadening of the molecular beam; the Lorentzian component comes from lifetime broadening of the molecule. On the basis of our value of 30 MHz, the first excited-state of PABA has a lifetime around 5.3 ns. This is much longer than estimated by Meijer, *et al.*,⁶ who put the lifetime at a few hundred picoseconds. If the lifetime were that short, the lines seen in our experiment would be much broader, and we would not observe a resolved spectrum.

Application of an electric field causes transitions seen in the field-free spectrum to split and shift in frequency, as shown in Figure B.4. The magnitudes of these shifts depend on both the field strength and dipole moment values. A special program⁹ was used, in conjunction with jb95, to simulate and fit the experimental Stark spectra. This program carries out an exact diagonalization of truncated matrices and uses the following Hamiltonian:

$$\hat{H} = \hat{H}_r + \hat{H}_e \quad (\text{B.1})$$

The first term, \hat{H}_r , is the rigid-rotor Hamiltonian,

$$\hat{H}_r = AJ_a^2 + BJ_b^2 + CJ_c^2 \quad (\text{B.2})$$

and \hat{H}_e is the Stark Hamiltonian,

$$\hat{H}_e = -E_Z \sum_{g=a,b,c} \mu_g \phi_{Z_g} \quad (\text{B.3})$$

Here, A, B and C are the rotational constants; J_a , J_b and J_c are the projections of the angular momentum on the a , b and c inertial axes; E_Z represents the electric field applied along the Z axis; μ_a , μ_b and μ_c are the dipole moment components along each inertial axis; and the direction cosines relating the lab and molecular frames are represented by ϕ . Other details have been described previously.⁹ Recently, an improvement was made that more fully integrated the programs. One of the main features is a set of trackbars that allows the user to change the dipole moment components and “instantly” see the effects on the simulation.

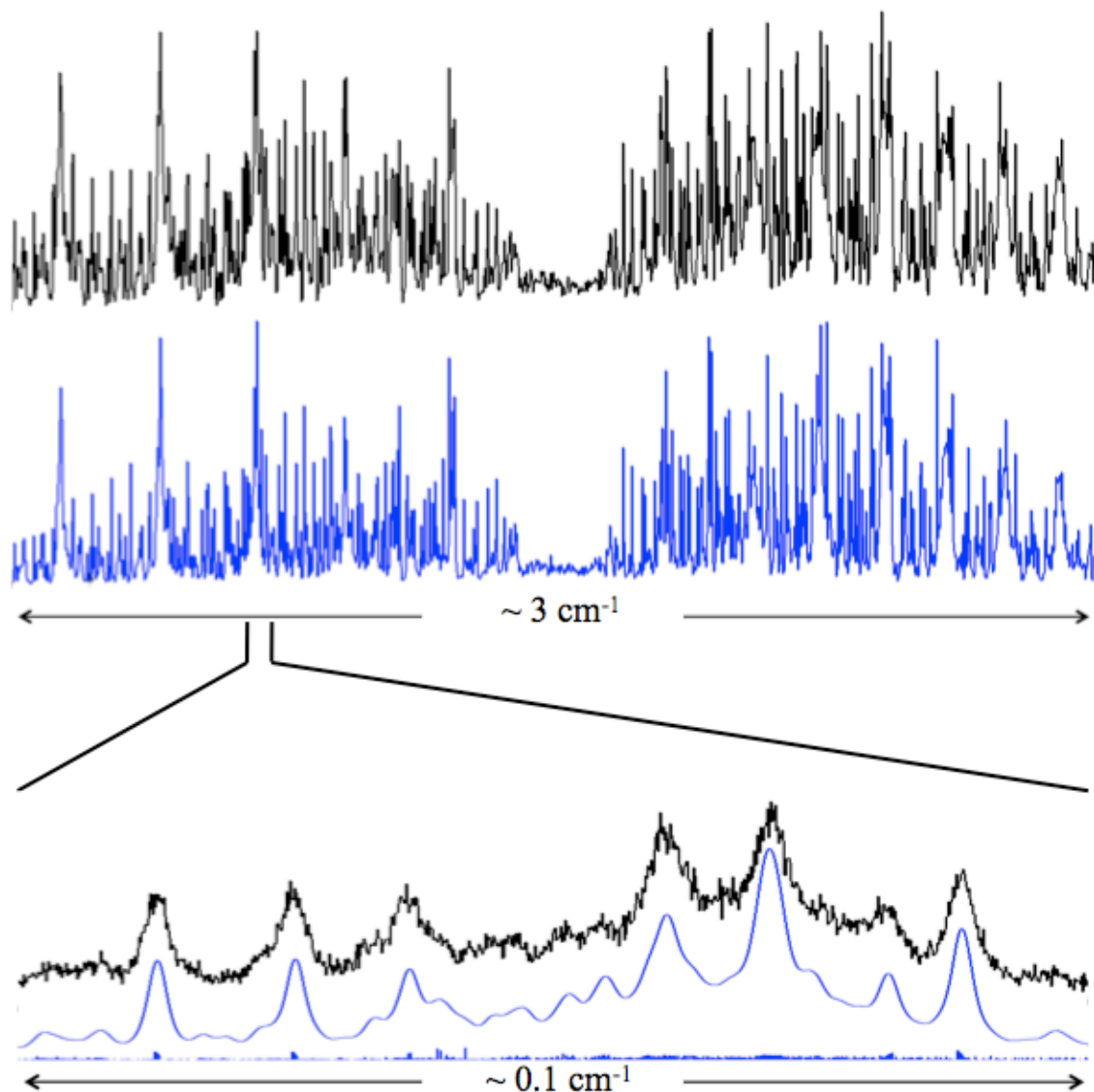


Figure B.4. Origin spectrum of PABA, at a calibrated electric field strength of 1184 V/cm. The black trace is the experimental spectrum, and the red trace is the simulated spectrum. The top portion shows the whole spectrum, while the bottom trace shows a close up of the highlighted section, again with and without a convoluted lineshape function.

Different transitions in the spectrum are affected differently by the application of the field. Certain transitions are more sensitive than others, both to the application of the electric field and to the different dipole moment components. This is illustrated in Figure B.5. The positions of P- and R-branch lines with high K values, particularly those equal or nearly equal to J , are especially sensitive to μ_a , the positions of Q-branch lines are especially sensitive to μ_b , and the positions of the lines with $K_a = 0$ are especially sensitive to μ_c . Thus, to fit the spectrum in Figure B.4 (and others at other field strengths), we first estimated μ_a , μ_b and μ_c using *ab initio* methods, simulated an overall spectrum, and then focused on individual transitions that are most sensitive to the different dipole moment components to obtain a final fit of the observed spectrum. This is also shown in Figure B.4. Typical OMC values of these fits are 7 MHz, substantially less than the line width.

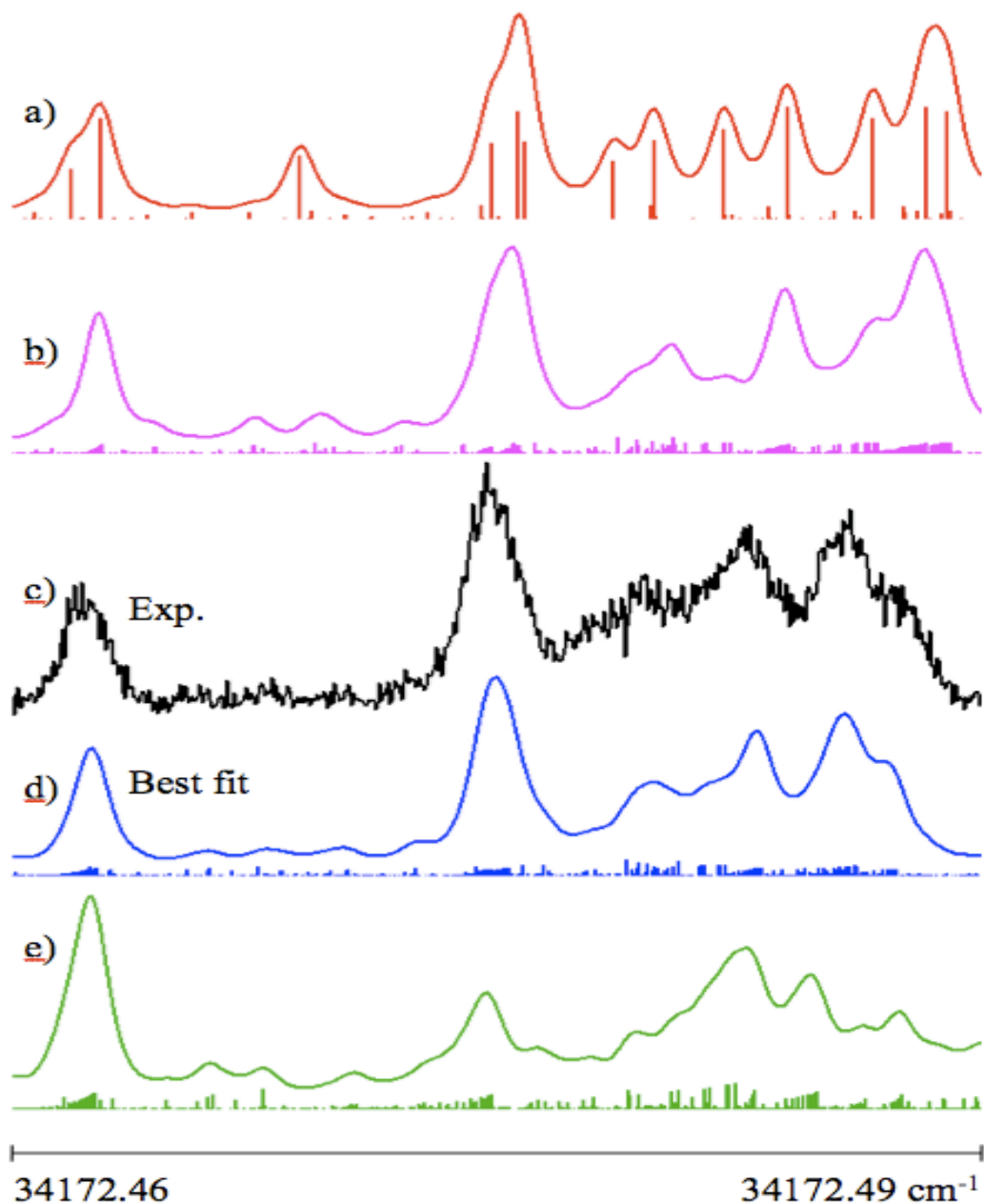


Figure B.5. Several simulations, both with and without a convoluted lineshape function, are compared to a portion of the Q-branch of the experimental spectrum to illustrate the dependence of the Stark spectra on the various dipole moment components. Simulation (a) is the zero-field spectrum, and traces (b) - (e) are at a calibrated field strength of 1184 V/cm. All simulations use the experimental rotational constants in Table 1. Simulation (b) assumes $\mu_a'' = 3.12$ and $\mu_a' = 4.21$ D, with the other components set to zero. The experimental spectrum (c) is shown for comparison. Below, simulation (d) is shown with $\mu_a'' = 3.12$, $\mu_a' = 4.21$, $\mu_b'' = 1.2$, $\mu_b' = 1.3$, $\mu_c'' = 0.0$ and $\mu_c' = 0.0$ D (the parameters obtained from our fits). Finally, simulation (e) was created with non-zero values of all dipole moment components, with $\mu_a'' = 3.12$, $\mu_a' = 4.21$, $\mu_b'' = 1.2$, $\mu_b' = 1.3$, $\mu_c'' = -1.26$ and $\mu_c' = -0.86$ D. The assumed values of μ_c are the calculated ones (Table A.2).

B.5 DISCUSSION

The value of μ_a obtained by electric deflection methods, 2.8 (2) D,⁴ is in reasonable agreement with our directly measured value of 3.12 (8) D. This is not too surprising, since PABA is a near symmetric top and behaves well in an electric field.^{5,15} In addition to the μ_a component, we are also able to measure the μ_b and μ_c components of the dipole moment, and we are able to measure all components in the electronically excited state. Thus, we also determine the orientation of the dipole moment in the molecular coordinate system and how it changes when the photon is absorbed.

The experimentally determined values of the dipole moment components are shown in Table B.2. In general, the measured values of the components of μ are substantially different from the calculated ones, with errors up to 30%. A special case is the out-of-plane component, μ_c . From our fits, μ_c was determined to be zero in both states, despite calculations predicting non-zero values; this has also been observed for AN.⁹ A planar molecule would have $\mu_c = 0$. PABA, like AN, is relatively planar, except for the amino group which is positioned out of the plane. Calculations estimate the dihedral angle between the NH_2 and $\text{C}_6\text{H}_4\text{N}$ planes to be $\sim 28^\circ$ in the ground state and $\sim 20^\circ$ in the excited state. In AN, the amino group undergoes an inversion motion that is fast relative to the rotational motion, resulting in an average value of zero for μ_c .^{9,17} We presume the same is true for PABA.

Figure B.6 shows a comparison of the molecular orbitals of AN and PABA. The HOMO-1 (ϕ_2), HOMO (ϕ_3), LUMO (ϕ_4), and LUMO+1 (ϕ_5) orbitals are depicted. For PABA, the nodal pattern of the LUMO and LUMO+1 orbitals are reversed, relative to

Table B.2. Experimental dipole moment values for PABA. (Parameters calculated at the MP2/6-31G** and CIS/6-31G** levels of theory have also been included for comparison.)

	Experimental	Calculated	% Error
S₀			
μ_a (D)	3.12 (8)	3.14	0.6
μ_b (D)	1.2 (2)	1.53	27.5
μ_c (D)	0.00 (1)	-1.26	
μ (D)	3.3 (2)	3.71	
S₁			
μ_a (D)	4.21 (8)	4.12	2.1
μ_b (D)	1.3 (2)	1.53	17.7
μ_c (D)	0.00 (1)	-0.86	
μ (D)	4.4 (1)	4.48	

AN. On the basis of results observed for different conformations of alkyl benzenes,¹⁸ this is not surprising; addition of the carboxyl group to AN breaks the symmetry of the molecule, rotating the positions of the nodal planes of the LUMO and LUMO+1 orbitals.

Calculations done at the CIS/6-31G** level of theory predict the S₁ state of AN to be a linear combination of one-electron excitations, $\Psi(S_1) = 0.28 (\phi_2\phi_5) + 0.64 (\phi_3\phi_4)$, with small contributions from other excitations. For PABA, calculations done at the same level of theory predict a similar combination; $\Psi(S_1) = 0.20 (\phi_2\phi_5) + 0.65 (\phi_3\phi_4)$, with small contributions from other excitations. The dominant excitation for both is HOMO to LUMO, and by multiplying the signs of these orbitals, we can predict the transition moment orientation of the excitation in PABA. The result of this multiplication is depicted in the lower portion of Figure B.6, and it shows that the predicted transition moment should lie parallel to the *a* axis for PABA. However, our experiments clearly show that the S₁←S₀ transition is *b*-type, which means that the ordering of the molecular orbitals must follow that of AN. We conclude that the slight breaking of the symmetry

by the carboxyl group must have a negligible effect on the positions of the nodal planes of the molecular orbitals of PABA.

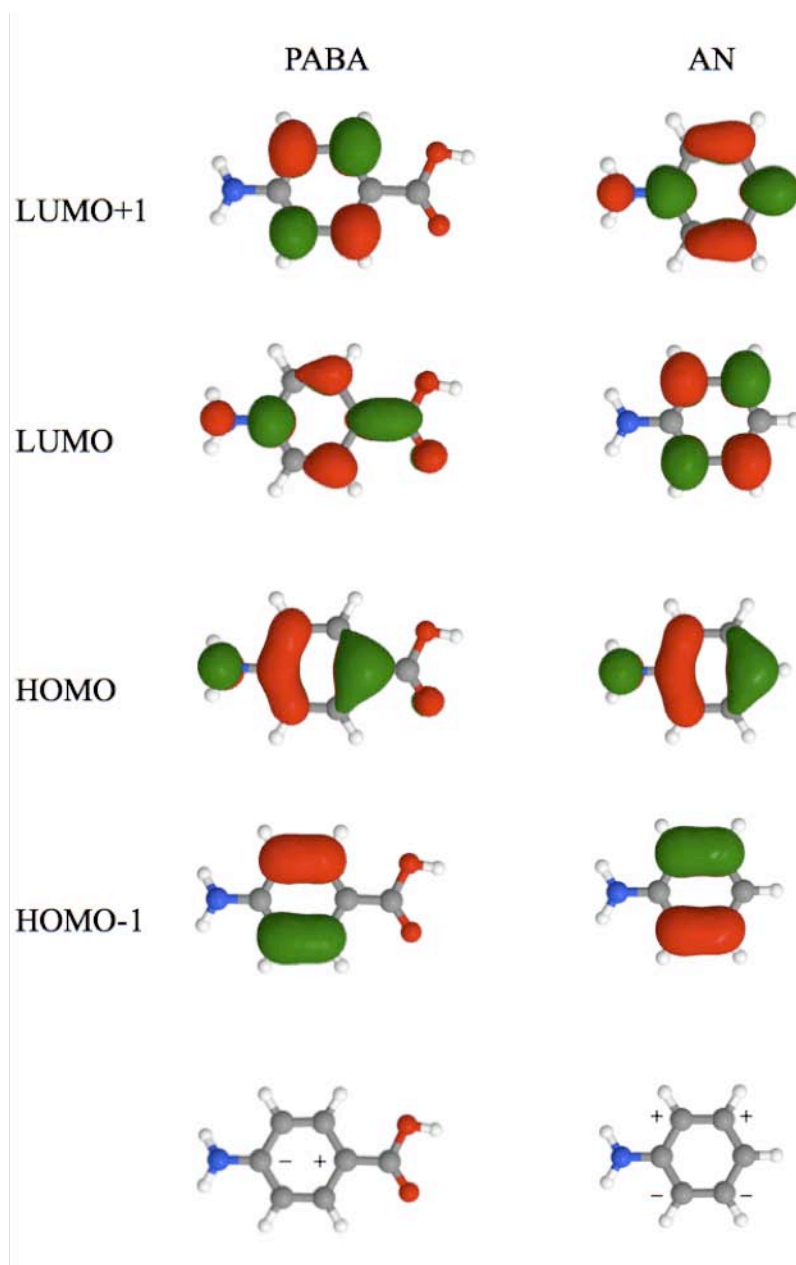


Figure B.6. HOMO-1 (ϕ_2), HOMO (ϕ_3), LUMO (ϕ_4), and LUMO+1 (ϕ_5) orbitals of PABA and AN, as predicted by CIS/6-31G** calculations. The bottom portion shows the result of multiplication of the signs of the ϕ_3 and ϕ_4 orbitals, giving predicted transition moment orientations.

The ground and excited state total dipole moments of PABA and AN are depicted in Figure B.7. It should be noted that we do not obtain the direction of the dipole components from our fits; the directions shown in the figure are based on chemical intuition and the results of *ab initio* calculations. A comparison of the dipole moment values of PABA and AN is made in Table B.3. The ground state μ_a dipole moment component of PABA, 3.12 (8) D, is larger than that of AN, 1.129 (5) D. This is due to the presence of the carboxyl group on PABA; -COOH groups are electron withdrawing (see Figure B.6). Another measure of this effect is the proton affinity of the molecule in the gas phase, the energy released in the reaction $B + H^+ \rightarrow BH^+$. AN has a proton affinity of 877 kJ/mol, whereas that for PABA is somewhat less, 864.7 kJ/mol,¹⁹ owing to the decrease in electron density on the -NH₂ group. Also notable is the magnitude μ_b of in PABA; the difference in the electron densities of the =O and -OH groups must be quite substantial, as μ makes large angles with the *a* axis ($\sim 21^\circ$ in S_0 and $\sim 18^\circ$ in S_1).

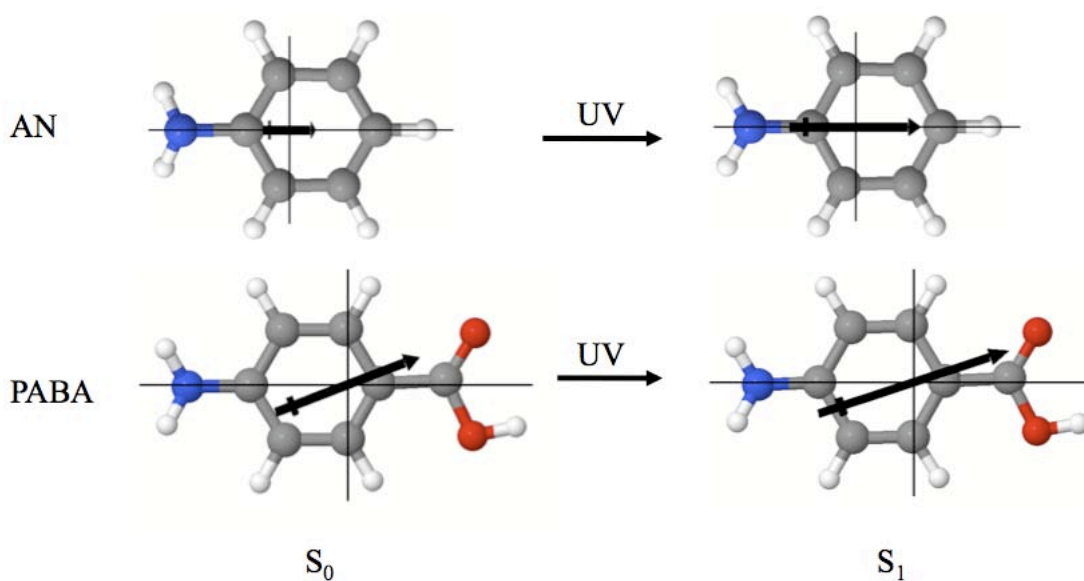


Figure B.7. Arrows depicting the dipole moment magnitudes and directions of PABA and AN in both the ground and excited states.

Table B.3. Comparison of experimental dipole moment values of PABA and AN.

	PABA	Aniline ^{9,16}
S₀		
μ_a (D)	3.12 (8)	1.129 (5)
μ_b (D)	1.2 (2)	0.00 (1)
μ_c (D)	0.00 (1)	0.00 (1)
μ (D)	3.3 (2)	1.129 (5)
S₁		
$\Delta\mu_a$ (D)	1.1 (2)	1.67 (1)
$\Delta\mu_b$ (D)	0.1 (4)	0.00 (1)
$\Delta\mu_c$ (D)	0.00 (2)	0.00 (1)
$\Delta\mu$ (D)	1.1 (3)	1.672 (7)

The change in μ_a upon excitation is larger in AN than in PABA. Figure B.8 shows electron density difference plots for AN and PABA, with light areas representing regions of electron density gain and dark areas representing electron density loss.²⁰ In AN, it can be seen that charge is transferred from the amino group to the ring, resulting in the 1.67 D increase in μ_a . The increase in μ_a (1.1 D) in PABA is smaller than this. The electron density difference plot of PABA shows that the amino group donates electron density to the ring, as it does in AN, and that the carboxyl group also donates electron density to the ring. The donation made by the amino group increases μ_a relative to the ground state because it occurs in the same direction as the ground state dipole. However, the donation of charge from the carboxyl group to the ring in PABA occurs in the opposite direction. Thus, the μ_a component still increases in PABA upon excitation, but the magnitude of the increase is less, relative to AN, due to the counteractive effect of the carboxyl group.

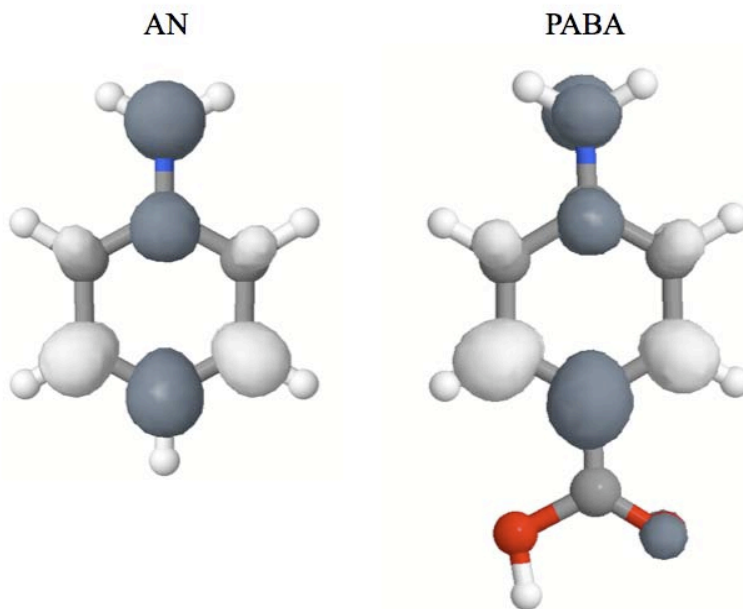


Figure B.8. Electron density difference plots for AN and PABA. Light areas represent regions of electron gain, and dark areas represent regions of electron loss.

B.6 CONCLUSIONS

Rotationally resolved electronic spectroscopy has been performed in the presence of an electric field to determine the permanent electric dipole moment values for PABA in the gas phase in both its ground and excited states. The value of μ_a in the S_0 state is in reasonable agreement with electric deflection measurements taken by Dugourd, *et al.*⁵ The dipole moments of PABA have also been compared to those of AN. The addition of the carboxyl group withdraws electron density from the ring, resulting in an overall ground state dipole moment that is larger than that of AN. There is also a significant μ_b component to the dipole in PABA; this indicates that there is a considerable electron density difference between the =O and -OH groups of the carboxyl. The change in μ_a of

PABA upon excitation is slightly smaller in magnitude compared to that of AN, and the percent change is much smaller. Calculations suggest that both the amino and carboxyl substituents transfer some electron density back to the ring upon excitation. Because the donation of electron density from the carboxyl group occurs in a direction opposite to the dipole moment, the affect of the donation from the amino group is mitigated, resulting in a smaller change in μ_a than in AN.

B.7 ACKNOWLEDGEMENTS

We would like to thank D. F. Plusquellic for his work on the Stark fitting program to further integrate it with the jb95 interface. We would also like to thank the Center for Molecular and Materials Simulations at the University of Pittsburgh for computing time, T. V. Nguyen for helpful discussions about using the Stark program, J. J. Grabowski for helpful discussions about proton affinities, and NSF for financial support (CHE-0615755).

B.8 REFERENCES

1. J. A. Reese, T. V. Nguyen, T. M. Korter and D. W. Pratt, *J. Am. Chem. Soc.* **2004**, 126, 11387.
2. T. V. Nguyen and D. W. Pratt, *J. Chem. Phys.* **2006**, 124, 054317.
3. R. Antoine, I. Compagnon, D. Rayane, M. Broyer, Ph. Dugourd, G. Breux, F. C. Hagemester, D. Pippen, R. R. Hudgins and M. F. Jarrold, *J. Am. Chem. Soc.* **2002**, 124, 6737.
4. Ph. Dugourd, R. Antoine, G. Breux, M. Broyer and M. F. Jarrold, *J. Am. Chem. Soc.* **2005**, 127, 4675.
5. I. Compagnon, R. Antoine, D. Rayane, M. Broyer and Ph. Dugourd, *J. Phys. Chem. A* **2003**, 107, 3036.
6. G. Meijer, M. S. de Vries, H. E. Hunziker, and H. R. Wendt, *J. Chem. Phys.* **1990**, 92, 7625.
7. I. Compagnon, R. Antoine, D. Rayane, M. Broyer and Ph. Dugourd, *Phys. Rev. Lett.* **2002**, 89, 253001.
8. M. Abd El Rahim, R. Antoine, L. Arnaud, M. Broyer, D. Rayane, A. Viard and Ph. Dugourd, *Eur. Phys. J. D.* **2005**, 34, 15.
9. T. M. Korter, D. R. Borst, C. J. Butler and D. W. Pratt, *J. Am. Chem. Soc.* **2001**, 123, 96.
10. W. A. Majewski, J. F. Pfanstiel, D. F. Plusquellic and D. W. Pratt, *Laser Techniques in Chemistry*. T. R. Rizzo and A. B. Meyers, Eds. J. Wiley & Sons. New York. **1995**, p. 101.
11. D. F. Plusquellic, R. D. Suenram, B. Maté, J. O. Jensen and A. C. Samuels, *J. Chem. Phys.* **2001**, 115, 3057.
12. J. M. Bello and R. J. Hurtubise, *Appl. Spectrosc.* **1988**, 42, 619.
13. D. M. Mitchell, Ph. D. Thesis, University of Pittsburgh, **2008**.
14. Gaussian 03, Revision 6.0, M. J. Frisch, G. W. Trucks, H. B. Schlegel, G. E. Scuseria, M. A. Robb, J. R. Cheeseman, J. A. Montgomery, Jr., T. Vreven, K. N. Kudin, J. C. Burant, J. M. Millam, S. S. Iyengar, J. Tomasi, V. Barone, B. Mennucci, M. Cossi, G. Scalmani, N. Rega, G. A. Petersson, H. Nakatsuji, M.

- Hada, M. Ehara, K. Toyota, R. Fukuda, J. Hasegawa, M. Ishida, T. Nakajima, Y. Honda, O. Kitao, H. Nakai, M. Klene, X. Li, J. E. Knox, H. P. Hratchian, J. B. Cross, V. Bakken, C. Adamo, J. Jaramillo, R. Gomperts, R. E. Stratmann, O. Yazyev, A. J. Austin, R. Cammi, C. Pomelli, J. W. Ochterski, P. Y. Ayala, K. Morokuma, G. A. Voth, P. Salvador, J. J. Dannenberg, V. G. Zakrzewski, S. Dapprich, A. D. Daniels, M. C. Strain, O. Farkas, D. K. Malick, A. D. Rabuck, K. Raghavachari, J. B. Foresman, J. V. Ortiz, Q. Cui, A. G. Baboul, S. Clifford, J. Cioslowski, B. B. Stefanov, G. Liu, A. Liashenko, P. Piskorz, I. Komaromi, R. L. Martin, D. J. Fox, T. Keith, M. A. Al-Laham, C. Y. Peng, A. Nanayakkara, M. Challacombe, P. M. W. Gill, B. Johnson, W. Chen, M. W. Wong, C. Gonzalez, and J. A. Pople, Gaussian, Inc., Wallingford CT, 2004.
15. M. Abd El Rahim, R. Antoine, M. Broyer, D. Rayane and Ph. Dugourd, *J. Phys. Chem. A*. **2005**, 109, 8507.
 16. D. G. Lister, J. K. Tyler, J. H. Høg and N. W. Larsen, *J. Mol. Struct.* **1974**, 23, 253.
 17. J. M. Hollas, M. R. Howson, T. Ridley, and L. Halonen, *Chem. Phys. Lett.* **1983**, 98, 611.
 18. R. T. Kroemer, K. R. Liedl, J. A. Dickinson, E. G. Robertson, J. P. Simons, D. R. Borst and D. W. Pratt, *J. Am. Chem. Soc.* **1998**, 120, 12573.
 19. E. P. Hunter and S. G. Lias, *J. Phys. Chem. Ref. Data*. **1998**, 27, 413.
 20. These plots were created by taking $(\phi_4^2 - \phi_3^2)$ for aniline and $(\phi_5^2 - \phi_3^2)$ for PABA (since the calculated LUMO and LUMO+1 are reversed). Ideally, each plot would have been generated from a normalized linear combination of the HOMO to LUMO and the HOMO-1 to LUMO+1 excitations. However, since the orbital ordering was reversed for PABA, we could not rely on the calculated coefficients.

APPENDIX C

ON THE ELECTRIC DIPOLE MOMENTS OF ASYMMETRIC TOPS. MEASUREMENT BY HIGH RESOLUTION ELECTRONIC SPECTROSCOPY IN THE GAS PHASE.^a

Diane M. Miller,^b Philip J. Morgan and David W. Pratt^c

Department of Chemistry, University of Pittsburgh
Pittsburgh PA 15260 USA.

^a Work supported by NSF (CHE-0615755).

^b Present address: Department of Chemistry, Marquette University, Milwaukee WI 53201.

^c Corresponding author: pratt@pitt.edu.

This work was published in *J. Phys. Chem. A* **113** (2009) 6964.

D. M. Miller and P. J. Morgan performed the experimental measurements; D. M. Miller analyzed the spectra and wrote the paper.

C.1 ABSTRACT

Reported here are Stark-effect measurements of the permanent electric dipole moments of two structural isomers of aminobenzonitrile, 2ABN and 3ABN, using high resolution laser molecular beam techniques. When combined with previous results on 4ABN, the data show that each structural isomer has a unique dipole moment, in both its ground (S_0) and electronically excited (S_1) states, thereby providing a means of distinguishing them. Possible applications of the method to other, biologically relevant molecules are discussed.

C.2 INTRODUCTION

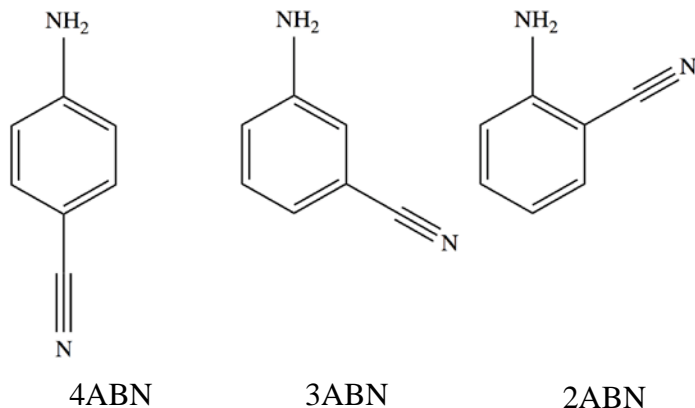
The “molecular design of life”¹ is significantly influenced by the properties of isolated molecules. Thus, the three-dimensional structures and functions of proteins depend upon the size, shape, and charge distributions of the side chains in the 20 different amino acid building blocks that are used to construct them. Protein-protein interactions, leading to aggregation and disease, are also believed by some to be influenced by the dipole moments of their components parts.² It is thus a bit surprising that the dipole moments of the individual amino acids, and their dependence on the conformation of the isolated molecule, remain largely unexplored by experimental techniques.

Significant progress towards achieving this goal has been made, beginning with the work of Brown and co-workers on glycine, histamine, alanine, and related molecules.

³ More recently, several neutral aliphatic amino acids in the gas phase have been studied

using laser ablation, molecular beam Fourier transform microwave spectroscopy,⁴ and their preferred structures determined by measurements of their rotational and ¹⁴N quadrupole coupling constants. Mons and co-workers,⁵ and others, have probed the structures of small peptides using IR/UV double resonance techniques. But the dipole moments of many of these species have yet to be reported. Compagnon *et al.*⁶ have coupled a matrix assisted laser desorption source to an electric beam deflection setup to measure the permanent electric dipole of tryptophan isolated in a molecular beam. More recently, this method has been applied to a variety of species, including glycine-based⁷ and alanine-based peptides.⁸ In the latter work, the authors concluded that alanine-based peptides formed β -sheets in the gas phase, rather than the α -helices normally observed in aqueous solution, because the observed dipole moments were much smaller than expected.

One possible explanation for this anomaly, offered first by Abd El Rahim, *et al.*⁹, is that the gas phase alanine-based peptides are actually helical in shape and that deviations from their expected deflection behavior are a consequence of the asymmetry of the molecule. This idea was tested, and it was indeed found that, in a family of aminobenzonitrile (ABN) molecules, there were increasing deviations from the calculated Stark-effect behavior with increasing asymmetry in the series 4ABN, 3ABN, and 2ABN, shown below.



Described herein are the results of Stark-effect experiments by high-resolution laser spectroscopy on two of these molecules, 2ABN and 3ABN. (Similar results for 4ABN have previously been reported.¹⁰) The objectives of this work were (a) to show that accurate values of the permanent electric dipole moments of these species could, in fact, be measured, (b) to compare the measured values with *ab initio* values upon which the calculations of Abd El Rahim, *et al.*⁹ were based, and (c) to validate (or invalidate) their explanation of the observed deflection behavior. We find that this explanation is correct, a fact that was anticipated by others.¹¹ But we also show, as a consequence, that the method described here (as well as related microwave methods) can still be relied upon for future measurements of the dipole moments of the “building blocks of life”.¹

C.3 EXPERIMENTAL

2ABN (98% purity) and 3ABN (99% purity) were purchased from Sigma-Aldrich and used as received. Vibrationally resolved fluorescence excitation spectra (FES) were obtained by heating the sample to ~ 40 °C, seeding the resulting vapor into 2-2.5 kTorr of

dry helium gas (> 90% purity), and expanding the mixture through a 1 mm diameter orifice pulsed valve (General Valve Series 9, operating at 10 Hz) into a vacuum chamber (10^{-5} Torr). The cooled sample was then crossed 2 cm downstream of the nozzle with the output of a Quanta Ray Nd³⁺: YAG (Model DCR-1A) pumped dye laser (Model PDL-1). DCM dye was used to obtain the correct visible laser frequency; this was then doubled externally with a potassium dihydrogen phosphate (KDP) crystal. Any remaining visible light was filtered, leaving ultraviolet (UV) light with a spectral resolution of $\sim 1 \text{ cm}^{-1}$. Fluorescence was collected with a photomultiplier tube (EMI 98139B) positioned at right angles to both the laser and nozzle beams. The data was processed by a boxcar integrator (Stanford Research Systems) and recorded using Quick Data Acquisition software (Version 1.0.5).

The molecular beam laser spectrometer used to obtain rotationally resolved spectra has been described elsewhere.¹² Briefly, the samples were each heated to ~ 120 °C, seeded in dry argon gas (> 99% purity), and expanded into a vacuum through a 240 μm quartz nozzle. The molecular beam was formed by skimming the expansion 2 cm downstream of the nozzle with a 1 mm diameter skimmer, and then crossed 15 cm downstream with the frequency-doubled output of a modified continuous ring dye laser. DCM dye was used for 2ABN, and DCM Special dye was used for 3ABN. The visible output of the dye laser was externally frequency-doubled by a Spectra-Physics Wavetrain using a 630 nm LBO crystal;¹³ $\sim 400 \mu\text{W}$ and $\sim 200 \mu\text{W}$ of UV light was produced at the 2ABN and 3ABN origin frequencies, respectively. Fluorescence was collected using spatially selective optics and detected by a photomultiplier tube (EMI 9813 QB) and photon counting system. All information was processed using the jba95 data acquisition

system.¹⁴ Absolute transition frequencies in the excitation spectrum were determined by comparison to the I₂ absorption spectrum (accuracy ~ 30 MHz), which was recorded simultaneously with the high resolution spectrum. Frequency markers also were collected; these were generated by passing a small portion of the fundamental through a stabilized etalon with a free spectral range of 299.7520 ± 0.0005 MHz. Fitting of the zero-field spectra was performed using the jb95 rotational least-squares fitting program.¹⁵ The experimental set-up of the Stark cell and the procedure for analyses of Stark spectra have been described in detail elsewhere;¹⁶ applied field strengths ranged from ~ 95 to 1900 V/cm.

C.4 RESULTS

Vibrationally resolved FES of 2ABN and 3ABN are shown in Figure C.1. Both spectra are consistent with previously published data on the two molecules.^{17,18} In comparison to the FES of 4-aminobenzonitrile (4ABN),¹⁸ the spectra of 2ABN and 3ABN show more vibrational activity. 4ABN contains a symmetry plane and is a near symmetric top molecule ($\kappa = -0.94$); 2ABN and 3ABN, to varying degrees, are less symmetric, allowing more transitions to be observed.

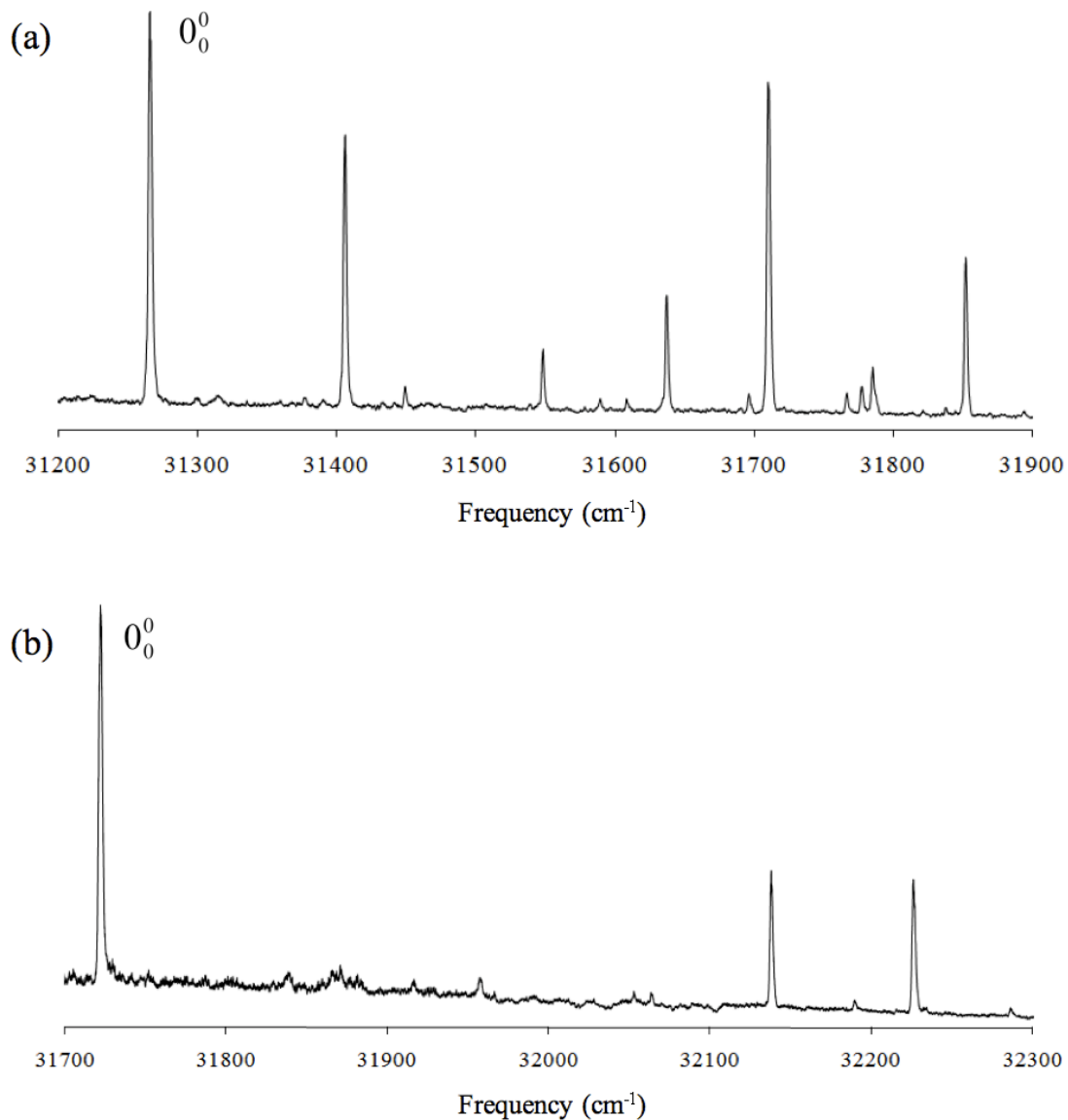


Figure C.1. Vibrationally resolved fluorescence excitation spectra of 2ABN (a) and 3ABN (b).

The rotationally resolved FES of the origin band of 2ABN at zero field is shown in Figure C.2a. The band shows 44/55 *a/b* hybrid character,¹⁹ with the transition moment lying between the *a* and *b* axes. Rotational constants obtained by *ab initio* calculations,²⁰ shown in Table C.1, were used to create an initial simulation. Transitions were assigned and the rotational constants were adjusted until the simulation was in good agreement

with the experimental spectrum. The parameters obtained from this fit are given in Table C.1. A portion of the simulation is shown in the lower part of Fig. C.2a, demonstrating its good agreement with experiment. Each line of the simulation represents an individual $|J'K_a'K_c'\rangle \leftarrow |J''K_a''K_c''\rangle$ transition; 101 transitions were assigned. Width has been added to reproduce the overall shape of the experimental spectrum. The best fit had an OMC (observed minus calculated standard deviation) of 1.9 MHz. The measured rotational constants are in good agreement with theoretical ones, with differences of less than 1% for the ground state and less than 2% for the excited state.

Figure C.2b shows the corresponding rotationally resolved FES of the origin band of 3ABN at zero field. An initial simulation was created using the *ab initio* values given in Table C.1, and transitions were assigned and the rotational constants were adjusted until the simulation was in good agreement with the experimental spectrum. A portion of the best-fit simulation, with and without added linewidth, is shown in the lower portion of Fig. C.2b. Over 100 transitions were assigned; the best fit had an OMC of 4.6 MHz. The measured rotational constants are shown in Table C.1, and they are again in good agreement with calculations, with differences of less than 1% for the ground state and less than 2% for the excited state. Fits of the spectral line intensities are consistent with a band having 25/75 *a/b* hybrid character. This is substantially different from the band character seen for 2ABN.

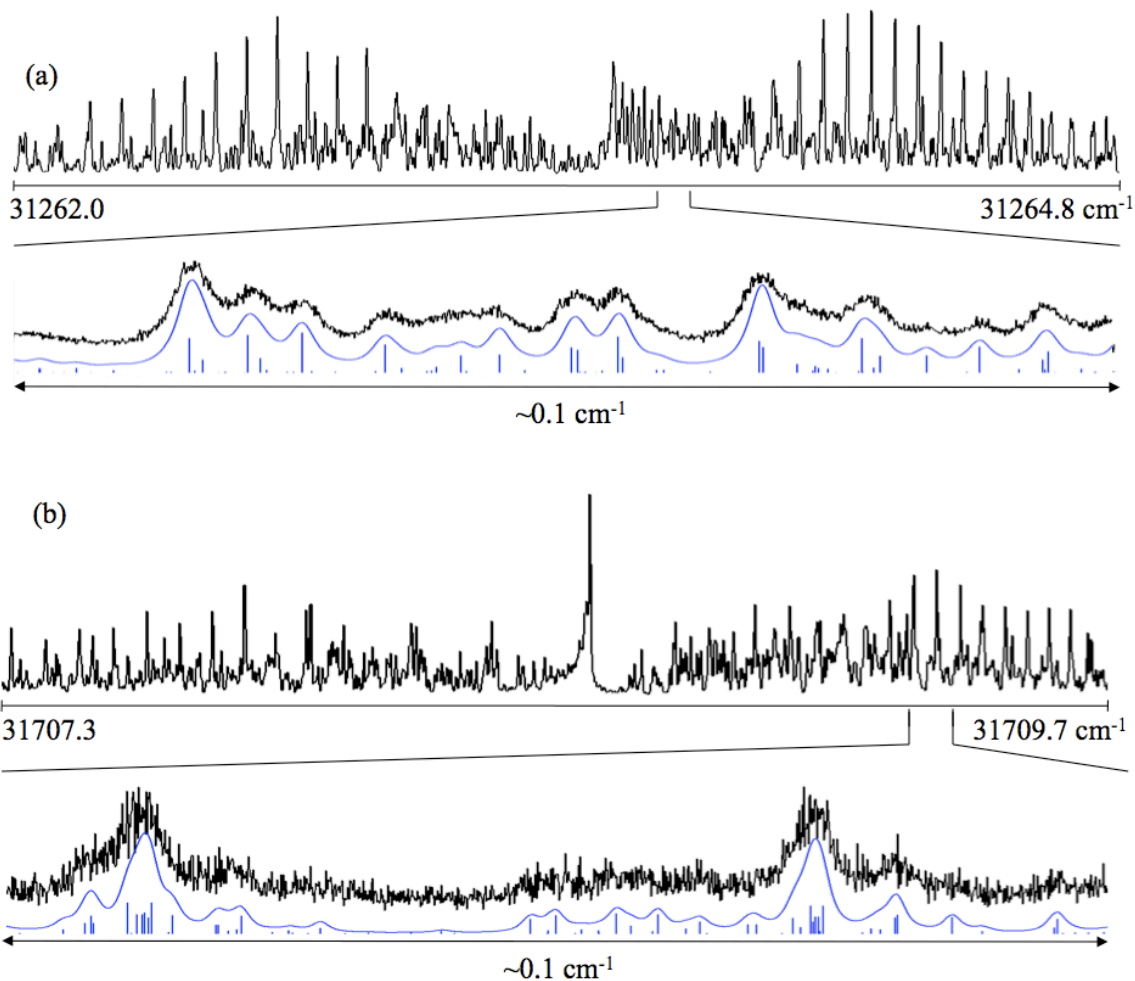


Figure C.2. (a) Field-free origin band spectrum of 2ABN, occurring at 31263.5 cm⁻¹. The bottom panel shows a comparison of a small portion of the experimental spectrum (black trace) with two simulated spectra (blue trace), with and without a convoluted lineshape function. (b) Field-free origin band spectrum of 3ABN, occurring at 31708.6 cm⁻¹. The bottom panel shows a comparison of a small portion of the experimental spectrum (black trace) with two simulated spectra (blue trace), with and without a convoluted lineshape function.

Table C.1. Experimental inertial parameters of 2ABN and 3ABN. Theoretical values calculated using the MP2/6-31G and CIS/6-31G** methods also have been included for comparison.**

	2ABN			3ABN		
	Experiment	Theory	Error (%)	Experiment	Theory	Error (%)
S₀						
A (MHz)	3009.0 (1)	2992.5	0.5	3372.7 (1)	3366.3	0.2
B (MHz)	1509.0 (1)	1499.1	0.6	1209.9 (1)	1201.1	0.7
C (MHz)	1005.2 (1)	999.8	0.5	890.8 (1)	886.0	0.5
ΔI (amu \AA^2)	-0.10	-0.52		-0.22	-0.50	
S₁						
A (MHz)	3093.8 (2)	3085.6	0.3	3373.6 (1)	3435.1	1.8
B (MHz)	1464.4 (1)	1488.1	1.6	1189.4 (1)	1201.0	1.0
C (MHz)	994.1 (1)	1003.9	1.0	879.5 (1)	890.0	1.2
ΔI (amu \AA^2)	-0.08	0.02		-0.08	-0.10	
<i>a/b/c</i>	45/55/0			25/75/0		
Origin(cm ⁻¹)	31263.5			31708.6		

Figure C.3 shows the spectrum of 2ABN in the presence of an electric field of 950 V/cm. To simulate the behavior of the spectrum in the presence of an applied electric field, a special program¹⁶ was used, in conjunction with jb95. This program carries out exact diagonalizations of truncated matrices and uses the following Hamiltonian:

$$\hat{H} = \hat{H}_r + \hat{H}_e \quad (\text{C.1})$$

The first term, \hat{H}_r , is the rigid-rotor Hamiltonian,

$$\hat{H}_r = AJ_a^2 + BJ_b^2 + CJ_c^2 \quad (\text{C.2})$$

and \hat{H}_e is the Stark Hamiltonian,

$$\hat{H}_e = -E_Z \sum_{g=a,b,c} \mu_g \phi_{Z_g} \quad (\text{C.3})$$

Here, A , B and C are the rotational constants; J_a , J_b and J_c are the projections of the angular momentum on the a , b and c inertial axes, E_Z represents the electric field applied along the Z axis, μ_a , μ_b and μ_c are the dipole moment components along each inertial axis, and ϕ represents the direction cosines relating the lab and molecular frames. Other details have been described previously.¹⁶ Application of an electric field causes transitions observed in the field-free spectrum to split and shift in frequency, as is apparent from eq C.3. The magnitudes of these shifts depend on both the field strength and dipole moment values.

By tracking the shifts of the spectral transitions in the presence of the external electric field, values of the dipole moment components of 2ABN were determined for both the ground and excited states. First, μ_a , μ_b and μ_c were estimated using *ab initio* methods, and an initial simulation of the overall spectrum was created. The components were then varied until the simulation resembled the experimental spectrum. Next, lines were assigned, paying particular attention to those transitions that were most sensitive to the dipole moment components. The positions of P- and R-branch lines with high K values, particularly those equal or nearly equal to J , are especially sensitive to μ_a ; the positions of the lines with $K_a = 0$ are especially sensitive to μ_c ; and the positions of Q-branch lines are sensitive to all three dipole moment components, especially μ_b . The assigned transitions were then fit and used to create a new simulation, and the process was iterated until the simulation was in good agreement with the experiment. An example of the fit for 2ABN is shown in the lower portion of Fig. C.3. Typical OMC values of these fits are ~ 6 MHz, substantially less than the linewidth.

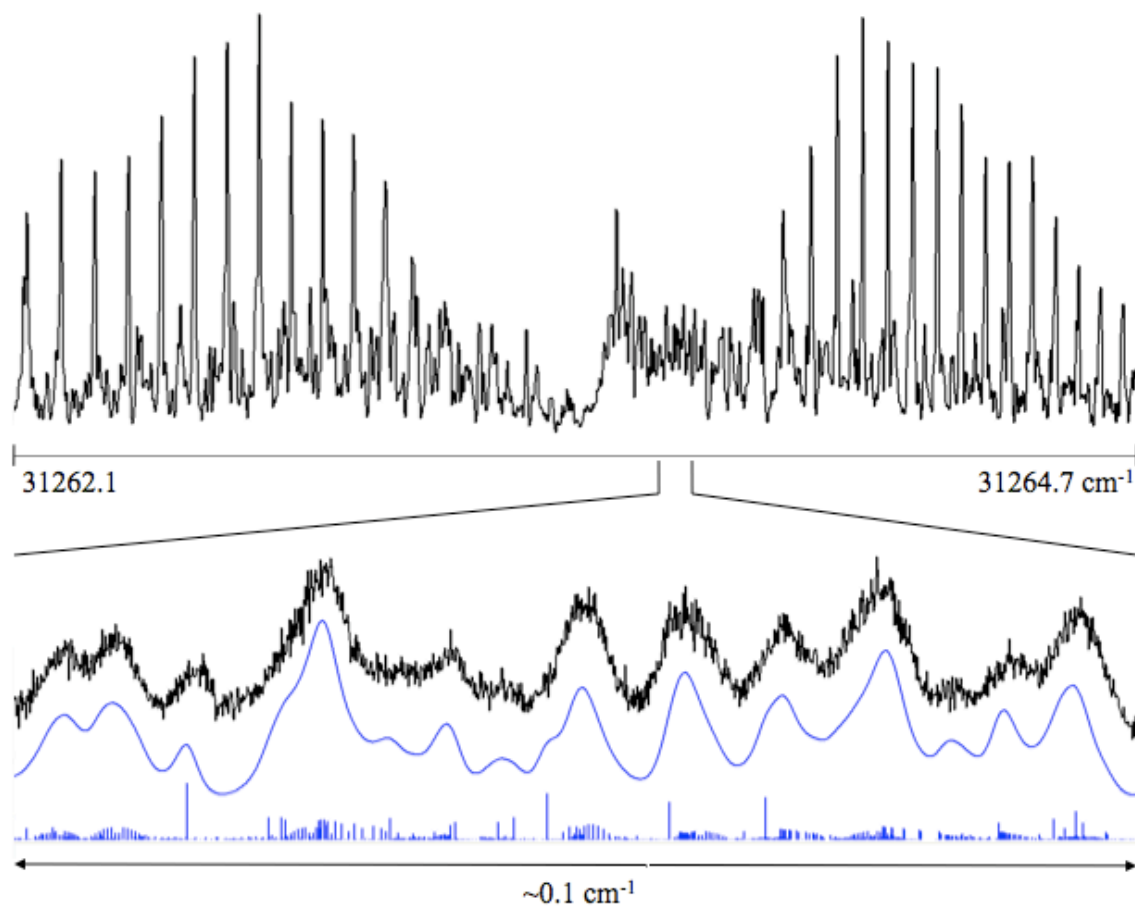


Figure C.3. Origin band spectrum of 2ABN, in presence of an electric field of 950 V/cm. The top panel shows the entire spectrum, and the bottom panel shows a comparison of a portion of the experimental spectrum (black trace) with two simulated spectra (blue trace), with and without a convoluted lineshape function.

Spectra of 3ABN taken with an applied electric field were fit in a manner similar to those of 2ABN, see Figure C.4. Relative to 2ABN, the spectra of 3ABN were somewhat noisier, and the fits were characterized by slightly larger OMC values (12 MHz or less). Still, it proved possible to extract relatively precise values of μ in both electronic states of each molecule based on fits of their Stark spectra at five different field strengths.

Table C.2 lists the derived values of μ that were obtained in this work. We note here that $\Delta\mu = \mu(S_1) - \mu(S_0)$ is relatively large for 3ABN and relatively small for 2ABN. We also note that the agreement between theory and experiment is poor, for both molecules in both electronic states. Differences in the values of μ_c are anticipated (see below). But the remaining calculated dipole moment components differ from the measured ones by as much as 50%. Clearly, 6-31G** methods are inadequate to the task of predicting accurate values of the permanent electric dipole moments of isolated large molecules. (Abd El Rahim, *et al.*⁹ have reported improved values using larger basis sets.) Despite this fact, the discrepancies between the measured and calculated values are not large enough to explain the “anomalous” electric deflection behavior of the three aminobenzonitriles.⁹

Both theory and experiment agree that the ABN's have pyramidal NH₂ groups, especially in their ground electronic states, necessitating non-zero values of μ_c . But this localized structure is just one well of the double minimum potential along this coordinate; the inverted structure has a value of μ_c that has the same magnitude but is opposite in sign. Ground state values of μ_c less than 0.1 D are required by our fits of the Stark behavior in ABN's. Since the calculated values are much larger than this (cf., Table C.2),

we conclude that motion along this coordinate is fast, compared to the frequency of rotational motion. A similar effect occurs in aniline, where the ground-state inversion barrier is of order 550 cm^{-1} .^{16, 21, 22}

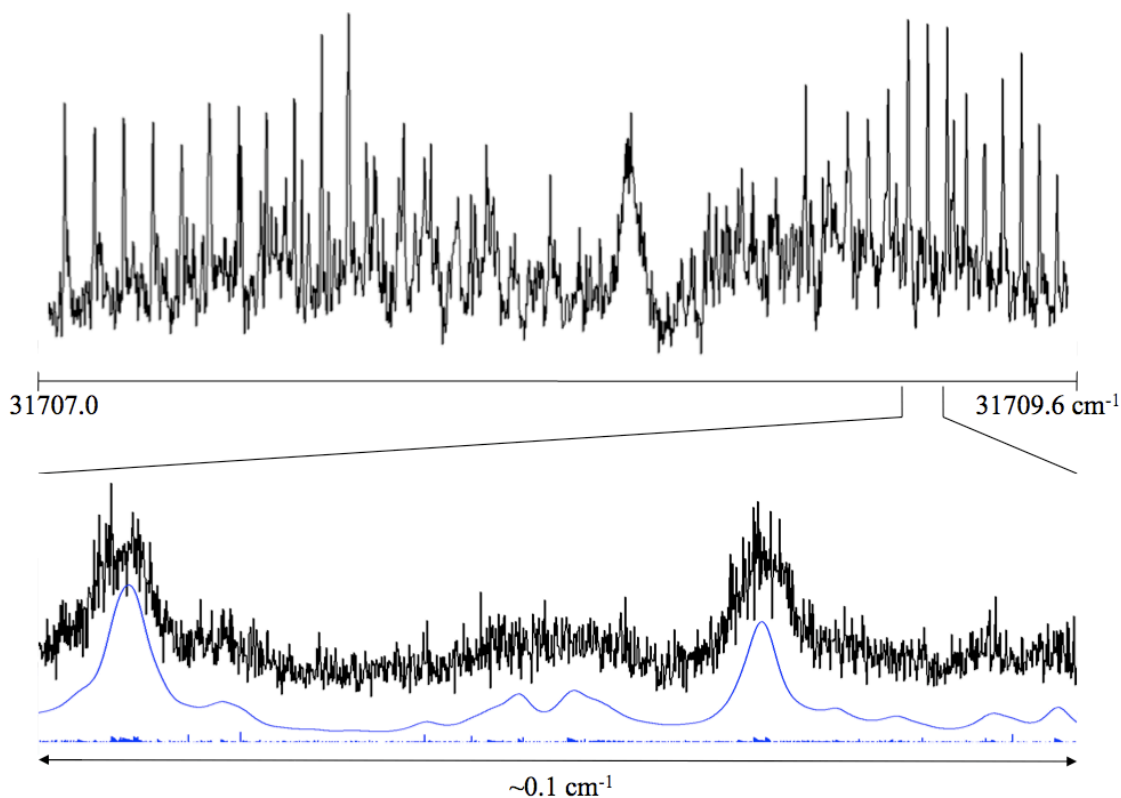


Figure C.4. Origin band spectrum of 3ABN, in presence of an electric field of 950 V/cm. The top panel shows the entire spectrum, and the bottom panel shows a comparison of a portion the experimental spectrum (black trace) with two simulated spectra (blue trace), with and without a convoluted lineshape function.

Table C.2. Experimental dipole moment values of 2ABN and 3ABN. Theoretical values calculated using the MP2/6-31G and CIS/6-31G** methods also have been included for comparison.**

	2ABN			3ABN		
	Experiment	Theory	Error (%)	Experiment	Theory	Error (%)
S₀						
μ_a (D)	3.6 (1)	3.4	6	4.8 (3)	5.1	6
μ_b (D)	1.9 (2)	1.7	10	1.2 (4)	0.6	50
μ_c (D)	0.0 (1)	1.1	-	0.0 (1)	1.2	-
μ (D)	4.1 (2)	4.0	2	4.9 (4)	5.3	8
$\theta, a/b$ (°)	28	27		14	7	
S₁						
μ_a (D)	3.4 (2)	3.9	15	6.8 (3)	8.1	19
μ_b (D)	3.4 (2)	3.5	3	0.0 (4)	-0.4	-
μ_c (D)	0.0 (1)	0.0	0	0.0 (1)	0.0	0
μ (D)	4.8 (3)	5.2	8	6.8 (3)	8.1	19
$\theta, a/b$ (°)	45	42		0	3	

C.5 DISCUSSION

Both 2ABN and 3ABN consist of a benzene ring to which amino (-NH₂) and nitrile (-CN) substituents are attached. But the different relative placement of these substituents has several consequences for their spectra. Moving the amino group from the 2- to the 3-position changes the orientation of the inertial axes and, consequently, the group's placement relative to the axis system of the molecule; see Figure C.5. In 2ABN, the amino group lies closest to the *b*-axis, but in 3ABN, the amino group lies closest to the *a*-axis. The difference in the location of the axes is apparent on comparison of the ground-state rotational constants, given in Table C.1. In 2ABN, the substituents are on opposite

sides of the a -axis, whereas in 3ABN the substituents are on opposite sides of the b -axis. Therefore, 2ABN has the smaller value of A , whereas 3ABN has the smaller value of B . Overall, 2ABN has a more compact shape, resulting in a larger value of C .

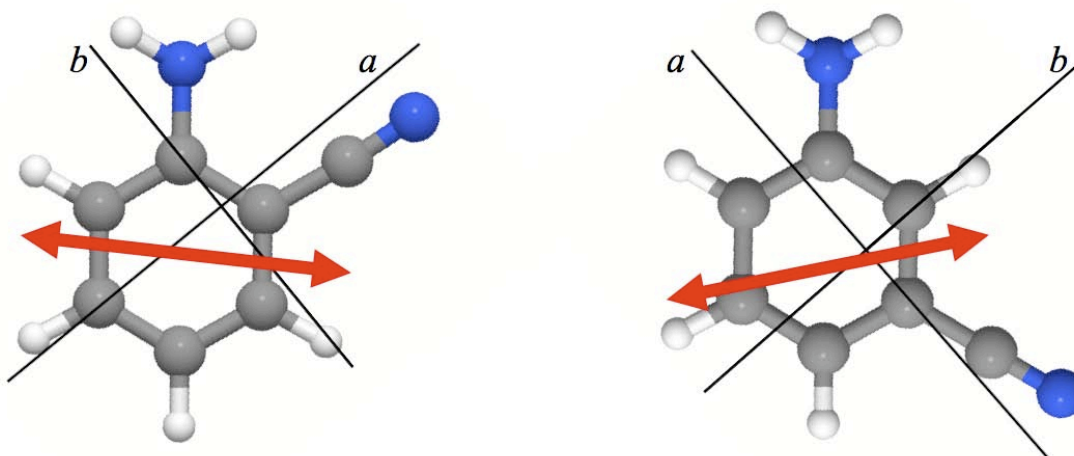


Figure C.5. Structures of 2ABN and 3ABN with the a and b inertial axes shown for reference. The red arrows represent the predicted transition moment orientations.

The appearances of the fully resolved electronic spectra of 2ABN and 3ABN also are quite different (Figure C.3). The spectrum of 2ABN (45/55, a/b) has much more a -character than that of 3ABN (25/75, a/b); their transition moment (TM) orientations must be very different. Thus, it is possible that the electronic structures of the two molecules are quite different. Alternatively, it may be that these differences are more simply explained by differences in the orientations of their respective inertial axes.

CIS/6-31G** calculations²⁰ were performed to address this issue. Figure C.6 summarizes the results for aniline (AN), benzonitrile (BN), and the two aminobenzonitriles, 2ABN and 3ABN. Comparisons of the molecular orbitals (MOs) of

the four molecules show that the highest occupied molecular orbital (HOMO) and HOMO-1 orbitals of 2ABN and 3ABN are very similar to those of AN. (There is some delocalization of charge onto the -CN substituent in the ABN's). Their lowest unoccupied molecular orbital (LUMO) and LUMO+1 orbitals are similar to those of both

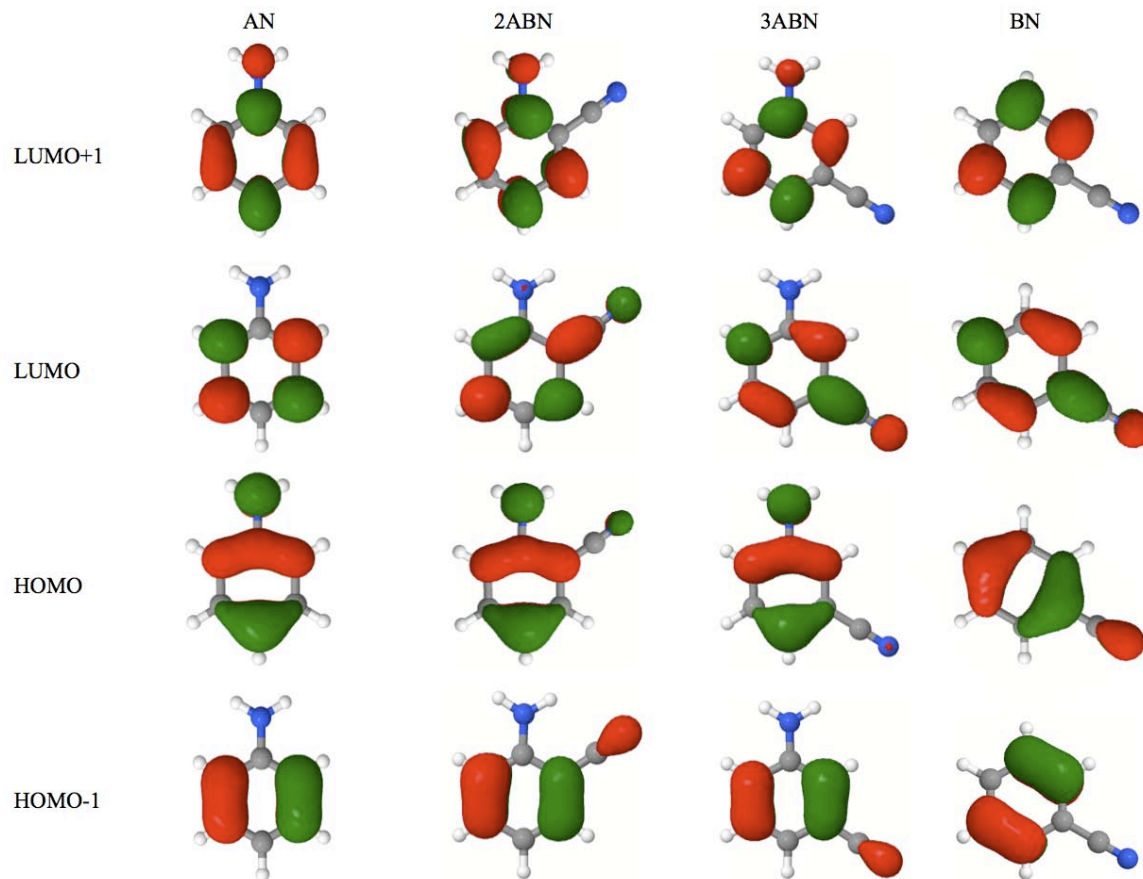


Figure C.6. HOMO-1 (ϕ_2), HOMO (ϕ_3), LUMO (ϕ_4), and LUMO+1 (ϕ_5) molecular orbitals of AN, 2ABN, 3ABN, and BN as predicted by CIS/6-31G calculations.**

AN and BN but bear a closer resemblance to those of BN. Both AN and BN display *b*-type spectra.^{9,15} In CIS, the S_1 state of AN is represented by the linear combination $\Psi(S_1) = 0.28 (\phi_2\phi_5) + 0.64 (\phi_3\phi_4)$, whereas the S_1 state of BN is represented by the linear

combination $\Psi(S_1) = 0.55 (\phi_2\phi_4) + 0.41 (\phi_3\phi_5)$. Similar calculations for the two ABN's yield the results $\Psi(S_1) = 0.19 (\phi_2\phi_5) + 0.67 (\phi_3\phi_4)$ for 2ABN and $\Psi(S_1) = 0.21 (\phi_2\phi_5) + 0.66 (\phi_3\phi_4)$ for 3ABN. Thus, the $-\text{NH}_2$ group dominates in both cases; the S_1 - S_0 TMs take up orientations that are perpendicular to the amino group, and these orientations differ between the two molecules because of the difference in the orientations of their inertial axes; see Figure C.5. Thus, the electronic structures of both 2ABN and 3ABN are very similar, when viewed in this way.

Permanent dipole moments are more sensitive measures of the charge distributions in the two molecules and how these change when the photon is absorbed. Parts a and b of Figure C.7 give visual images of these changes. Amino groups and cyano groups attached to an aromatic ring are electron donating and electron withdrawing, respectively. Thus, to a first approximation, the measured dipole moments of the two ABNs would be expected to be equal to the vector sums of the two substituent dipoles, $-\text{NH}_2$ and $-\text{CN}$, at least in the ground electronic state. This prediction was tested by forming the vector sums of the two dipoles using the measured dipole moments of AN^{16} and BN^{10} and the *ab initio* geometries of the two ABNs; the results are shown in Table C.3. 2ABN has a predicted dipole moment of 4.0 D, compared to the measured value of 4.1 D; the resultant dipole vector makes a smaller angle with *a* than with *b* ($\mu_a/\mu_b \sim 1.9$). 3ABN has a predicted dipole moment of 5.1 D compared to the measured value

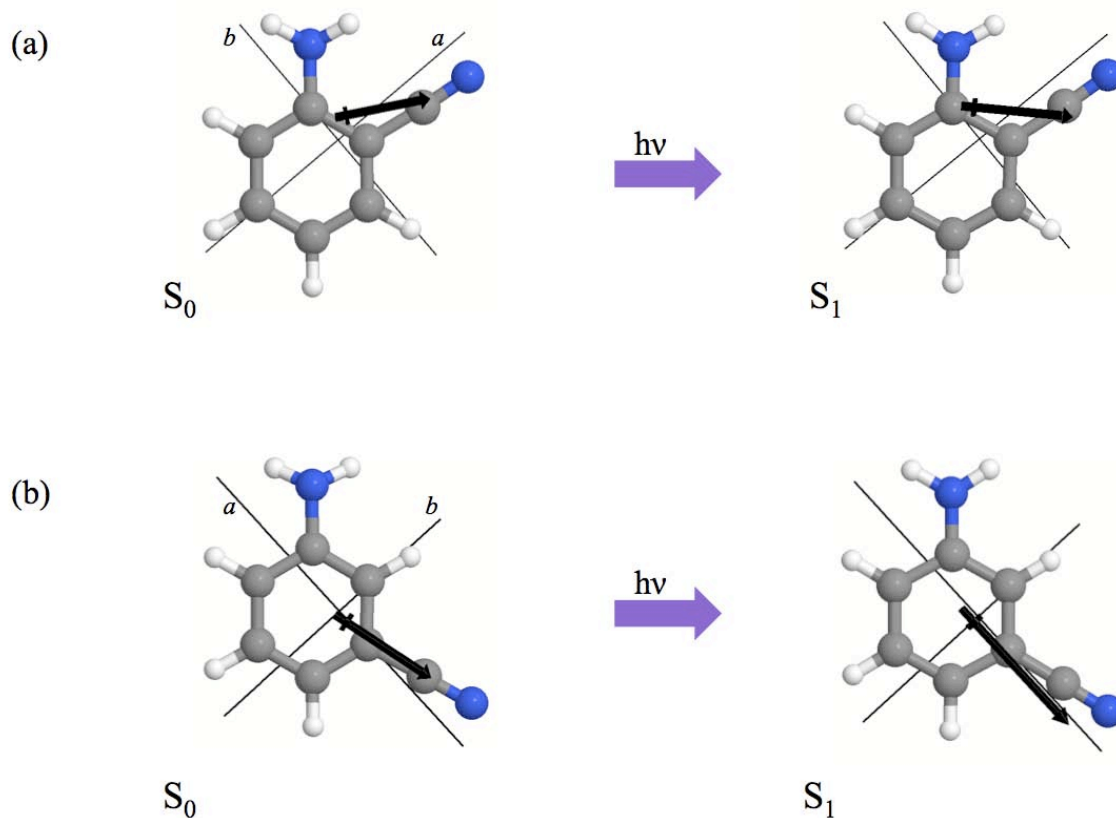


Figure C.7. Measured dipole moments are shown on the structures of 2ABN (a) and 3ABN (b) in both the ground and excited electronic states.

of 4.9 D; the resultant dipole vector makes an even smaller angle with a than with b ($\mu_a/\mu_b \sim 4$). Thus, to a reasonable approximation, the dipole moments of 2ABN and 3ABN are the vector sums of the two component dipoles, in the ground electronic state. A similar conclusion has been reached for 4ABN.¹⁰

Table C.3. Predicted and measured dipole moments of 2ABN and 3ABN, compared to the previously measured values for AN, BN, and 4ABN, based on the vector addition model.

	AN ¹⁶	BN ¹⁰	2ABN		3ABN		4ABN ¹⁰	
			Predicted	Measured	Predicted	Measured	Predicted	Measured
S₀								
μ_a (D)	1.13	4.48	3.7	3.6 (1)	5.1	4.8 (3)	5.61	6.41 (3)
μ_b (D)	0.00	0.00	1.6	1.9 (2)	0.7	1.2 (4)	0.00	0.00
μ (D)	1.13	4.48	4.0	4.1 (2)	5.1	4.9 (4)	5.61	6.41 (3)
S₁								
μ_a (D)	2.80	4.57	2.6	3.4 (2)	6.5	6.8 (3)	7.37	7.20 (3)
μ_b (D)	0.00	0.00	2.6	3.4 (2)	-0.6	0.0 (4)	0.00	0.00
μ (D)	2.80	4.57	3.7	4.8 (3)	6.5	6.8 (3)	7.37	7.20 (3)

Excitation of both molecules to their S₁ states leads to large increases in both the magnitudes and orientations of their dipole moment vectors. In 2ABN, the increase in the magnitude of μ (4.8 D in the S₁ state) is caused by large increase in μ_b and a small decrease in μ_a , effects that are nicely captured by the vector addition model. The -NH₂ group is a stronger donor, and the -CN group is a stronger acceptor, in the S₁ state. In 3ABN, owing to the aforementioned change in the inertial axes, the larger value of μ (6.8 D in the S₁ state) is caused by a large increase in μ_a and a small decrease in μ_b , again reflecting the stronger electron donor/acceptor character of the -NH₂/-CN groups. More striking is the change in orientation of the dipole moment vectors; these change by +/- 15° when the photon is absorbed. Large solvatochromic shifts of the fluorescence spectra of both molecules would be expected in the condensed phase.²³

Deviations from the “additivity rule” are most pronounced for the S₀ state of 3ABN, where the predicted value is high, and for the S₁ state of 2ABN, where the predicted value is low. These effects may be traced to the MOs of the two molecules

shown in Figure C.6. As noted, although similar to the orbitals of AN and BN, the HOMO and HOMO-1 orbitals of the ABNs more closely resemble those of AN, whereas the LUMO and LUMO+1 orbitals bear a stronger resemblance to BN. Hence, it is reasonable that the dipole moment components are not strictly additive across the entire series of molecules.

Previous attempts to measure the permanent electric dipole moments of the three structural isomers of ABN by molecular beam deflection methods have led to ambiguous results.⁹ Increasing deviations of the measured deflections compared to Stark-effect calculations were observed in the series 4ABN, 3ABN, and 2ABN. These deviations were attributed to the increasing asymmetry of the molecules across the series. To support this view, it was shown by first-principles calculations that the Stark-split energy levels of asymmetric tops begin to repel each other at high fields. These level repulsions lead to a mixing of rotational energy levels and a reduced energy shifting of the eigenvalues as the electric field is increased. That large molecules (whether asymmetric or not) excited to a single ro-vibrational eigenstate are not deflected by an inhomogeneous electric field in a high density-of-states region was earlier established by the elegant infrared experiments of Fraser and Pate,¹¹ so the results of Abd El Rahim *et al.*⁹ are not surprising.

Although the ABNs are certainly asymmetric (the κ values of 2ABN, 3ABN and 4ABN in their electronic ground state are -0.50, -0.74, and -0.94), their Stark-split energy levels are not dominated by avoided crossings at *low* field. This is shown explicitly for 2ABN in Figure C.8. In fields up to 5 kV/cm, only three avoided crossings appear in the plots of state energy versus field at low J . Even fewer appear at higher J , at low field

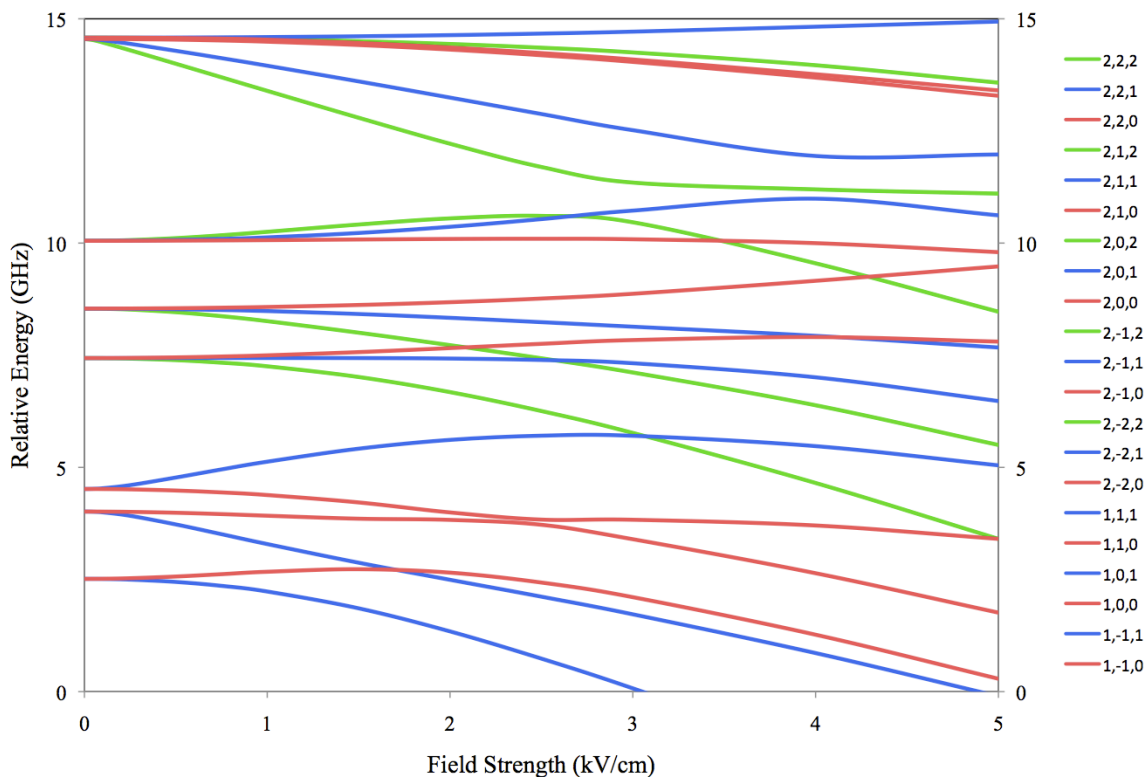


Figure C.8. Stark-splitting energy level diagram for the ground state $J = 1$ and 2 rotational levels of 2ABN as a function of electric field. The simulation was run with the experimentally determined rotational constants and dipole moments. The labels on the right designate the J , τ , and M values of the represented levels.

strengths. Thus, the energy levels of both symmetric and asymmetric rotors are *regular*, not irregular, at low field strengths. Higher field strengths do lead to extensive level mixing, forming the basis for a number of creative applications, including studies of the dynamics of molecules in aligned rotational states (“pendular” states)²⁴ and the spatial separations of the structural isomers of neutral molecules according to their mass-to-dipole-moment ratios.²⁵ But, as the present application shows, lower field strengths are also useful. Selective excitation of the Stark-split spectra of large molecules leads to an unambiguous determination of the magnitude and orientation of their permanent dipole moments in different electronic states. Further experiments will exploit this fact in

studies of the charge distributions of biologically relevant molecules in the gas phase and how they are affected by the absorption of light.

C.6 ACKNOWLEDGEMENTS

This work was supported by NSF (CHE-0615755). We thank A. J. Fleisher and R. A. Christie for assistance and useful discussions, D. F. Plusquellic for helping with Figure 8, and the Center for Molecular and Material Simulations at the University of Pittsburgh for computing time. We also are especially grateful to Robert Zalesny from the Wrocław University of Technology for advice on the dipole moment calculations.

C.7 REFERENCES

1. J. M. Berg, J. L. Tymoczko, and L. Stryer, *Biochemistry* (6e), W. H. Freeman and Co., San Francisco, **2006**
2. G. G. Tartaglia, A. Cavalli, R. Pellarin, and A. Caflisch, *Protein Sci.* **2004**, *13*, 1939
3. R. D. Brown, P.D. Godfrey, J. W. V. Stovey, and M. –P. Bassez, *J.C.S. Chem. Comm.* **1978**, 547; B. Vogelsanger, P. D. Godfrey, and R. D. Brown, *J. Am. Chem. Soc.* **1991**, *113*, 7864; P. D. Godfrey, S. Firth, L. D. Hatherley, R. D. Brown, and A. P. Pierlot, *J. Am. Chem. Soc.* **1993**, *115*, 9867
4. See, for example, M. E. Sanz, A. Lesari, M. I. Peña, V. Vaquero, V. Cortijo, J. C. Lopez, and J. L. Alonso, *J. Am. Chem. Soc.* **2006**, *128*, 3812.
5. See, for example, E. Gloaguen, F. Pagliarulo, V. Breuner, W. Chin, F. PiuZZi, B. Tardivel, and M. Mons, *Phys. Chem. Chem. Phys.* **2007**, *9*, 4491
6. I. Compagnon, F. C. Hagemester, R. Antoine, D. Rayane, M. Broyer, P. Dugourd, R. R. Hudgins, and M. F. Jarrold, *J. Am. Chem. Soc.* **2001**, *123*, 8440.
7. R. Antoine, I. Compagnon, D. Rayane, M. Broyer, P. Dugourd, G. Breaux, F. C. Hagemester, D. Pippen, R. R. Hudgins, and M. F. Jarrold, *J. Am. Chem. Soc.* **2002**, *124*, 6737.
8. P. Dugourd, R. Antoine, G. Breaux, M. Broyer, and M. F. Jarrold, *J. Am. Chem. Soc.* **2005**, *127*, 4675.
9. M. Abd El Rahim, R. Antoine, M. Broyer, D. Rayane, and P. Dugourd, *J. Phys. Chem. A*, **2005**, *109*, 8507.
10. D. R. Borst, T. M. Korter, and D. W. Pratt, *Chem. Phys. Letters*, **2001**, *350*, 485.
11. G. T. Fraser and B. H. Pate, *J. Chem. Phys.* **1994**, *100*, 6210, and references therein, especially R. G. J. Fraser, *Molecular Beams*, Methuen and Co, London, **1937**.
12. W. A. Majewski, J. F. Pfanstiel, D. F. Plusquellic and D. W. Pratt, in *Laser Techniques in Chemistry*, A. B. Myers and T. R. Rizzo, Eds. J. Wiley & Sons, New York, **1995**.
13. D. M. Miller, Ph. D. Thesis, University of Pittsburgh, **2009**.
14. D. F. Plusquellic, Thesis, University of Pittsburgh, **1992**.

15. D. F. Plusquellic, R. D. Suenram, B. Maté, J. O. Jensen and A. C. Samuels, *J. Chem. Phys.* **2001**, *115*, 3057.
16. T. M. Korter, D. R. Borst, C. J. Butler and D. W. Pratt, *J. Am. Chem. Soc.* **2001**, *123*, 96.
17. P. Kolek, K. Pirowska and J. Najbar. *Phys. Chem. Chem. Phys.* **2001**, *3*, 4874.
18. R. Howell, E. M. Joslin, A. G. Taylor and D. Phillips, *J. Chem. Soc., Faraday Trans.* **1992**, *88*, 1605.
19. G. Herzberg, *Electronic Spectra of Polyatomic Molecules*, D. van Nostrand, Princeton, 1966.
20. Gaussian 03, Revision 6.0, M. J. Frisch, G. W. Trucks, H. B. Schlegel, G. E. Scuseria, M. A. Robb, J. R. Cheeseman, J. A. Montgomery, Jr., T. Vreven, K. N. Kudin, J. C. Burant, J. M. Millam, S. S. Iyengar, J. Tomasi, V. Barone, B. Mennucci, M. Cossi, G. Scalmani, N. Rega, G. A. Petersson, H. Nakatsuji, M. Hada, M. Ehara, K. Toyota, R. Fukuda, J. Hasegawa, M. Ishida, T. Nakajima, Y. Honda, O. Kitao, H. Nakai, M. Klene, X. Li, J. E. Knox, H. P. Hratchian, J. B. Cross, V. Bakken, C. Adamo, J. Jaramillo, R. Gomperts, R. E. Stratmann, O. Yazyev, A. J. Austin, R. Cammi, C. Pomelli, J. W. Ochterski, P. Y. Ayala, K. Morokuma, G. A. Voth, P. Salvador, J. J. Dannenberg, V. G. Zakrzewski, S. Dapprich, A. D. Daniels, M. C. Strain, O. Farkas, D. K. Malick, A. D. Rabuck, K. Raghavachari, J. B. Foresman, J. V. Ortiz, Q. Cui, A. G. Baboul, S. Clifford, J. Cioslowski, B. B. Stefanov, G. Liu, A. Liashenko, P. Piskorz, I. Komaromi, R. L. Martin, D. J. Fox, T. Keith, M. A. Al-Laham, C. Y. Peng, A. Nanayakkara, M. Challacombe, P. M. W. Gill, B. Johnson, W. Chen, M. W. Wong, C. Gonzalez, and J. A. Pople, Gaussian, Inc., Wallingford CT, 2004.
21. A non-zero value of μ_c would also connect the even and odd symmetry levels of an inverting molecule, producing additional Stark shifts in the spectra (Ref. 22). However, given the anticipated large separation of these levels, and an experimental resolution, we consider this unlikely.
22. W. Gordy and R. L. Cook, *Microwave Molecular Spectra*, J. Wiley and Sons, New York, 1984.
23. S. Jiang and D. H. Levy, *J. Phys. Chem. A* **2003**, *107*, 6785.
24. B. Friedrich and D. R. Herschbach, *Nature* **1991**, *353*, 412.
25. F. Filsinger, U. Erlekam, G. Von Helden, J. Kuepper, and G. Meijer, *Phys. Rev. Lett.* **2008**, *100*, 13303.

APPENDIX D

CHARGE TRANSFER BY ELECTRONIC EXCITATION: DIRECT MEASUREMENT BY HIGH RESOLUTION SPECTROSCOPY IN THE GAS PHASE.

Adam J. Fleisher, Philip J. Morgan and David W. Pratt

Department of Chemistry, University of Pittsburgh
Pittsburgh, PA 15260 USA

Parts of this work was published in *J. Phys. Chem.* **131** (2009) 211101.

A. J. Fleisher and P. J. Morgan performed the experimental measurements; A. J. Fleisher analyzed the spectra and wrote the paper.

D.1 ABSTRACT

We report a quantitative measurement of the amount of charge that is transferred when the single ammonia complex of the photoacid β -naphthol (2HNA) is excited by light. The measurement was made by comparing the permanent electric dipole moments of *cis*-2HNA in its ground (S_0) and excited (S_1) states, determined by Stark-effect studies of its fully resolved $S_1 \leftarrow S_0$ electronic spectrum. While the increase in electron transfer from the donor (NH_3) to the acceptor (2HN) upon excitation is small ($\sim 0.05 e$), it is sufficient to red-shift the electronic spectrum of the complex by $\sim 600 \text{ cm}^{-1}$ ($\sim 0.1 \text{ eV}$). Thereby explored is the incipient motion of the acid-base complex along the excited state (electron-coupled) proton transfer coordinate.

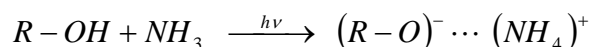
D.2 INTRODUCTION

The electronic structure of isolated molecules is of paramount importance to their chemical behavior. Organic molecules must communicate efficiently with a variety of other entities to create a working biological system. The most important building blocks of life, including nucleic acids,¹⁻⁵ the amino acids that form proteins,^{6,7} and light harvesting chromophores comprising photosynthetic systems⁸⁻¹⁰ cannot function without charge transfer (CT) processes. Complex systems such as membrane ion pumps, molecular wires, and bulk solvent systems all require organized charge motion along specific intra- and intermolecular coordinates.¹¹ In the field of nonlinear optics, CT states

in organometallic systems often have large hyperpolarizabilities, and therefore important second-order optical properties essential for various materials science applications.^{12,13}

Several experimental techniques have been used to directly observe CT in molecular systems. These include optical absorption and emission spectroscopy,^{14,15} laser induced fluorescence (LIF) spectroscopy in a collision-free supersonic expansion,¹⁶⁻¹⁹ resonance enhanced multi-photon ionization,²⁰ optical Stark spectroscopy,²¹ argon predissociation spectroscopy and other infrared spectroscopies,²²⁻²⁴ time resolved microwave conductivity,^{25,26} and Fourier transform microwave spectroscopy.²⁷⁻³⁰ Resonance techniques are capable of analyzing electron spin effects when free radicals form (*via* EPR),³¹ and also of interpreting changes in proton and carbon-13 chemical shifts as the local electronic environment with which they interact evolves (*via* NMR).³² Several electrochemical methods are relevant in extreme cases where charge transfer leads to ion formation, such as alternating current conductance titrations, cyclic voltammetry, and polarography.³³

Importantly, very few of these methods are capable of measuring the actual amount of charge transferred between the components parts of the studied molecular system, particularly in excited electronic states. Here, we demonstrate that this desirable objective can be achieved by comparing the permanent electric dipole moments (EDM's) of a solvent-solute cluster and its component parts before and after they are excited by light, to promote CT.



Our “proof-of-principle” experiment was performed on a single conformer of the 1:1 acid-base complex of β -naphthol and ammonia (*cis*-2HNA), using rotationally resolved

electronic Stark-effect spectroscopy in a molecular beam.^{34,35} Previous experiments¹⁹ have shown that this reaction occurs with unit efficiency in large clusters 2HNA_n , with $n \geq 4$. We thus explore the incipient motion along the excited state proton transfer coordinate.

D.3 EXPERIMENTAL

2HN was purchased from Sigma Aldrich and used without further purification. Rotationally resolved $S_1 \leftarrow S_0$ excitation experiments were performed in the collision-free environment of a molecular beam, described elsewhere.³⁶ Briefly, for the bare molecule spectra of both *cis*- and *trans*-2HN, the sample was heated to $\sim 150^\circ \text{C}$ in a quartz source, seeded in dry argon gas (>99% purity), and expanded through a 190 μm nozzle. The 1:1 *cis*-2HN ammonia complex (2HNA) was produced by seeding the sample in a stream of 3% ammonia in a dry argon gas. The expansion was skimmed ~ 2 cm downstream with a 1 mm diameter skimmer to form a molecular beam and then crossed 15 cm downstream of the nozzle with a laser beam operating in the UV. The laser radiation was generated by a modified continuous ring dye laser operating in the visible (DCM dye). The visible output of the dye laser was externally frequency doubled by a Spectra-Physics Wavetrain using a 655 nm LBO crystal, producing $\sim 500 \mu\text{W}$ of UV with a spectral resolution of ~ 1 MHz. Fluorescence was collected with spatially selective optics and detected by a photon counting system and a PMT. All spectra were recorded using the jba95 data acquisition software.³⁷ Typical scan lengths were 3 cm^{-1} over 2000-8000 sec. The I_2

absorption spectrum³⁸ was used to determine the absolute transition frequencies of the excitation spectra to an accuracy of ± 30 MHz. A stabilized etalon was used to produce relative frequency markers having a mode-matched free spectral range of 599.5040 ± 0.0005 MHz in the UV, corresponding to a free spectral range of 299.7520 ± 0.0005 MHz in the visible. The resulting field free spectra were fit using the jb95 least squares fitting program.³⁹

Stark spectra were recorded in analogous manner as the bare molecule and ammonia complex spectra, with exception of the collection optics. Within the spatially selective collection optics, two stainless steel wire grids, separated by ~ 1 cm, product the desired homogeneous electric field, where the point of orthogonal intersection of the laser and molecular beams is at its center.⁴⁰ This arrangement, with the electric field direction perpendicular to the laser polarization, forces a $\Delta M_J = \pm 1$ selection rule. The electric field strength was calibrated using the μ_a component of the ground state dipole moment of aniline, determined to be 1.129 D from microwave Stark experiments. A special program, integrated with jb95, was utilized in fitting applied-field Stark data.⁴¹ The Stark addition implements slide bars for each dipole moment component, for both ground and excited states, which allow for instantaneous changes in the simulated fits when a dipole moment component is changed manually.

Supplementing the experimental work, *ab initio* calculations at ground state MP2/6-31G** and excited-state CIS/6-31G** levels were performed by using the Gaussian 03⁴² suite of electronic structure programs on personal computers.

D.4 RESULTS

We report the rotationally resolved electronic spectra of the $S_1 \leftarrow S_0$ transitions in both *trans*- and *cis*-2HN, as well as *cis*-2HNA, in several homogeneous electric fields. For 2HN, previously determined rotational constants⁴³ were used in fitting field-free spectra, wherein over 200 transitions could be assigned. For *cis*-2HNA, previously determined rotational constants (*A* and *E* sub-bands) and torsion-rotation coupling constants (*E* sub-band)⁴⁴ were used in fitting field-free spectra. In the more complicated *cis*-2HNA spectra, approximately 50 transitions could be assigned in each sub-band. The same rotational constants, torsion-rotation coupling constants, and origin locations determined from these field-free spectra were used at the onset of fitting Stark spectra, and were not varied during the Stark fitting process.

The field-free spectra of *trans*-2HN and *cis*-2HN can be seen in Figures D.1 and D.2, respectively. The two bands were fit using rigid-rotor Hamiltonians for both the ground and excited states.⁴⁵ Both origin band spectra are hybrid bands, consisting of both *a*-type and *b*-type transitions, but dominated by the *b*-type transitions, indicating a transition moment located primarily along the *b*-inertial axis of both molecules. The linewidth of individual transitions within both spectra is ~33 MHz. The experimental spectra were simulated using a Voigt profile,⁴⁶ combining a Doppler-limited Gaussian linewidth of 27 MHz and a Lorentzian linewidth of 9 MHz.⁴³ The Lorentzian linewidth yields an estimated lifetime of ~ 17.7 ns for both *trans*- and *cis*-2HN. The inertial parameters are listed in Table D.1.

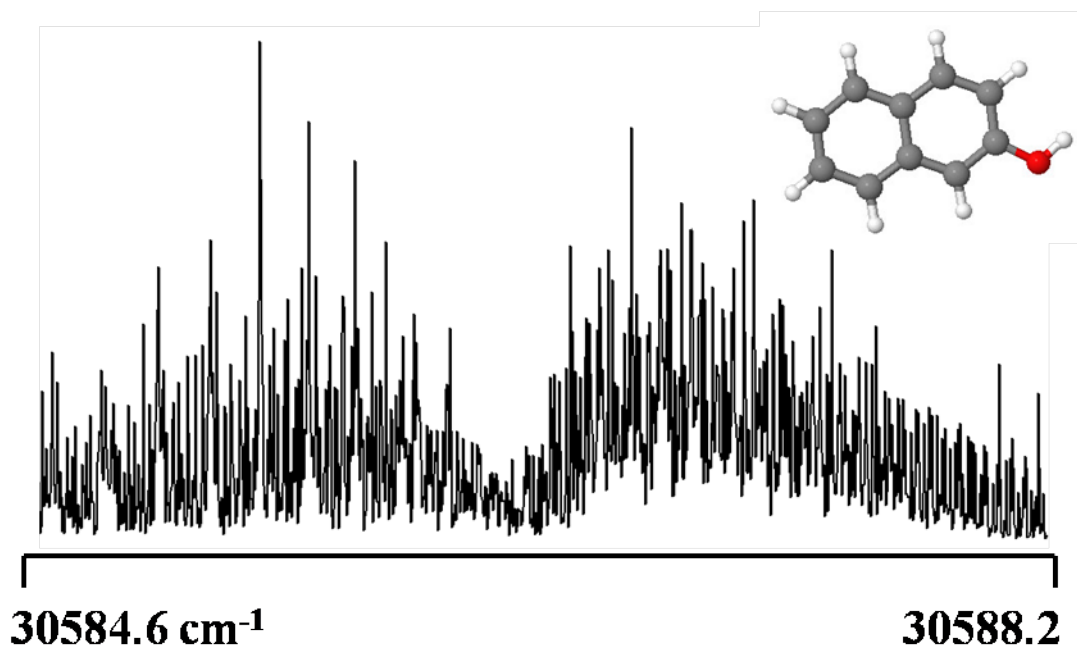


Figure D.1. Field-free rotationally resolved electronic spectrum of *trans*-2HN.

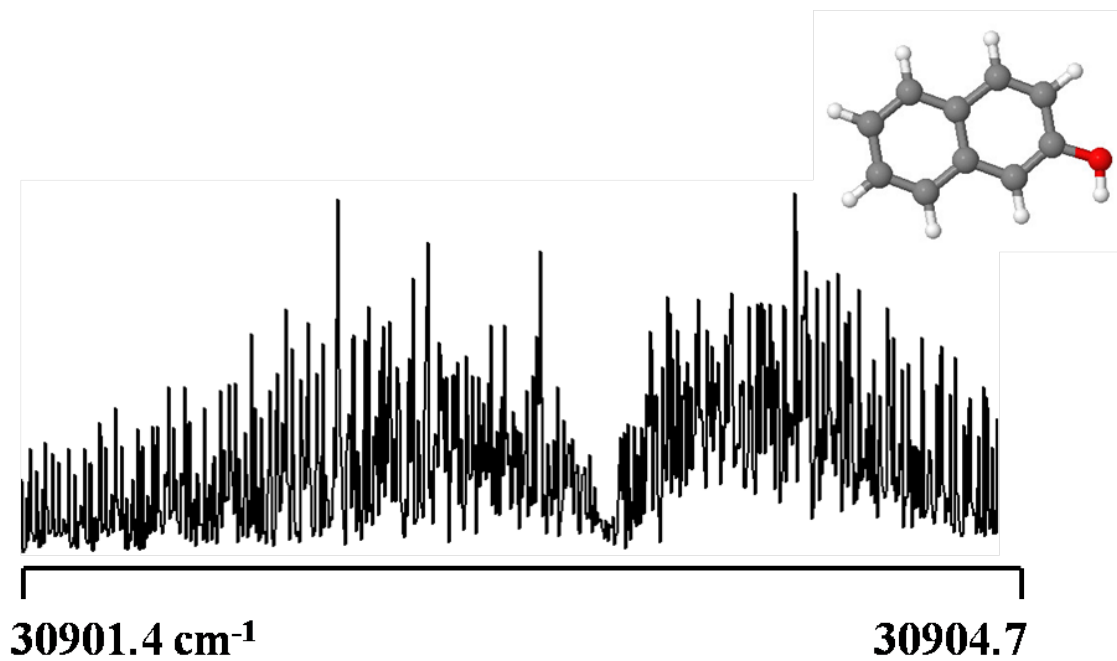


Figure D.2. Field-free rotationally resolved electronic spectrum of *cis*-2HN.

Table D.1. Inertial parameters obtained from fits of *trans*- and *cis*-2HN origin bands.

Parameters	Experimental		Theoretical	
	<i>trans</i> -2HN	<i>cis</i> -2HN	<i>trans</i> -2HN ^a	<i>cis</i> -2HN ^a
A" (MHz)	2845.3 (1)	2849.2 (1)	2841.1	2850.6
B" (MHz)	825.5 (1)	824.6 (1)	825.1	823.5
C" (MHz)	640.1 (1)	639.7 (1)	639.4	638.9
$\Delta I''$ (amu Å ²)	-0.291	-0.229	0.008	0.029
<hr/>				
A' (MHz)	2772.4 (1)	2769.0 (1)	2863.8	2859.8
B' (MHz)	822.7 (1)	821.7 (1)	825.7	825.0
C' (MHz)	634.7 (1)	633.9 (1)	640.9	640.3
$\Delta I'$ (amu Å ²)	-0.334	-0.300	0.013	-0.014
<hr/>				
Origin(cm ⁻¹)	30586.3	30903.3		
<i>a/b/c</i> type	8/92/0	17/83/0		

^aCalculations performed at the MP2/6-31G** and CIS/6-31G** levels of theory.

The field-free spectrum of *cis*-2HNA is shown in Figure D.3 with its inertial parameters listed in Table D.2. As mentioned before, both sub-bands were fit with previously reported values.⁴⁴ The two bands are observed due to the tunneling motion of the hydrogen bonded NH₃ group along its torsional coordinate. The detailed analysis of the *E* sub-band and its K-dependent splitting of the normally degenerate rovibronic transitions due to coupling by the torsion-rotation interaction is discussed elsewhere.⁴⁴ The differences in the rotational constants of the bare molecule and the complex can be used to determine the center-of-mass (COM) coordinates of the ammonia molecule in the principal axis frame of the bare molecule and complex frame, using Kraitchman's equations.⁴⁵ The assumption in this analysis is that complex formation does not change the structure of the isolated molecule.⁴⁷ This data is shown in Table D.3.

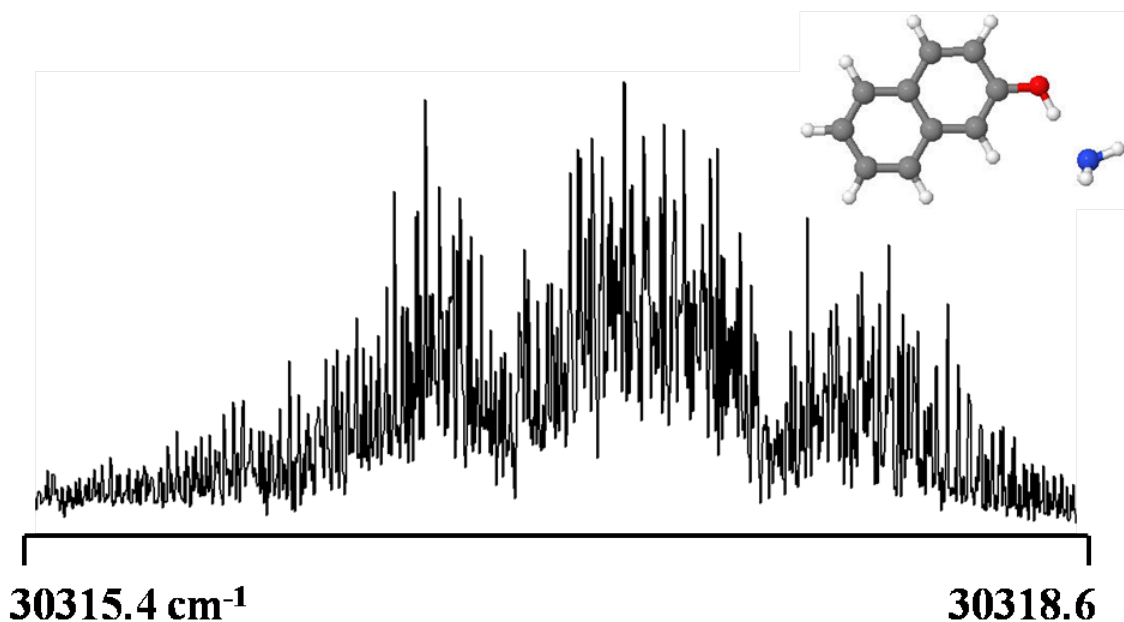


Figure D.3. Field-free rotationally resolved electronic spectrum of *cis*-2HNA.

Table D.2. Inertial parameters obtained from fits of 0_{a_1} and $1e$ bands of *cis*-2HNA.

Parameter	<i>cis</i> -2HNA 0_{a_1}	<i>cis</i> -2HNA $1e$
A'' (MHz)	1770.7 (1)	1763.8 (2)
B'' (MHz)	546.0 (1)	545.7 (1)
C'' (MHz)	417.7 (1)	417.9 (1)
$\Delta I''$ (amu \AA^2)	-0.950	-3.446
D _a '' (MHz)		1291.4 (5)
D _b '' (MHz)		489.4 (3)
A' (MHz)	1726.8 (1)	1720.9 (1)
B' (MHz)	554.8 (1)	554.4 (1)
C' (MHz)	420.4 (1)	420.6 (1)
$\Delta I'$ (amu \AA^2)	-1.309	-3.721
D _a ' (MHz)		920.9 (4)
D _b ' (MHz)		396.9 (3)
Origin(cm^{-1})	30317.7	30316.9

Table D.3. Experimentally determined location of ammonia, treated as a point mass of 17 amu, within the inertial frame of *cis*-2HN and *cis*-2HNA, respectively. The error in the ammonia position is limited by the accuracy in rotational constants (0.1 MHz).

	<i>cis</i> -2HN	<i>cis</i> -2HNA
S₀		
<i>x</i> (Å)	3.93 (2)	4.38 (2)
<i>y</i> (Å)	-3.48 (2)	-1.70 (2)
R _{CM}	5.25 (3)	4.70 (3)
S₁		
<i>x</i> (Å)	3.80 (2)	4.27 (2)
<i>y</i> (Å)	-3.48 (2)	-1.73 (2)
R _{CM}	5.16 (3)	4.61 (3)

Figure D.4 and D.5 show the spectra of *trans*- and *cis*-2HN in the presence of several applied electric fields. The program used to fit the experimental Stark spectra carries out an exact diagonalization of truncated matrices using the Hamiltonian for a system with no internal rotation.

$$\hat{H} = \hat{H}_r + \hat{H}_e \quad (\text{D.1})$$

The first term, \hat{H}_r , is the rigid rotor Hamiltonian,

$$\hat{H}_r = AP_a^2 + BP_b^2 + CP_c^2 \quad (\text{D.2})$$

where A , B , and C are the rotational constants, and P_a , P_b , and P_c are the projections of the total angular momentum on the respective inertial axes. The second term, \hat{H}_e , is the Stark Hamiltonian,

$$\hat{H}_e = -\boldsymbol{\mu} \cdot \boldsymbol{E} = -E_z \sum_{g=a,b,c} \mu_g \phi_{Zg} \quad (\text{D.3})$$

where E_z is the applied electric field along the space-fixed Z axis, μ_g ($g = a, b, c$) are the projections of $\boldsymbol{\mu}$ (the dipole) on the molecule-fixed inertial axes, and ϕ_{Zg} are the relevant

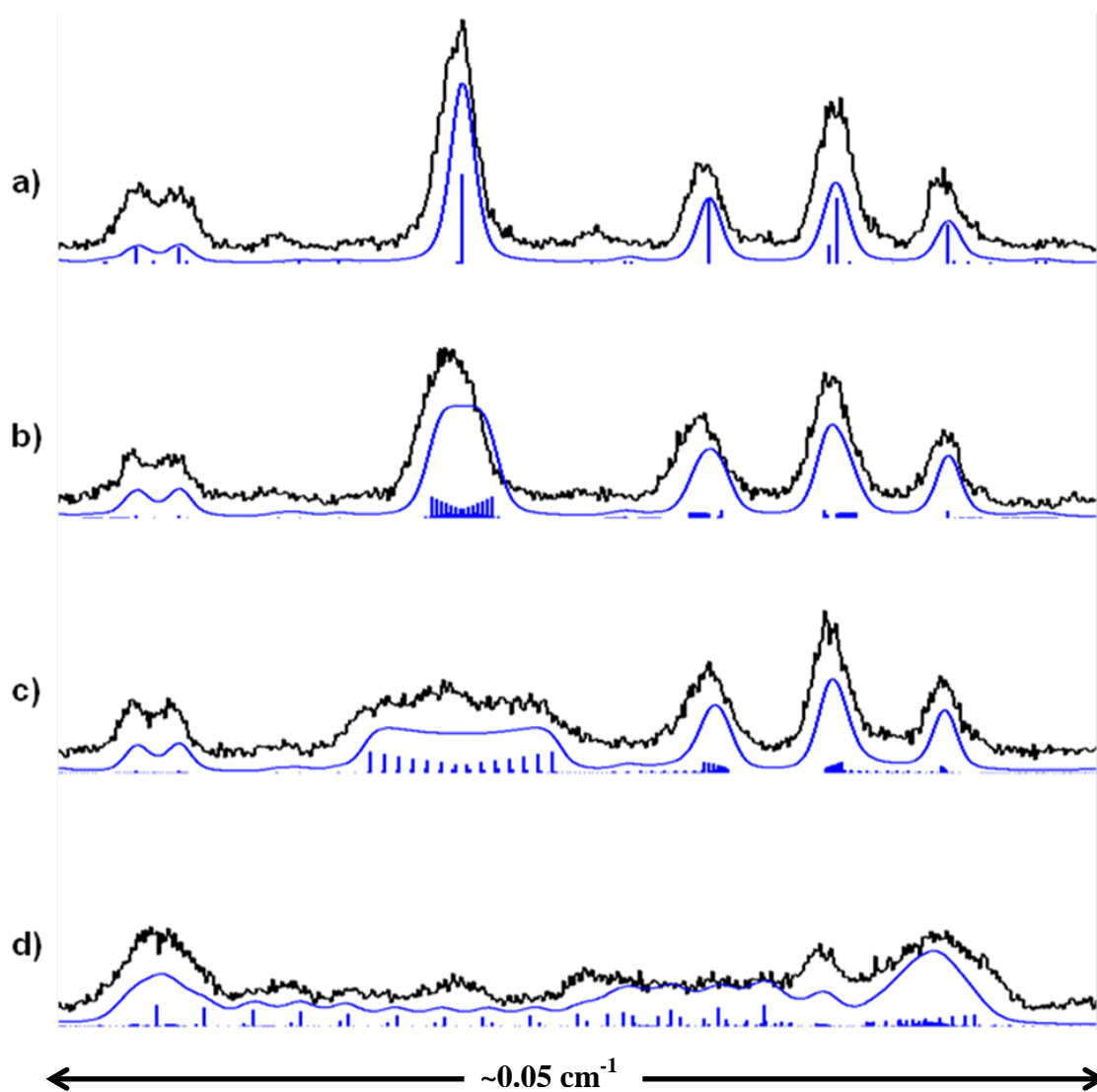


Figure D.4. Rotationally resolved electronic spectrum of *trans*-2HN in the P-branch at a) zero field, b) 211, c) 634, and d) 2115 V/cm, respectively. The most intense line in a) is assigned to the $|8,5,4\rangle \leftarrow |9,6,3\rangle$ transition.

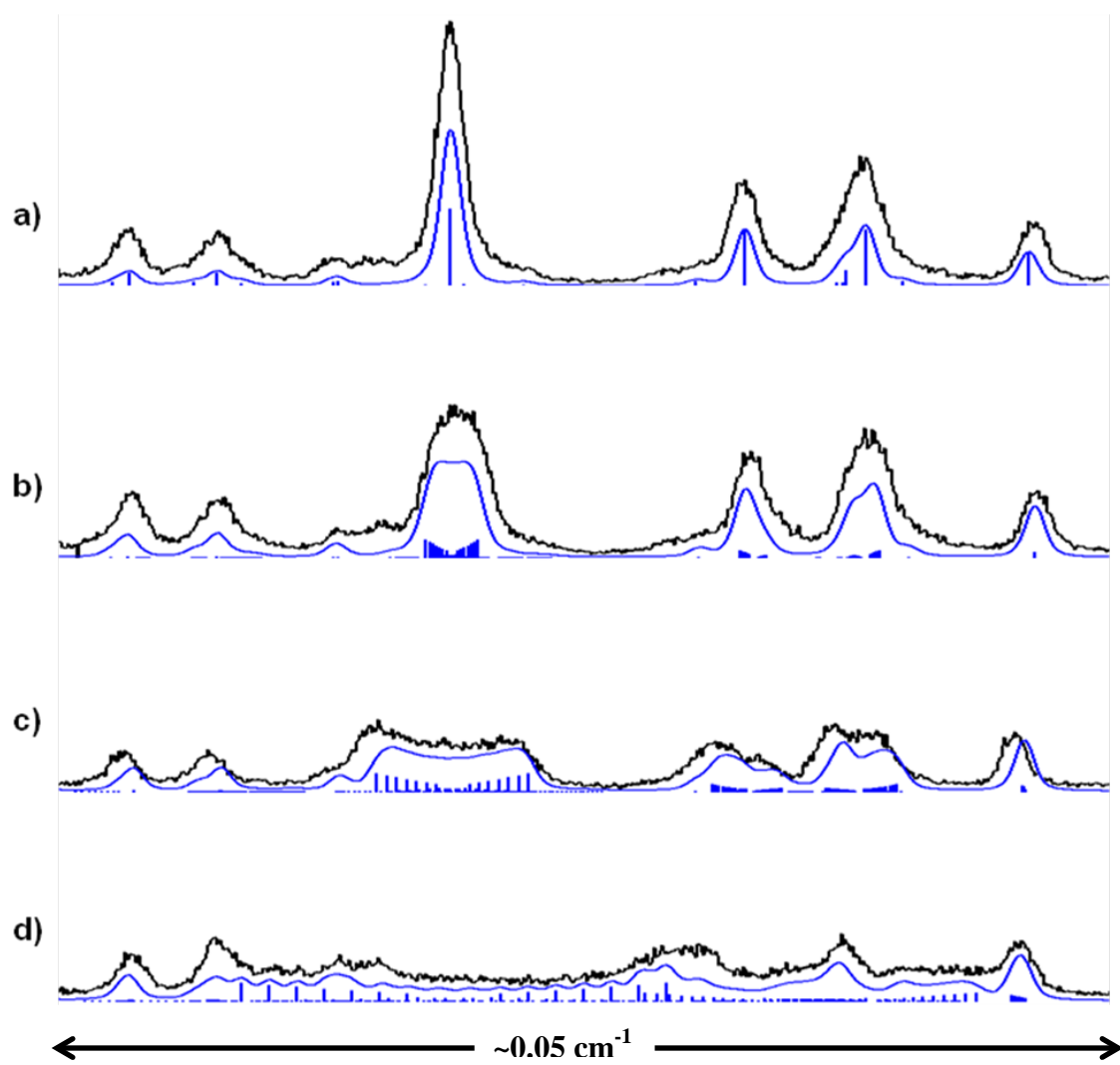


Figure D.5. Rotationally resolved electronic spectrum of *cis*-2HN in the P-branch at a) zero field, b) 211, c) 634, and d) 1776 V/cm, respectively. The most intense line in a) is assigned to the $|8,5,4\rangle \leftarrow |9,6,3\rangle$ transition.

Table D.4. Experimentally determined permanent dipole moments of *trans*- and *cis*-2HN.

Parameters	<i>trans</i> -2HN		<i>cis</i> -2HN	
	Experimental	Theoretical ^a	Experimental	Theoretical ^a
μ_a'' (D)	-0.41 (1)	-0.22	0.344 (3)	0.32
μ_b'' (D)	-1.36 (1)	-1.75	-0.951 (8)	-1.11
μ_c'' (D)	0.00 (1)	0.00	0.000 (2)	0.00
μ'' (D)	1.42 (1)	1.76	1.01 (1)	1.15
θ_a	253.2 (5) ^o	262.8 ^o	70.1 (4) ^o	73.8 ^o
μ_a' (D)	-1.05 (1)	-0.92	-0.159 (3)	0.26
μ_b' (D)	-1.05 (1)	-1.15	-1.160 (8)	1.38
μ_c' (D)	0.00 (1)	0.00	0.00 (2)	0.00
μ' (D)	1.48 (1)	1.47	1.17 (1)	1.41
θ_a	225.2 (1) ^o	231.2 ^o	97.8 (4)	79.4

^aCalculations performed at the MP2/6-31G** and CIS/6-31G** levels of theory.

direction cosines which transform from the space fixed axes system to the molecular axes system. Further detail is given elsewhere.⁴¹ The experimentally determined dipole moments of ground and excited state *trans*- and *cis*-2HN, along with their projections on each inertial axis, are reported in Table D.4.

The change in dipole moment between the S_0 and S_1 states is *trans*-2HN is best illustrated by calculating the angle the dipole moment vector makes with respect to the *a*-inertial axis, θ_a , measured counterclockwise from the positive *a*-axis. In *trans*-2HN, the dipole moment rotates upon photon absorption by negative 28(1)^o, a rotation towards the positive *a*-axis. The change in magnitude of the dipole moment is a small, positive 0.06(2) Debye (D).

In *cis*-2HN, the dipole moment rotates upon photon absorption by *positive* 27.7(8)^o, a rotation *away* from the positive *a*-axis. This $\Delta\theta_a$, though nearly equal in magnitude to that of *trans*-2HN, is in the *opposite* direction with respect to the positive *a*-

axis. The change in magnitude of the dipole moment is again a small, positive value (0.16(2) D).

Next, several electric fields were applied to origin band of the *cis*-2HNA, shown in Figure D.6. The *A* sub-band provided the largest number of transitions in which changes in intensities and energies could be followed, independent of *E* band lines, as a function of the applied electric field. We assume that the differences in vibrationally average structure within an electronic state (between *A* and *E* sub-bands) do not greatly affect the electronic properties of the complex. Therefore, the fit of Stark spectra is made easier by simultaneously using the contour fit of the *E* sub-band to verify dipole moment components determined from specific *A* sub-band transitions. We have found the dipole moment of the *A* and *E* sub-bands to be the same, within experimental error. These values are reported in Table D.5. The dipole moment components and standard deviations shown are taken from a fit of 87 lines within the *A* band at a field of 1269 V/cm, with an observed-minus-calculated (OMC) of 5.1 MHz. Figure D.7 shows the high accuracy of fits for both the *A* and *E* bands over several applied electric fields.

The values in Table D.5 clearly show that the magnitude of the complex dipole moment is larger than the vector sum of its individual molecular components (*cis*-2HN = 1.01 D in S_0 , 1.17 D in S_1 ; and $A = 1.472 \text{ D}^{48}$). Therefore, the addition of one solvent molecule significantly enhances the dipole moment of the parent *cis*-2HN. The interplay between the individual dipole moments, the overall electric field of ammonia, and the molecular polarizability of *cis*-2HN is discussed in the following section.

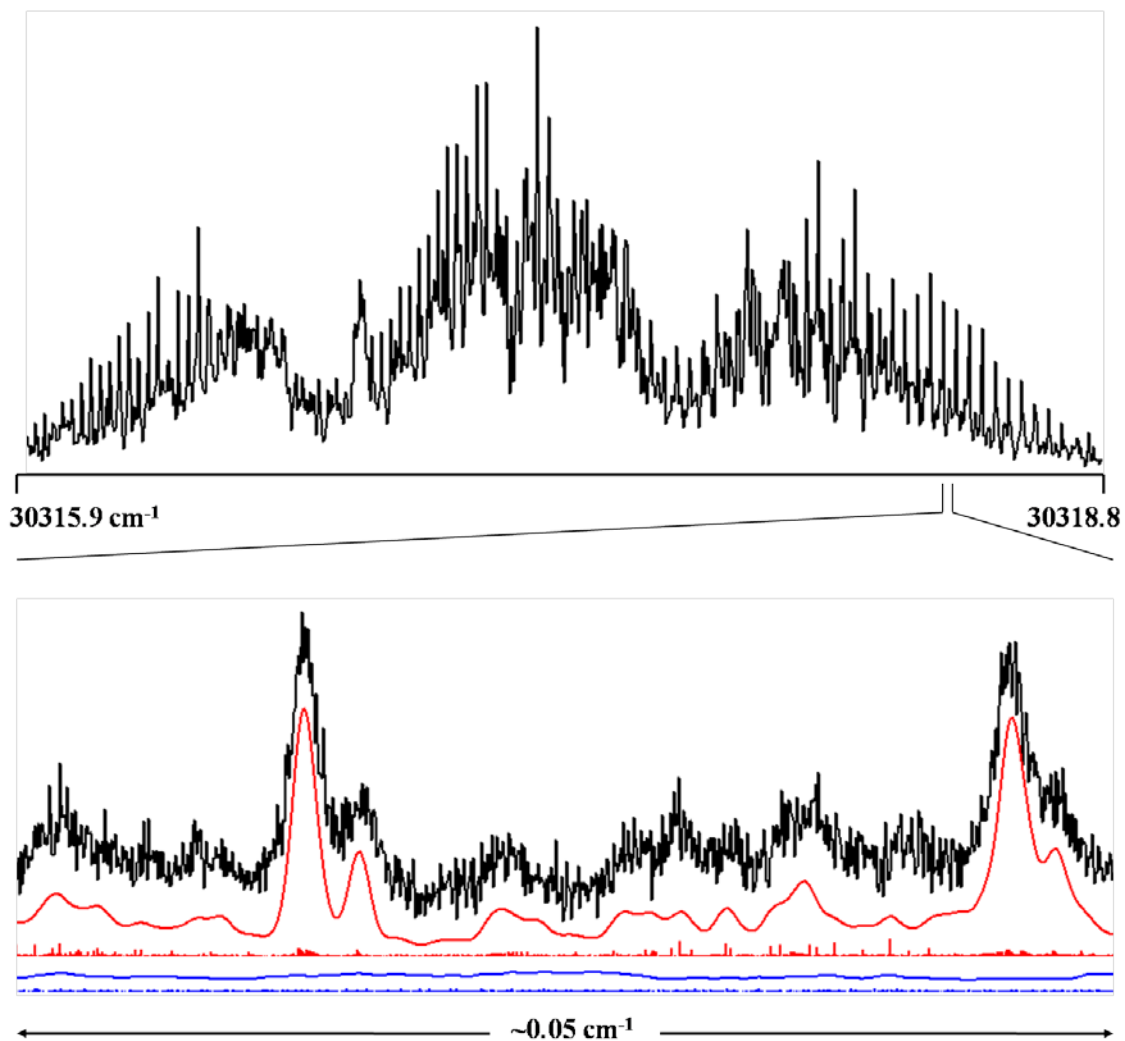


Figure D.6. The top portion is the entire *cis*-2HNA spectrum at an applied voltage of 1269 V/cm. The bottom portion shows the A band transitions in red and E band transitions in blue, respectively, at rotational resolution.

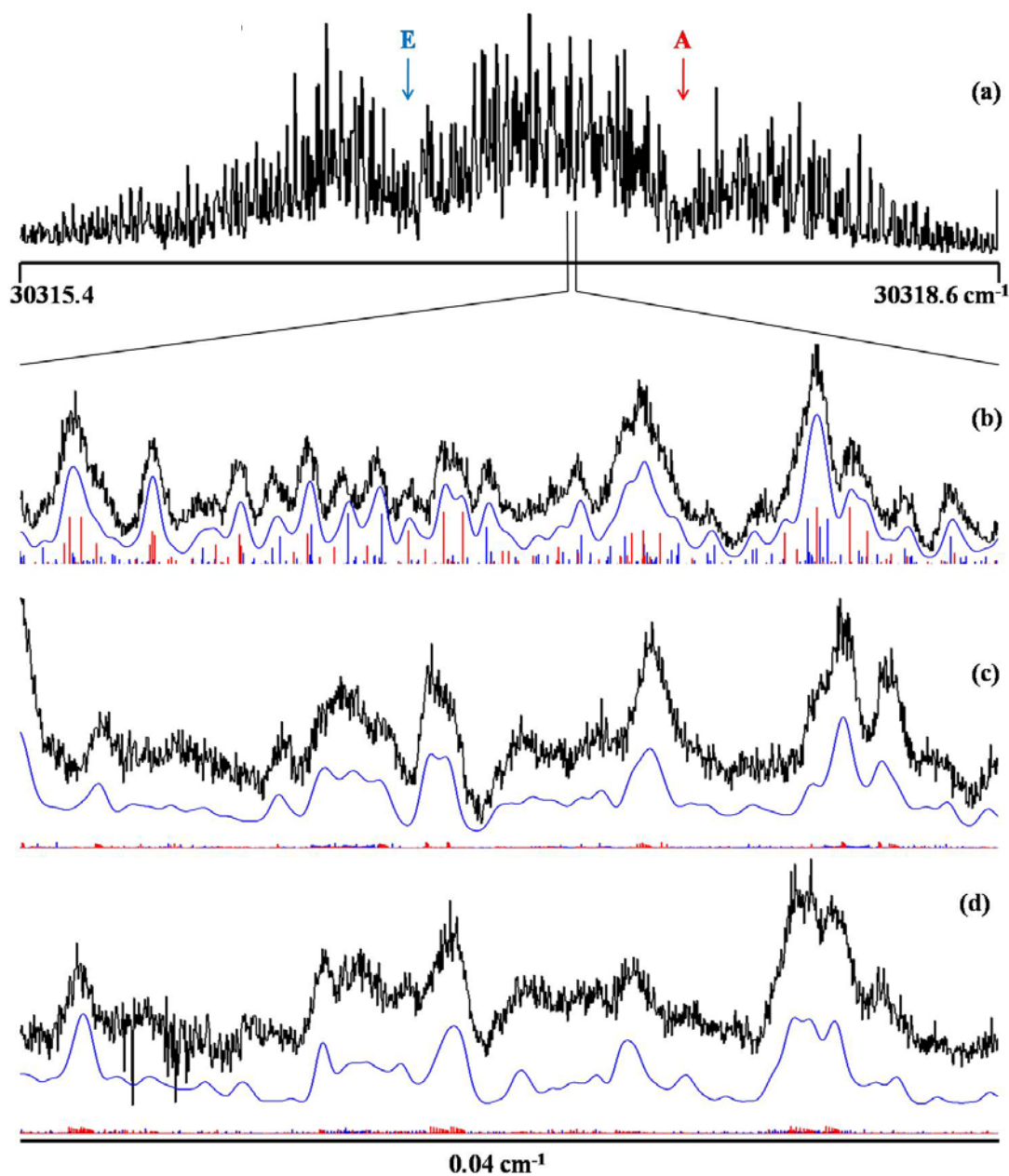


Figure D.7. Shown in (a) is the zero-field origin of the $S_1 \leftarrow S_0$ electronic spectrum of *cis*-2HNA, containing the overlapping *A* and *E* sub-bands. At full rotational resolution, (b) contains the zero-field experimental spectrum (black trace) compared to the simulated spectrum (blue trace, *A* sub-band transitions in blue, *E* sub-band transitions in red) using a convoluted line shape at a rotational temperature of 5 K and the addition of both simulated sub-bands. Spectra obtained at (c) 423 V/cm and (d) 1269 V/cm are shown along with simulated spectra.

Table D.5. Experimentally determined permanent dipole moments of *cis*-2HNA along with theoretical values.

Parameters	Experimental	Theoretical		
		MP2/CIS 6-31G**	MP2/CIS 6-31++G**	B3LYP/CIS 6-31++G**
μ_a'' (D)	-2.56 (2)	-3.14	-2.70	-3.08
μ_b'' (D)	-2.93 (4)	-3.20	-3.08	-2.92
μ_c'' (D)	0.00 (2)	-0.04	0.04	0.00
μ'' (D)	3.89 (4)	4.49	4.10	4.25
θ_a	131.2 (9) $^\circ$	134.4 $^\circ$	131.2 $^\circ$	136.4 $^\circ$
μ_a' (D)	-3.76 (2)	-3.51	-3.33	-3.33
μ_b' (D)	-3.21 (3)	-3.13	-2.91	-2.91
μ_c' (D)	0.00 (1)	0.00	-0.01	-0.01
μ' (D)	4.94 (4)	4.70	4.42	4.42
θ_a	139.6 (9) $^\circ$	138.3 $^\circ$	138.9 $^\circ$	138.9 $^\circ$

D.5 DISCUSSION

D.5.1 Electronic Dipole Moments of the Bare Naphthol Conformers

In the case of 2HN, conformational assignments have already been made using rotationally resolved electronic spectroscopy.⁴³ All previously reported differences and trends in rotational constants between the two conformers were reproduced in the field-free work. Reproduction of accurate field-free data was necessary to ensure that the correct 2HN origin bands were located before any Stark spectra were taken.

The frontier molecular orbitals of both 2HN conformers are shown in Figure D.8, along with the orbitals of naphthalene (N). The orbitals are calculated at the CIS/6-31G**

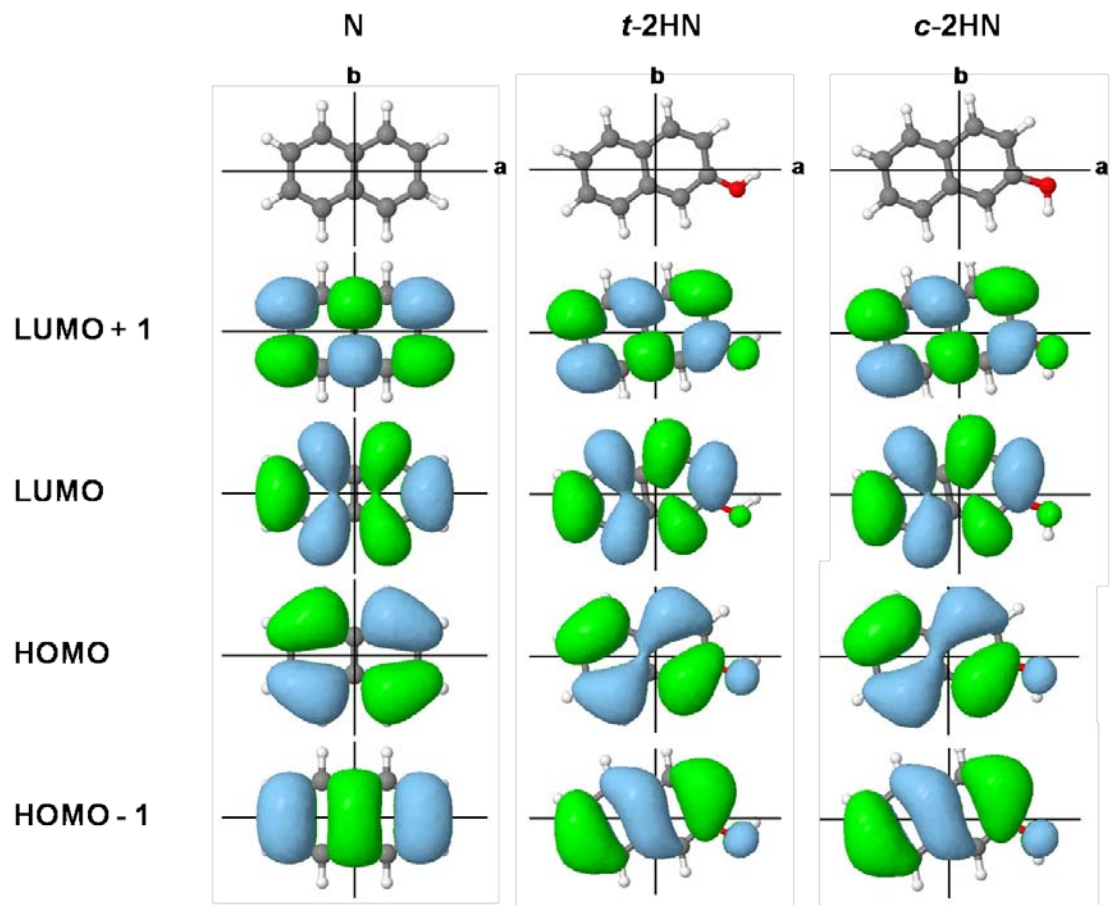


Figure D.8. Calculated frontier molecular orbitals of *trans*- and *cis*-2HN at the CIS/6-31G** level. The calculated molecular orbitals of naphthalene (N) are included for comparison.

level of theory, a significantly higher level of theory than previously reported.⁴³ The higher level of theory qualitatively reproduces the orientation of the previous STO 3-21G orbitals. The dominant one-electron excitations that participate in the $S_1 \leftarrow S_0$ transition for both *trans*- and *cis*-2HN are listed in Table D.6, along with naphthalene. The transition to the first excited state in 2HN is dominated by a HOMO \rightarrow LUMO transition, very similar to the S_2 state of naphthalene. Therefore, like the S_2 state of naphthalene, the transition moment orientation in the case of 2HN is predominantly along the short *b*-axis.

Table D.6. Dominant one-electron excitations for the listed molecules.

One-Electron Excitation	<i>trans</i> -2HN ^a	<i>cis</i> -2HN ^a	Naphthalene ^a	
			S ₁	S ₂
HOMO \rightarrow LUMO	0.654	0.649	-	0.653
HOMO-1 \rightarrow LUMO+1	0.223	0.234	-	0.237
HOMO-1 \rightarrow LUMO	-	-	0.490	-
HOMO \rightarrow LUMO+1	-	-	-0.494	-

^aValues calculated at CIS/6-31G** level of theory.

Creating electron density difference maps between the S_0 and S_1 states of 2HN is a useful way to visualize the change in electronic properties upon excitation. These weighted electron density differences are shown in the center of Figure D.9, superimposed on each conformer. The purple indicates areas of electron density gain, whereas the yellow indicates areas of electron density loss, upon excitation.

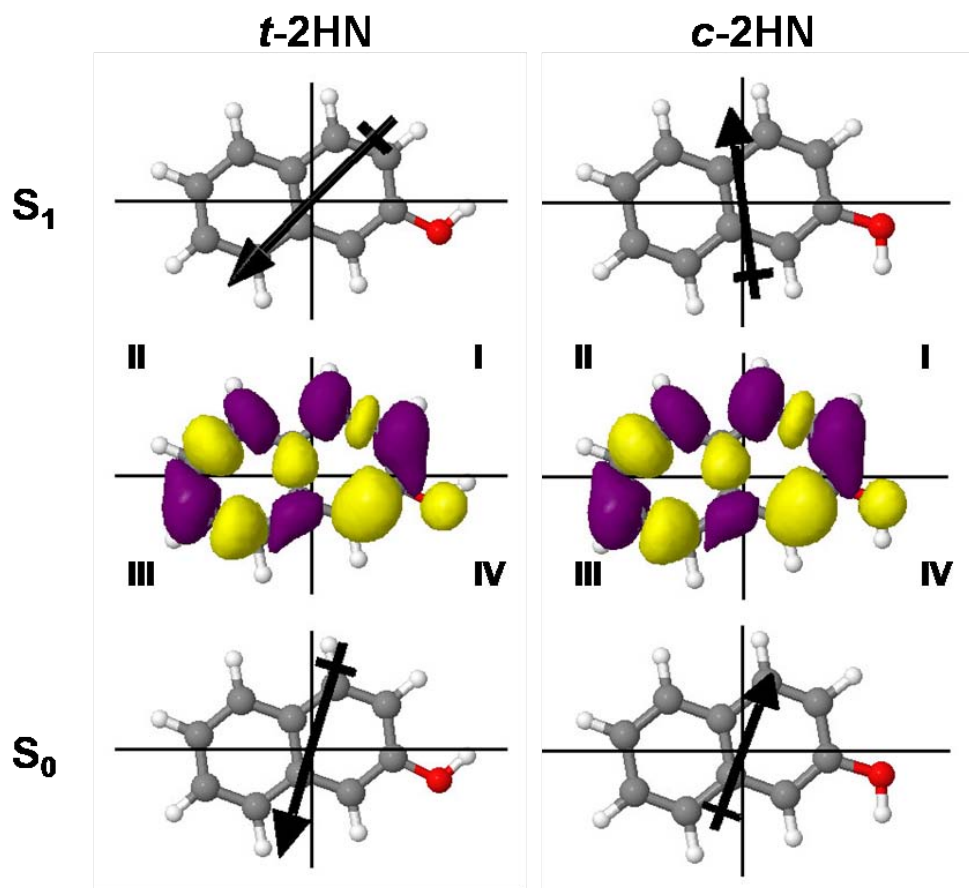


Figure D.9. Experimental ground and excited state dipole moments of *trans*- and *cis*-2HN (scale: 1.0 D = 4.0 Å). The center images are the weighted electron density differences upon $S_1 \leftarrow S_0$ excitation calculated at the CIS/6-31G** level. Purple indicates electron density gain upon excitation, whereas yellow indicates electron density loss.

The aim of Figure D.9 is to visually display a three-step description of the change in permanent EDM of both *trans*- and *cis*-2HN upon electronic excitation. First, in the bottom image, the experimentally determined S_0 dipole moments of each conformer are shown. With the aid of theory, the dipole moment orientations were determined by the fitting procedure describe earlier. It is clear from each dipole moment orientation in the a/b coordinate plane, that the lone pairs of electrons on each oxygen dominate the overall dipole moment orientation. The ground state dipole moment of *trans*-2HN points from quadrant I ($+a, +b$) into quadrant III ($-a, -b$), with the arrow head always defined as the negative end of the dipole vector. In *cis*-2HN, the opposite is true. The ground state dipole moment vector points from quadrant III into quadrant I.

Second, the electron density differences are shown above the ground state dipole moments in Figure D.9. As expected, the electron density differences for both conformers are very similar, since the transitions are made of essentially equivalent molecular orbitals, and nearly identically weighted orbital contributions. A careful examination of the overall change in electron density for each conformer provides an explanation for the directionally *different* change in permanent dipole moment of each conformer upon excitation.

Finally, the third part of Figure D.9 is the top visualization of the experimentally determined S_1 dipole moments of *trans*- and *cis*-2HN. Beginning with *trans*-2HN, the reported $\Delta\mu = 0.06(2)$ D is small. However, the $\Delta\theta_a = -28(1)^\circ$ is a more significant change. Quadrants I, II, and III are dominated by electron density gain, while quadrant IV contains the largest amount of electron density loss. Therefore, calculation suggests that electron density is donated from the oxygen to the naphthalene ring upon excitation. This

is confirmed in *trans*-2HN by the experimentally determined dipole moment magnitudes along the molecular axes. Remembering that the excited state dipole moment must obey the orientation of the oxygen atom lone pairs, as in the ground state, it is evident in Figure D.9 that the arrow head has repositioned itself in order to follow the gain in electron density within the naphthalene ring.

In *cis*-2HN, it is again the overall gain in naphthalene electron density that dictates a $\Delta\theta_a$ that is now a $+27.7(8)^\circ$. Again, the overall dipole moment in the S_1 state must still be directionally oriented by the oxygen lone pairs. The crossed end of the ground state dipole moment also rotates upon excitation towards the largest area of electron density loss, quadrant IV ($+a, -b$). This produces a S_1 dipole moment vector pointing from quadrant IV towards quadrant II. As in *trans*-2HN, the *cis*-2HN $\Delta\mu = 0.16(2)$ D is also small.

D.5.2 Electronic Dipole Moments of Naphthol Ammonia Complex

Previous studies of 1:1 solute-solvent complexes show that the magnitude and direction of the complex dipole moment is not always reproduced by a simple vector addition model (VAM) of the dipole moments of the component parts, especially in excited states.⁴⁹⁻⁵¹ The difference between the complex total dipole moment and the vector addition model is termed the induced dipole moment, μ^* . The induced dipole moment results from the redistribution of electronic charge on the solute molecule upon the

addition of solvent. In general, μ^* is defined as the polarizability (α) of the parent solute molecule times the electric field of the perturbing solvent molecule.

$$\mu^* = \alpha E \quad (\text{D.4})$$

The total EDM of the *cis*-2HNA complex is then the vector addition of three components,

$$\mu_{c2HNA} = \mu_{c2HN} + \mu_A + \mu^* \quad (\text{D.5})$$

where μ_A is the dipole moment of ammonia. All dipole moments in Equation D.5 must be represented in the inertial axes system of the complex.

The ground state dipole moment of ammonia is known experimentally from microwave Stark spectroscopy to be 1.472 D.⁴⁸ Using this value for ammonia, and the experimentally determined value for *cis*-2HN from this work, we have calculated the dipole moment induced by ammonia when in complex with *cis*-2HN, in the S_0 and S_1 states. Kang *et al.*⁴⁹ have previously used Equation C.4 by treating the electric field, E , of the solvent molecule as a multipole expansion,

$$\mu^* = \mu_A \frac{2\alpha}{R_{CM}^3} + \Theta_A \frac{3\alpha}{R_{CM}^4} \quad (\text{D.6})$$

where α is now the molecular polarizability volume of the parent in \AA^3 , and R_{CM} is the distance between the center of mass of *cis*-2HN and A in \AA . By applying the appropriate transformation into the coordinate system of the complex, Equation D.6 was used to calculate both μ_a^* (using $\mu_{A,a}$, Θ_a , and α_a) and μ_b^* (using $\mu_{A,b}$, Θ_b , and α_b). The component values in the complex inertial frame are listed in Table D.7. In using Equation D.6 to calculate the excited state induced dipole moment, we have assumed that the dipole moment of ammonia (more specifically, its entire perturbing electric field) remains unchanged upon the absorption of a photon. This assumption is substantiated by previous

Table D.7. Electronic properties of *cis*-2HN and NH₃ needed to use Equation 6. All quantities are expressed in the inertial frame of the complex.

	NH ₃		<i>cis</i> -2HN	
	S ₀	S ₁	S ₀	S ₁
μ_a (D)	-0.930 ^a	-0.882 ^a	-0.011(4)	-0.556(4)
μ_b (D)	1.141 ^a	1.179 ^a	1.01(1)	1.03(1)
Θ_a (D Å)	0.070 ^b	0.074 ^b		
Θ_b (D Å)	-0.090 ^b	-0.093 ^b		
α_a (Å ³)			17.48 ^c	23.69 ^d
α_b (Å ³)			12.93 ^c	12.85 ^d

^a reference ³⁴

^b reference ⁴¹

^c MP2/6-31G**

^d CIS/6-31G**

Table D.8. Comparison of both the induced and total dipole moments from the VAM of Equation 5 and from experiment.

	μ^*		<i>cis</i> -2HNA	
	VAM	Experiment	VAM	Experiment
S₀				
μ_a (D)	-0.22	-1.65 (1)	-1.16	-2.56 (2)
μ_b (D)	0.19	0.86 (1)	2.34	-2.93 (4)
μ_c (D)	0.00	0.00 (1)	0.00	0.00 (2)
μ (D)	0.29	1.86 (1)	2.62	3.89 (4)
S₁				
μ_a (D)	-0.29	-2.35 (1)	-1.73	-3.76 (1)
μ_b (D)	0.21	1.08 (1)	2.42	-3.21 (3)
μ_c (D)	0.00	0.00 (1)	0.00	0.00 (1)
μ (D)	0.36	2.59 (1)	2.98	4.94 (4)

work indicating that excited state proton transfer does not take place in the single ammonia complex.⁵²⁻⁵⁴

Table D.8 compares the values from the molecular electrostatic model of Equation D.6 and from experiment. The magnitude of μ^* and μ_{c2HNA} in the S_0 and S_1 states is not reproduced by the molecular polarizability model. We therefore postulate the existence of an additional contribution to the EDM of *cis*-2HNA, charge transfer (CT) between the “solvent” and “solute”, and write:

$$\vec{\mu}_{c2HNA} = \vec{\mu}_{c2HN} + \vec{\mu}_{NH_3} + \vec{\mu}_{ind} + \vec{\mu}_{CT} \quad (D.7)$$

Here, $\vec{\mu}_{c2HNA}$ is the permanent EDM of the complex, $\vec{\mu}_{c2HN}$ is the permanent EDM of bare *cis*-2HN, $\vec{\mu}_{NH_3}$ is the permanent EDM of ammonia, $\vec{\mu}_{ind}$ is the induced EDM (calculated from the molecular polarizability of *cis*-2HN and the dipole and quadrupole moments of NH_3 ,^{48,55} separated by R_{CM} , the distance between the centers of mass of *cis*-2HN and NH_3 ³⁵), and $\vec{\mu}_{CT}$ is the contribution to $\vec{\mu}_{c2HNA}$ from CT, in both electronic states. (All vectors contributing to $\vec{\mu}_{c2HNA}$ have been expressed in the principal axis system of the complex,⁴⁵ and are illustrated in Figure D.10.) Then, after completing the vector subtraction

$$\vec{\mu}_{CT} = \vec{\mu}_{c2HNA} - \vec{\mu}_{c2HN} - \vec{\mu}_{NH_3} - \vec{\mu}_{ind} \quad (D.8)$$

and taking the projection of the remaining EDM onto the hydrogen bond axis (assumed to be the internal rotation axis of NH_3), the magnitude of charge transfer was calculated using $\vec{\mu}_{CT} = Qd$, where d is the heavy atom separation along the hydrogen bond, in both electronic states.³⁵ We find, from experiment, the magnitude of CT to be $Q = 0.101 e$ in

S_0 , and $Q^* = 0.147 e$ in S_1 . (The derived values of Q and Q^* are very sensitive to the hydrogen bond axis orientation.)

We can test our experimentally determined values of Q and Q^* by using them to calculate the electronic stabilization energy of the complex, relative to the bare molecule, from the relation

$$E_{complex,rel}^{S_0,S_1} = E_{\mu\mu} + E_{\alpha\mu} + E_{CT} \quad (D.9)$$

Here, $E_{\mu\mu}$ is the interaction energy of two dipoles separated by the distance R_{CM}

$$E_{\mu\mu} = \frac{-\mu_1\mu_2}{4\pi\epsilon_0 r^3} (2 \cos \theta_1 \cos \theta_2 - \sin \theta_1 \sin \theta_2 \cos \phi), \quad (D.10)$$

$E_{\alpha\mu}$ is the interaction energy of the polarizable *cis*-2HN with the electric field of NH_3 (at the same distance R_{CM}),

$$E_{\alpha\mu} = -\frac{1}{2} \frac{\mu^*}{4\pi\epsilon_0} \left[\frac{\mu_2^2}{r^6} (3 \cos^2 \theta_2 + 1) \right]^{1/2}, \quad (D.11)$$

and E_{CT} is the interaction energy between two point charges, separated by the previously mentioned heavy atom distance d .⁵⁶

$$E_{CT} = \frac{-\mu_1\mu_2}{4\pi\epsilon_0 r^3} (2 \cos \theta_1 \cos \theta_2 - \sin \theta_1 \sin \theta_2 \cos \phi) \quad (D.12)$$

The resulting values are listed in Table D.9. Comparing the values of $E_{complex,rel}$ for the two states leads to an estimate of the red-shift of *cis*-2HN solvated by a single ammonia molecule. The result is $\Delta E_{complex,rel}^{S_1 \leftarrow S_0} = -601 \text{ cm}^{-1}$, in excellent agreement with the experimental value of -585 cm^{-1} . This agreement validates our derived values of Q and

Q^* , and shows that CT is the dominant component of the stabilization energy, $E_{complex,rel}$ (~ 85%).

It is noteworthy that the measured value of charge separation in the formation of the hydrogen bond in the ground state of *cis*-2HNA, $Q \sim 0.1 e$, is consistent with previous estimates of this quantity obtained for other systems through theoretical calculations using a Mulliken population analysis,²⁴ and by microwave spectroscopy.³⁰ The hydrogen bond in ground state *cis*-2HNA is 10% ionic, 15% ionic in the excited state.

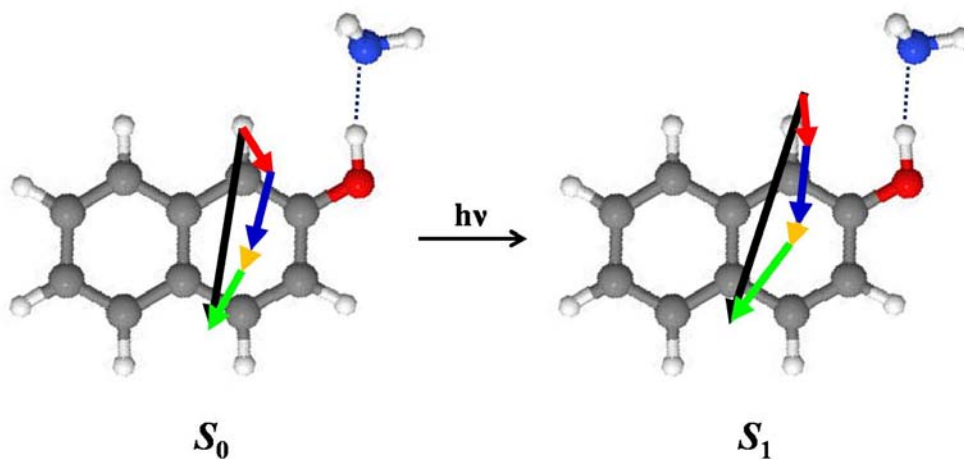


Figure D.10. The S_0 and S_1 dipole moments of *cis*-2HNA (black). This figure illustrates the components of Equation 7, where $\vec{\mu}_{c2HN}$ (red), $\vec{\mu}_{NH_3}$ (blue), $\vec{\mu}_{ind}$ (orange), and $\vec{\mu}_{CT}$ (green) add to reproduce $\vec{\mu}_{c2HNA}$ (black).

Table D.9. Calculated dipole-dipole, polarizability-electric field, and charge-charge interaction energies of *cis*-2HNA. Below, *cis*-2HN is designated as 1, and NH₃ is designated as 2. The angles θ_1 and θ_2 are the angles μ_1 and μ_2 make with the line R_{CM} .^a

	S₀	S₁
μ_1 (D)	1.01	1.17
μ_2 (D)	1.472 ^b	1.472 ^b
μ_{ind} (D)	0.29	0.36
θ_1 (deg)	9.22	19.14
θ_2 (deg)	47.81	10.70
R_{CM} (Å)	5.250 ^c	5.156 ^c
Q (e)	0.101	0.147
d (Å)	2.77 ^c	2.62 ^c
$E_{\mu\mu}$ (cm ⁻¹)	-62.4	-113.6
$E_{q\mu}$ (cm ⁻¹)	-23.6	-43.5
E_{CT} (cm ⁻¹)	-427.7	-958.0
$E_{complex,rel}$ (cm ⁻¹)	-513.7	-1115.1

^a Ref. 42

^b Ref. 34

^c Ref. 30

D.6 CONCLUSION

Rotationally resolved electronic spectroscopy has been performed in the presence of an electric field to determine the permanent electric dipole moment values for *trans*- and *cis*-2-naphthol and its single ammonia complex in the gas phase in both the ground and excited states. A quantitative measurement of the amount of charge that is transferred when the single ammonia complex (2HNA) is excited by light has also been determined. The measurement was made by comparing the permanent electric dipole moments of *cis*-2HNA in its ground (S_0) and excited (S_1) states. While the increase in electron transfer from the donor (NH_3) to the acceptor (2HN) upon excitation is small ($\sim 0.05 e$), it is sufficient to red-shift the electronic spectrum of the complex by $\sim 600 \text{ cm}^{-1}$ ($\sim 0.1 \text{ eV}$).

D.7 ACKNOWLEDGEMENTS

We would like to thank the Center for Molecular and Materials Simulations (CMMS) at the University of Pittsburgh for computing time. We also thank D. M. Miller for discussions about the jb95 Stark program, C.-H. Kang for discussions concerning induced dipole moments, D. J. Fox for discussions regarding theoretical polarizabilities, and the NSF for financial support (CHE-0615755).

D.8 REFERENCES

1. B. Xu, P. Zhang, X. Li, and N. Tao, *Nano Lett.* **4**, 1105 (2004).
2. H. Cohen, C. Nogues, R. Naaman, and D. Porath, *Proc. Natl. Acad. Sci. U.S.A.* **102**, 11589 (2005).
3. T. Kubar, P. B. Woiczikowski, G. Cuniberti, and M. Elstner, *J. Phys. Chem. B* **112**, 7937 (2008).
4. T. Kubar and M. Elstner, *J. Phys. Chem. B* **112**, 8788 (2008).
5. S. S. Mallajosyula, A. Gupta, and S. K. Pati, *J. Phys. Chem. A* **113**, 3955 (2009).
6. C. J. Chang, M. C. Y. Chang, N. H. Damrauer, and D. G. Nocera, *Biochim. Biophys. Acta* **1655**, 13 (2004).
7. C. Wittekindt, M. Schwarz, T. Friedrich, and T. Koslowski, *J. Am. Chem. Soc.* **131**, 8134 (2009).
8. E. L. Read, G. S. Engel, T. R. Calhoun, T. Mancal, T. K. Ahn, R. E. Blankenship, and G. R. Fleming, *Proc. Natl. Acad. Sci. U.S.A.* **104**, 14203 (2007).
9. T. K. Ahn, T. J. Avenson, M. Ballottari, Y.-C. Cheng, K. K. Niyogi, R. Bassi, and G. R. Fleming, *Science* **320**, 794 (2008).
10. E. Romero, M. Mozzo, I. H. M. van Stokkum, J. P. Dekker, R. van Grondelle, and R. Croce, *Biophys. J.* **96**, L35 (2009).
11. R. A. Marcus, *Adv. Chem. Phys.* **106**, 1 (1999).
12. N. J. Long, *Angew. Chem., Int. Ed.* **34**, 21 (1995).
13. S. D. Cummings, L.-T. Cheng, and R. Eisenberg, *Chem. Mater.* **9**, 440 (1997).
14. N. Mataga and T. Kubota, *Molecular Interactions and Electronic Spectra* (Marcel Dekker, New York, 1970).
15. P. Suppan, *J. Photochem. Photobiol. A* **50**, 293 (1990).
16. D. H. Levy, *Adv. Chem. Phys.* **106**, 203 (1999).
17. S. Jiang and D. H. Levy, *J. Phys. Chem. A* **107**, 6785 (2003).

18. C. A. Southern, D. H. Levy, J. A. Stearns, G. M. Florio, A. Longarte, and T. S. Zwier, *J. Phys. Chem. A* **108**, 4599 (2004).
19. T. Droz, R. Knochenmuss, and S. Leutwyler, *J. Chem. Phys.* **93**, 4520 (1990).
20. Y. Matsumoto, T. Ebata, and N. Mikami, *J. Mol. Struct.* **552**, 257 (2000).
21. H. Wang, T. C. Steimle, C. Apetrei, and J. P. Maier, *Phys. Chem. Chem. Phys.* **11**, 2649 (2009).
22. J. R. Roscioli, E. G. Diken, M. A. Johnson, S. Horvath, and A. B. McCoy, *J. Phys. Chem. A* **110**, 4943 (2006).
23. S. Horvath, A. B. McCoy, J. R. Roscioli, and M. A. Johnson, *J. Phys. Chem. A* **112**, 12337 (2008).
24. J. M. Herbert and M. Head-Gordon, *J. Am. Chem. Soc.* **128**, 13932 (2006).
25. M. P. De Haas and J. M. Warman, *Chem. Phys.* **73**, 35 (1982).
26. W. Schuddeboom, S. A. Jonker, J. M. Warman, M. P. de Haas, M. J. W. Vermeulen, W. F. Jager, B. de Lange, B. L. Feringa, and R. W. Fessenden, *J. Am. Chem. Soc.* **115**, 3286 (1993).
27. A. D. Buckingham, P. W. Fowler, A. C. Legon, S. A. Peebles, and E. Steiner, *Chem. Phys. Lett.* **232**, 437 (1995).
28. A. C. Legon, in *Structure and Bonding*, edited by P. Metrangolo and G. Resnati (Springer-Verlag, Berlin, 2008) Vol. 126, p. 17.
29. M. E. Ott and K. R. Leopold, *J. Phys. Chem. A* **103**, 1322 (1999).
30. D. L. Fiacco, Y. Mo, S. W. Hunt, M. E. Ott, A. Roberts, and K. R. Leopold, *J. Phys. Chem. A* **105**, 484 (2001).
31. S. Sensfuss, A. Konkin, H. K. Roth, M. Al-Ibrahim, U. Zhokhavets, G. Gobsch, V. I. Krinichnyi, G. A. Nazmutdinova, and E. Klemm, *Synth. Met.* **137**, 1433 (2003).
32. M. Gu, S. Wang, J. Wu, D. Feng, and W. Xu, *Chem. Phys. Lett.* **411**, 167 (2005).
33. F. Gutmann, C. Johnson, H. Keyzer, and J. Molnar, *Charge Transfer Complexes in Biological Systems* (Marcel Dekker, New York, 1997).
34. J. R. Johnson, K. D. Jordan, D. F. Plusquellic, and D. W. Pratt, *J. Chem. Phys.* **93**, 2258 (1990).

35. D. F. Plusquellic, X. Q. Tan, and D. W. Pratt, *J. Chem. Phys.* **96**, 8026 (1992).
36. W. A. Majewski, J. F. Pfanstiel, D. F. Plusquellic, and D. W. Pratt, in *Laser Techniques in Chemistry*, edited by A. B. Myers and T. Rizzo (Wiley, New York, 1995), p. 101.
37. D. F. Plusquellic, Jb95 Spectral fitting program.
38. S. Gerstenkorn and P. Luc, CRNS, Paris (1978 and 1982).
39. D. F. Plusquellic, R. D. Suenram, B. Mate, J. O. Jensen, and A. C. Samuels, *J. Chem. Phys.* **115**, 3057 (2001).
40. Lister, D. G.; Tyler, J. K.; Hoeg, J. H.; Larsen, W. *J. Mol. Struct.* **1974**, 23, 253.
41. Korter, T. M.; Borst, D. R.; Butler, C. J.; Pratt, D. W. *J. Am. Chem. Soc.* **2001**, 123, 96.
42. M. J. Frisch, G. W. Trucks, H. B. Schlegel, G. E. Scuseria, M. A. Robb, J. R. Cheeseman, J. A. J. Montgomery, T. Vreven, K. N. Kudin, J. C. Burant, J. M. Millam, S. S. Iyengar, J. Tomasi, V. Barone, B. Mennucci, M. Cossi, G. Scalmani, N. Rega, G. A. Petersson, H. Nakatsuji, M. Hada, M. Ehara, K. Toyota, R. Fukuda, J. Hasegawa, M. Ishida, T. Nakajima, Y. Honda, O. Kitao, H. Nakai, M. Klene, X. Li, J. E. Knox, H. P. Hratchian, J. B. Cross, V. Bakken, C. Adamo, J. Jaramillo, R. Gomperts, R. E. Stratmann, O. Yazyev, A. J. Austin, R. Cammi, C. Pomelli, J. W. Ochterski, P. Y. Ayala, K. Morokuma, G. A. Voth, P. Salvador, J. J. Dannenberg, V. G. Zakrzewski, S. Dapprich, A. D. Daniels, M. C. Strain, O. Farkas, D. K. Malick, A. D. Rabuck, K. Raghavachari, J. B. Foresman, J. V. Ortiz, Q. Cui, A. G. Baboul, S. Clifford, J. Cioslowski, B. B. Stefanov, G. Liu, A. Liashenko, P. Piskorz, I. Komaromi, R. L. Martin, D. J. Fox, T. Keith, M. A. Al-Laham, C. Y. Peng, A. Nanayakkara, M. Challacombe, P. M. W. Gill, B. Johnson, W. Chen, M. W. Wong, C. Gonzalez, and J. A. Pople, Gaussian 03, Revision 6.0 (Gaussian, Inc., Wallingford CT, 2004).
43. Johnson, J. R.; Jordan, K. D.; Plusquellic, D. F.; Pratt, D. W. *J. Chem. Phys.* **1990**, 93, 2258.
44. Plusquellic, D. F.; Tan, X. Q.; Pratt, D. W. *J. Chem. Phys.* **1992**, 96, 8026.
45. W. Gordy and R. L. Cook, *Microwave Molecular Spectra*, 3rd ed. (Wiley, New York, 1984).
46. Olivero, J. J.; Longbothum, R. L. *Journal of Quantitative Spectroscopy and Radiative Transfer* **1977**, 17, 233.

47. T. Brupbacher, J. Makarewicz, and A. Bauder, *J. Chem. Phys.* **101**, 9736 (1994).
48. Marshall, M. D.; Muentzer, J. S. *J. Mol. Spectrosc.* **1981**, 85, 322.
49. Kang, C.; Korter, T. M.; Pratt, D. W. *J. Chem. Phys.* **2005**, 122, 174301/1.
50. Borst, D. R.; Korter, T. M.; Pratt, D. W. *Chem. Phys. Lett.* **2001**, 350, 485
51. Reese, J. A.; Nguyen, T. V.; Korter, T. M.; Pratt, D. W. *J. Am. Chem. Soc.* **2004**, 126, 11387.
52. Oikawa, A.; Abe, H.; Mikami, N.; Ito, M. *J. Phys. Chem.* **1984**, 88, 5180.
53. Droz, T.; Knochenmuss, R.; Leutwyler, S. *J. Chem. Phys.* **1990**, 93, 4520.
54. Matsumoto, Y.; Ebata, T.; Mikami, N. *J. Mol. Struct.* **2000**, 552, 257.
55. S. G. Kukolich, *Chem. Phys. Lett.* **5**, 401 (1970).
56. G. C. Maitland, M. Rigby, E. B. Smith, and W. A. Wakeham, *Intermolecular Forces* (Clarendon Press, Oxford, 1981)